Technical Report Documentation Page

1. Report No.	2. Government Accession No.	3. Recipient's Catalog No.
FHWA/TX-12/0-6604-1		

4. Title and Subtitle	5. Report Date
UNKNOWN FOUNDATION DETERMINATION FOR SCOUR	October 2011 Published: April 2012
	6. Performing Organization Code
7. Author(s)	8. Performing Organization Report No.
Jean-Louis Briaud, Zenon Medina-Cetina, Stefan Hurlebaus, Mark Everett, Stacey Tucker, Negin Yousefpour, and Rungroj Arjwech	Report 0-6604-1
9. Performing Organization Name and Address	10. Work Unit No. (TRAIS)
Texas Transportation Institute The Texas A&M University System College Station, Texas 77843-3135	11. Contract or Grant No. Project 0-6604
12. Sponsoring Agency Name and Address	13. Type of Report and Period Covered
Texas Department of Transportation Research and Technology Implementation Office P.O. Box 5080 Austin, Texas 78763-5080	Technical Report: September 2009–August 2011
	14. Sponsoring Agency Code

15. Supplementary Notes

Project performed in cooperation with the Texas Department of Transportation and the Federal Highway Administration.
Project Title: Unknown Foundation Determination for Scour
URL: http://tti.tamu.edu/documents/0-6604-1.pdf

16. Abstract

Unknown foundations affect about 9,000 bridges in Texas. For bridges over rivers, this creates a problem regarding scour decisions as the calculated scour depth cannot be compared to the foundation depth, and a very conservative costly approach must be taken. The objective was to develop a global approach, which will reduce significantly the level of uncertainty associated with unknown foundations. This approach was developed in two parts: a data mining and inference approach where no testing at the site was necessary, and a testing approach where new tests for unknown foundations were used. The data mining and inference task made use of existing data such as soil type, known foundations on neighboring bridges, design practice, and the age of the bridge to infer the type and length of unknown foundation elements. The testing task consisted of developing two geophysical techniques, resistivity and induced polarization imaging, to obtain a picture of the soil and foundation below the surface level or river bottom. The outcome was a global framework in which one of the approaches or any combination thereof, as well as the most useful current techniques (nondestructive testing methods if necessary), can be used to decrease dramatically the uncertainty associated with the unknown foundation. The inference process was trained by using bridges where the foundation was known and verified by comparison against case histories. The two testing techniques mentioned above were tested at the National Geotechnical Testing Site on Texas A&M's Riverside campus and then against full-scale bridges selected in cooperation with TxDOT.

17. Key Words	18. Distribution Statement
Unknown Bridge Foundations, Scour, Artificial Neural Network, Resistivity, Induced Polarization	No restrictions. This document is available to the public through NTIS: National Technical Information Service Alexandria, Virginia 22312 http://www.ntis.gov

19. Security Classif. (of this report)	20. Security Classif. (of this page)	21. No. of Pages	22. Price
Unclassified	Unclassified	358	

Form DOT F 1700.7 (8-72) **Reproduction of completed page authorized**

UNKNOWN FOUNDATION DETERMINATION FOR SCOUR

by

Jean-Louis Briaud
Research Engineer, Texas A&M University

Zenon Medina-Cetina
Assistant Professor, Texas A&M University

Stefan Hurlebaus
Assistant Professor, Texas A&M University

Mark Everett
Professor, Texas A&M University

Stacey Tucker
Graduate Student, Texas A&M University

Negin Yousefpour
Graduate Student, Texas A&M University

and

Rungroj Arjwech
Graduate Student, Texas A&M University

Report 0-6604-1
Project 0-6604
Project Title: Unknown Foundation Determination for Scour

Performed in cooperation with the
Texas Department of Transportation
and the
Federal Highway Administration

October 2011
Published: April 2012

TEXAS TRANSPORTATION INSTITUTE
The Texas A&M University System
College Station, Texas 77843-3135

DISCLAIMER

This research was performed in cooperation with the Texas Department of Transportation (TxDOT) and the Federal Highway Administration (FHWA). The contents of this report reflect the views of the authors, who are responsible for the facts and the accuracy of the data presented here. The contents do not necessarily reflect the official view or policies of the FHWA or TxDOT. This report does not constitute a standard, specification, or regulation. This report is not intended for construction, bidding, or permit purposes. The engineer in charge of the project was Jean-Louis Briaud, P.E. #48690. The geoscientist in charge of the field work was Mark Everett, P.G. #5141. The United States Government and the State of Texas do not endorse products or manufacturers. Trade or manufacturers' names appear here solely because they are considered essential to the object of this report.

ACKNOWLEDGMENTS

This project was conducted in cooperation with TxDOT and FHWA. The authors thank the project director John G. Delphia and the members of TxDOT's Project Monitoring Committee. Kayvon Jahedkar in the Bryan District was instrumental to the success of the data-mining process followed by Anthony Garcia. Also, we thank Mark McClelland for his assistance with the bridge design process within TxDOT. Thank you to the Haynes Coastal Lab and John Reed for assisting with the laboratory experiments at the beginning of the project. We also thank Brad Carr at Advanced Geosciences, Inc. (AGI) for his continual support with the geophysical systems.

TABLE OF CONTENTS

LIST OF FIGURES

LIST OF TABLES

EXECUTIVE SUMMARY

BACKGROUND

There are approximately 60,000 bridges across the United States identified as having unknown foundations as of 2005. Most of the bridges were built between 1950 and 1980, which coincides with the construction of the Interstate Highway System. Texas alone has over 9,000 bridges with unknown foundations, 85 percent of which are over local roads. Local government entities such as counties or private companies typically designed and constructed these bridges, often categorized as "off-system" bridges. The missing substructure information associated with unknown foundations has made the safety monitoring of bridges very difficult, especially the scour-critical bridges.

The FHWA has required all states to eliminate their unknown foundations from the National Bridge Inventory (NBI). Specifically, this means updating Item 113, Scour-Critical Bridges that are coded as "U," bridges with unknown foundations that have not been evaluated for scour. TxDOT can use the methods developed in the project as new mediums to determine the substructure characteristics for unknown bridge foundations to accommodate the scour evaluation for these bridges.

APPROACH TO SOLVE THE PROBLEM

The approach to solve this problem has two components: an evidence-based approach and an experiment-based approach. The proposed evidence-based methodology consists of a deterministic and a probabilistic approach. Both approaches are based on a case study of bridges in the Bryan District of TxDOT. Data are collected for approximately 185 bridges over-river with known foundations. This database provides sufficient data for inferences about bridge foundations, the regional design, and construction criteria, as well as characteristics of the soil.

The dead load and live load of a bridge foundation is computed without going through the time-consuming exact methods using a proposed load approximation method. The dead load, live load, and bearing capacity are estimated for piers of bridges in the collected database.

The deterministic approach is to apply Artificial Neural Networks (ANN) to recognize the inherent pattern in bridge substructure design and to generalize this pattern to unknown foundation bridges (UFB). This allows for making predictions on substructure type and dimension with a reasonable accuracy with no need to perform time-consuming and costly experiments.

The probabilistic approach, on the other hand, aims to generate a number of possible answers for an unknown foundation, each with a certain amount of plausibility. Probabilistic predictions on substructure type, dimensions, and soil characteristics based on the evidence provided by collected data are made using Bayesian methods of inference.

The proposed experiment-based methodology consists of a vibration method, electrical resistivity imaging, and induced polarization imaging. Through laboratory and field experiments, each of these methods aims to identify the depth of bridge foundations. The electrical resistivity imaging (ERI) and induced-polarization imaging are conducted beneath the bridge and do not contact the structure. This is an advantage over the vibration method, which uses the super structure of the bridge.

OUTCOME OF THE STUDY

The deterministic approach first establishes what the type of the foundation is and then, if the foundation is recognized to be deep (either concrete, steel piling, or drilled shafts), it selects the appropriate ANN model based on the availability of soil-boring data to predict the depth of the foundation. The ANN model approximates the pile embedment depth based on the bridge load, soil properties, location, and year built.

The probabilistic approach also selects the appropriate ANN model based on the foundation type and soil-boring data availability in order to make a prediction on the bearing capacity of the foundation. The bridge load, soil properties, location, and the year built are used to approximate the bearing capacity. Markov Chain Monte Carlo (MCMC) simulations are performed using the predicted bearing capacity. MCMC simulations obtain probability distributions for foundation type, foundation dimensions, and soil resistance parameters, depending on the availability of information about each of these elements.

The vibration method is based on the principle that a foundation that is embedded deeper will be stiffer than a shallow foundation. By measuring the vibration of bridge piers using accelerometers after they are excited, the accelerations can be transformed in the frequency domain using a Fast Fourier Transform. From this, the amplitude of the response versus the frequency is obtained. A deeper, and therefore stiffer, structure will have a higher frequency response.

Electrical resistivity imaging provides a fast and efficient geophysical method for determining whether a foundation is embedded to 5 m (16.40 ft) depth or greater. Researchers can deploy the method in moderate to heavily vegetated, water-covered environments using underwater electrodes, such as those specially designed for this project. While 3-D resistivity imaging can be done, it is not recommended for routine bridge foundations. Similarly, induced polarization (IP) imaging can be used in moderate to heavily vegetated environments. IP is not recommended for water-covered areas at this time. IP provides the depth of foundations when the depth of penetration of the data is deeper than the foundation and provides a minimum depth of foundations when the depth of penetration is shallower than the foundation.

SIGNIFICANCE OF THE STUDY

Results of predicted versus actual pile depth show that the ANN models proposed in this study are able to fairly accurately predict the embedment depth of deep foundations (R^2 value >0.85). ANN models also were successfully able to predict the bearing capacity of bridge foundations. MCMC simulations provide posterior distributions and cumulative density functions for foundation type, foundation dimension, and soil properties. Posterior distribution allows for probabilistic inversion of bridge unknown parameters. This includes estimating the expected value, standard deviation, and confidence intervals for bridges of unknown parameters.

Despite the promising laboratory work using the vibration method, the researchers shifted their efforts to enhance the geophysical team with IP testing because a dominant frequency could not be identified in field work and because numerical modeling showed that the frequency did not change dramatically with a change in the pile depth of embedment. The researchers find, in general, that it is possible to image and identify foundations that possess large resistivity contrasts. Similarly, IP can be used in conjunction with resistivity testing to provide more clarity to the resistivity testing as the arrays used are very similar.

PART I.
BACKGROUND

Chapter 1.
UNKNOWN BRIDGES ACROSS TEXAS

Following the FHWA requirement to inspect and monitor all bridges across the nation, the Departments of Transportation (DOTs) across the United States have implemented different measures to determine the bridges' vulnerability to failure. As a result, researchers found that for a considerable number of bridges, the substructure information was not available. This unavailability has made it extremely difficult to evaluate the bridge safety due to hydraulic hazards such as scour because the foundation properties (type and dimension) are essential for determining the bridge vulnerability to scour.

As of 2005, approximately 60,000 bridges throughout the United States have been identified as having unknown foundations. Most of these bridges were built between 1950 and 1980, which coincides with the construction of interstate system. These bridges are mostly classified as off-system bridges, those that counties and local agencies built and owned, and later a DOT inherited. Therefore, it is expected that these types of bridges be located on local roads and arterials. Table 1-1 shows the number of unknown foundation bridges (UFB) across the United States based on their functional classification specified in item 26 of NBI. Figure 1-1 shows the distribution of these bridges over the years (Stein and Sedmera 2006).

The number of UFBs is significantly different across states. It varies from states where the number of bridges is relatively high but the majority of which are located on local and minor roads to states where the number is relatively low but the majority are located on principal arterials. In other words, both the number and the functional classification of UFBs determine the potential risk associated with unknown foundation bridges.

Texas has the largest population of bridges with unknown foundations in the United States (9,113). Among those only 33 (0.4 percent) are located on principal arterials. By contrast, Alaska has only 151 bridges with unknown foundations, but a significantly higher percentage of these are located on principal arterials (37 bridges or 25 percent). Although researchers expected to see very few UFBs built in recent years, 69 UFBs are located on principal arterials and were built between 2000 and 2005 (Stein and Sedmera 2006).

Table 1-1. Number of Unknown Foundation Bridges across the United States (Stein and Sedmera 2006).

	Rural Functional Classification						Urban Functional Classification						
	1	2	6	7	8	9	11	12	14	16	17	19	
State	**Principal Arterial — Interstate**	**Principal Arterial-Other**	**Minor Arterial**	**Major Collector**	**Minor Collector**	**Local**	**Principal Arterial — Interstate**	**Principal Arterial — Other**	**Minor Arterial**	**Major Collector**	**Minor Collector**	**Local**	**Totals**
Alabama	4	70	79	503	843	1,662	4	5	25	39	55	164	**3,453**
Alaska	7	29	4	19	23	46	1	0	1	7	1	13	**151**
Arizona	0	0	0	1	0	33	0	0	1	3	5	25	**68**
Arkansas	0	1	11	48	4	10	0	0	1	2	0	2	**79**
California	4	23	112	318	305	993	3	9	71	84	60	126	**2,108**
Colorado	1	2	9	4	3	8	0	0	0	1	1	0	**29**
Connecticut	0	0	0	0	0	0	0	0	0	0	0	0	**0**
Delaware	0	0	0	0	0	0	0	0	0	0	0	0	**0**
DC	0	0	0	0	0	0	0	0	0	0	0	8	**8**
Florida	3	110	111	224	188	837	13	27	74	136	280	444	**2,447**
Georgia	3	346	434	1,227	565	1,780	0	32	178	288	188	406	**5,447**
Hawaii	0	0	0	0	0	0	0	0	0	2	0	8	**10**
Idaho	0	1	1	71	74	318	0	0	3	6	9	14	**497**
Illinois	0	0	0	1	0	1	0	0	0	0	0	0	**2**
Indiana	0	1	0	140	263	828	0	0	42	101	75	156	**1,606**
Iowa	0	1	3	92	256	1,371	0	0	0	11	6	30	**1,770**
Kansas	0	0	0	0	1	5	0	0	0	0	0	0	**6**
Kentucky	0	0	0	0	0	1	0	0	0	0	0	1	**2**
Louisiana	17	13	180	527	488	2,963	12	1	30	84	58	401	**4,774**
Maine	6	2	1	4	3	76	2	0	0	2	5	4	**105**
Maryland	0	0	0	0	0	4	0	0	0	0	0	1	**5**
Massachusetts	2	0	10	25	16	70	0	1	42	95	45	52	**358**
Michigan	3	36	43	157	13	360	2	2	9	10	11	11	**657**
Minnesota	0	0	2	16	24	161	0	0	0	4	2	7	**216**
Mississippi	0	16	11	1,205	187	4,790	0	0	32	54	101	137	**6,533**
Missouri	0	0	1	6	1	0	0	0	0	0	0	0	**8**
Montana	2	1	5	1	429	1,244	0	0	0	1	0	2	**1,685**
Nebraska	0	0	0	0	0	0	0	0	0	0	0	0	**0**
Nevada	0	0	2	1	3	24	0	0	1	10	1	3	**45**
New Hampshire	0	0	0	3	6	22	0	0	2	5	4	1	**43**

Table 1-1. Number of Unknown Foundation Bridges across the United States (Stein and Sedmera 2006) (Continued).

	Rural Functional Classification						Urban Functional Classification						
	1	2	6	7	8	9	11	12	14	16	17	19	
State	**Principal Arterial — Interstate**	**Principal Arterial — Other**	**Minor Arterial**	**Major Collector**	**Minor Collector**	**Local**	**Principal Arterial -Interstate**	**Principal Arterial — Other**	**Minor Arterial**	**Major Collector**	**Minor Collector**	**Local**	**Totals**
New Jersey	0	6	7	11	7	53	0	4	20	23	20	14	**165**
New Mexico	0	7	7	46	41	254	1	0	13	27	39	33	**468**
New York	0	0	0	1	1	13	0	2	7	9	4	12	**49**
North Carolina	0	29	95	464	700	3,949	0	2	30	81	77	379	**5,806**
North Dakota	0	0	3	210	0	1,780	0	0	0	5	3	7	**2,008**
Ohio	0	2	1	13	23	222	0	0	2	1	5	12	**281**
Oklahoma	0	0	9	1	1	9	1	2	5	0	0	0	**28**
Oregon	5	58	90	425	235	801	4	2	18	50	51	56	**1,795**
Pennsylvania	0	0	0	0	1	7	0	0	0	0	0	0	**8**
Rhode Island	0	0	0	0	0	0	0	0	0	0	0	0	**0**
South Carolina	21	49	125	592	443	1,904	6	0	20	49	96	144	**3,449**
South Dakota	0	0	0	1	0	0	0	0	0	0	0	0	**1**
Tennessee	6	8	32	74	252	654	0	0	8	27	24	73	**1,158**
Texas	9	18	40	199	190	6,524	2	4	205	463	319	1,140	**9,113**
Utah	0	0	0	1	0	4	0	0	1	0	0	2	**8**
Vermont	0	2	5	29	26	155	0	0	2	4	9	6	**238**
Virginia	0	0	0	0	2	16	0	0	0	0	0	0	**18**
Washington	0	0	1	47	39	102	0	0	5	4	3	5	**206**
West Virginia	0	0	0	0	0	0	0	0	0	0	0	0	**0**
Wisconsin	0	0	0	0	0	0	0	0	0	0	0	0	**0**
Wyoming	0	0	1	0	43	347	1	0	0	3	7	13	**415**
Puerto Rico	0	0	21	70	40	77	0	0	9	23	36	36	**312**
Totals	93	831	1,456	6,777	5,739	34,478	52	93	857	1,714	1,600	3,948	**57,638**

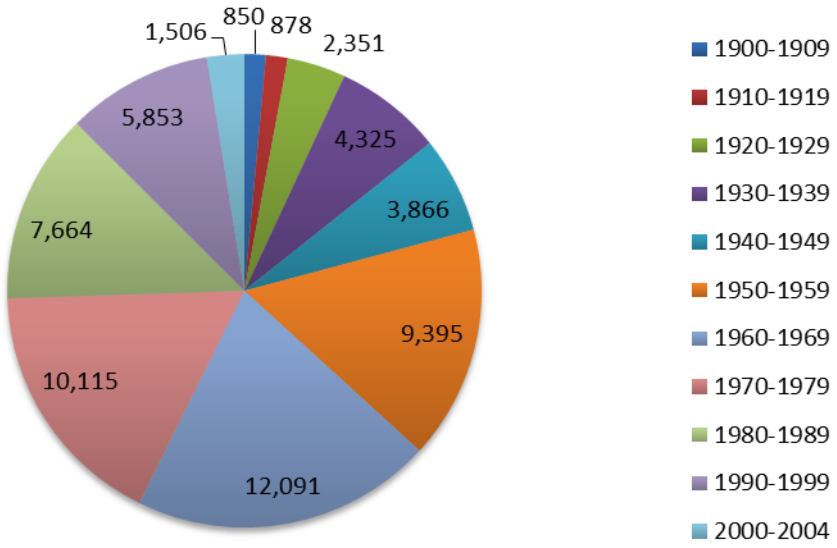

Figure 1-1. Number of UFBs, according to Year of Construction.

Chapter 2.
COMPUTING METHODS FOR DETERMINATION OF UNKNOWN FOUNDATION OF BRIDGES

INTRODUCTION

Researchers have tackled the problem of unknown foundations in the United States with different approaches and occasionally a combination of different methods. There are a number of studies on applying nondestructive testing (NDT) methods to obtain information about unknown bridge foundations, while very few studies have used statistical, computational, and numerical solutions to infer foundation properties. Regarding the uncertainty of results given by these methods and the uncertain nature of scour, risk-based approaches have shown potential to perform more rational assessment and classification of UFBs.

This section introduces a comprehensive review on computing methods and risk-based approaches for predicting pile depth and reviews scour depth at bridge piers. Special attention will be placed on the use of soft-computing methods such as Artificial Neural Networks (ANNs) and in probabilistic methods such as Bayesian.

ANNs are massively parallel computational models initially proposed by McCulloch and Pitts (Haykin 1999). ANNs have been widely used in various geotechnical applications including pile capacity prediction, soil modeling, site characterization, settlement of structures, slope stability, liquefaction, soil permeability and hydraulic conductivity, soil compaction, soil swelling, and classification of soils (Shahin 2008).

Bayesian methods originated from Bayes' Theory and the definition of conditional probability that Thomas Bayes presented. Due to the large degree of uncertainty associated with current geotechnical engineering design and practice (such as laboratory tests, field measurements, and constitutive modeling of geomaterials), Bayesian methods of inference can be extremely useful in this field (Yuen 2010).

APPLICATION OF NEURAL NETWORK FOR DETERMINATION OF BRIDGE FOUNDATIONS AND SCOUR DEPTH EVALUATION

A number of studies have applied ANNs to infer scour depth at bridge piers, but only a few used probabilistic neural network (PNN) analysis. Also, some studies have explored the use of ANNs to interpret the results of NDTs for determination of UFBs.

Zounemat-Kermani et al. (2009) used ANNs to model the maximum scour depth at pile groups under clear-water scour condition. Two ANN models (feed forward back propagation [FFBP] and radial basis function [RBF]), along with a neuro-fuzzy inference model, were used to predict the depth of the scour. Networks with different combination of input variables like flow depth, mean flow velocity, critical flow velocity, soil grain mean diameter, pile diameter, distance between the piles (gap), number of piles normal to the flow, and the number of piles in-line with flow, were considered for the network training. They also trained a network with dimensionless parameters. Results showed that the FFBP-NN model provided a better prediction rather than the RBF model. Figure 2-1 shows the observed versus predicted for calibration and validation data sets. A sensitivity analysis on the results showed that the pile diameter in dimensional variables and the ratio of pile spacing to pile diameter in non-dimensional parameters were the most relevant parameters affecting scour depth prediction (Zounemat-Kermani et al. 2009).

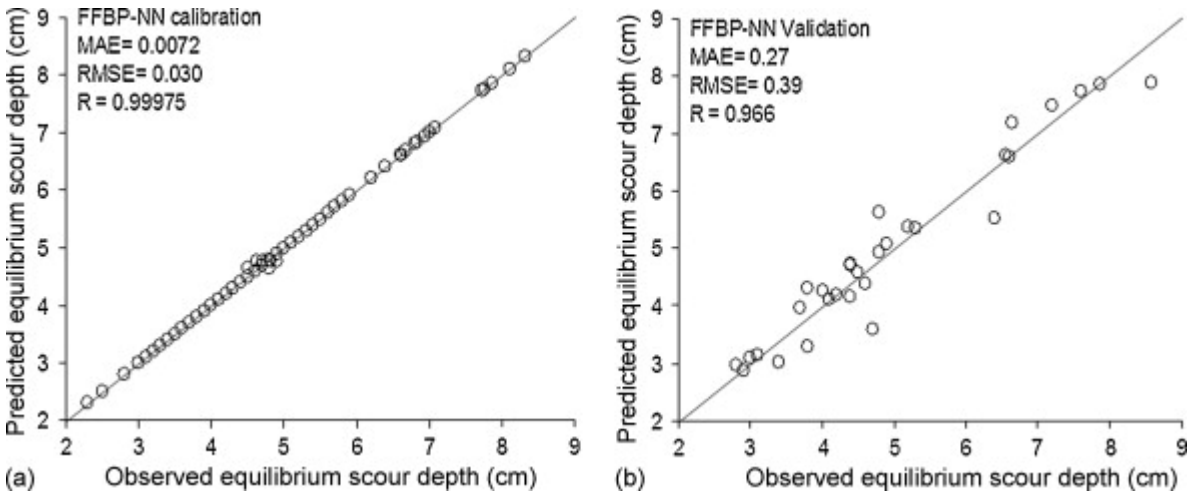

Figure 2-1. Observed Scour Depth versus Predicted Scour Depth for FFBP-NN Model (Zounemat-Kermani et al. 2009).

Kaya (2010) performed an ANN analysis to study the pattern of local scour at bridge piers. This study contained 380 measurements at 56 bridges in 13 states using the FHWA database. A three-layer feed-forward neural network with Levenberg-Marquardt optimization algorithm was designed. Bed load conditions, pier shape, type, skew, length and width, flow depth and velocity, and grain size were considered as input variables, while the scour depth was defined as the output or target variable. Figure 2-2 shows the ANN's prediction results for scour depth..

Lee et al. (2007) also applied back propagation neural network to predict the local scour depth at bridge piers. Normalized velocity, grain size, and flow depth were the inputs of model. Also, different numbers of hidden units and model optimization parameter values (learning rate and momentum factor) were examined to obtain the optimized network (Lee et al. 2007).

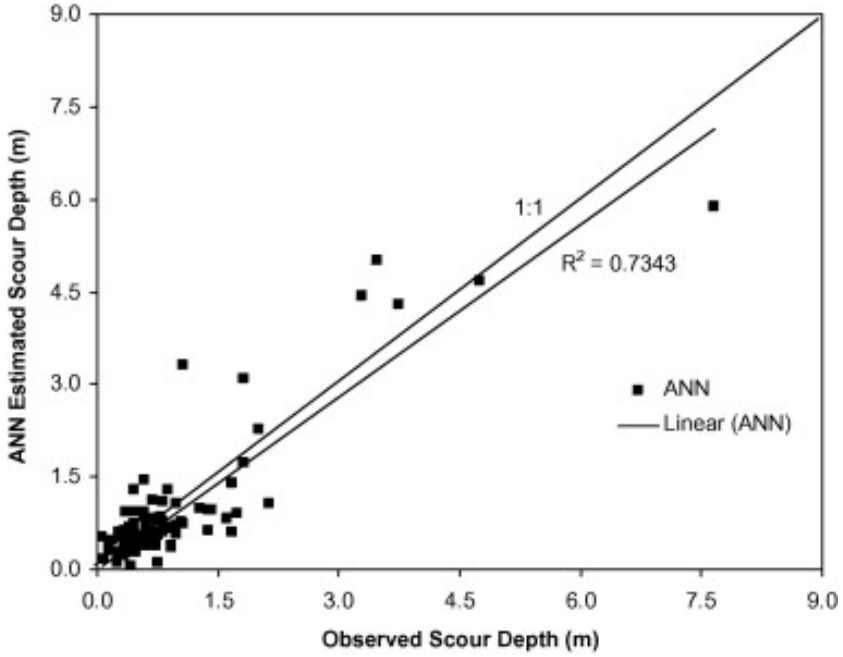

Figure 2-2. ANN Prediction Results for Scour Depth (Kaya 2010).

Bateni et al. (2007) proposed multilayer perceptron (MLP) and radial basis function (RBF) networks to predict scour depth at bridge piers. They defined scour depth to be a function of flow depth, mean velocity, critical flow velocity, mean grain diameter, and pier diameter. A neuro-fuzzy adaptive model was also designed with the same input variables. Results showed that MLP and neuro-fuzzy adaptive models can predict scour depth much more accurately than the existing methods (Bateni et al. 2007).

Rix (Rix 1995) used ANNs to predict the length of piles from synthetic sonic mobility test data. An ANN was used to enhance the interpretation of noisy non-destructive test results. A two-dimensional element shown in Figure 2-3 was considered to represent the foundation geometry (pile cap and pile bent). A force applied on top of the element and the response (particle velocity) was measured at the same location to obtain sonic mobility data. The ANN was trained with 500 synthetic mobility curves generated from randomly selected foundation geometries and material properties. Each sonic mobility curve was composed of 100 discrete frequencies evenly spaced from 0 to 1000 Hz. The ANN was able to properly map the frequencies in the mobility curves with the pile length (Rix 1995).

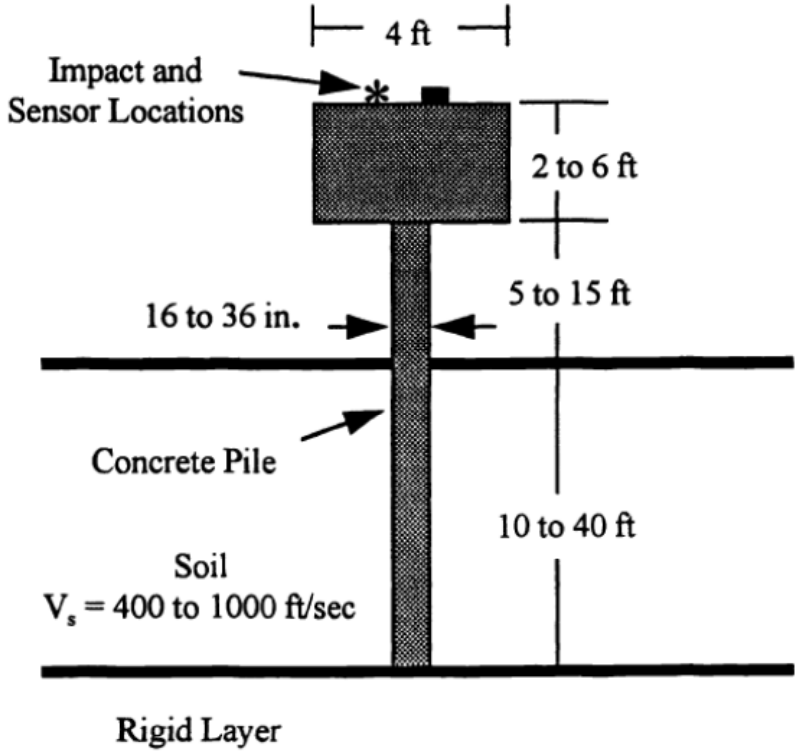

Figure 2-3. Foundation Geometry and Material Properties (Rix 1995).

RISK-BASED AND COMPUTATIONAL APPROACHES FOR DETERMINATION OF UNKNOWN BRIDGE FOUNDATIONS

NCHRP Risk-Based Approach (Stein and Sedmera 2006)

Stein and Sedmera (2006) proposed a risk-based approach to manage bridges with unknown foundations that were susceptible to natural hazards such as scour. Their procedure consisted of collecting appropriate data, estimating risk of failure from an estimated failure probability and associated economic losses, and selecting the appropriate management plan based on the computed risk. Risk was defined as the product of probability of failure and cost of failure of a given bridge. The total cost of failure was defined as the sum of bridge replacement, detour costs (time and mileage), and the cost of life losses.

The proposed risk-management guideline consists of three phases as shown in Figure 2-4; the first phase states that if the bridge is categorized as high priority, then an aggressive plan such as foundation reconnaissance, countermeasure/retrofit, bridge replacement, or closure is required. The second phase verifies if the bridge meets the minimum performance level (MPL) or not. If not, the bridge should be qualified for the most aggressive plan of actions (POAs). The third phase compares the risk of bridge failure with the cost of installing countermeasures. Eventually, the bridge is eligible for either countermeasures or automated monitoring.

The general risk guideline was applied specifically for scour failure by using HYRISK methodology. Investigations showed that scour vulnerability estimation given by HYRISK methodology was strongly correlated with the scour vulnerability specified in NBI item 113. The probability of failure was estimated based on interviews with transportation officials from 25 states about historical scour failures. These data suggest the average probability of failure is about 1 in 5000 per year (0.002). However, the average annual probability of failure given by HYRISK for all over-water bridges was unreasonably large and led to an exaggerated risk values. Thus, the original probability of failure produced by HYRISK was adjusted downward according to the probability of failure based on interviews.

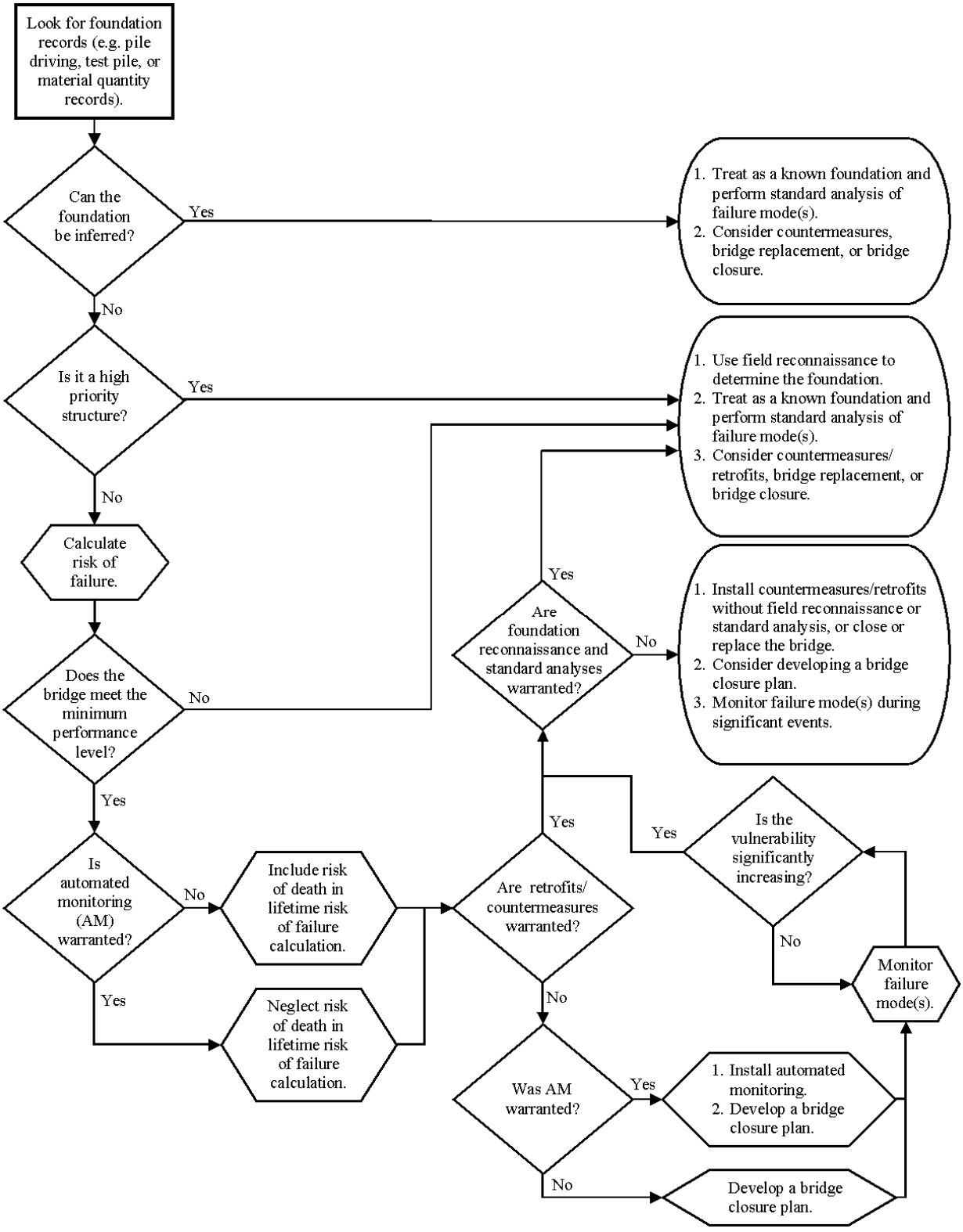

Figure 2-4. General Risk Management Guidelines Flowchart (Stein and Sedmera 2006).

In order to validate the method performance, the research team used 60 case studies (bridges with known foundations) from six states. Results revealed that the proposed method of risk calculation could successfully identify the required POA for bridges corresponding to their known scour evaluation.

Florida DOT Method for Reclassifying Unknown Foundations (McLemore et al. 2010)

The FHWA issued a memorandum to all the state departments of transportation requesting that they address their bridges with unknown foundations by November 2010. In response to this, the Florida Department of Transportation (FDOT) developed a set of risk-based guidelines to assist bridge owners in evaluating and prioritizing plans of action—including investigation, countermeasures, monitoring, rehabilitation, or replacement—for managing bridges with unknown foundations.

According to the FHWA recommendations, the following procedures were included in the FDOT approach to reclassify the UFBs:

- Locate historical standard sheets, construction specifications, and design guidance.
- Risk-based evaluation based on the NCHRP.
- ANN.
- Reverse engineering.
- NDT.

The guideline starts with an attempt to locate the as-built plans for as many bridges as possible, performing scour evaluations based on foundation geometry specified in the plans, and finally updating item 113 (scour vulnerability of bridge) of the NBI. Figure 2-5 shows the guideline flowchart.

For bridges with missing plans, the next phase would be to calculate the risk of failure and follow the risk-based approach that NCHRP proposed. The NCHRP procedure was slightly modified to address Florida's bridges.

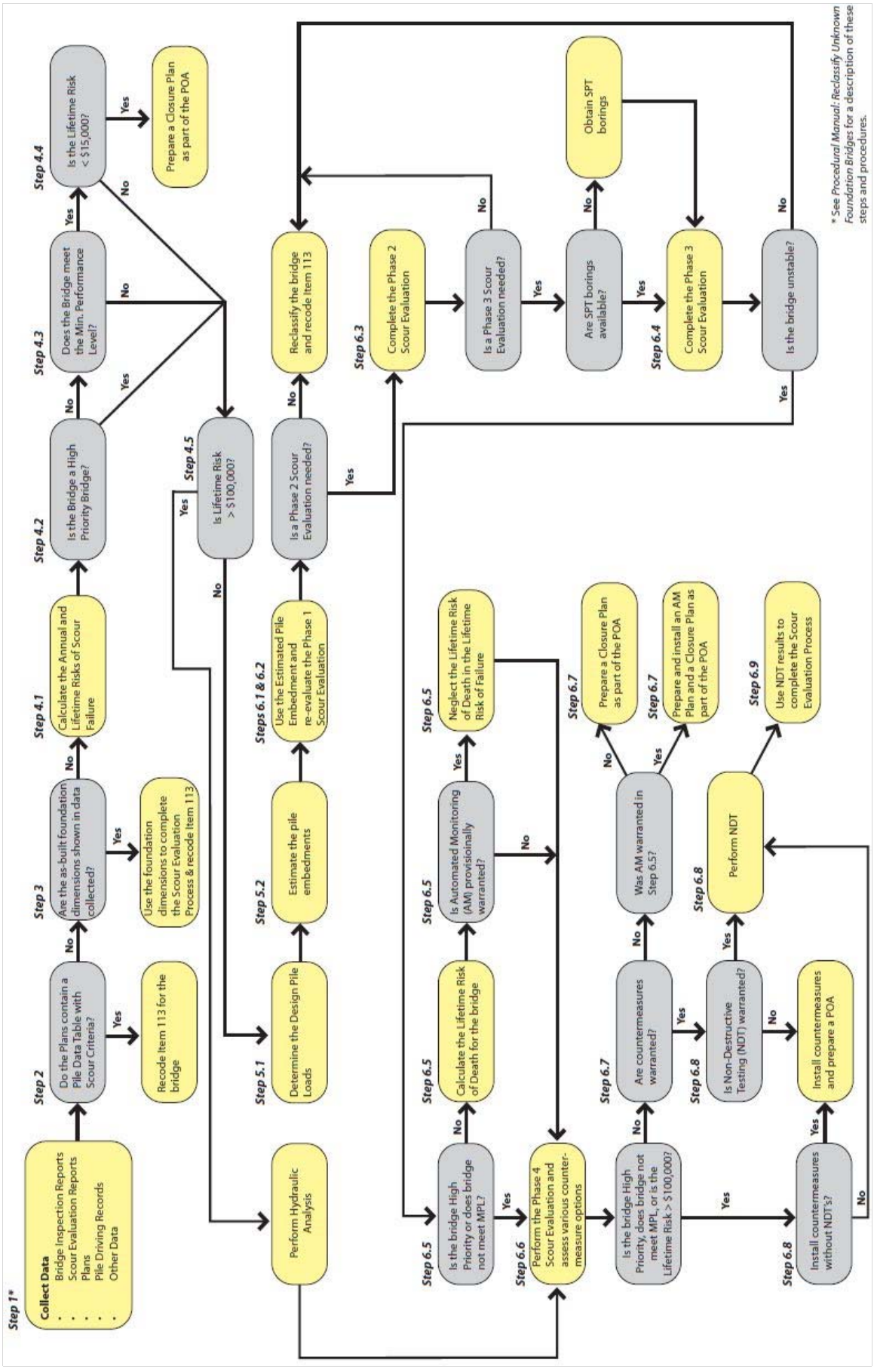

Figure 2-5. Florida DOT Unknown Foundation Evaluation Process (McLemore et al. 2010).

For low-priority bridges meeting the MPL and having lifetime risks of failure smaller than $15,000, a closure plan was recommended as a POA. Otherwise, if the lifetime risk of the bridge is greater than $100,000 or if the bridge is found to be unstable from scour evaluation, performing countermeasures or NDT methods was required.

For bridges with lifetime risks between $15,000 and $100,000, ANN, a geotechnical method, and a hybrid method were applied to infer foundation dimensions and evaluate the bridge scour vulnerability accordingly.

The Alachua and Collier counties were originally selected at the beginning of the project to populate the study database. However, more data were sampled from other counties to make the pilot study applicable to the entire state.

The methods considered for evaluating the foundation embedment were only applicable to piles (concrete, steel, and timber) because it was understood that these were the only foundation types existent in UFBs population in Florida. Pile loads are calculated based on a reverse-engineering method that basically consisted of reevaluating the dead load and live load sustained by the bridge piers. An alternative and simpler approach proposed in this study suggested the use of an ANN model based on a data sample of bridges with known pile loads. Figure 2-6 shows the ANN predictions for pile load versus the real load values obtained from the plans.

After computing the pile loads, three methods were proposed to obtain the pile embedment: ANN predictive models, a Geotechnical method, and a hybrid approach. An MLP neural network with one hidden layer and with Levenberg-Marquardt algorithm was created to predict the pile depth based on a number of input variables associated with the bridge including:

- Pile size.
- Pile design load.
- Slope of the bearing capacity curve between 0 and 20 ft.
- Slope of the bearing capacity curve between 20 and 40 ft.
- Pile construction year.

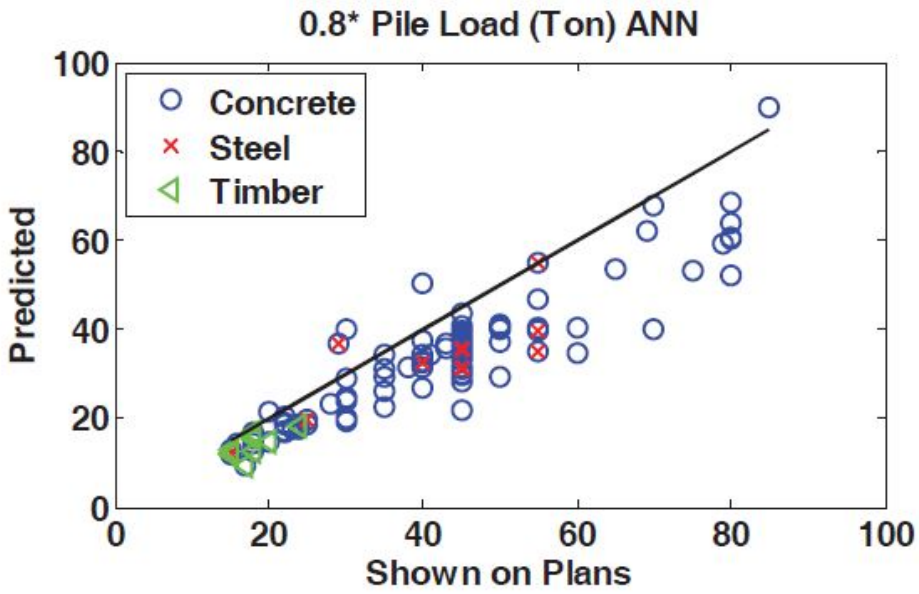

Figure 2-6. ANN Predictions of Pile Load versus Actual Pile Loads (McLemore et al. 2010).

This model was called CPILE and is only applicable for concrete piles. It imposed a minimum prediction of 10 ft and a maximum of 70 ft. Also, to make sure that predicted depth is less than the actual depth, the model results are factored by 0.7. In other words, although the correlation between observed and predicted pile embedment is rather weak, applying the factor of safety could guarantee that the model generates a conservative minimum embedment for the bridge pier. Also for those bridges where a hard layer exists near soil surface, the pile embedment was equal to the depth of the hard layer. Figure 2-7 shows the CPILE prediction of the Florida study. Note that no measure of model prediction accuracy is presented for ANN prediction in this study.

Another approach was proposed to cover the weak points of the ANN predictive models. The method consists of using the soil boring or wash-boring data for a number of known bridges and developing bearing capacity curves using the FB-Deep software for different pile types and sizes. The pile embedment was then determined using the corresponding bearing capacity curves and the required design load. Figure 2-8 shows the bearing capacity curves for different values of SPT-N for a number of 12-inch concrete piles based on the actual pile embedment and the design load (or the allowable bearing capacity) extracted from pile driving records.

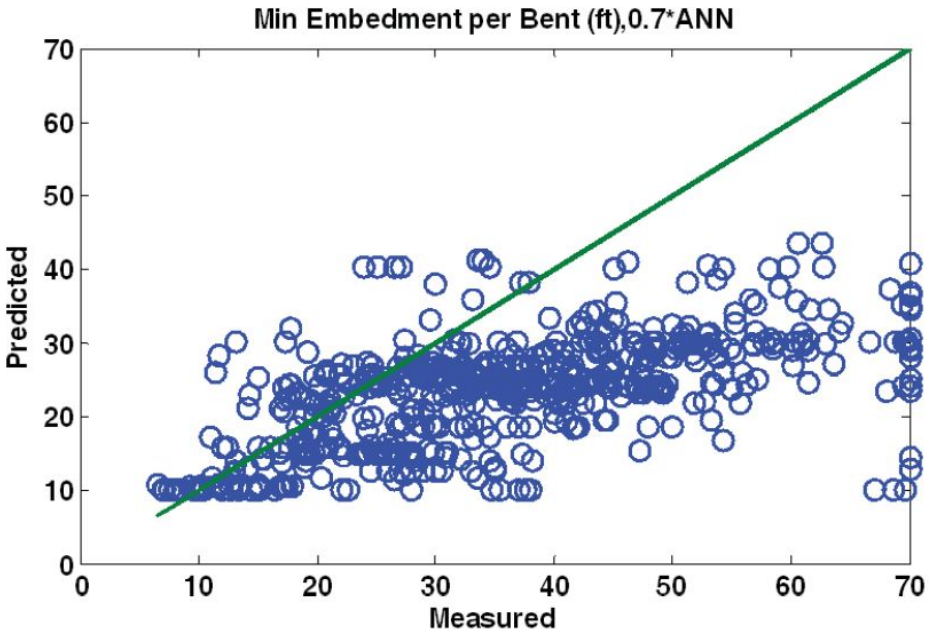

Figure 2-7. CPILE Prediction versus Measured Minimum Pile Embedment per Bent (McLemore et al. 2010).

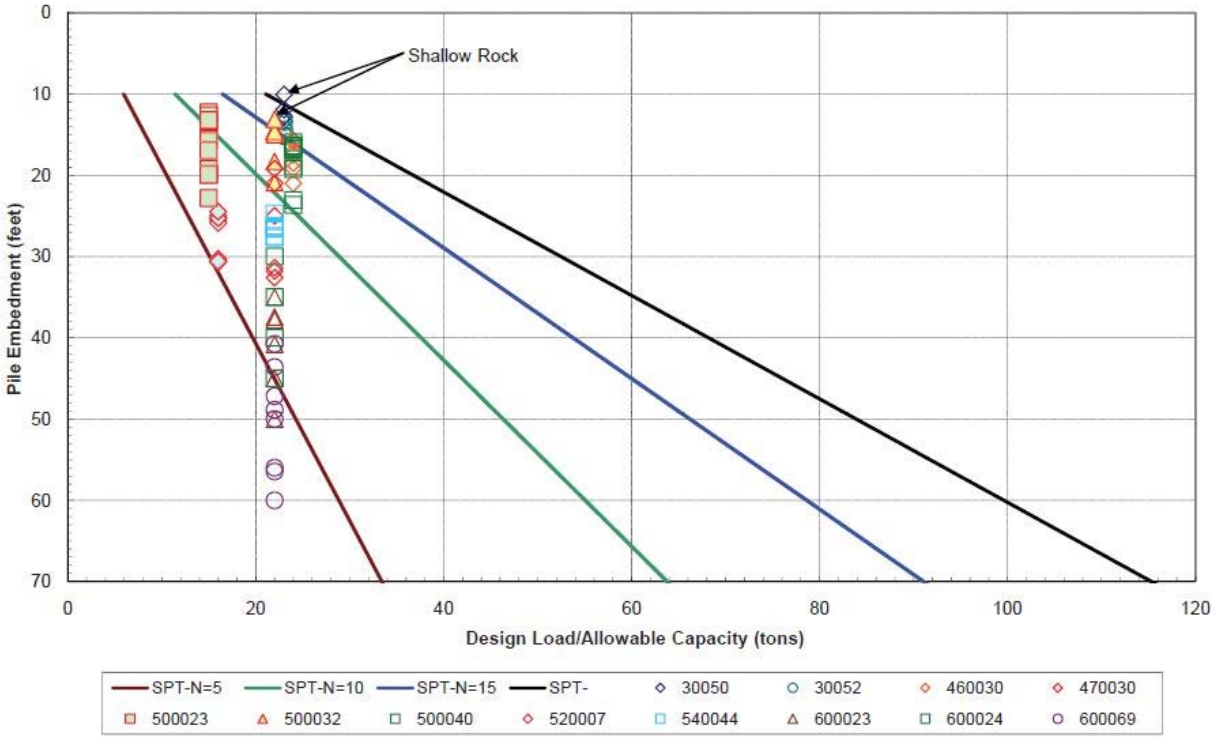

Figure 2-8. Pile Embedment versus Design Load Obtained from Pile Driving Records for 12-Inch Concrete Piles (McLemore et al. 2010).

If the bridge loads were not available, they had to be obtained via one of the previously mentioned methods of load estimation. If soil-boring data were not available, a uniform soil profile with constant SPT N-value was assumed. The SPT N-value of 15 is considered the optimum value and is recommended for establishing the standard bearing capacity curve for concrete and timber piling. However, the Florida DOT recommended that SPT N-value of 20 be used to establish the standard bearing capacity curve for steel H-piles. Figure 2-9 shows the pile embedment prediction for bridges with SPT boring data and the bearing capacity curves for 15-inch concrete piling. To make sure that predicted pile embedment were less than the actual values, results of the geotechnical method were reduced by a factor of 0.8.

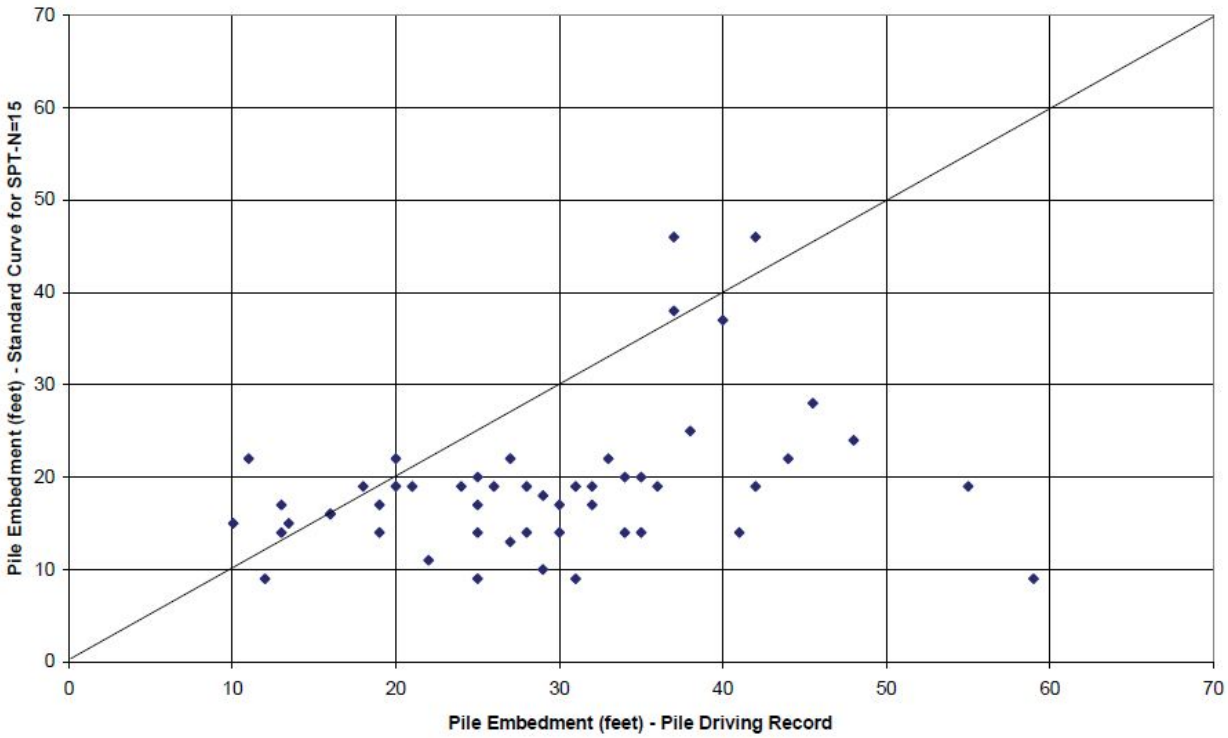

Figure 2-9. Comparison of Pile Embedment from Pile Driving Records versus FB-Deep Analysis Using SPT-N = 15 for Concrete Piles (McLemore et al. 2010).

Finally, the hybrid method consisted of performing both the ANN and the geotechnical method and selecting the minimum value as the pile embedment. Figure 2-10 shows comparison of the accuracy of the proposed methods. The objective was to maximize the total accuracy while minimizing the over-prediction. The colored lines on the plot show how the errors can be changed by a constant multiplier (safety factor). The curve was generated by changing the magnitude of the

safety factor, and the numbers along the geotechnical curve are the values of the safety factor at that point on the curve. The circles show the recommended safety factors for each method. These factors are 0.8 for the geotechnical, 0.7 for the ANN, and 1.0 for the hybrid method.

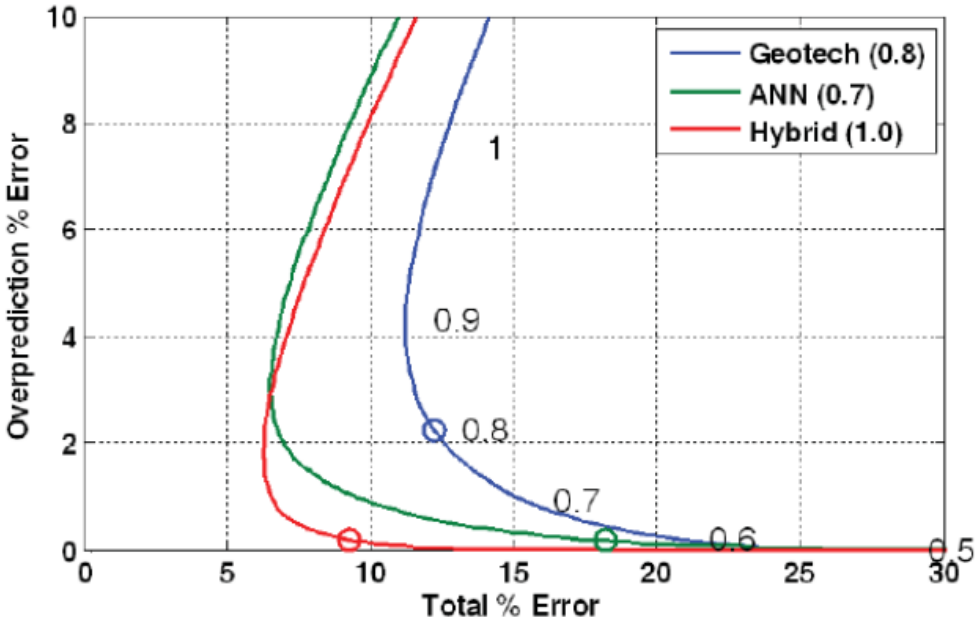

Figure 2-10. Over-Prediction Error versus Total Error for Minimum Pile Embedment per Bridge for 3 Methods and 25 Bridges (McLemore et al. 2010).

Figure 2-11 shows the flowchart to estimate the pile embedment for unknown foundations.

Static/Back-Calculating (S/B-C) Method (Sayed et al. 2011)

The S/B-C method was developed to reclassify UFBs from unknown to known by predicting reasonable minimum foundation depths. This method was based on the static equilibrium of the bridge, i.e., the equality of current service load factored by two or three according to Load and Resistance Factor Design (LRFD) design or the ultimate load based on the allowable stress design to the resistance of the foundation.

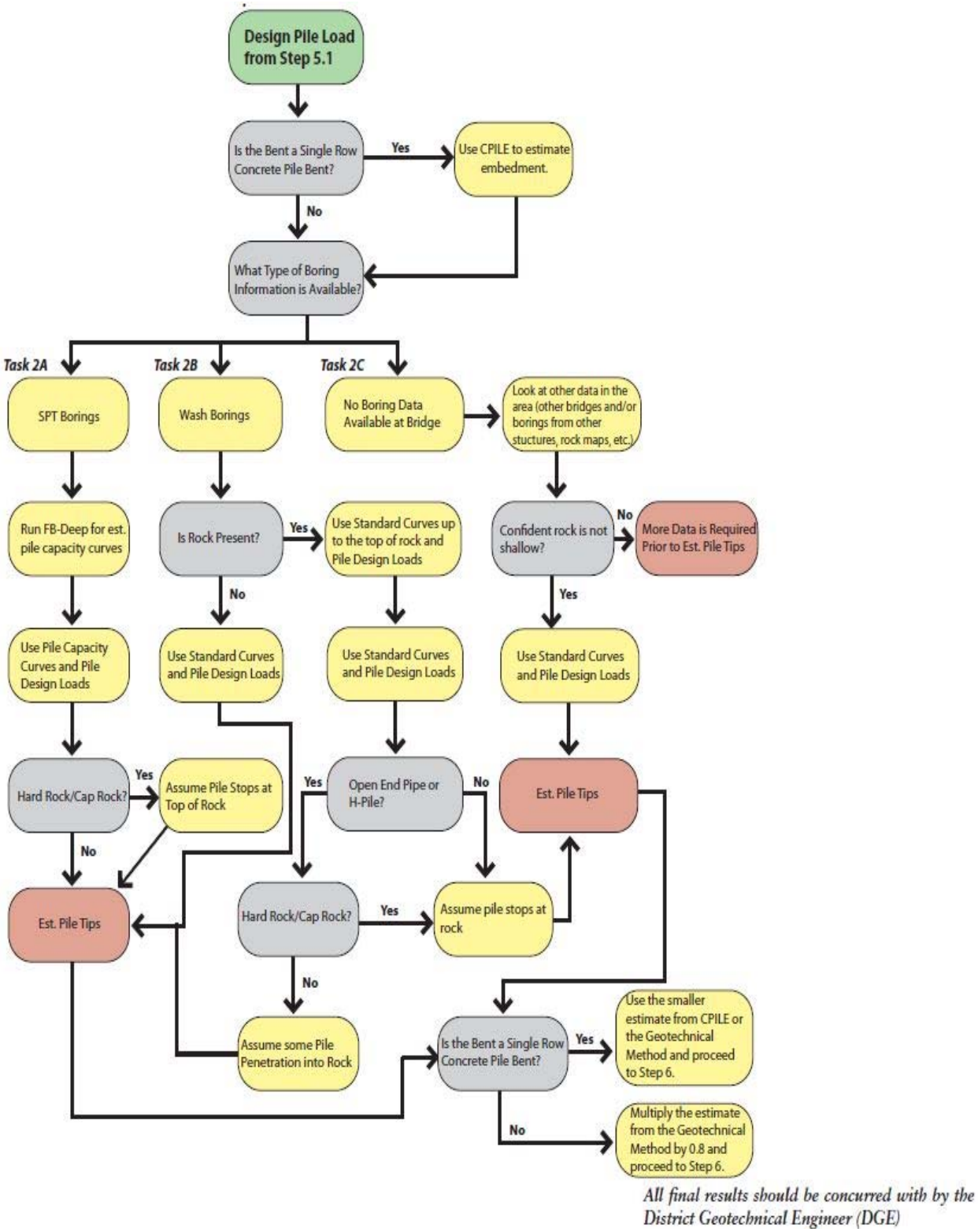

Figure 2-11. Flowchart Depicting Florida Method for Estimation of Pile Embedment of Unknown Foundations (McLemore et al. 2010).

This method is reliable and valid only when:

- The foundation is pile or shaft.
- Only the minimum reasonable depth is determined, not the actual depth.
- The foundation geometry (diameter, pile group layout) is somehow known (e.g., using NDT testing).
- The borehole data are available at the bent (pier).
- The bridge is in Florida (this method may not give good response for bridges in other states).

Figure 2-12 shows a flow diagram describing the implementation of the S/B-C method. The physical measurements of the components of the super structure and top of the foundation elements (layout, type, and size) allowed for back-calculation of bridge service load (reverse engineering). Therefore, the ultimate load was calculated with a reasonable factor of safety for Allowable Stress Design (ASD) and LRFD.

A 3D finite element model of the bridge pier was generated using the non-linear program FB-Multiplier/FB-PIER V4. The computation is carried out iteratively until reaching the stability/instability embedment.

The S/B-C approach was validated by several case studies of known foundation bridges in Florida and has proven successful in predicting the minimum depth of piles. Figure 2-13 shows the predicted versus actual pile length for the given case studies.

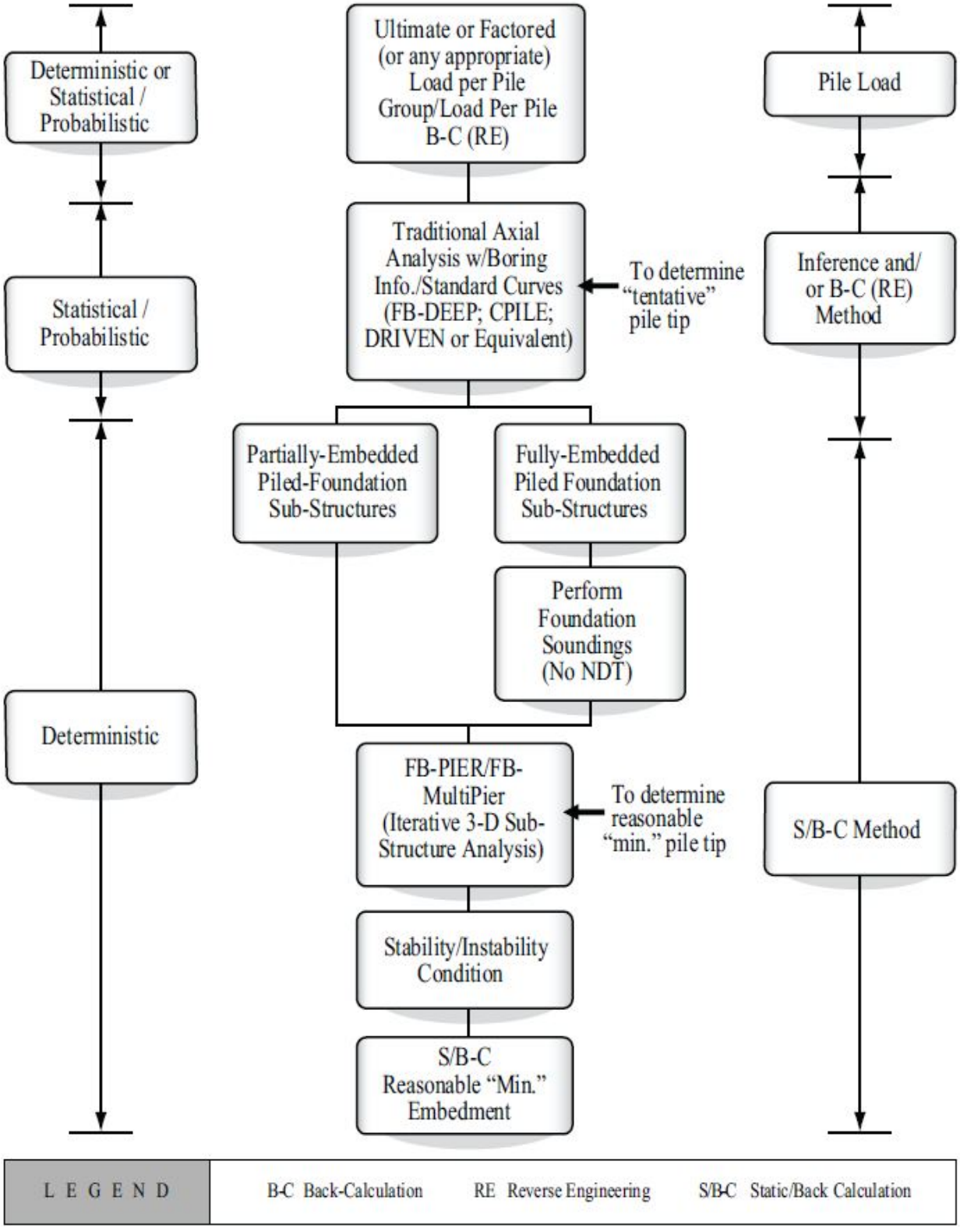

Figure 2-12. Static/Back-Calculation (S/B-C) (Sayed et al. 2011).

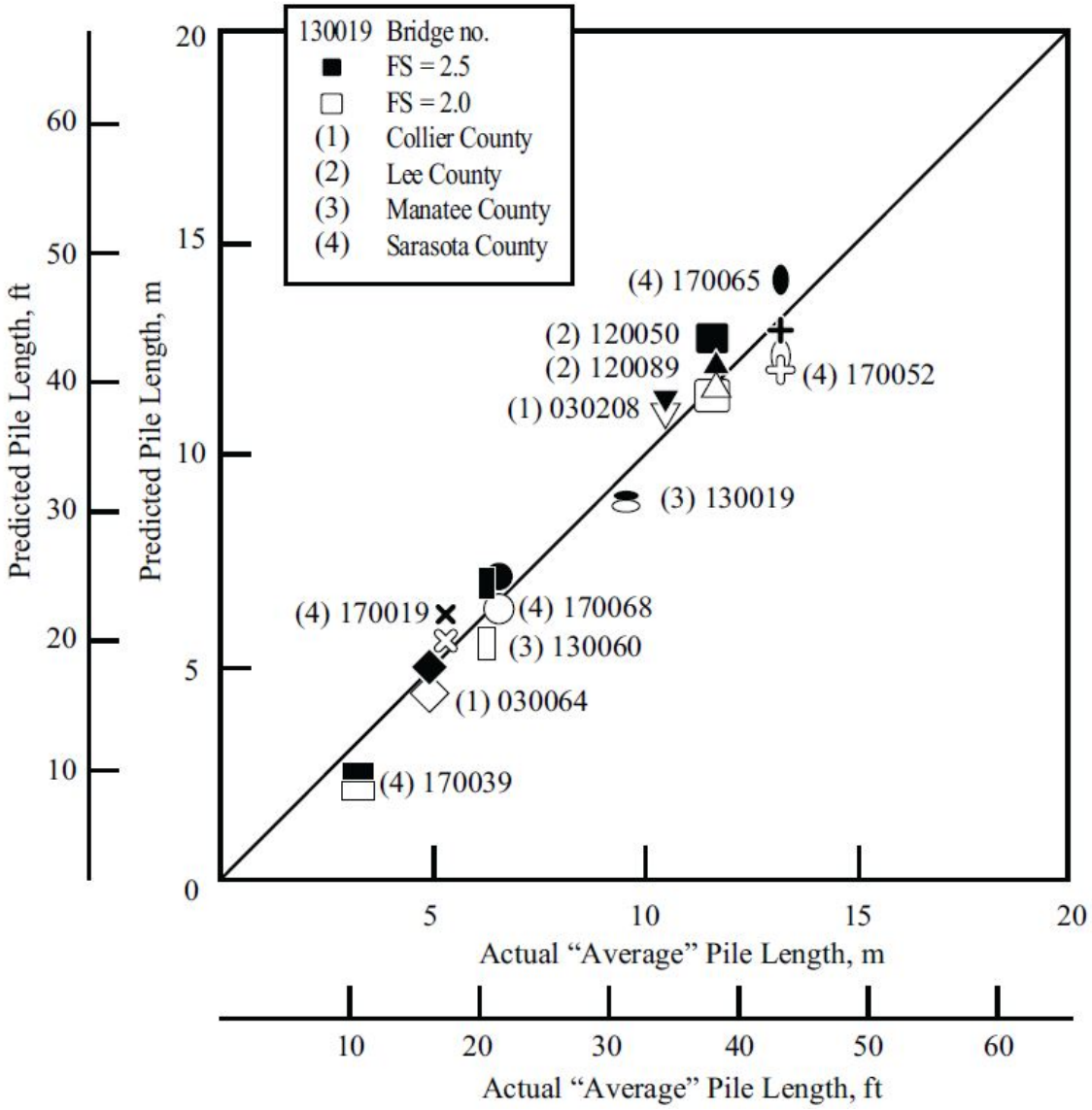

Figure 2-13. S/B-C Predicted versus Actual Pile Length (Sayed et al. 2011).

Chapter 3.
EXISTING EXPERIMENTAL METHODS

INTRODUCTION

There are approximately 9,000 bridges in Texas with unknown foundations. The bridges spanning water are of critical importance due to the risk of potential scour. States nationwide are identifying their unknown foundations to update bridge databases; however, current techniques are typically invasive and costly. Many reports with extensive research have been published on current surface and subsurface tests (Maser et al. 1998; Mercado and O'Neil 2003; Olson et al. 1998; Olson 2005; and Robinson and Webster 2008). Some of the capabilities and limitations of these methods are presented in this chapter. Bridges are made up of many different components; common variables of a bridge are shown in Figure 3-1.

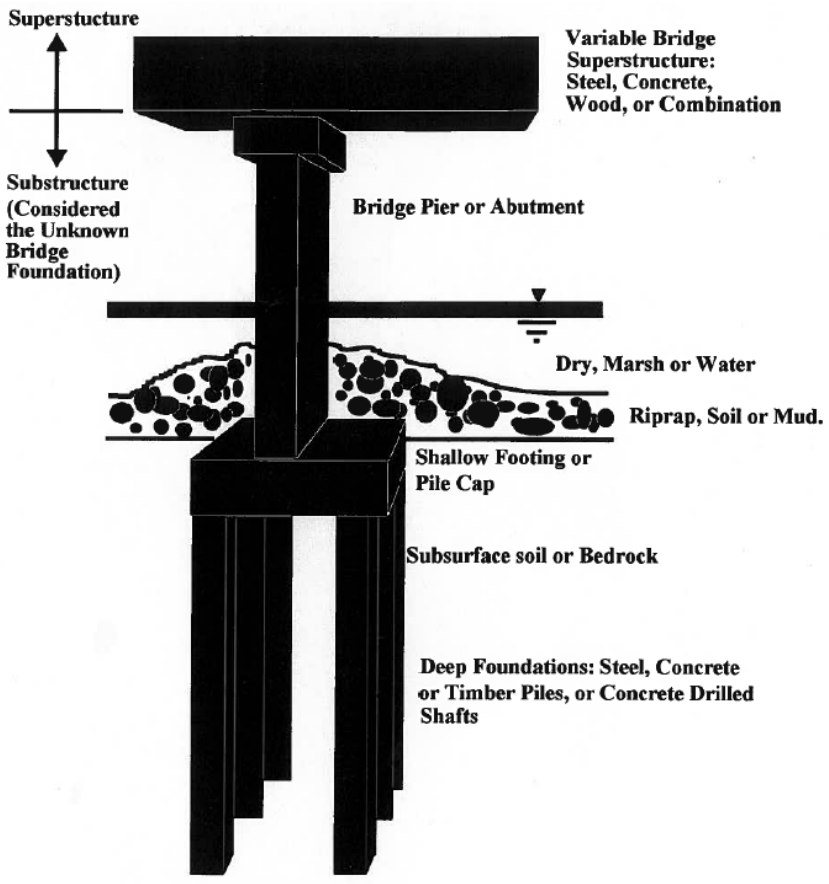

Figure 3-1. Variables of an Unknown Bridge Foundation (Olson et al. 1998).

While there are several elements of a foundation that are important, the foundation type and depth are the most pertinent when determining an unknown foundation. This is important to note because most existing methods are limited to determining the foundation depth only and are often hindered by the type of a foundation.

Conventional excavation is the most effective method for successfully identifying the type and depth of a foundation, which is independent of the type of the foundation. Excavation results in exposing a portion of the bridge foundation for visual confirmation. This is not typically done because, first, it is extremely expensive, especially when the bridge is over water, requiring the area to be sheeted and dewatered. If the bridge is large, excavations may also be difficult due to a lack of access, and if the bridge is over water, costly barges may be necessary. Also, excavation can be very dangerous and difficult for workers. Precautions have to be taken so the foundation is not undermined and the bridge does not collapse. For this reason, the need for nondestructive testing was emphasized. This chapter is an overview of existing unknown foundation field methods.

SURFACE METHODS

Surface methods are generally preferred over subsurface methods for many reasons. First, boreholes for subsurface methods create an upfront cost for each subsurface test and take time before the testing can begin. The costs of boreholes increase with common bridge variables such as water and limited access. Surface methods avoid this initial issue; however, generating useable results with them can be more difficult as they are often dependent on access to bridge foundations and the type of the foundation. This section describes the existing surface methods for unknown bridge foundations.

The simplest nondestructive testing method is a driving rod test which is used to determine if the foundation is shallow or deep. A half-inch diameter steel rod is driven with a 15 lb hammer dropped 2 ft near the bridge foundation. Blow counts per foot are recorded until the rod cannot be driven further. This test can provide the depth to weathered rock, dense sand layers, or soft layers. Shallow foundations are presumed if the results indicate a strong material or rock near the surface. While this test is very cost-effective, it is highly dependent on inferences made by the rod refusal. It is commonly used for small bridges as a first estimate before using a more reliable method.

The sonic echo test was developed to evaluate the integrity and length of newly constructed piles. For new piles, the source and receiver are placed on the top of the pile. The source generates an impulse of known magnitude. Using this magnitude, the velocity of the wave can be estimated. Using this known velocity and the known dimensions of the recently constructed pile, defects in the pile can be detected. This method was applied to determine the depth of unknown foundations by placing the receiver on the top or side of an exposed pile underneath a bridge. If the top was not exposed, at least two receivers were placed on the side of the structure. Using a handheld hammer, the compression waves were generated. The depth of the foundation was determined using the arrival time of the reflected compression wave to the receiver (see Figure 3-2).

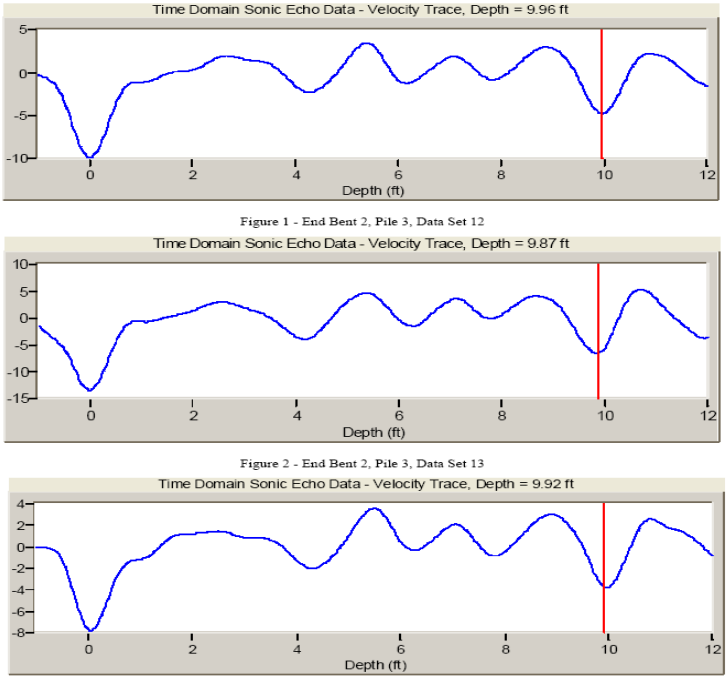

Figure 3-2. Results of a Sonic Echo Test.

This method is very effective for columnar substructures. Unfortunately, it is limited because it was found that the compression waves generated by the impulse are often diffused into other components, like the pile cap shown in Figure 3-1. Also, it was found, "as a rule of thumb, when embedded length to diameter ratios are greater than 20:1 to 30:1 in stiffer soils, there will be no identifiable bottom echoes due to excessive damping of the compression wave energy in the Sonic Echo" (Olson et al. 1998).

The bending wave test is similar to the sonic echo test; however, it uses bending waves instead of compression waves. At least two horizontal receivers are placed on the same side of the pile as the impact (see Figure 3-3).

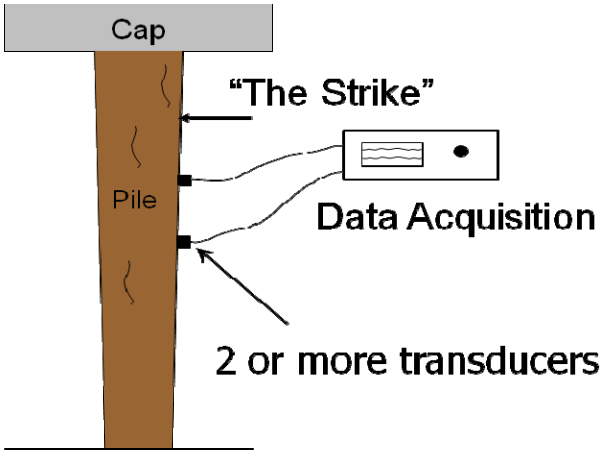

Figure 3-3. Bending Wave Testing Principle.

Like the sonic echo test, the depth of the foundation is calculated using the velocity of the wave and the measured arrival times. The velocity of the stress wave is, however, not constant as bending waves are highly dispersive. The dispersive nature of bending waves sometimes hinders the effectiveness as the impulse must be a certain amplitude. Also, a major constraint is the amount of the pile that must be exposed above the ground surface for the two transducers, which must be spaced over a meter (3.28 ft) apart still with space above the top transducer for the impact. This test is also only applicable to columnar structures like the sonic echo test.

The ultraseismic test is another wave propagation test; however, it uses geophysical digital data processing to analyze the propagation of the compression and bending waves. Unlike the sonic echo test, the ultraseismic test uses multiple channels of data, so it requires access to at least 1.52 m (5 ft) of the surface of the substructure. Ultraseismic was researched in an attempt to address the incapability of the sonic echo test and the bending wave test on non-columnar foundations. Ultraseismic again uses a handheld hammer to generate the waves, but the arrivals and the reflections of both the compression and bending waves are analyzed using seismic processing. The compression waves are generated by striking the foundation vertically and the bending waves by striking it horizontally. Olson et al. (1998) determined that this method has the broadest impact in

determining unknown foundations of all the surface methods investigated in their study. While ultraseismic proved to be more successful at testing more complex columnar piers than the previously described methods, the waves are still not able to travel through pile caps or other components on top of piles. This led to false results indicating shallower foundations than exist (see Figure 3-4).

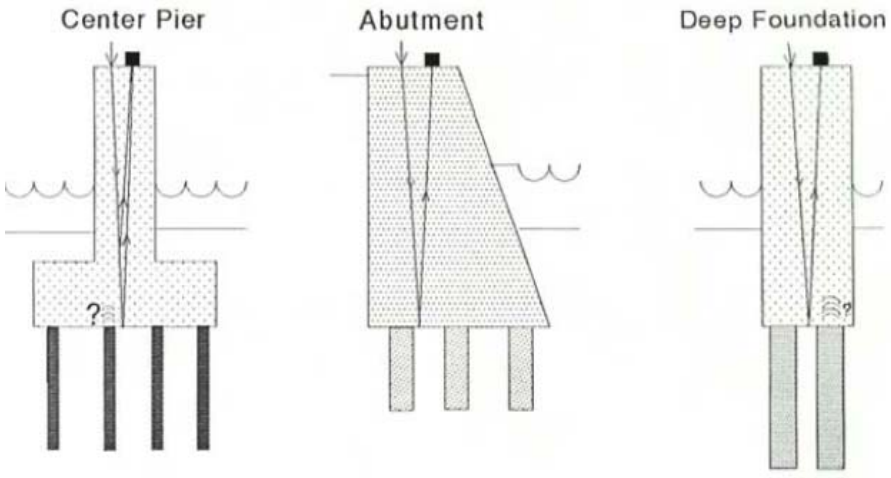

Figure 3-4. Impedance of Wave Propagation by Complex Foundations (Olson et al. 1998).

Another surface method, the Dynamic Foundation Response Method, (Olson et al. 1998) uses a 5.45 kg (12 lb) impulse hammer with a built in force transducer to excite the bridge in vertical and horizontal directions along the frame of the substructure as a form of modal analysis. It was introduced to differentiate between shallow and deep foundations, as other surface methods were unable to detect piles beneath a pile cap. For this modal analysis, the substructure is struck with a known force and the accelerometers measure the resulting vibrations. Using these data, the transfer function is calculated and plots of the transfer function versus the frequency of the structure are created. This was done under the principle that, all other components of the structuring being the same, a shallow foundation will exhibit a lower resonance frequency than a deep foundation. The researchers noted, however, that they needed more powerful vibrations to excite the bridge to low frequencies comparable to the natural frequencies identified in numerical modeling. They suggested using other methods to excite the bridge because of this observation. In a later study, (Olson 2005) again attempted to excite bridges using handheld devices. Researchers

used a 1.36 kg (3 lb) impulse hammer, a 45.4 kg (100 lb) vibrator, and a 5.45 kg (12 lb) impulse sledge hammer; however, again these did not generate enough energy to excite the bridge.

Ultimately, Olson (2005) used the Vibroseis truck from the University of Texas to excite the substructure from the bridge deck level because the truck could generate a low frequency output. While the bridge was excited to necessary frequencies, modeling the data was not yet successful although several approaches were researched. Olson attempted to use parameter estimation for finding a solution to different pile cases; however, results were consistently incorrect. Also, parameter estimation was used to solve for the first vertical mode of vibration of the structure. However, it was concluded that this method is not feasible for estimating foundation damage because the effects of the damage are too small to model.

Maser et al. (1998) believed that the approaches such as dynamic and seismic testing were too complex, requiring specialized knowledge and equipment that are not readily available, thus making some projects unfeasible. They wanted to implement a simple and low-cost approach using a stiffness matrix created from measurements that loaded dump trucks caused. They measured axle loads driving slowly across a bridge while continuously taking measurements. These methods of excitation differ from those proposed in the vibration-based approach because the methods reviewed excited the bridge deck enough that compression waves or vertical stiffness values could be measured. Because this excitation must go through the deck and all the way down the foundation, more energy must be generated to be effective. The team generated six models to find stiffness matrices for different foundation types and conducted field tests on two bridges with different known foundations. Unfortunately, at the time of publication, the measured stiffness matrices did not show similarities to the models. The team did, however, find that for both the measured and field tests, the stiffness matrices had distinctly different patterns of coefficients for spread footings versus pile foundations.

Maser et al. (1998) hypothesized that each foundation type has a unique pattern of stiffness coefficients. Because the bridge was loaded with a truck that has known properties, they assumed the loading and certain known displacements to generate a stiffness matrix. While they had not determined the coefficients at the time of publishing, they showed that the pattern of the coefficients is different for shallow versus deep foundations, and these differences were similar to

those predicted by theory. Similarly, Suzuki et al. (2007) used the ratios of a theoretical stiffness to indicate scour on bridge piers. Accelerometers were attached to the top of bridge piers to measure the vertical and horizontal accelerations of the pier. Suzuki et al. (2007) noted that a change in the horizontal stiffness occurs when scour removes the soil from one side of a foundation. This unbalance of stiffness is being used as a monitoring system for bridges over water.

SUBSURFACE METHODS

Another way to determine the depth of an unknown bridge foundation is by investigating it using a subsurface method after drilling a borehole. Many borehole methods exist; however, drilling a borehole is expensive and can be difficult if the bridge is over water, particularly deep water. The parallel seismic method is one of the common subsurface methods that is currently used (see Figure 3-5.) The borehole must be drilled within 1 to 1.5 m (3.28 to 4.92 ft) of the foundation, and it must be drilled at least 3 m (9.84 ft) deeper than the estimated foundation depth in order to determine the depth of the foundation. Once the borehole is drilled, a hydrophone or geophone is lowered at set intervals as the top or side of the exposed foundation is impacted with a handheld hammer. Hitting the top of the foundation generates better compression waves; however, the side of the structure can be hit if it is angled downwards should the top of the foundation be inaccessible. If a hydrophone is used, the cased borehole is filled with water. Also, hydrophones only work well when the soils around the foundation are fully saturated. The impulse generates wave energy, and the geophone tracks the arrival times of the refracted waves into the soil. Parallel seismic not only identifies the depth of the foundation, but also the depth of the scour zone (Mercado and O'Neil 2003).

The depth of the foundation is noted when the stress wave arrival time is delayed due to the wave being transmitted through soil instead of the substructure. Olson et al. (1998) observed that the bottom of more massive foundations can be identified by a peak hyperbolic curve created when the foundation acts as "a point diffractor…emitting both upward and downward travelling waves into the borehole" (Olson et al. 1998). They also noted that the parallel seismic method has the broadest application for determining unknown foundations of the ten that were investigated.

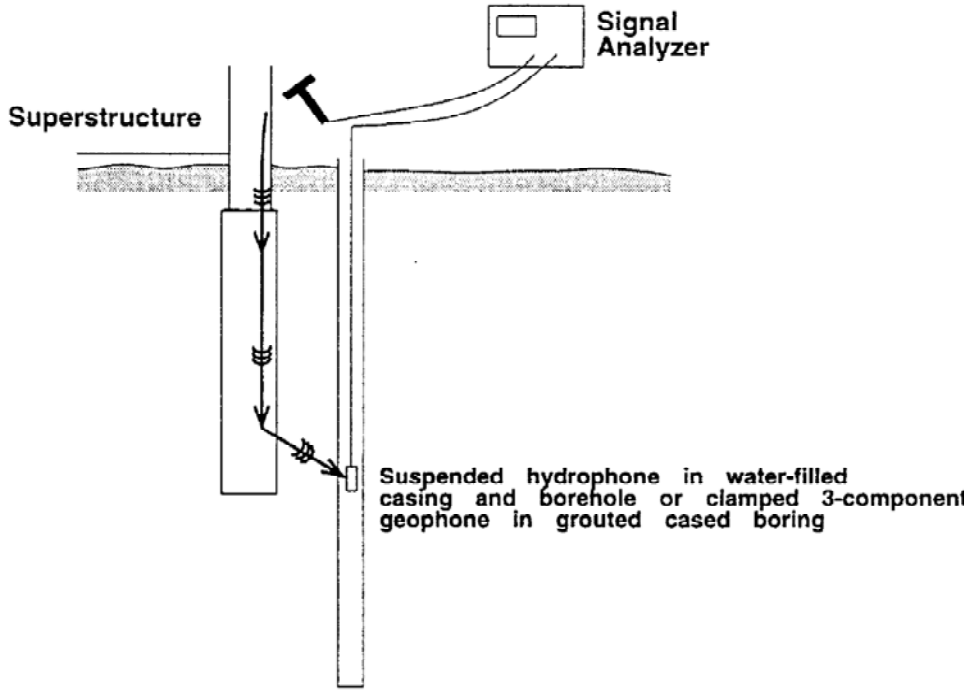

Figure 3-5. Parallel Seismic Test Method (Olson et al. 1998).

The borehole sonic test uses compression and shear wave echoes to determine the depth of the foundation by noting when the arrival time of the wave changes. Two boreholes are drilled next to the foundation: one which has the source lowered in it and one which has the receiver. Lowering the source in the borehole requires that the source be significant enough to generate waves that will hit the foundation and reflect back. The borehole sonic test is limited by the type of foundation. It works well for large foundations that have a surface big enough that the body waves can reflect. However, it does not work well for smaller foundations like piles. The waves can go around these piles, causing the reflections to not be identified. Borehole radar is similar to borehole sonic in that it relies on reflections from the soil/foundation boundary to determine the bottom of the foundation. These reflections are also caused by different material with changing properties; however, borehole radar relies on the changing dielectric constants instead of differences in stiffness and only one borehole is used. Relying on dielectric constants means that changes in water content will greatly affect the results, with more water resulting in a lower depth of penetration of the signal. Also, "environmental factors such as salt water, conductive soils, ground moisture conditions, buried electrical power lines, etc., can critically limit and/or confuse radar signals" (Olson et al. 1998).

The induction method, used in North Carolina (Robinson and Webster 2008), is performed by lowering an induction sensor in a borehole, which creates a magnetic field. The borehole must be drilled within 45.72 cm (18 in) of the foundation in order for the induction test to be successful. The field is interrupted by metal objects, such as rebar in a foundation. This disruption allows for the rebar in the foundation to generate its own magnetic field, which is detected by the induction sensor in the borehole. The received voltages read by the induction sensor are measured at a minimum of every 0.31 m (1 ft). The depth at which the receiver no longer indicates a voltage reading is the estimated foundation length. Figure 3-6. shows a successful induction test at a bridge in North Carolina. The borehole was drilled to 6.55 m (21.5 ft), and the foundation was determined to penetrate 0.30 m (1 ft) into the weathered rock.

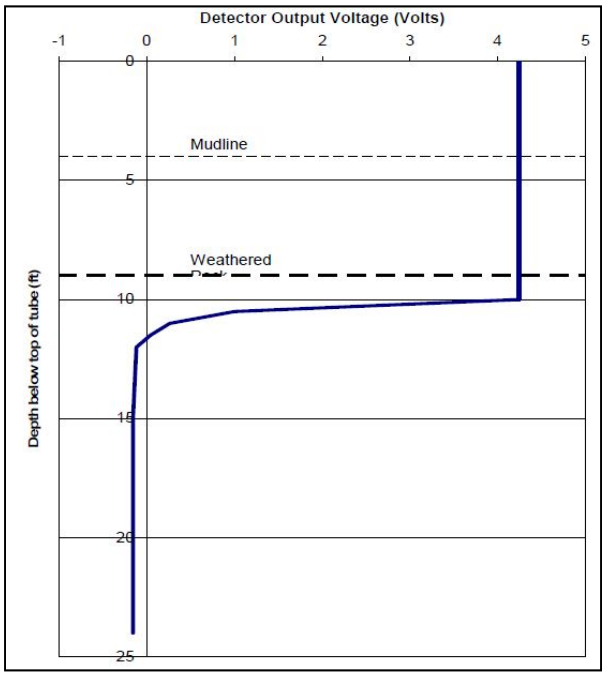

Figure 3-6. Induction Method Results at NCDOT Bridge (Robinson and Webster 2008).

This method is highly dependent on metal within the substructure, which is not always available. It also assumes that the rebar within the substructure is continuous down to the bottom of the foundation. Like all borehole methods, it is dependent on access being available for the borehole to be drilled because for a successful test, the borehole must be drilled very close, within 45.72 cm (18 in).

Methods are often hindered by the assumptions researchers make based on typical foundation construction practices. Unfortunately, some of the bridges with unknown foundations may not have been built with standard construction methods. For example, there is a story of a bridge that was temporarily closed because it was discovered that an unknown salt mine beneath the bridge collapsed. Despite the collapse, engineers were able to go into the salt mine to investigate the bridge foundation. While beneath the surface, they discovered that the concrete substructure did not contain reinforcing steel. For reasons like this, methods that depend on certain components of a substructure that are assumed to always be used could be ineffective in cases when those components are not included.

PART II.
EVIDENCE-BASED APPROACH

Chapter 4.
GENERAL METHODOLOGY

INTRODUCTION

Texas has more than 9,000 bridges with unknown foundations where approximately 85 percent are located on local roads. These bridges are often categorized as off-system bridges that counties or private companies originally designed and constructed, and that TxDOT inherited later. The bridge plans for most of these bridges are missing, and their substructure characteristics are unknown (i.e., type of foundation, foundation's geometry, soil stratigraphy, and soil mechanical properties). On-system bridges, on the other hand, are defined as bridges that TxDOT designed and constructed, and their design and construction records are available. Missing substructure information has made safety monitoring of bridges very difficult, especially for over-river bridges susceptible to scour.

Following the FHWA's national request to remove as many UFBs from the NBI, TxDOT has implemented a set of actions to update item 113 (scour-critical bridges) of the NBI for those bridges coded as U in Texas. The purpose of this study is to provide a set of guidelines for TxDOT not only to determine the substructure characteristics of UFBs, but also to provide a confidence measure about their assessment.

The proposed evidence-based approach consists of a deterministic and a probabilistic method. Due to the timeframe of this project, the proposed approach is based on a case study of bridges located only in TxDOT's Bryan District, with the expectation that this can be implemented later in all the other TxDOT districts.

The proposed approaches require evidence to condition the inferences about UFBs. For this purpose, a database is populated from the review of 185 over-river bridges with known foundations. Notice that one of the key hypotheses of the evidence-based approach is that the collected database is a representative sample of the population describing the district's bridges, which allows for generating inferences about bridge foundations that are unknown in the same district, given the particular characteristics of the UFB's superstructure.

The effort placed in retrieving information from each bridge inspection folder of known foundations is to populate a database capturing characteristics about the effect of regional design and construction criteria, as well as mechanical characteristics of the soil.

The deterministic method applies ANNs to recognize the inherent pattern in bridges substructure design and to generalize this pattern to UFBs. This allows for making predictions on substructure type and dimension with a reasonable accuracy with no need to perform time-consuming and costly experiments.

The probabilistic method, on the other hand, aims to generate not only a single prediction of the foundation's characteristics as with the ANN, but also a number of likely combinations, so that joint probability density functions can be integrated. This approach requires that prior knowledge about the foundation's characteristics be defined in the form of probability density functions and also requires defining a physically based equilibrium connection to both the known and unknown foundations: the foundation's bearing capacity. For this purpose, the proposed Bayesian method is used to make probabilistic predictions about the UFB's substructure type and dimensions and the mechanical characteristics of the supporting soil.

METHODOLOGY

Figure 4-1 and Figure 4-2 present the general flowchart for the deterministic and the probabilistic methods. The deterministic approach is applicable only for deep foundations (piling or drilled shafts) while the probabilistic approach can be used for piling, drilled shafts, and spread footing.

The deterministic method first determines what the type of foundation is. If the foundation is recognized to be deep (either concrete, steel piling, or drilled shafts), the method selects the appropriate ANN model based on the availability of soil-boring data to predict the depth of the foundation.

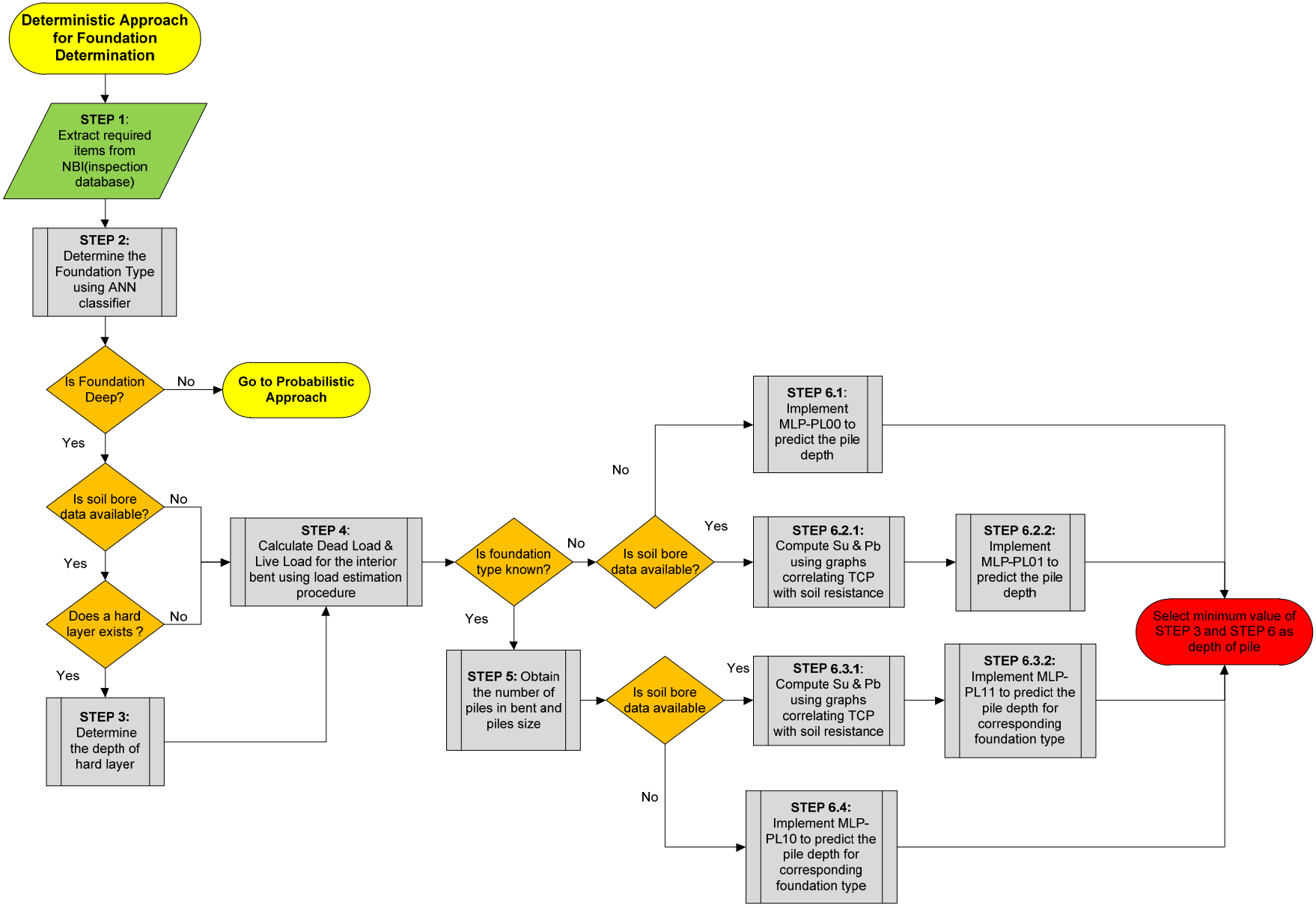

Figure 4-1. Deterministic Approach Flowchart.

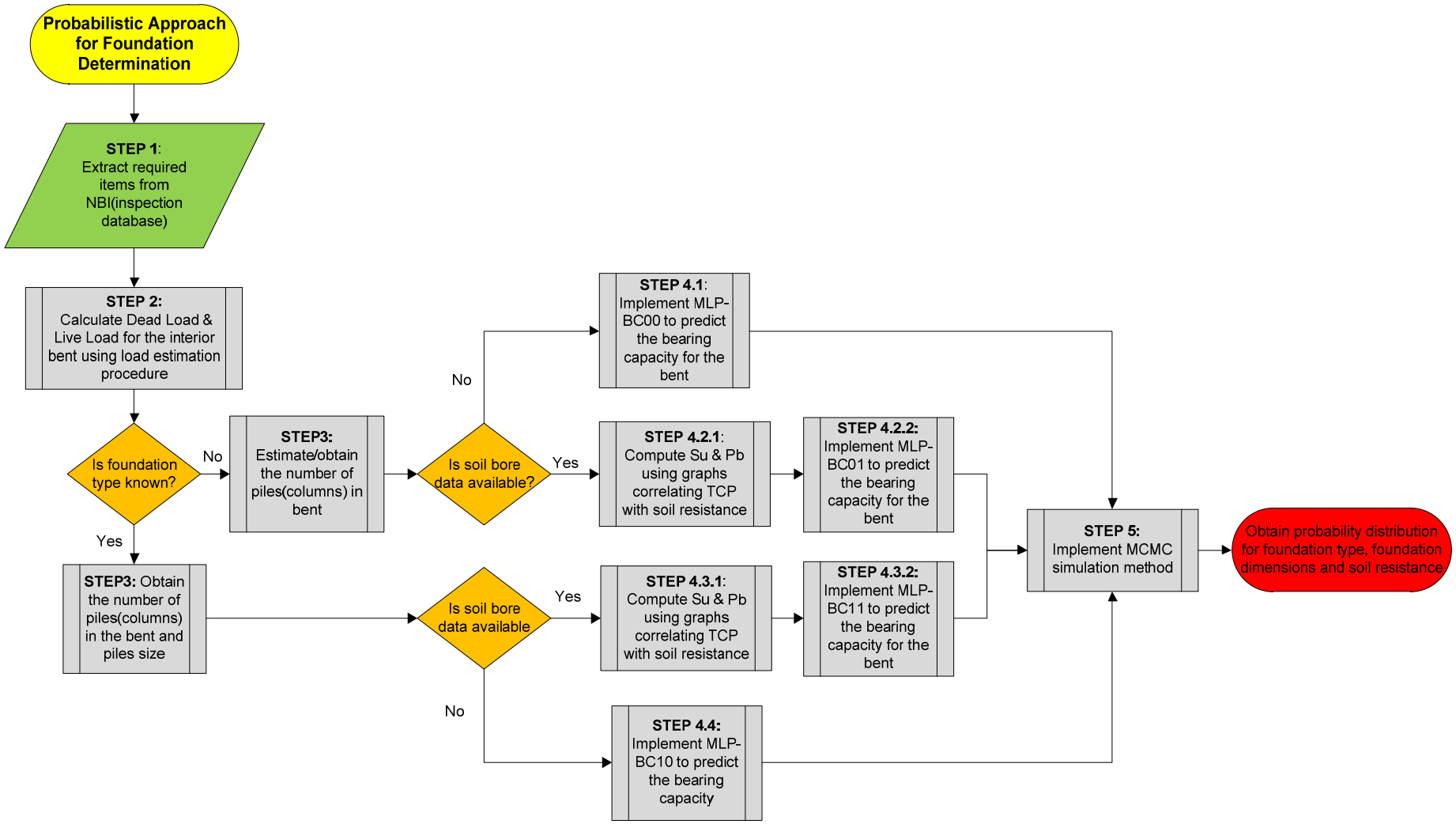

Figure 4-2. Probabilistic Approach Flowchart.

The probabilistic method also selects the appropriate ANN model based on the foundation type and soil-boring data availability in order to make prediction on bearing capacity of the foundation. The predicted bearing capacity is then used to solve the probabilistic inverse problem via Markov Chain Monte Carlo (MCMC) simulations to obtain probability distributions for foundation type and dimensions and soil resistance parameters, depending on the availability of information about each of these elements.

The basic steps of each method are described below, and more details about each step can be found in the following chapters.

DETERMINISTIC APPROACH

Step 1: Data Collection

A number of input parameters are identified as most relevant for prediction of foundation type and deep-foundation depth. The following items are required and can be obtained from NBI or from the Bryan District inspection database:

- Item 3: County (code).
- Item 16: Latitude (to be converted to degrees).
- Item 17: Longitude (to be converted to degrees).
- Item 27: Year built.
- Item 43.1: Main span type.
- Item 44.1-D1: Substructure type above ground for main spans.
- Item 46: Total number of spans in bridge.
- Item 48: Max span length (ft).
- Item 51: Roadway width (ft).

Step 2: Determining the Foundation Type Using ANN

The type of foundation is predicted using a classifier ANN model. The ANN model is first trained with a number of bridge examples and learns the existing pattern in relation between bridge input

parameters and foundation type. The proposed ANN model can be used to predict almost all common foundation types.

The ANN classifier is also used to distinguish between deep and shallow foundations, because it is usually possible to identify foundation type from the substructure above ground, once one knows that foundation is deep. Also, the proposed ANN model is not capable of making predictions about foundation dimensions for spread footings; however, it is possible to predict deep-foundation depth without knowing exactly what the foundation type is (whether it is a concrete pile, steel pile, or a drilled shaft).

Chapter 7 gives more details on the ANN classifier model, its input parameters, and implementation.

Step 3: Determining the Depth of Hard Layer

If soil bore data are available for the foundation or for a foundation reasonably close, then it is recommended to identify if a hard layer such as rock or shale exists in the soil profile and to determine the depth of the hard layer.

Based on the TxDOT *Geotechnical Manual* (2006), drilled shafts shall penetrate in hard layer at least for one shaft diameter, if the hard layer is more than three shaft diameters below surface. Otherwise, if the hard layer is close to surface, shafts are recommended to have a minimum length of three shaft diameters. However, pile driving is normally stopped upon refusal, which occurs when reaching a layer with TCP >100 (blows/ft) (TxDOT 2006).

The bridge plans for the over-river bridges in the Bryan District's database also show that driven piles and drilled shafts are extended up to the hard layer as a precaution and safety measure when considered appropriate. Figure 4-3 shows an example of a bridge plan and where piles are cut off upon reaching the hard layer.

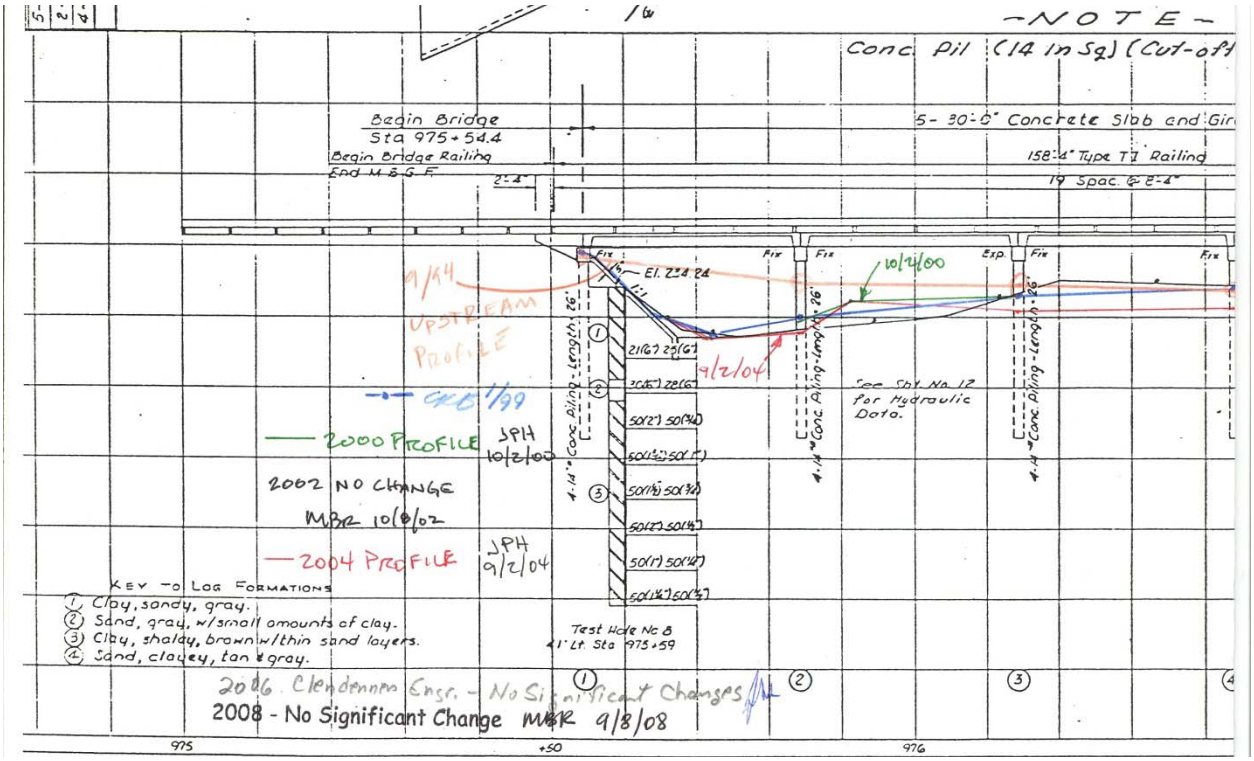

Figure 4-3. Bridge Plan Example.

Step 4: Calculating Dead Load and Live Load

A simple, fast method is proposed in this study to estimate the dead load and live load for bridge foundation. This procedure is based on standard bridge design sheets that TxDOT provided. The total load for a bridge bent is obtained using the standard tables based on roadway width and span length. The live load is calculated with the corresponding standard design vehicle based on AASHTO-LRFD specification. Chapter 6 provides details about the assessment of loads.

Step 5: Obtaining Foundation Properties

In a condition where the foundation type is known, introducing to the model some of the above-ground properties of the foundation, such as size and number of piles for a bridge bent, will enhance the ANN model predictions

Step 6: Predicting Pile Depth Using ANN Models

Depending on the soil bore data and foundation type information availability, one of the following sub-steps is implemented:

- Step 6-1: If the foundation type is known to be deep but neither the foundation type nor the soil bore data are available, the ANN model called MLP-PL00 is recommended to predict foundation depth. This particular case assumes that foundation type cannot be inferred with the desired level of confidence from the ANN classifier or from site investigation. It may be used simply because the user is only interested in inferring the depth.
- Step 6-2: This step addresses the condition in which the foundation type is known to be deep, the exact foundation type is not known (or cannot be inferred using the desired confidence level from an ANN classifier), but soil-boring data are available.
    - Step 6-2-1: Compute the average ultimate skin friction (Su) based on TCP values along the piles and point-bearing capacity (Pb) using the TCP value at the tip of the piles from the nearest soil bore data, using graphs presented in Figures 4-4 to 4-7, proposed in TxDOT *Geotechnical Manual* (2006). Chapter 5 has more details about computing average skin friction along the pile and point-bearing capacity at tip of the pile.
    - Step 6-2-2: Implement the ANN model, MLP-PL01 to predict foundation (pile) depth.
- Step 6-3: This step addresses the condition in which both the foundation type and soil information are known.
    - Step 6-3-1: The same procedure as in Step 6-2-1 is performed to obtain average soil skin friction (Su) and point-bearing capacity (Pb) of the piles based on TCP values from bore hole data.
    - Step 6-3-2: Implement MLP-PL11 to predict the pile depth.
- Step 6-4: If foundation type is known or is inferred using the ANN classifier or by site investigation but soil bore data are not available, then one can implement the ANN model called MLP-PL10 to infer foundation depth.

The proposed ANN model's architecture, algorithm, learning process and input variables as well as results of prediction for Bryan District bridges are fully described in Chapter 7. A number of examples are also presented in Chapter 8.

The minimum value between the depth of the hard layer and the predicted pile depth by the ANN model is selected as the pile depth.

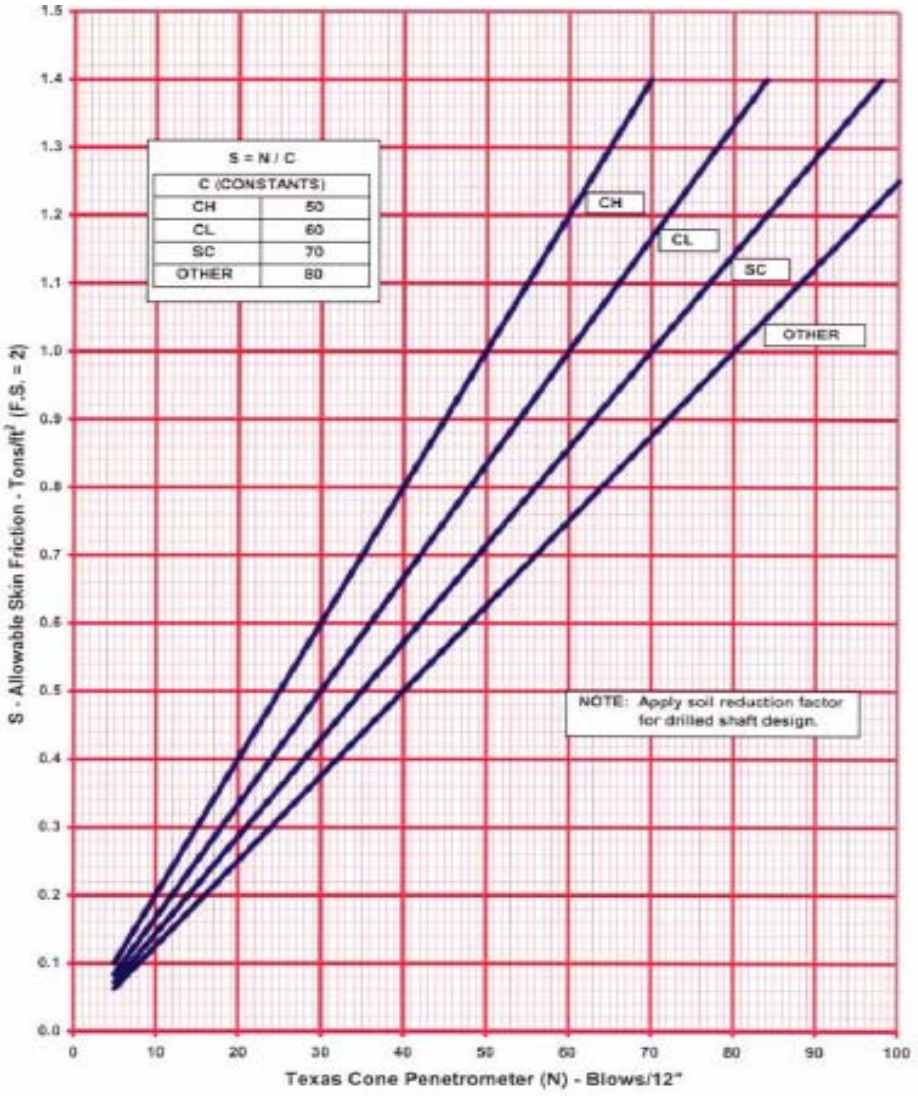

Figure 4-4. Skin Friction versus TCP (for TCP<100 Blows/ft).

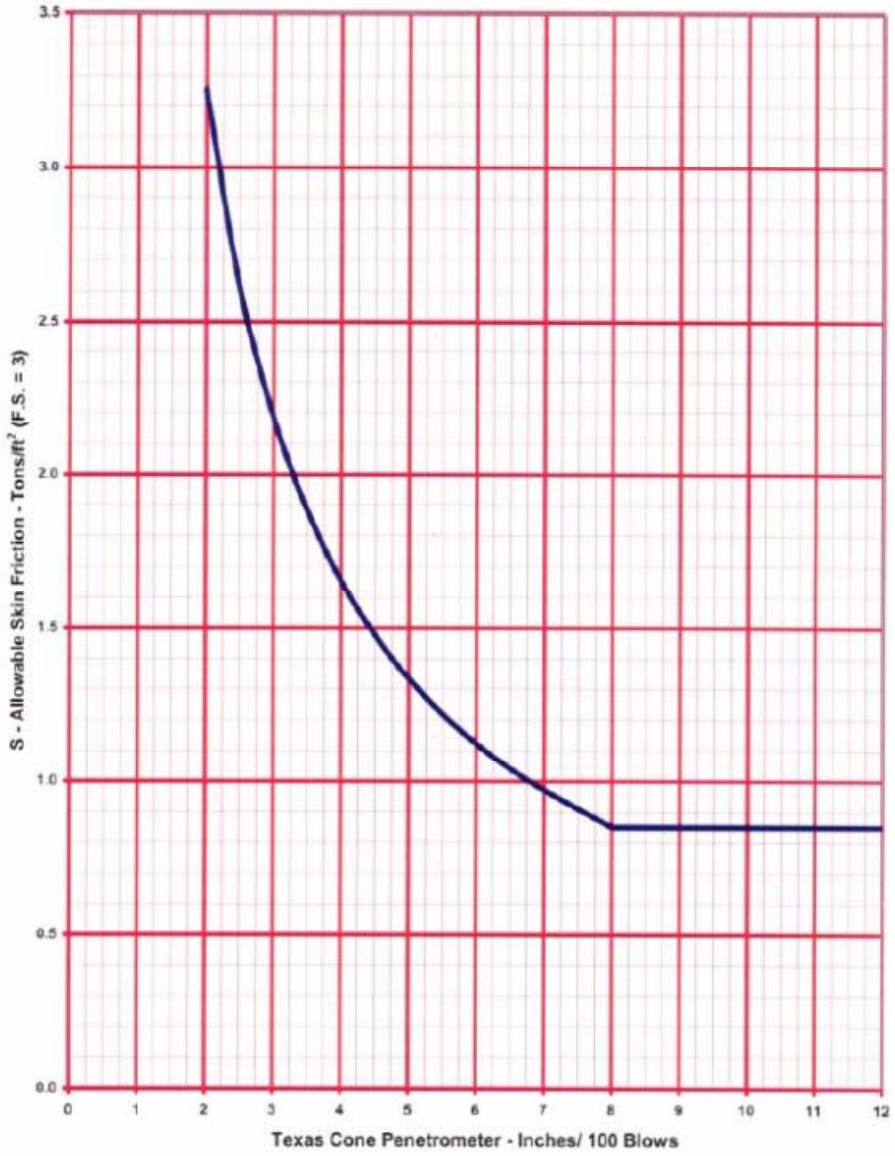

Figure 4-5. Skin Friction versus Inches of Penetration for 100 Blows (for TCP>100 Blows/ft).

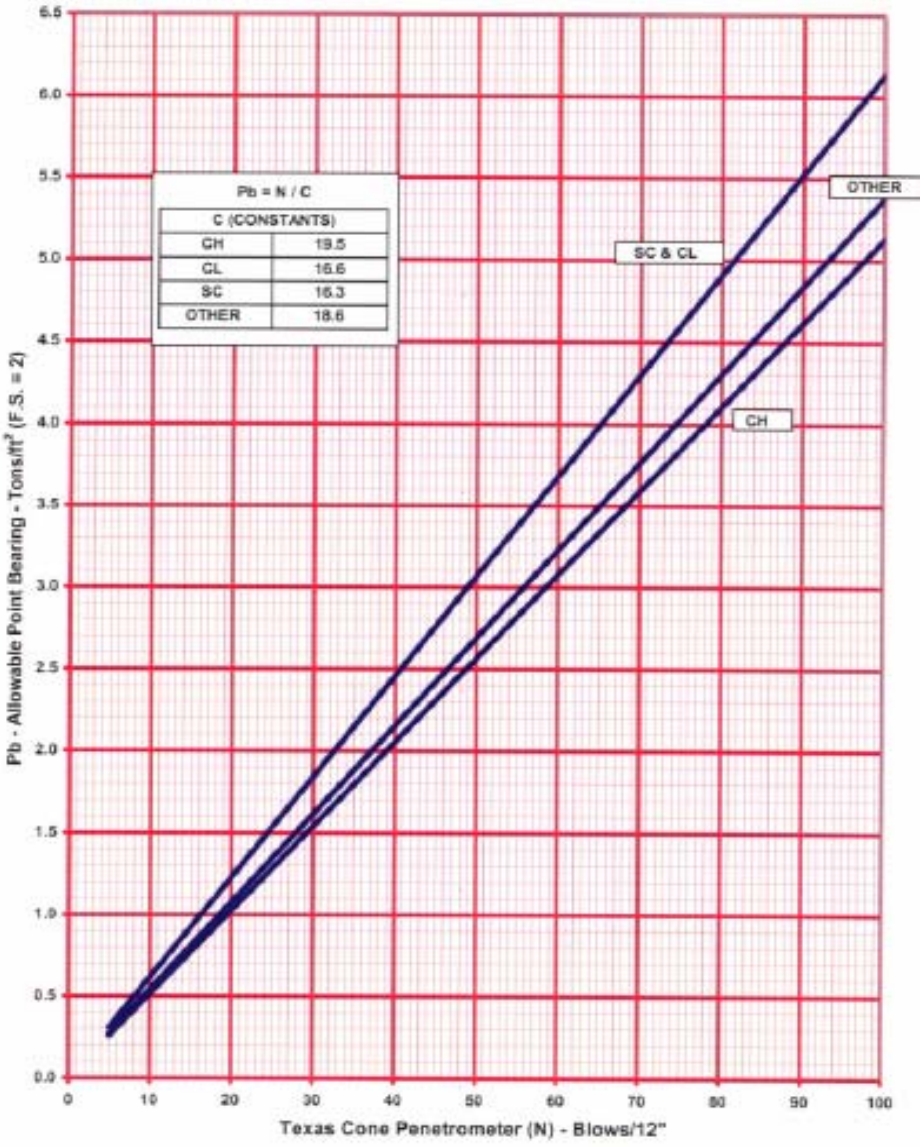

Figure 4-6. Point Bearing versus TCP (TCP<100 Blows/ft).

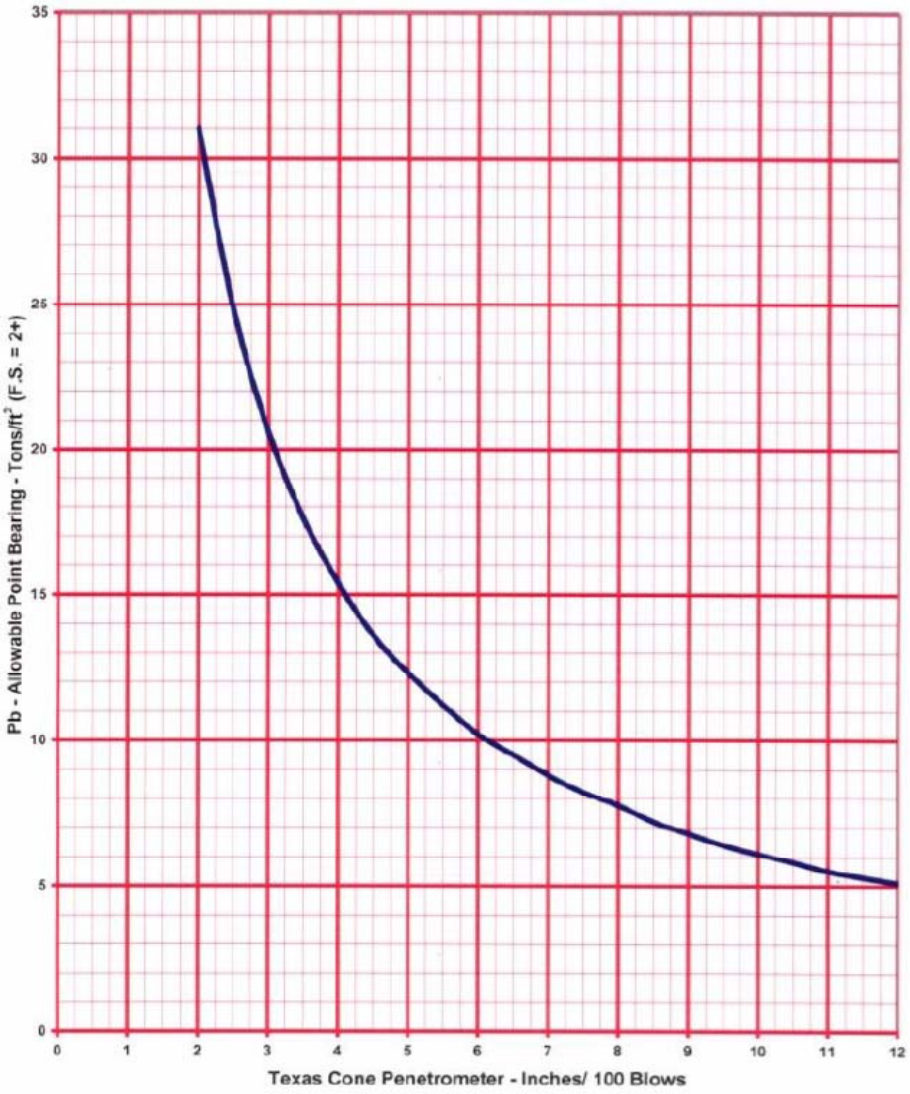

Figure 4-7. Point Bearing versus Inches of Penetration for 100 Blows (for TCP>100 Blows/ft).

PROBABILISTIC APPROACH

Step 1: Data Extraction

The set of data items required for implementing the probabilistic approach can be retrieved from the NBI. These parameters are used as input data for ANN models in order to first estimate bearing capacity and later to use the bearing capacity to implement the Bayesian inference. The input parameters from the NBI required for bearing capacity estimation via ANN are:

- Item 3: County (code).
- Item 16: Latitude (to be converted to degrees).
- Item 17: Longitude (to be converted to degrees).
- Item 27: Year built.

Step 2: Dead Load and Live Load Calculation

This step is similar to Step 4 of the deterministic approach.

Step 3: Obtaining Foundation Properties

In a condition where foundation type is known, size and number of piles (columns) for a bridge bent is required for predicting bearing capacity for each pile. If the foundation type is unknown, at least the number of piles per bent needs to be estimated based on the roadway width of the bridge or by other means such as visiting the bridge.

Step 4: Predicting Bearing Capacity Using ANN

Depending on the soil bore data and foundation type information availability, one of the following sub-steps is implemented:

- Step 4-1: If the foundation type is known to be deep but neither the foundation type nor the soil bore data are available, the ANN model called MLP-BC00 is recommended to predict bearing capacity for the interior bent of the bridge. It is assumed here that foundation type cannot be inferred with the desired level of confidence from an ANN classifier or from site investigation.
- Step 4-2: This step addresses the condition in which the foundation type is unknown (or cannot be inferred from the ANN classifier with the desired confidence level) but soil-boring data are available.
    - Step 4-2-1: Compute the average ultimate skin friction (Su) and point-bearing capacity (Pb) of the piles as described in Step 6.2.1 of the deterministic approach.
    - Step 4-2-2: Implement the ANN model, MLP-BC01, to predict bearing capacity of the bridge interior bent.

- Step 4-3: This step addresses the condition in which both the foundation type and soil information is known.
    - Step 4-3-1: The same procedure as described in Step 4-2-1 is performed to obtain average soil skin friction (Su) and point-bearing capacity (Pb) of the piles based on TCP values from the nearest borehole data.
    - Step 4-3-2: Implement MLP-BC11 to predict the bearing capacity of the bridge interior bent.
- Step 4-4: If foundation type is known or is inferred using the ANN classifier or by site investigation but soil bore data are not available, then one can implement the ANN model called MLP-BC10 to predict bearing capacity of the bridge interior bent.
- Step 4-5: The probabilistic solution of the inverse problem is implemented by the use of the Bayesian paradigm and MCMC simulations. This process uses samples from predefined distributions for each of the unknown variables (prior) and, based on the matching between the ANN-predicted bearing capacity and a geotechnical model prediction, populates another sample for each variable (posterior).

Finally, this method provides probability distributions for foundation type, foundation dimensions, and soil resistance (skin friction and point-bearing capacity), depending on what the unknowns are.

Chapter 5.
DATA COLLECTION

CASE STUDY—BRYAN DISTRICT OF TXDOT

In order to create both ANN-based and Bayesian-type methodology for determination of unknown foundations, a case study was defined in the Bryan District of TxDOT.

There are about 1,700 bridges in the Bryan District. Among those, 1,100 are crossing rivers and streams, which are those of concern due to scour vulnerability. Information from the Bryan District showed that not all types of data are available for all bridges. According to the availability of data, including the original as-built layouts and inspection data, bridges are separated into two broad categories:

- On system: In this set, TxDOT mostly constructed the bridges; as-built layouts and documents are available.
- Off system: In this set, there are no as-built plans for bridges. Inspections are performed to obtain data for these bridges, so only inspection data are available. Table 5-1 shows the number of bridges in each category in different counties.

Table 5-1. Bridges in Different Counties for On-System and Off-System Categories.

County	No. of On-System Bridges	No. of Off-System Bridges
Brazos	71	65
Freestone	67	41
Leon	65	33
Milam	59	51
Robertson	54	39
Madison	53	28
Washington	50	10
Grimes	49	88
Walker	45	30
Burleson	44	42
Sum	**557**	**527**

Different Types of Superstructures

Different types of superstructures for Bryan District bridges are:

- Prestressed concrete I-beam (PSC Gir [MULT]): This is a very common type of bridge in Bryan District.
- Pan Girder Bridge (Con Slab and Gir [PF]): This is the most common bridge type; the curve in the girder forms an arch, which helps in shear resistance.
- Prestressed concrete box beam bridge (PSC BoxGir [MULT]).
- T-beam bridge (ConGir TB).
- Multiple steel I-beam (Steel IB).
- Prestressed concrete slab span (Con Slab [VD]).
- Concrete flat slab (Con Flat Slab).

Figure 5-1 illustrates percentage of each type of superstructures for bridges in Bryan District.

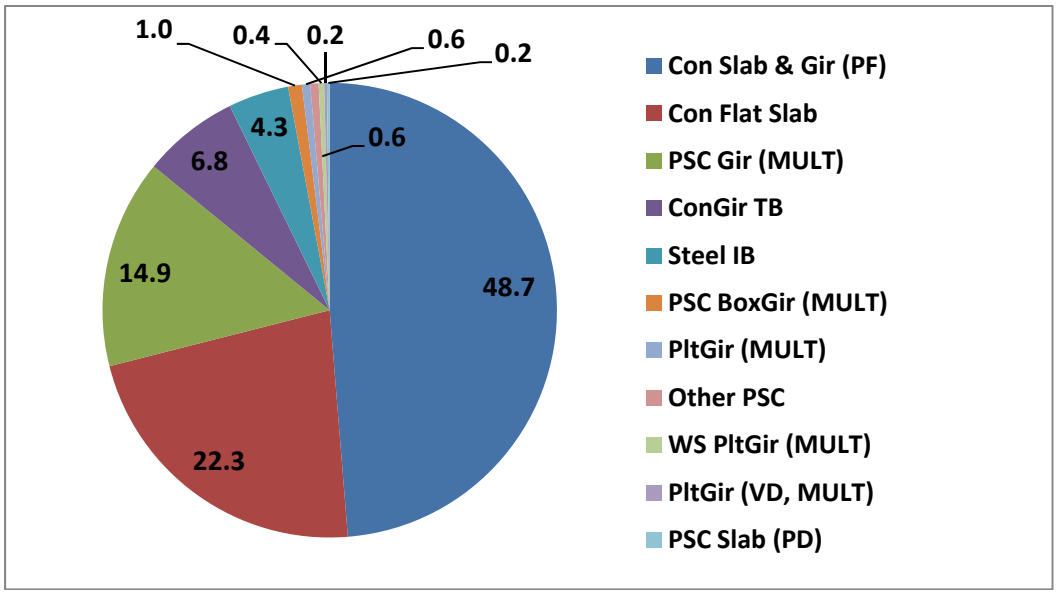

Figure 5-1. Percentage of Superstructure Type (%).

Different Types of Substructure

Different types of substructures for Bryan District bridges are:

- Multiple concrete columns (DrSh/Mult Col Bent).
- Multiple concrete columns with a tie beam (DrSh/Conc Col Bent w/Tie Beam).
- Concrete pile (Conc Piling/Pile Bents).
- Multiple concrete columns with a web wall (DrSh/Conc Col Bent Wall).
- Concrete pier on a spread footing (Spread Footing/ConcPier).
- Concrete pier on a pile cap with concrete piles (Pile Cap on Conc Piling/ConcPier).
- Concrete column on a pile cap with steel piles (Pile Cap on Steel/Mult Col Bent).
- Single concrete column on drilled shafts (DrilSh/Sing Col Bent).
- Multiple steel pile, usually H pile (S Piling/Pile Bents).
- Masonry pier on a spread footing foundation (Spread Footing/Masonry Pier).
- Multiple timber pile (T Piling/Pile Bents).

Table 5-2 presents the number and percentage of different substructure types for bridges in the Bryan District. Also, Figure 5-2 shows the pie distribution of different substructures (below ground) types.

Table 5-2. Percentage of Different Types of Substructures.

Substructure Type/ Above Gr.	No.	%	Substructure Type/ Below Gr.	No.	%	Cap Type	No.
Pile Bents	339	66.3	Steel Piling	62	12.1	Concrete Cap	484
Single Column Bent	0	0.0	Concrete Piling	276	54.0	Steel Cap	0
Multiple Column Bent	126	24.7	Timber Piling	3	0.6	Timber Cap	0
Concrete Column Bent w/ Tie Beam	2	0.4	Drilled Shaft	110	21.5	Masonry Cap	0
Concrete Column Bent Wall	1	0.2	Spread Footing	18	3.5	Other	0
Concrete Pier	14	2.7	Pile Cap on Steel Piling	10	2.0	**N/A**	**27**
Masonry Pier	2	0.4	Pile Cap on Concrete Piling	4	0.8		
Trestle (all)	0	0.0	Pile Cap on Timber Piling	1	0.2		
Other	0	0.0	Other	0	0.0		
N/A	**27**	**5.3**	**N/A**	**27**	**5.3**		
Sum	**511**		**Sum**	**511**		**Sum**	**511**

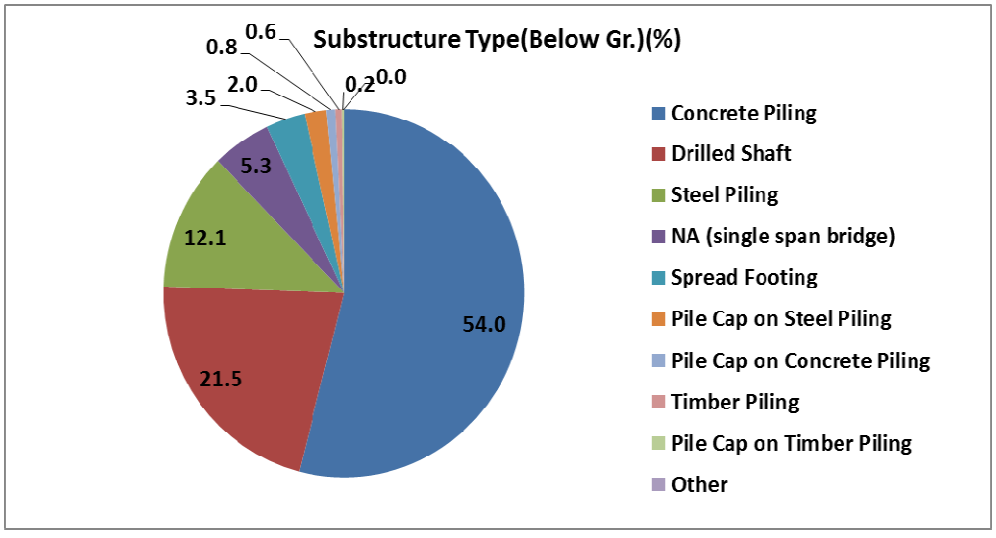

Figure 5-2. Percentage of Substructure (below Ground) Type.

DATA SAMPLING

A set of meetings were held in the Bryan District office to investigate the possibility of collecting data for bridges in Bryan. Data collection was then started by finding bridge inspection folders and scanning the relevant documents such as bridge plan, bridge inspection sheets, etc. Data were collected for about 40 percent of on-system bridges over rivers (about 185) with known foundations. These bridges were sampled from four populations of bridges with major foundation types (drilled shafts [DrSh], concrete piling [Conc], steel piling [St], and spread footing) in the Bryan District with the same proportions.

For each of the bridges' interior bents, relevant data for a representative pile of that bent was collected. Relevant information was identified for the purpose of ANN and Bayesian modeling based on the design procedures and standards instructed by:

- AASHTO standards (*LRFD Highway Bridge Design Specifications* [2007]).
- *AASHTO Standard Specifications for Highway Bridges* (2002).
- TXDOT bridge standard manual (*Bridge Inspection Manual* [2006], *Geotechnical Manual* [2006]).

Data are mostly collected from the inspection database provided by the TXDOT and from the design and construction plans found in bridge inspection folders. Data collected from these bridges forms a database that provides parameters required for ANN model training and also useful information about distribution of different relevant parameters for the Bayesian method of estimation. These parameters include superstructure elements, substructure elements, load elements, and soil properties.

Data from As-Built Layouts

As-built plans include several types of documents, including general documents, traffic control plans, roadway documents, bridge documents, and environmental documents. Most of our required data were found in the bridge documents section. Generally this includes hydraulic and hydrologic data, scour analysis, bridge layouts, and soil-boring data. Figure 5-3 and Figure 5-4 show a typical bridge plan and soil-boring data.

As demonstrated in Figure 5-3, the soil type and strength are determined by performing a specific test named Texas cone penetration test (TCP), which is very similar to the standard cone penetration test.

The procedure as described in TxDOT's *Geotechnical Manual* (2006) is outlined below:

- Attach a 76 mm (3 in) diameter penetrometer cone on the bottom of the drill stem and lower it to the bottom of the cored hole.
- Attach the anvil to the top of the drill stem, and position the 77 kg (170 lb) hammer above it.
- Drive the penetrometer cone 12 blows or approximately 152 mm (6 inches), whichever comes first, to seat it in the soil or rock.

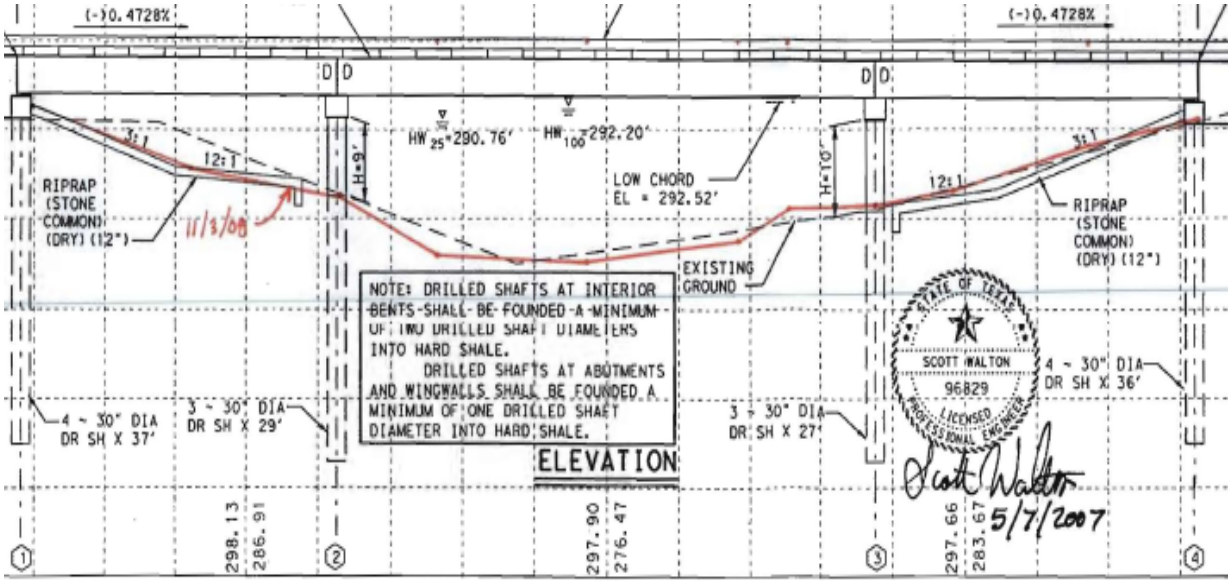

Figure 5-3. A Typical Bridge Plan.

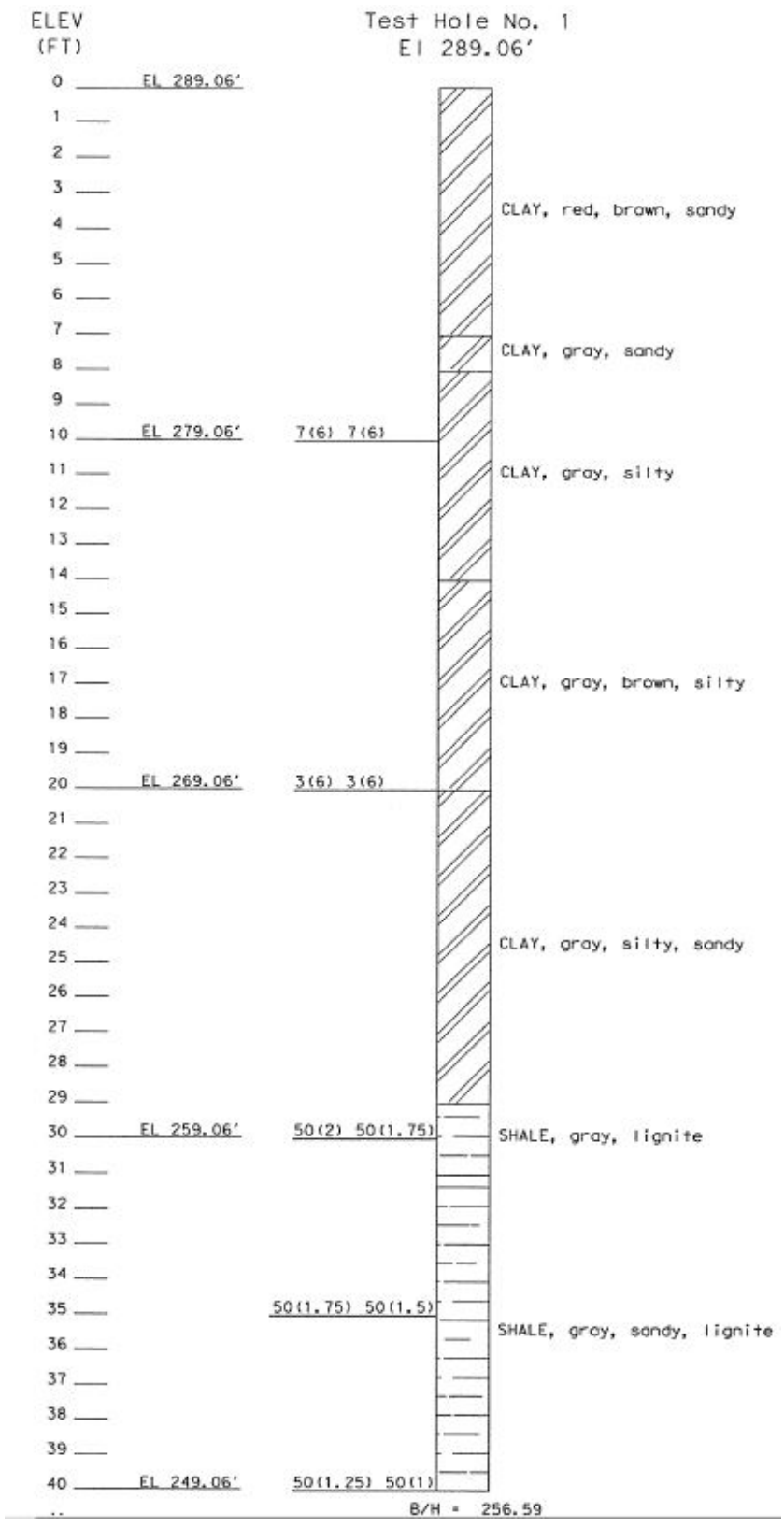

Figure 5-4. Typical Soil-Boring Data.

Skin friction and point-bearing capacity based on Texas cone penetration data can be estimated from Figures 5-5 to 5-7.

The following data are collected from as-built bridge plans for each interior bent:

- Foundation dimensions at the time of design, this includes:
  - Pile embedment depth, referred as pile depth (dp) in this study.
  - Pile cross section dimensions/area (Dia for DrSH/Dim for Conc pile/A_{St} for steel pile).
  - Spread footing width and length and depth of embedment (B, L, Df).
  - Left and right span lengths for the bent.
  - Number of piles in the bent (Pile group number, GN).
- Soil-boring data for the nearest borehole to the bent including:
  - Average TCP (blows/ft) value along the pile (avg. TCP).
  - TCP value at pile tip (or at bottom of the foundation) in blows/ft (point TCP).

  Note: For TCP greater than 100 (blows/ft), amount of penetration for 100 blows reported in the boring log is converted to the virtual number of blows required for 12 inches of cone penetration.
  - Average skin friction along the pile (su).
  - Point-bearing (Pb) at tip of the pile.

Data from TxDOT Inspection Database (NBI)

The following items are extracted from NBI for each bridge interior bent:

- Item 3, County.
- Item 27, Year built.
- Item 31, Design load.
- Item 34, Bridge skew.
- Item 43, Span type.
- Item 44, Substructure type.
- Item 48, Max span length.
- Item 51, Roadway width (ft).

- Item 52, Deck width (ft).
- Item 107, Deck type.
- Item 109, AADT truck percent.
- Item 114, Future AADT.

Descriptive Statistics

Figure 5-5 to Figure 5-6 show histograms for different parameters in the database. Note that each of the bridges had one or more interior bents, and the total number of records is two to three times greater than the total number of bridges (185).

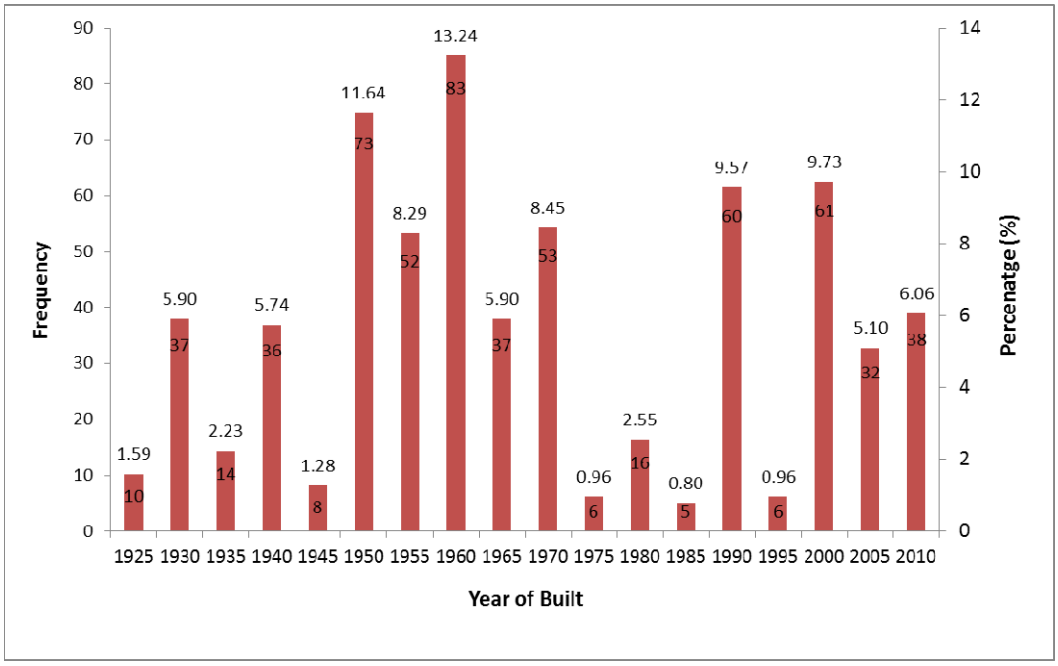

Figure 5-5. Histogram for Bridge Year Built.

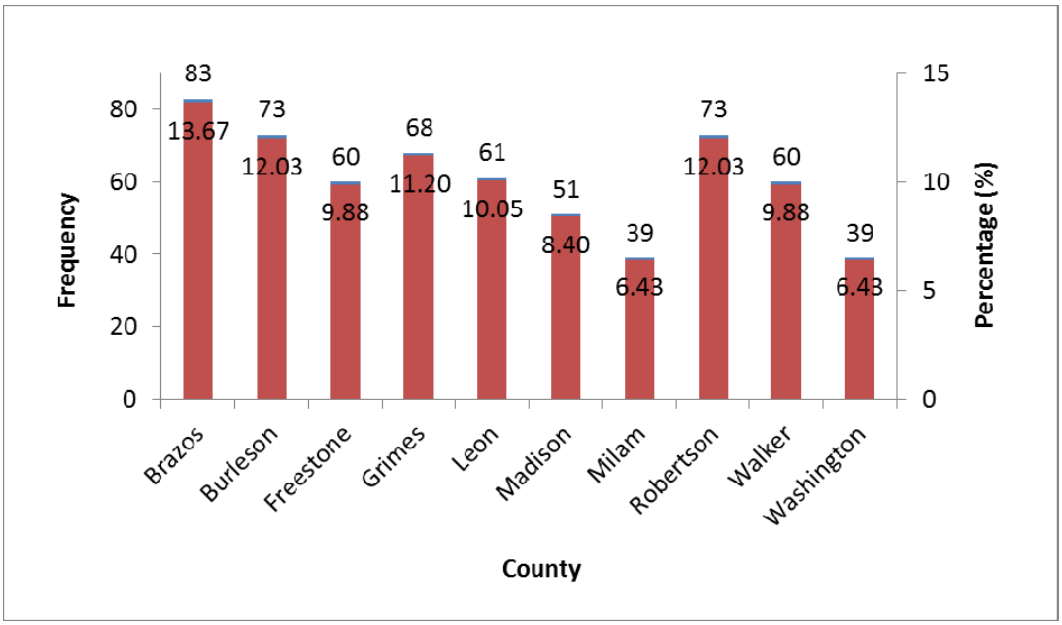

Figure 5-6. Histogram for Number of Bridges in Each County.

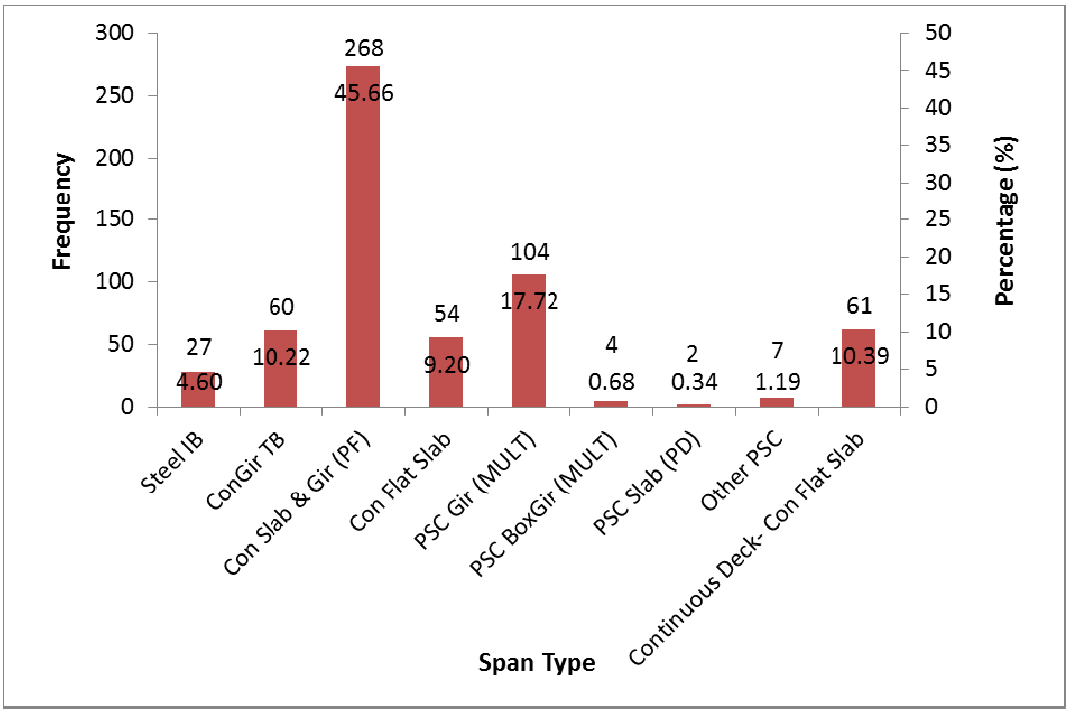

Figure 5-7. Histogram for Superstructure Type.

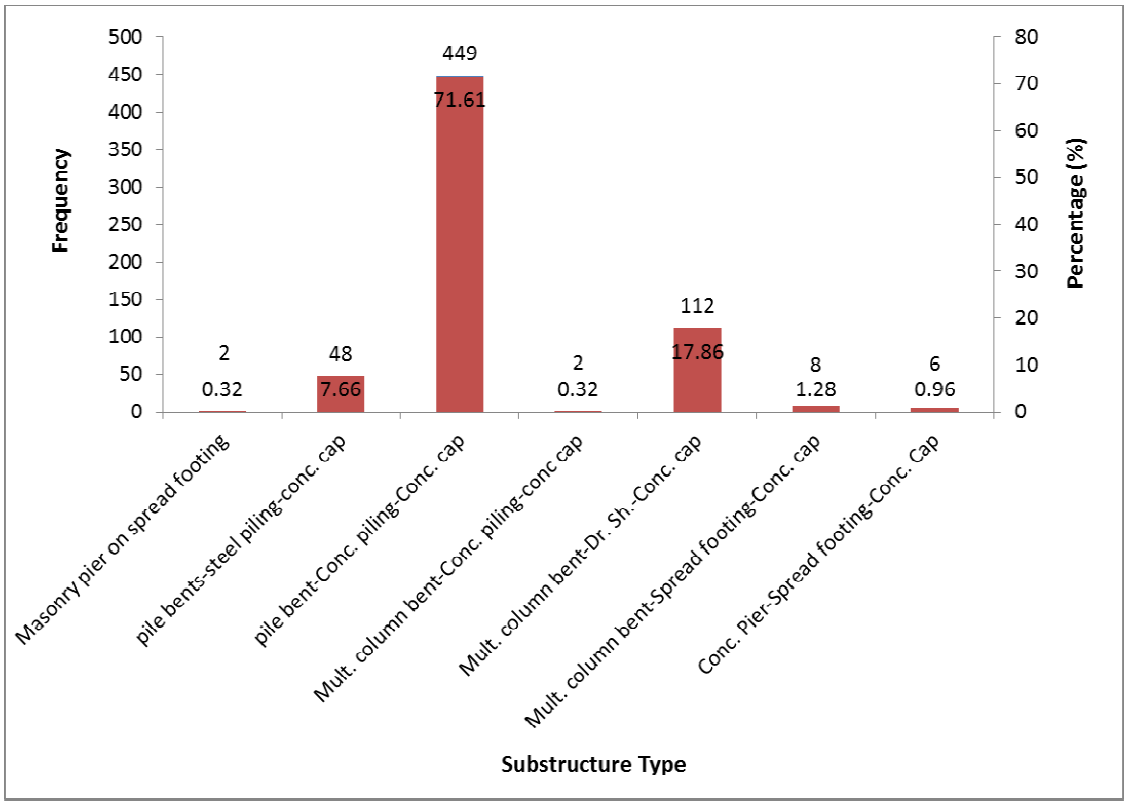

Figure 5-8. Histogram for Substructure Type.

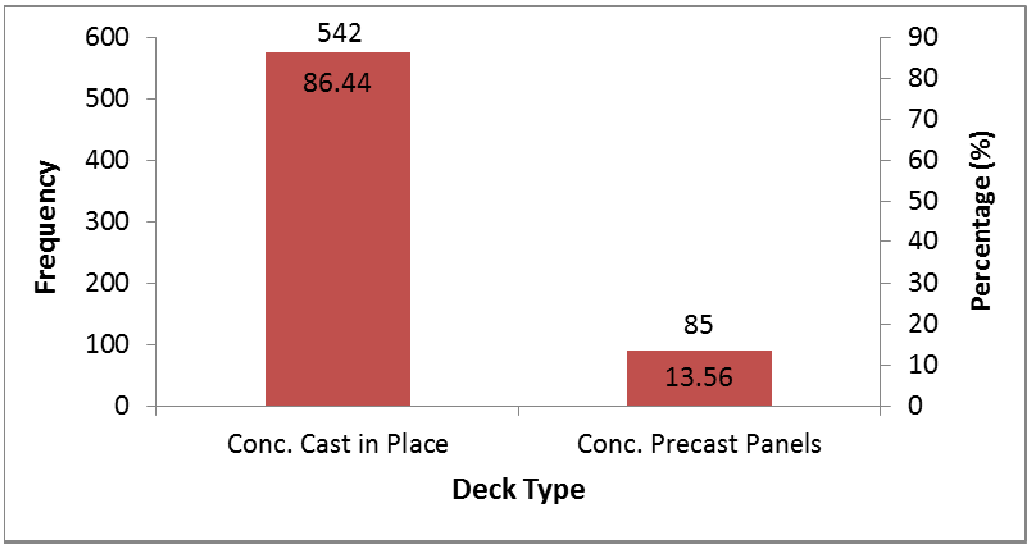

Figure 5-9. Histogram for Deck Type.

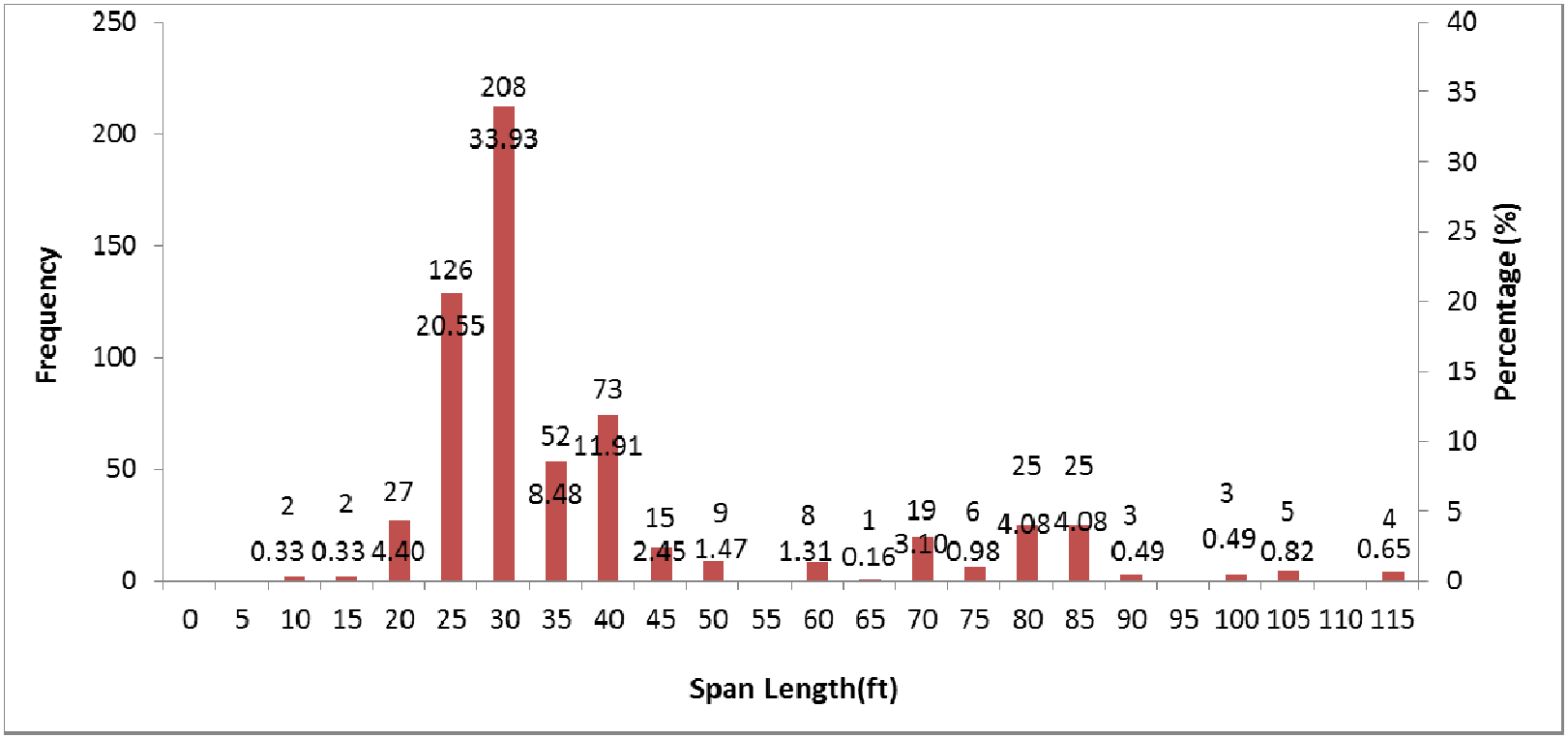

Figure 5-10. Histogram for Span Length (ft).

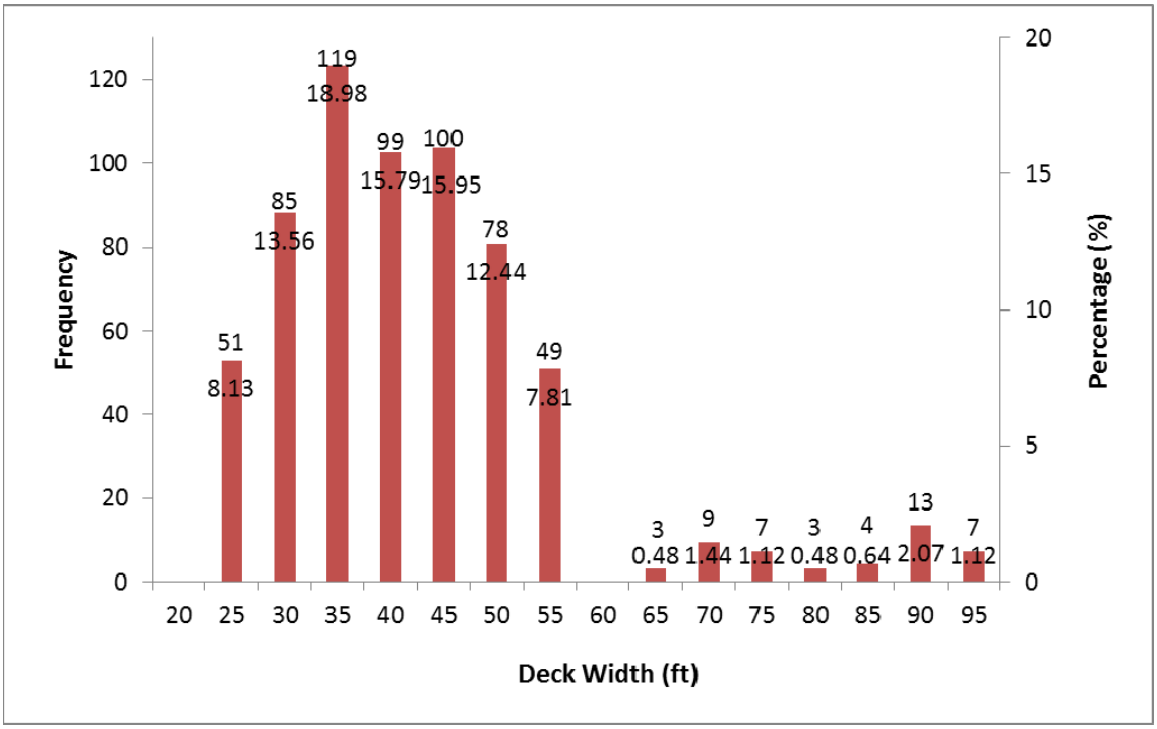

Figure 5-11. Histograms for Deck Width (ft).

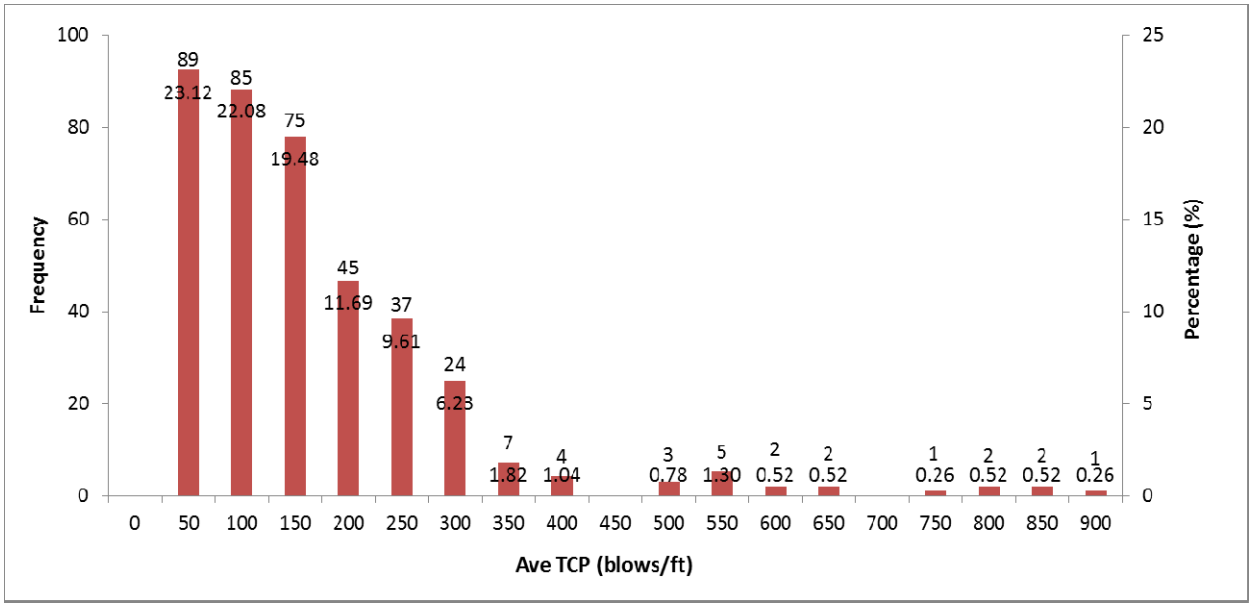

Figure 5-12. Histogram for Average TCP (Blows/ft).

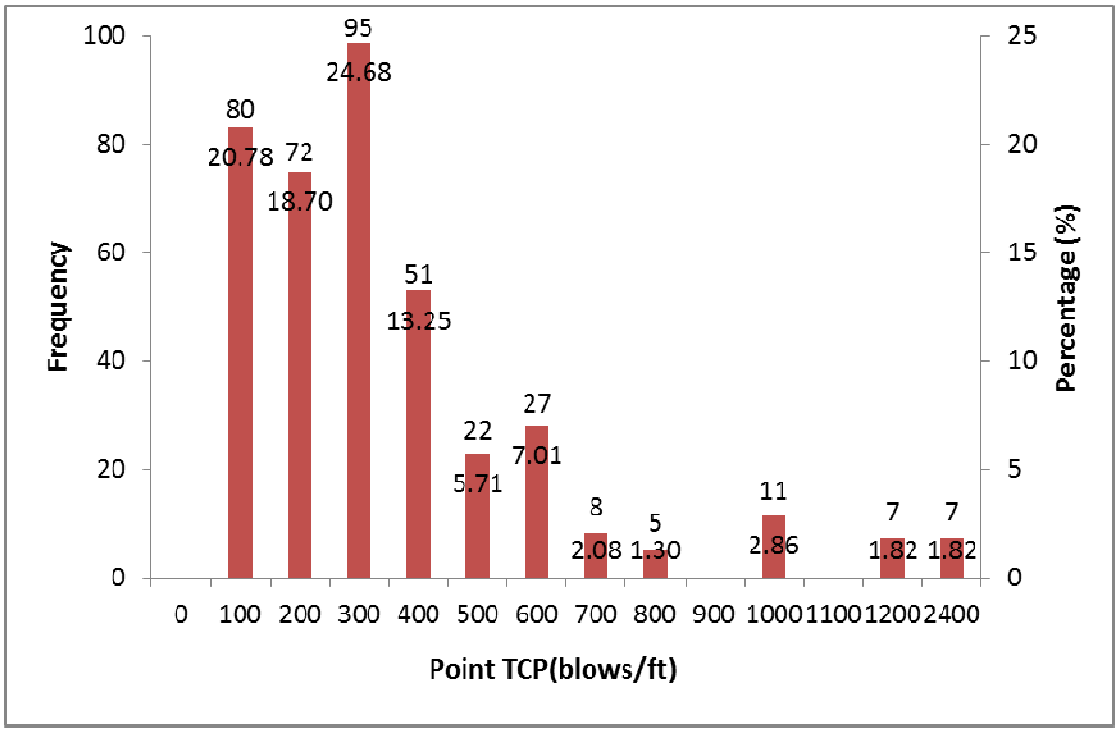

Figure 5-13. Histogram for Point TCP (Blows/ft).

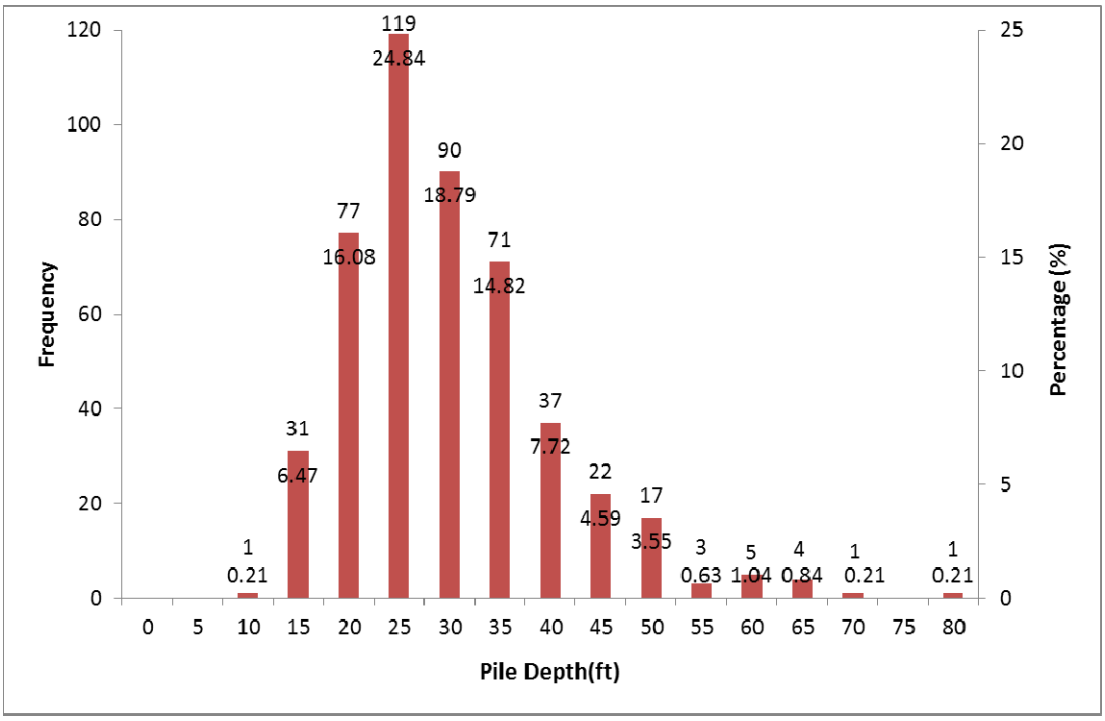

Figure 5-14. Histograms for Pile Depth (ft).

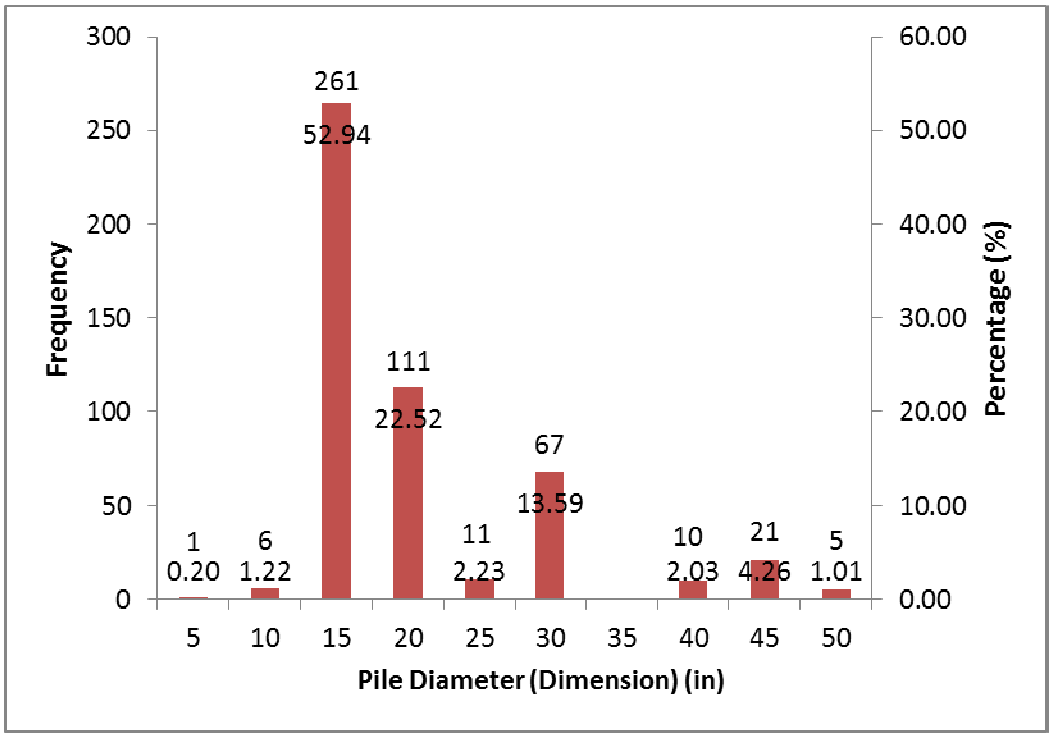

Figure 5-15. Histograms for Pile Diameter (Dimension) (Inches).

SPATIAL FEATURES

To demonstrate the risk components distribution over the collected bridges, a set of GIS maps were developed. The aim was to visualize different components of scour failure for collected bridges in this study.

Figure 5-16 demonstrates the location of bridges in the Bryan District of TxDOT used in this study along with the scour-critical index and average annual daily traffic (AADT). This map allows for determining the most and the least scour-critical bridges as well as making a rough assessment about the life-loss risk associated with these bridges. Note that the scour-critical index decreases as the scour vulnerability increases. Only three bridges are identified as scour critical, having red or yellow color in the map. The good news is that these bridges have small AADT, which make us less worried about life-loss risk.

Figure 5-17 presents the location of bridges along with scour-critical index and year built. It is observed that the three scour-critical bridges were built before 1960. Also, a trend is observed about the association of the age of bridges with the scour-critical index. As the age of the bridge increases, the lower the scour-critical index (the more sensitive the bridge is to scour).

Figure 5-18 shows the location of bridges along with scour-critical index and population density over the Bryan District. The two most critical bridges are located in Burleson County, where the population density is relatively low.

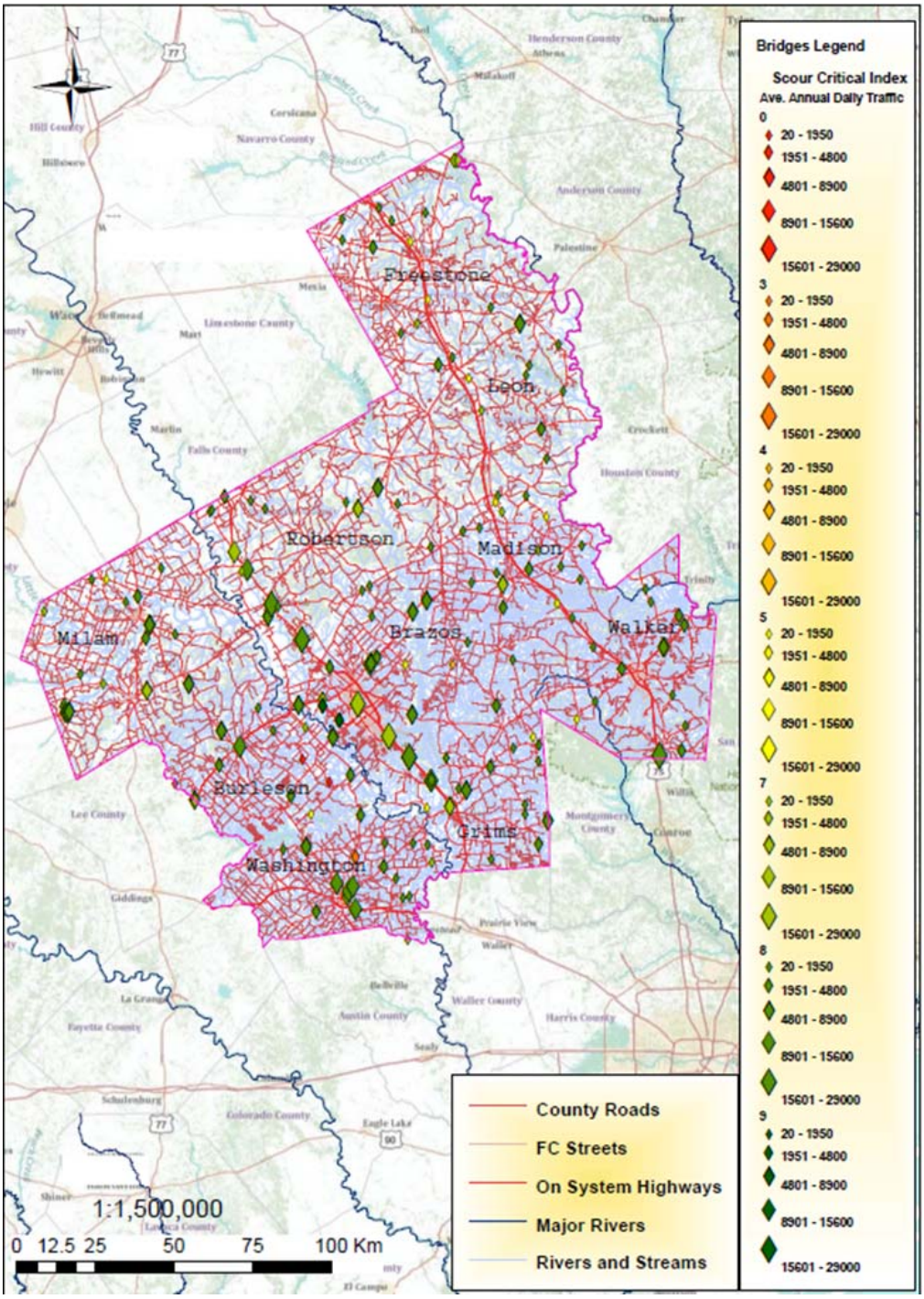

Figure 5-16. The Bridges in Bryan District of TxDOT Collected for This Study, Showing the Scour-Critical Index and AADT for the Bridges.

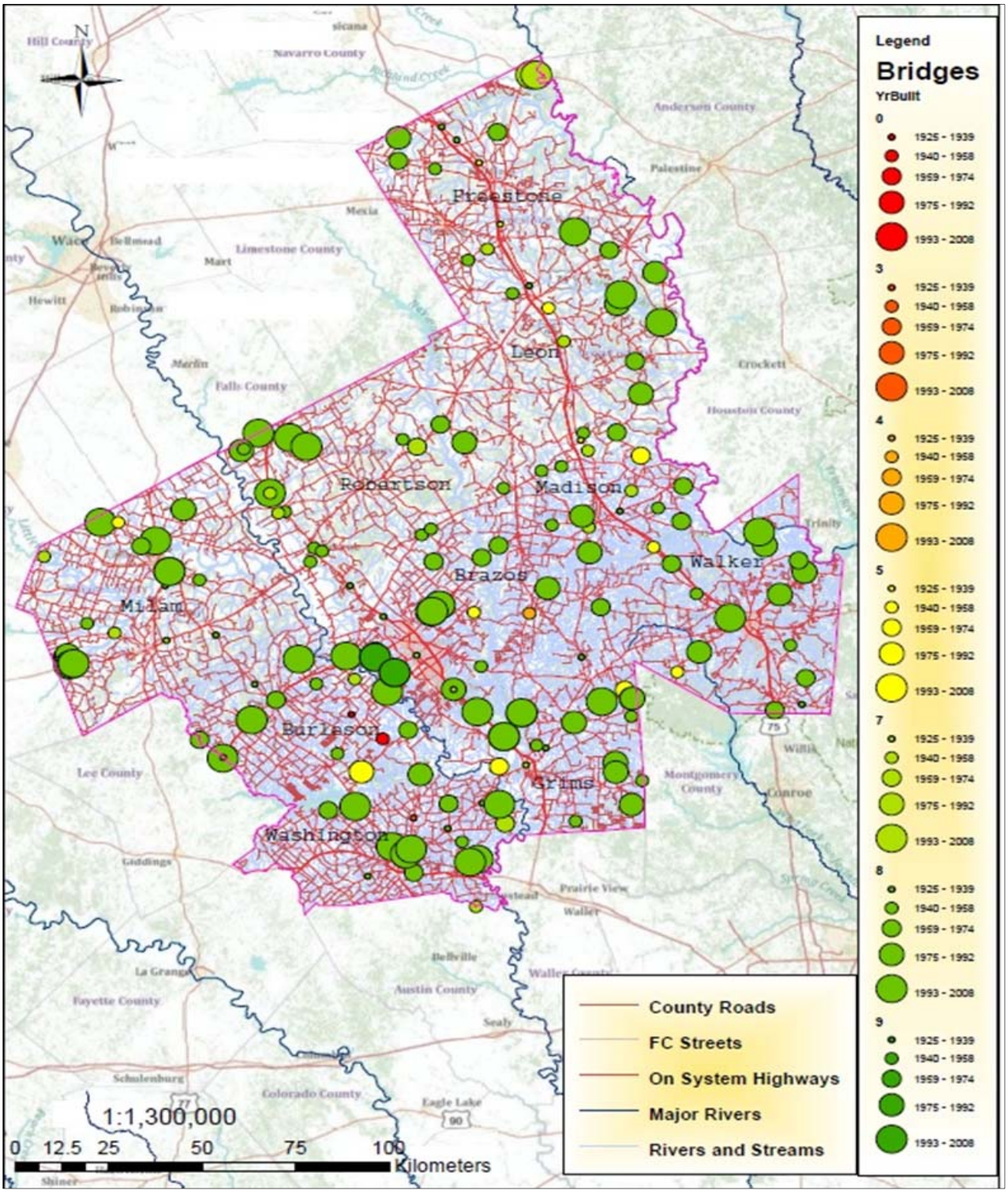

Figure 5-17. The Bridges in Bryan District of TxDOT Collected for this Study, Showing the Scour-Critical Index and Year Built for the Bridges.

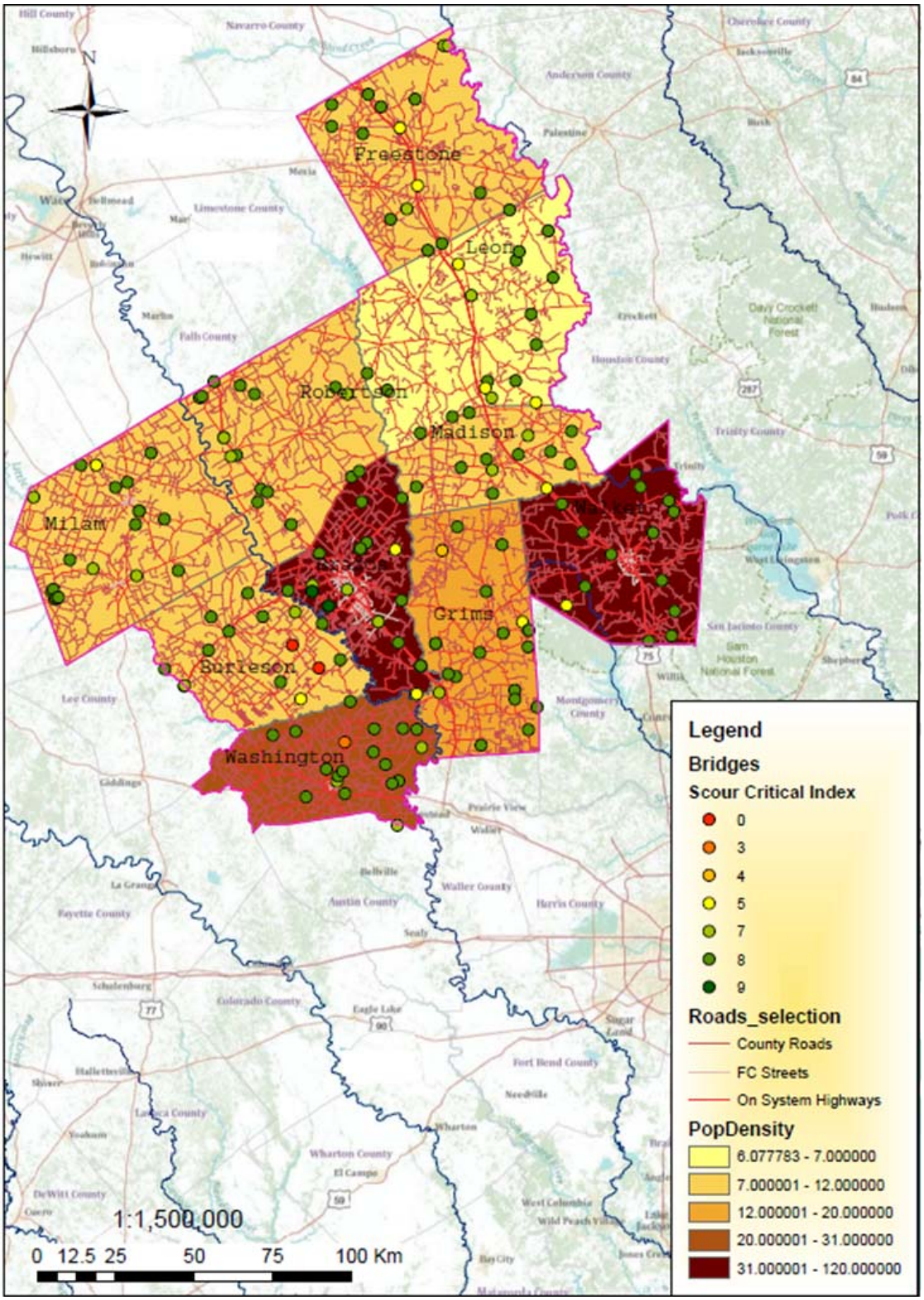

Figure 5-18. The Bridges in Bryan District of TxDOT Collected for This Study, Showing the Scour-Critical Index for Bridges and the Population Density over the Counties.

Chapter 6.
LOAD AND BEARING CAPACITY CALCULATION

INTRODUCTION

To implement both the deterministic and probabilistic approaches for identifying unknown foundations, it is required to assess the loads sustained by the bridge's interior bent. It is also necessary to compute the bearing capacity (BC) corresponding to the set of known foundation bridges, which will serve as the dependent variable to train the ANNs that will allow a probabilistic assessment of the bridges with unknown foundations.

This estimate of loads can be considered the lower bound threshold for the foundation allowable bearing capacity, what ensures that the bridge system is in static equilibrium. The loads for the prediction of all foundation types were not factored, as dictated in the TxDOT's *Geotechnical Manual*. In practice, it is expected to find over-designed bridges where loads are smaller than the allowable BC estimates due to the conservative design. Therefore, a departure from a linear pattern between loads and the actual BC computed from the as-built information is expected.

This chapter describes the process to estimate the dead load and live load for bridge bents and also the standard procedure used to compute bearing capacity for different types of known bridge foundations.

CALCULATING ULTIMATE BEARING

According to AASHTO standard specifications for highway bridges (AASHTO 2002), bridge foundations are designed using the load factor design method (LFD) (i.e., strength design method) or allowable stress design (ASD) (i.e., service load design method) methods. The AASHTO LRFD standard recommends the load-resistance factor design for all limit state designs (2007). As of 2000, LFD is to be used for on-system bridges. Either ASD or LFD may have been used for off-system bridges (TxDOT *Bridge Inspection Manual* [2006]).

The bearing capacity of foundations is calculated from soil strength and foundation geometry as indicated by the TxDOT's *Geotechnical Manual* (2006), except for the case of spread footings, where the AASHTO LRFD Standard (2002) is followed. This is because the TxDOT's

Geotechnical Manual does not include spread footings, and is expected to provide a conservative approach with similar design criteria as that used for shafts and piling. The formulation and procedure is described below for different foundation types.

Drilled Shaft

The ultimate load bearing capacity for drilled shafts is computed using the following equation,

$$q_{ult} = P_b A_p + S_u A_s \qquad \text{(Eq. 6-1)}$$

where q_{ult} is the ultimate load bearing capacity, P_b is the point-bearing capacity, and S_u is the skin friction. The variables P_b and S_u are obtained using the graphs proposed in TxDOT's *Geotechnical Manual,* which correlate the TCP value with the allowable skin friction and point-bearing capacity (2006). Allowable bearing capacity is calculated by factoring both skin friction and point-bearing capacity. In addition to the resistance factor, a reduction factor of 0.7 should be applied to skin friction because of the soil disturbance during the drilling. For LFD, the resistance factor for skin friction in clay is 0.65; for point-bearing, it is 0.55.

For drilled shafts in interior bents of river crossing bridges, the first 10 ft of the soil surface is disregarded in foundation design according to the TxDOT *Geotechnical Manual* (2006). This procedure is due to potential erosion from scour, future excavation, and seasonal soil moisture variations. If the shaft tip is drilled in a hard layer overlain by soft strata, the skin friction contribution of the soft layer could be ignored. Also, if soft layers exist within two shafts diameter of the proposed tip, the allowable point-bearing capacity for soft soil should be considered in the design.

Bearing capacity is mostly dominant for the design of foundations rather than structural stability, except when a hard layer exists very near to the surface. Table 6-1 shows the allowable service load for drilled shafts.

Table 6-1. Maximum Allowable Drilled Shaft Service (TxDOT *Geotechnical Manual* [2006]).

Diameter (in)	Load (Tons)
30	275
36	400
42	525
48	700
54	900
60	1100

Concrete and Steel Piling

Piling is typically used in soft soil conditions because of its small tip area. The point-bearing contribution is modest and is often disregarded in design according to the TxDOT *Geotechnical Manual* (2006). The bearing capacity is calculated using the same procedure described for the drilled shafts. The maximum recommended value for skin friction for piling design is 1.4 tons per square foot (tsf). As for drilled shafts, if a soft layer exists within two diameters of the proposed tip depth, the point-bearing capacity should be obtained based on the soft layer. Also, when a pile encounters a hard layer with TCP value greater than 100 blows per foot, it often refuses to advance, and it can be assumed that the pile has developed the maximum allowable service load as specified in Table 6-2.

Table 6-2. Maximum Allowable Pile Service Loads (TxDOT *Geotechnical Manual* [2006]).

Diameter (in)	Maximum length (ft)	Footing (per pile)
16	85	125
18	95	175
20	105	225
24	125	300

The tip area for steel piling is calculated assuming that a soil plug is formed at the tip in soft soils. The safety factor used for allowable stress design is 2. The resistance factor for skin friction of clay varies between 0.5 and 0.7, and is 0.7 for point (tip) bearing. The reduction factors for skin friction and point bearing of sand obtained using SPT are 0.45 and 0.55, respectively, when obtained by CPT records.

Spread Footing

According to TxDOT's *Geotechnical Manual* (2006), foundations of bridges should be designed as either drilled shafts or piling. However, a few bridges were identified with spread footing in the Bryan District.

According to the LRFD specifications (AASHTO 2002), the following equations are proposed to obtain the ultimate bearing capacity for spread footings in saturated clay, which is the dominant surface soil in Bryan area. No specifications were designated in TxDOT's *Geotechnical Manual* for the design of spread footings (2006). The ultimate bearing capacity is found using:

$$q_{ult} = CN_{cm} + \gamma' D_f N_{qm} \qquad \text{(Eq. 6-2)}$$

where C equals s_u, the undrained shear strength; N_{cm}, N_{qm} are the modified bearing capacity factors that are functions of footing shape, embedment depth, soil compressibility, and load inclination; γ' is the buoyant density of soil (tcf); D_f is the embedment depth taken to the bottom of footing; and N_{qm} is 1 for saturated clay and relatively level ground and 0 for footing on sloping ground or adjacent to sloping ground.

For $D_f / B > 2.5$ and $H / V < 0.4$,

$$N_{cm} = N_c \left[1 + 0.2\left(\frac{D_f}{B}\right)\right]\left[1 + .02\left(\frac{B}{L}\right)\right]\left[1 - 0.3\left(\frac{H}{V}\right)\right] \qquad \text{(Eq. 6-3)}$$

For $D_f / B < 2.5$ and $H / V < 0.4$,

$$N_{cm} = N_c \left[1 + 0.2\left(\frac{B}{L}\right)\right]\left[1 - 1.3\left(\frac{H}{V}\right)\right] \qquad \text{(Eq. 6-4)}$$

where N_c is 5.0 for Eq. 6-3 on relatively level ground and 7.5 for Eq. 6-4 on relatively level ground. Also, B is the width of the foundation, L is the length of the foundation, H is the horizontal load, and V is the vertical load.

The nominal (ultimate) bearing capacity of a layer of cohesionless soil such as sands or gravels, in tsf, is defined by:

$$q_{ult} = 0.5\gamma B C_{w1} N_{\gamma m} + \gamma C_{w2} D_f N_{qm} \qquad \text{(Eq. 6-5)}$$

where C_{w1} and C_{w2} are coefficients as specified in Table 6-3 as a function of D_w; D_w is the depth of the water surface taken from the ground surface; and $N_{\gamma m}$ is the modified bearing capacity factor.

Table 6-3. C_{w1} and C_{w2} versus D_w.

D_w	Cw1	Cw2
0	0.5	0.5
D_f	0.5	1
>1.5 B+D_f	1	1

Notice that for intermediate positions of ground water table, interpolation is allowed.
The bearing capacity factors are defined by:

$$N_{\gamma m} = N_\gamma s_\gamma c_\gamma i_\gamma \qquad \text{(Eq. 6-6)}$$

and

$$N_{qm} = N_q s_q c_q i_q d_q \qquad \text{(Eq. 6-7)}$$

in which N_γ and N_q are bearing capacity factors. These are defined as:

$$N_\gamma = 2\left(N_q + 1\right)\tan\left(\phi_f\right) \qquad \text{(Eq. 6-8)}$$

and

$$N_q = e^{\pi \tan\left(\phi_f\right)\frac{1+\sin(\phi_f)}{1-\sin(\phi_f)}} \qquad \text{(Eq. 6-9)}$$

Also, S_q and S_γ are foundation shape factors, defined as:

$$S_\gamma = 1 - 0.4\left(\frac{B}{L}\right) \qquad \text{(Eq. 6-10)}$$

and

$$S_q = 1 + \left(\frac{B}{L}\right)\tan\left(\phi_f\right) \qquad \text{(Eq. 6-11)}$$

while c_γ and c_q are the soil compressibility factors. The compressibility factors are defined as:

$$c_q = c_\gamma = e^{\left(-4.4+\frac{0.6B}{L}\right)\tan\left(\phi_f\right)+\frac{\left(3.07\sin\left(\phi_f\right)\left[\log\left(2I_r\right)\right]\right)}{1+\sin\left(\phi_f\right)}} \leq 1 \qquad \text{(Eq. 6-12)}$$

and

$$I_r = 2D_r\sqrt{\frac{P_a}{q}} \qquad \text{(Eq. 6-13)}$$

where D_r is the relative density in percentage, q is the effective overburden pressure, and P_a is the atmospheric pressure taken as 1.05 tsf. The variables i_q and i_γ are the load inclination factors defined as:

$$i_\gamma = \left(1 - \frac{H}{V}\right)^n \qquad \text{(Eq. 6-14)}$$

In the case where the load is inclined in the direction of the width, n is 2.50 for a square footing, 2.67 for a footing with $L/B = 2$, and 2.00 for footing with $L/B \geq 10$. For a load inclined in the direction of the length, n is 2.50 for a square footing, 2.33 for a footing with $L/B = 2$, and 2.00 for footing with $L/B \geq 10$. Finally, d_q is the depth factor:

$$d_q = 1 + 2\tan\left(\phi_f\right)\left(1 - \sin\left(\phi_f\right)\right)^2 \tan^{-1}\left(\frac{D_f}{B}\right) \qquad \text{(Eq. 6-15)}$$

In Texas, it can be assumed that horizontal load is negligible comparing to vertical load for bridges where the earthquake and wind loads are not dominant. Thus, it can be assumed that H/V is almost zero and that the load inclination factors are roughly equal to one.

The allowable bearing capacity is obtained by applying a resistance factor. According to LRFD specifications, these factors depend on foundation type, design method, and in-situ tests (SPT, CPT) by which soil strength is obtained. For shallow foundations on sand, this factor is 0.35 if ϕ_f is obtained by SPT and 0.45 if obtained by CPT. Likewise, for shallow foundations on clay, the resistance factor is 0.6 if ϕ_f is measured in a laboratory and 0.6 if obtained by the CPT method.

In this study, the friction angle of cohesionless soil is obtained from the graph presented in TxDOT's *Geotechnical Manual* (2006) (Figure 6-1), using the TCP value at bottom of the spread footing. Also, the unit weight of the soil is required to calculate the bearing capacity of spread footings. The soil unit weight is obtained from Table 6-4 depending on the SPT value. The relation between SPT and TCP is presented in Table 6-5.

Figure 6-1. Angle of Friction for Cohesionless Soils.

Table 6-4. Unit Weight of Soil versus SPT (Bowles 1968).

Granular		Cohesive	
SPT(N-Value)	γ(lb/ft3)	SPT(N-Value)	γ(lb/ft3)
0 to 4	70-100	0 to 4	100-120
4 to 10	90-115	4 to 8	110-130
10 to 30	110-130	8 to 32	120-140
30 to 50	110-140		
>50	130-150		

Table 6-5. SPT and TCP Relation (Touma and Reese 1969).

Cohesionless			Cohesive		
Soil	N TCP	N SPT	Soil	N TCP	N SPT
very loose	0 to 8	0.5 N TCP	very soft	<3	0.7 N TCP
loose	8 to 20	0.5 N TCP	soft to medium	3 to 11	0.7 N TCP
medium	20 to 60	0.5 N TCP	stiff	11 to 21	0.7 N TCP
dense	60 to 100	0.5 N TCP	very stiff	21 to 43	0.7 N TCP
very dense	>100	0.5 N TCP	hard	>43	0.7 N TCP

Concrete Cap on Group of Piles

The ultimate bearing capacity for this type of foundation is obtained based on LRFD specifications for group of pile axial load resistance.

Cohesive Soils

For cohesive soils, the ultimate bearing capacity is:

$$Q_g = \eta n q_{ult} \qquad \text{(Eq. 6-16)}$$

where η is the efficiency (reduction) factor. The efficiency factor is 0.65 for center-to-center spacing of 2.5 diameters and 1 for center-to-center spacing of 6.0 diameters. Also, n is the number of piles in a group.

If the piles cap is in firm contact with the ground, no reduction factor is needed. If not, but the soil is stiff, still no reduction factor shall be used. However, if the cap is not in firm contact with the piles and if the soil is soft at the surface, individual resistance factors of each pile shall be multiplied by an efficiency factor.

Furthermore, it is necessary to check for failure mechanisms and design for the case that yields the minimum bearing capacity. For a pile group of width X, length Y, and depth Z the bearing capacity for block failure is:

$$Q_g = (2X + @Y)Z\overline{S_u} + XYN_cS_u \qquad \text{(Eq. 6-17)}$$

where $\overline{S_u}$ is the average undrained resistance along the depth of penetration of the piles (tsf) and S_u = undrained shear strength at the base of the group (tsf).

For $Z/X \leq 2.5$,

$$N_c = 5\left(1+\frac{0.2X}{Y}\right)\left(1+\frac{0.2X}{Y}\right) \qquad \text{(Eq. 6-18)}$$

For $Z/X \geq 2.5$,

$$N_c = 7.5\left(1+\frac{0.2X}{Y}\right) \qquad \text{(Eq. 6-19)}$$

Cohesionless Soils

The bearing capacity for pile group in cohesionless soil is equal to sum of the resistance of all the piles in the group (i.e., the efficiency factor is 1 whether the pile cap is or is not in contact with soil).

Care should be taken when a weak soil layer exists beneath a strong soil. The potential for a punching failure and large settlement should be considered.

The allowable bearing capacity is computed by applying a resistance factor as designated in LRFD specifications. The resistance factors for pile groups are the same as for single piles.

LOAD DETERMINATION FOR BRIDGE FOUNDATIONS: METHOD I

Dead Load

Dead load for a foundation in an interior bent is obtained by adding up all permanent loads that are sustained by the foundation from all components of the superstructure, including the deck, girders (beams), bent cap, column, and railing weights.

For simple span bridges, the tributary area is one-half of the spans on each side of the interior bent. For continuous span bridges, the distribution of loads is more complex due to the fact that loads are

distributed somewhat differently. However, choosing one-half of each adjacent span will produce a reasonable answer.

For determination of bridge superstructure dead load, the weights of the individual components are summed. For beam-type bridges, the weight (per linear foot) of the beams must be known or determined, as well as the weight of the bridge deck and the bridge railings. For monolithic beam/deck structures like pan form bridges, the dead load is most easily determined from the volume of concrete used in the superstructure.

The TxDOT as-built bridge plans are used to obtain the superstructure construction details for different superstructure types. From these standard sheets, one can obtain the total weight of reinforcing steel and the total volume of concrete for the slab, girders or beams, and bent caps.

Most bridges have concrete barriers, and TxDOT standard detail sheets are based on this type of barrier. A typical concrete barrier (T551) has a weight of 380 plf. In rare cases, it may be useful to adjust foundation weights for the specific barrier found on the structure, thus, for reasonable estimates, a concrete barrier is assumed for all bridges.

Live Load

Prior to the adoption of the LRFD specifications, there were at least four different versions of AASHTO live-load standard computation methods. The H series modeled single unit trucks, while the HS series modeled semi-trucks. Note that the HS series has a variable dimension shown between the rear two axles. For the purpose of foundation load determination, this dimension will always be set at 14 ft, which serves to concentrate the maximum load over the interior bent.

Figure 6-2 shows diagrams of the various load configurations. The lane loading (the uniform shown in Figure 6-2) generally controls bridges with longer spans (>70 ft). Most structures on unknown foundations are locally owned (off-system) bridges with relatively short span lengths, so the truck loadings will generally control. Note that the concentrated loads shown in the calculation of foundation loads are used to obtain the live load, rather than the higher-concentrated load designated for shear.

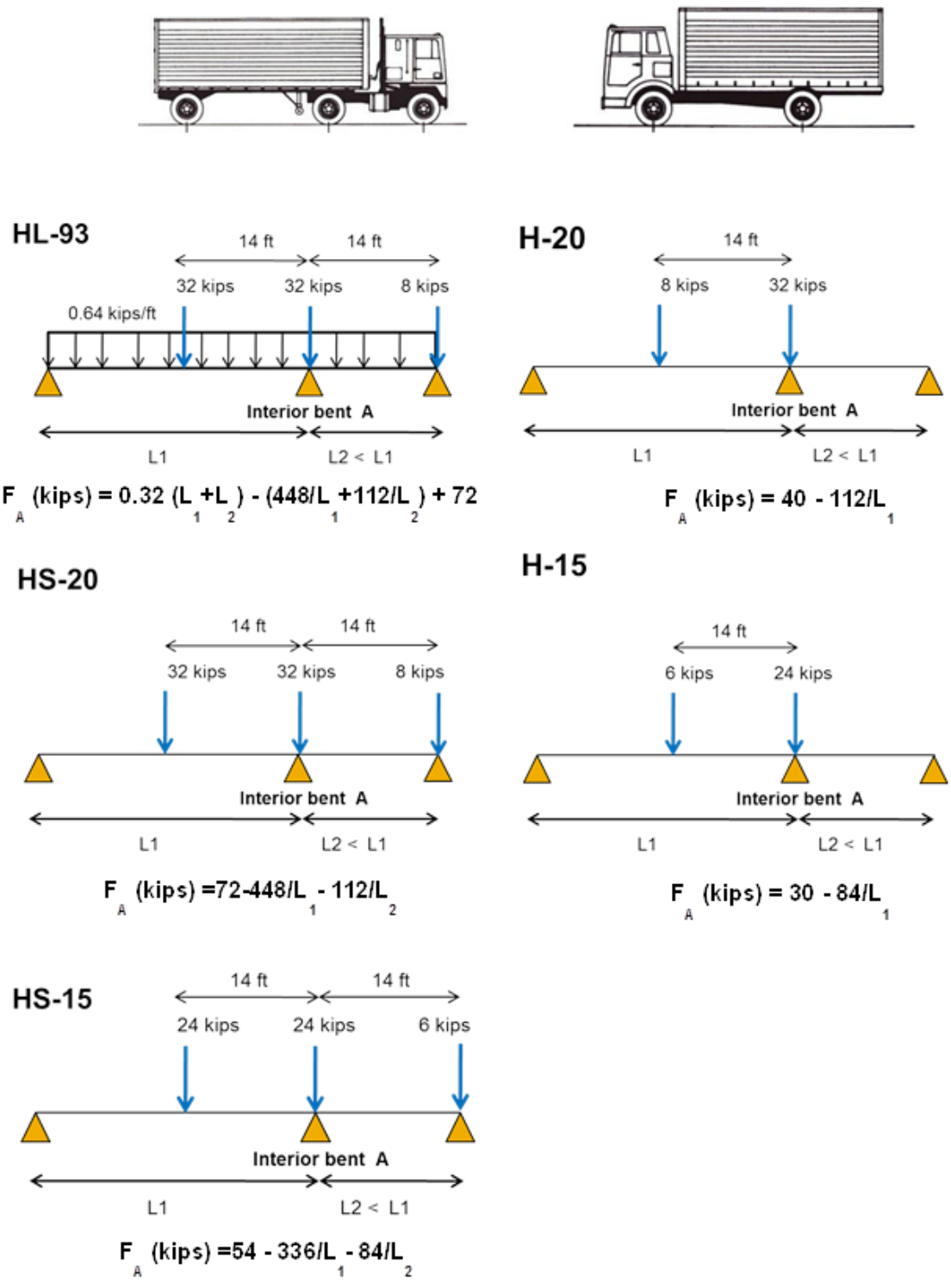

Figure 6-2. Standard AASHTO Design Loads and Maximum Reaction of an Interior Bridge Bent with Single Spans.

The current design vehicle designated by the LRFD standard is referred to as the HL-93. This load is the combination of the HS-20 truck load with the uniform load portion (640 lb per linear ft) of the HS-20 lane loads. Since the LRFD design has been applied to structures built only in the past 10 years, there should not be LRFD-designed bridges on unknown foundations. However, the current on-line bridge standard sheets are all designed with the HL-93 live load.

When determining live loads on interior bents, the H series truck is placed with the heavy axle directly over the interior bent and the lighter axle sitting on the longer adjacent span (if spans are not equal). The HS series truck is placed with the center axle directly over the bent, the heavier end axle on the longer adjacent span (if spans are not equal), and the lightest axle on the other adjacent span.

The number of live load lanes placed on a bridge is a function of the roadway width. The roadway width is divided by 12 ft, and the integer portion of the result is considered the number of lanes on the bridge. For structures designed with more than two lanes, a reduction factor is applied to live load to account for the probability that all lanes will not be fully loaded simultaneously. The factors typically used are 1.0 for bridges with one or two lanes, .90 for bridges with three lanes, and .75 for bridges with four or more lanes.

Actual Live load = N (No. of bridge lanes) × F_A (of std. design vehicle, item 31) × R.F. (for multiple presence in all lanes): (Eq. 6-20)

where

R.F. = 1 for two lanes

and

R.F. = 0.9 for three lanes

and

R.F. = 0.75 for four and more lanes.

AASHTO design code calls for an impact multiplier to be used on live loads when designing superstructure components. However, the impact factor is not used in the calculation of foundation

loads, since the superstructure and substructure attenuate the impact as the load travels down to the foundation elements.

LOAD DETERMINATION FOR BRIDGE FOUNDATIONS: METHOD II

Dead load determination using the previous method (Method I) requires the collection of a number of details from the superstructure, which makes the process very time-consuming. Therefore another method is proposed to make the process faster. As mentioned earlier, TxDOT provides online resources that can be used for the design of bridges. These resources include the "standard design sheets" for different bridge types (TxDOT 2011). The foundation loads are estimated for sample cases of each superstructure type. Therefore, the total foundation load can be estimated with an acceptable accuracy using these sheets. Figure 6-3 shows the flowchart for obtaining foundation loads using the TxDOT standard sheets.

The load assessment process starts with identifying the superstructure type and finding corresponding standard design sheets based on the bridge roadway width and bridge skew. Table 6-6 presents different types of superstructures found in the database. There is a little difference in terminology used for superstructure types by TxDOT and the terminology used in the inspection database as shown in Table 6-6.

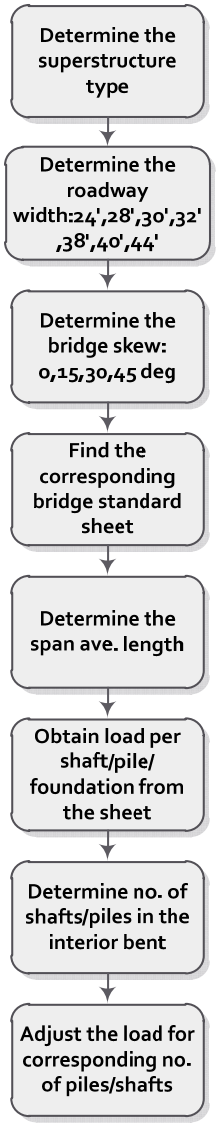

Figure 6-3. The Flowchart to Obtain the Total Load Using TxDOT Bridge Design Standard Sheets.

Table 6-6. Different Superstructure Types Used by TxDOT for Standard Design Sheets.

Superstructure Type-Code	TxDOT Standard Design
Prestressed Concrete I-beam-1131	**Prestressed I-Girder** standards are available for structures with Type Tx28 thru Tx62 girders. These are included in the issued set of Prestressed Concrete I-Girder standards.
Concrete flat slab-1126	**Cast-In-Place Concrete Slab Span** standards are available for structures using a 14″ or 16″ slab depth. These are included in the TXDOT-issued set of C-I-P Concrete Slab Span standards.
Multiple steel I-beam-1111	**Steel Beam** standards are available for structures with Type W18, W21, W24, W27, W30, W33, W36, or W40 beams. These are included in the TXDOT-issued set of Steel Beam standards.
Prestressed concrete slab span-1137	**Prestressed Slab Beam** standards are available for structures with Type SB12 or SB15 beams using 5″ cast-in-place slab as a topping. These are included in the TXDOT- issued set of Prestressed Concrete Slab Beam standards. .
Prestressed concrete box beam bridge-1133	**Prestressed Box Beam** standards are available for structures with Type B20, B28, and B34 beams using 5″ cast-in-place slab or 2″ ACP overlay as toppings. These are included in the TXDOT-issued set of Prestressed Concrete Box Beam standards.
Other Prestressed Concrete-1139	**Prestressed Concrete Double T-beam**
Concrete Slab and Girder (Pan Form)-1125	**Concrete Slab and Girder (Pan Form)** standards are available. These are included in the TXDOT-issued set of Concrete Slab and Girder standards.

The next step is to determine the roadway width using the bridge layout, which can be found in the inspection database item 51 or using the bridge layout. The standard sheets are prepared for a typical roadway width of 24, 28, 30, 32, 38, 40, 42, or 44 ft, while there is a wide range (between 19 and 90 ft) of roadway width of bridges in the Bryan District. To overcome this limitation, it is reasonable to extrapolate load estimates for widths greater than 44 ft.

Finally, the bridge skew can be found in item 34 of the inspection database or from the bridge layout. The bridges skew varies between 0°, 15°, 30°, and 45°.

Once the superstructure type is found and the roadway width and the bridge skew are defined, it is possible to find the corresponding TxDOT standard design sheet for a particular bridge. Standard sheets normally provide the load per pile/shaft based on various span lengths, but this value is for a specific number of piles or shafts per bent for a reference case used in the standard sheet. Therefore, the value obtained for the load per pile/shaft should be adjusted according to the number of piles/shafts per bent for the desired bridge. Another observation on the use of the design sheets is that the span length for each bent is obtained by averaging the left and right span lengths. Table 6-7 shows the foundation load table obtained from a standard bridge design sheet for 24 ft, prestressed concrete I-beam, 15° skewed.

Table 6-7. Foundation Loads Table for 24 ft PSC I-Beam Bridge with a 15° Skew.

FOUNDATION LOADS ④				
Span Average	Drilled Shaft Loads	Pile Load (Tons/Pile)		
		3 Pile Ftg	4 Pile Ftg	5 Pile Ftg
Ft	Tons/Shaft			
30	96	35	27	22
35	106	39	30	24
40	115	42	32	26
45	125	45	34	28
50	134	48	37	30
55	143	51	39	32
60	152	54	41	34
65	161	57	43	35
70	169	60	46	37
75	178	63	48	39
80	187	66	50	41
85	196	68	52	42

A set of regression lines are developed based on various loads versus span lengths for both column (shaft) and pile bent for each bridge standard sheet. Figure 6-4 shows the regression lines for prestressed concrete I -beams for a 24-ft roadway width and different bridge skews. The regression coefficients are obtained for each combination of roadway width and bridge skew for each of the

existing superstructure types. Table 6-8 presents the load coefficients of column bent for a prestressed concrete I-beam bridge.

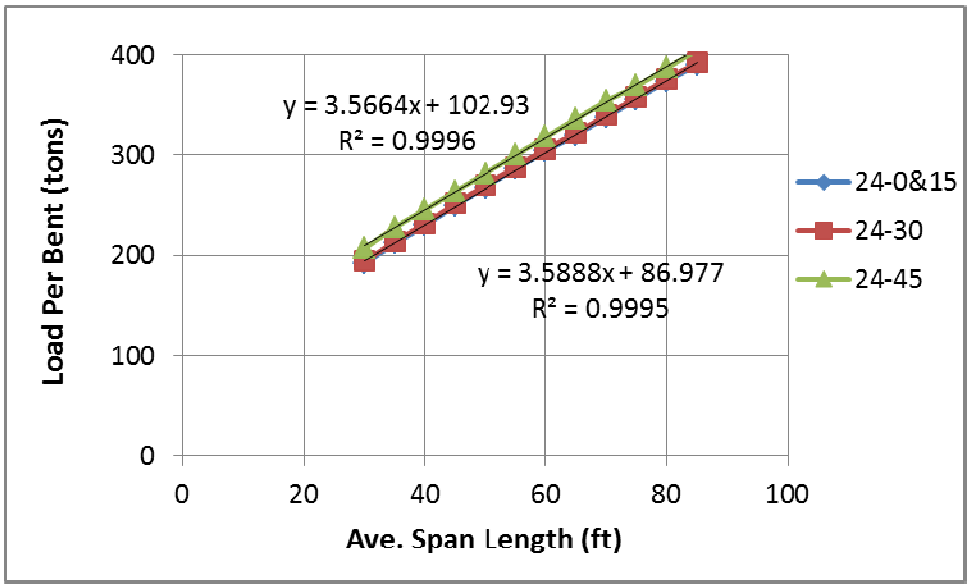

Figure 6-4. Load versus Average Span Length for Prestressed Concrete I-Beams.

A MATLAB code is developed to automate the process of load assessment (included in the Appendix). These programs input the table of coefficients as well as a table containing roadway width, average span length, and skew for bridge bents and outputs for the total estimated load for each bridge bent.

Although the loads obtained from the standard sheets are reasonable, they are based on current TxDOT standards that are based on LRFD design requirements. The live-load model for the LRFD code uses heavier loading conditions than the live-load models used in previous design specifications. Consequently, the resulting foundation loads will be higher. However, for highway bridges, the dead load of the structure is generally higher than the live load. For long-span concrete bridges, the ratio of dead load to live load can exceed 80 percent. So while the current live load has resulted in an increase in foundation loads, experience has shown the increase in overall load to be on the order of 10 to 20 percent.

Table 6-8. Load Estimation Coefficients for a Column Bent of Prestressed Concrete I-Beam Bridge.

RW	SQ	a	b
24	0	3.59	86.98
24	15	3.59	86.98
24	30	3.59	88.98
24	45	3.57	102.93
28	0	3.90	98.59
28	15	3.90	98.59
28	30	3.89	101.92
28	45	3.79	106.23
30	0	4.07	98.29
30	15	4.04	100.91
30	30	4.03	103.15
30	45	3.90	107.59
38	0	4.89	122.60
38	15	4.89	122.60
38	30	4.87	127.13
38	45	4.80	140.00
44	0	5.48	133.87
44	15	5.39	141.24
44	30	5.48	137.87
44	45	5.37	157.44

In order to adjust the total load for the design vehicle and also to split the contributions for dead and live load, the following procedure is proposed:

- Assess the total load (live load + dead load) using the bridges design standard sheets as explained in the Load Determination for Bridge Foundations – Method II section.
- Assess the live load based on the design vehicle HL93, as explained in the Live Load section.
- Subtract the live load obtained from previous step from the total load to obtain the dead load.
- Obtain the live load based on the real design vehicle of the bridge designated in item 31 (design vehicle).

VALIDATION OF THE PROPOSED LOAD ESTIMATION PROCEDURE

In order to validate the proposed dead-load estimation method, a couple of bridges with different superstructure types are selected. The dead load for the interior bent of the bridge is exactly calculated by summing weights of different structural elements including the bent cap, slab/beams, shafts/piles, and railing. The weights of these elements are given in the table of quantities available in the bridge plan.

The estimated value is then compared to the value given by the proposed approximate method for five bridges. The average error between the estimated and actual loads is about 11 percent, as presented in Table 6-9. A detailed computation for one of the bridges is presented in the Appendix.

Table 6-9. Load Estimation Error for Five Sample Bridges.

Bridge	Error (%)
17-82-2144-01-002	2.56
17-21-0050-02-123	18.13
17-21-0050-01-001	8.33
17-239-0315-08-016	15.22
17-21-0049-09-43	12.80
Avg. Error	**11.41**

Chapter 7.
DETERMINISTIC APPROACH—ARTIFICIAL NEURAL NETWORK MODELS

INTRODUCTION

An Artificial Neural Network (ANN) is a soft computing approach that can be applied to regression and classification problems with high accuracy (Haykin 1999, Shahin 2008). Here, this approach has been applied for predicting the foundation's:

- Type.
- Embedment depth for deep foundations.
- Bearing capacity.

The first two items defines the deterministic approach, while the last one is part of the probabilistic approach (discussed later in Chapter 8).

ARTIFICIAL NEURAL NETWORKS

Attempts for simulating the process of learning, perception, and cognition in the human brain leads to creation of parallel computing networks called Artificial Neural Networks. Since the first neural models proposed by McMulloch and Pitts (1943), ANNs have been developed over time and modified to solve more complex problems in pattern recognition, prediction, optimization, associative memory, and control. ANNs can be viewed as weighted directed graphs in which artificial neurons are nodes and directed edges (with weights) are connections between neuron outputs and neuron inputs.

Updating network architecture and connection weights so that networks can efficiently perform a task, is considered learning in ANNs. The network is usually trained by presenting a set of input-output data, similar to a regression problem. The ANN is able to learn from the underlying rules, like implicit relation between inputs and outputs acting as an artificial intelligent model, achieving great success in non-linear regression problems.

Radial Basis Function (RBF) and Multi-Layer Perceptron (MLP) networks are recognized as universal approximators. These networks have proven to perform satisfactorily for different

function approximation and regression problems in geotechnical engineering (Haykin 1999). A variant of RBF is the Generalized Regression Neural Network (GRNN) (Specht 1991). These three network types are examined for assessing foundation depth and bearing capacity in this study. PNN and the MLP network are considered for the classification-type problems for the purpose of foundation-type determination. The architecture and learning algorithm for each type of ANN is described in following sections.

MULTILAYER PERCEPTION NETWORKS

MLPs are feed-forward neural networks with at least one hidden layer consisting of neurons with sigmoid activation function. The learning procedure is to adjust the weights of connections in the network to minimize the objective or error function. The objective function is the mean square error (*MSE*) between targets (real values) and outputs of the network (measured values) for all data points in a training set. *MSE* is calculated by:

$$MSE = \frac{1}{n}\sum_{i=1}^{n}\left(d_i - y_i\right)^2 \qquad \text{(Eq. 7-1)}$$

where d_i is the desired response vector, y_i is the output of network, and n is the number of training examples.

The most popular algorithm of error function minimization is the back propagation algorithm, which is based on the gradient decent method. This method starts with any set of weights and repeatedly changes each connection weight by an amount proportional to gradient of the error function with respect to that weight. However, this method is often very slow, giving preference to high-performance algorithms that converge much faster than gradient decent, such as the Levenberg-Marquardt algorithm, Conjugate Gradient algorithm, Quasi-Newton algorithms, and Bayesian Regularization algorithms.

Error back-propagation learning consists of conducting two rounds: a forward pass and a backward pass. In the forward pass, an input vector is applied to the sensory nodes of the network, and its effect propagates through the network layer by layer. Back propagation can be considered as generalization of the least mean square algorithm (LMS) (Haykin 1999). During the forward pass, the synaptic weights of the networks are not changing; however, during the backward pass, the

synaptic weights are all adjusted based on an error-correction rule. Basically in MLP networks, actual response of the network is subtracted from a desired response to produce an error signal. The weights are then adjusted to make the difference between the response of the network and the desired response as small as possible. Figure 7-1 shows the MLP network architecture used in this study. This model consists of one hidden layer and an output layer consisting of one single neuron.

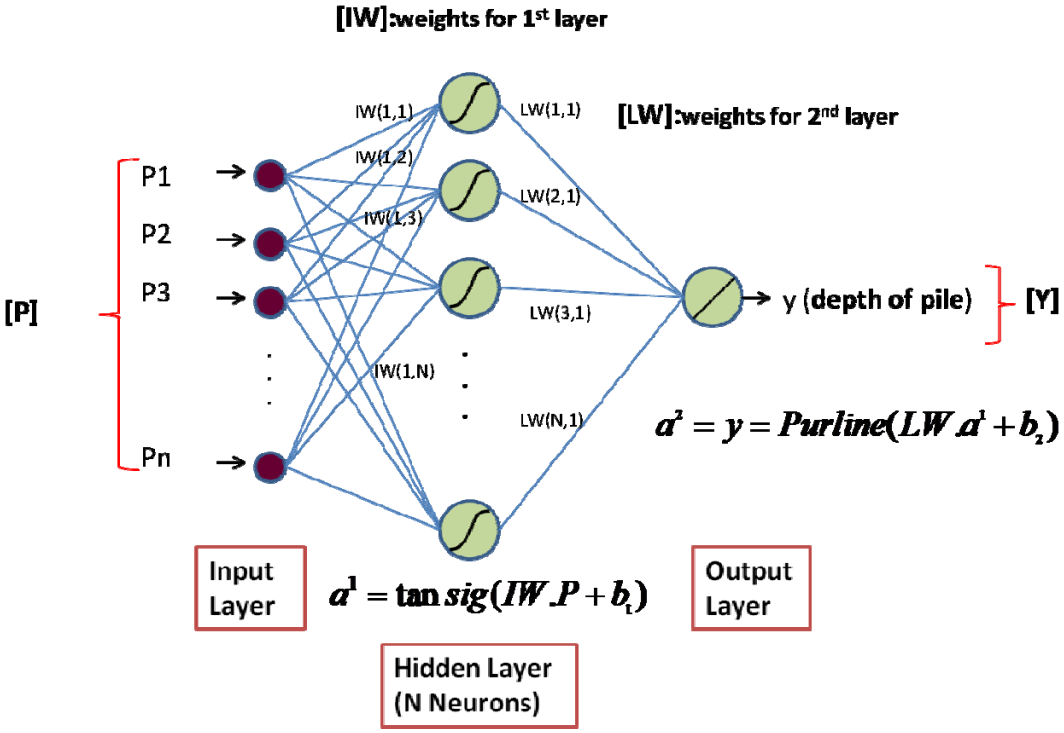

Figure 7-1. MLP Network Architecture.

Radial Basis Network

RBF networks are used both for complex pattern classification and approximation problems in high-dimensional spaces. Learning can be viewed as finding a surface in a multidimensional space that provides the best fit to the training data. RBF networks are designed as feed-forward networks consisting of three layers: input, hidden, and output. According to Cover's theorem, in interpolation problems, the network performs a nonlinear mapping from the input space to hidden space and then a linear mapping from the hidden space to the output space (Haykin 1999).

The first layer consists of input nodes, which applies input vector containing a specific number of elements to the next layer (hidden layer). The hidden layer is composed of nonlinear neurons that are connected directly to all of the neurons in the output layer. The number of nodes in the output layer depends on the number of the elements in the targets (outputs) of the problem.

The (weighted) distance of the inputs from hidden units' centers are computed and then passed through the radial basis function (in the case of Gaussian neurons, these values are transferred using a Gaussian function). In this sense, a unit will have maximum value when the new input exactly matches its center. The outputs of the hidden units are then multiplied by the weights of the second layer (output layer) and are transferred using a linear function. In this sense, the outputs of the network would be superimpositions of the activities of all the radial functions in the network (Poggio and Girosi 1990).

The network weights (connection weights) are updated during learning by minimizing an objective function, which is defined as the measure of error between the network's outputs and actual values of targets for the training points. In addition to weights, the centers of the radial basis and the width (spread) of the radial functions are also updated during learning (Poggio and Girosi 1990).

RBF and MLP NNs are recognized as universal approximators; however, despite having similarities, one of the fundamental differences between MLP and RBF is the way in which hidden units combine values coming from preceding layers in the network. MLPs use inner products, while RBFs use the Euclidean distance. According to the literature, MLP needs more time for training because of back propagating the error, while RBF networks are faster in learning.

Generalized Regression Neural Network

A variant of RBF, GRNN was introduced by Specht (1991). RBF and GRNN have similar architectures, and the only difference between them is in adjusting the second-layer weights.

In RBF networks, the weights and biases in the second layer are computed by minimizing the difference between the output of second hidden layer and actual (measured) outputs. This usually caused the network to generate exact solutions or zero error for training data.

The weights in the second layer of GRNN are not adjusted using error minimization. Instead, the weights are set equal to the value of the outputs (targets), so the hidden layer has the same number of neurons as input/target pairs. Figure 7-2 presents the architecture of RBF and GRNN networks used in this study.

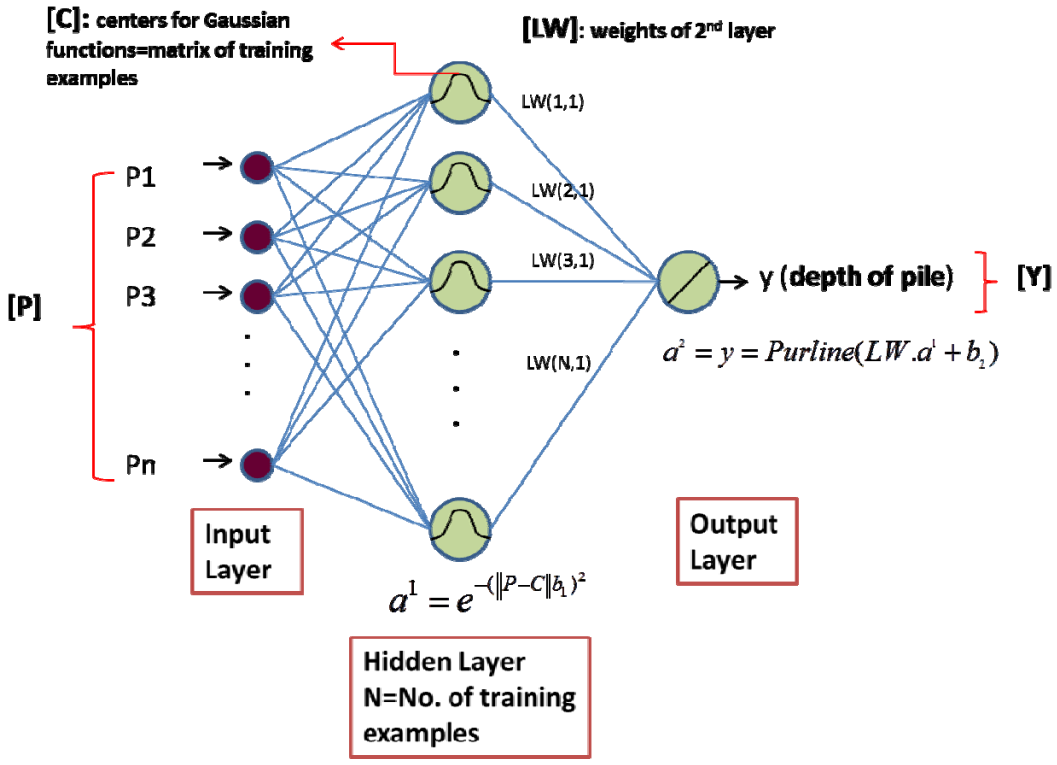

Figure 7-2. RBF and GRNN Network Architecture.

Probabilistic Neural Network

PNN has similar architecture as GRNN networks. However, PNNs perform classification where the target variable is categorical, while GRNN is used for regression-type problems where the target is a continuous variable. The output layer for PNN is a decision-making layer and has as many neurons as number of classes (categories) of input parameters. The transfer function of output neurons for PNNs is not linear as in GRNNs; rather, it is a function that compares inputs of all neurons and outputs (one for the largest value and zero for others.)

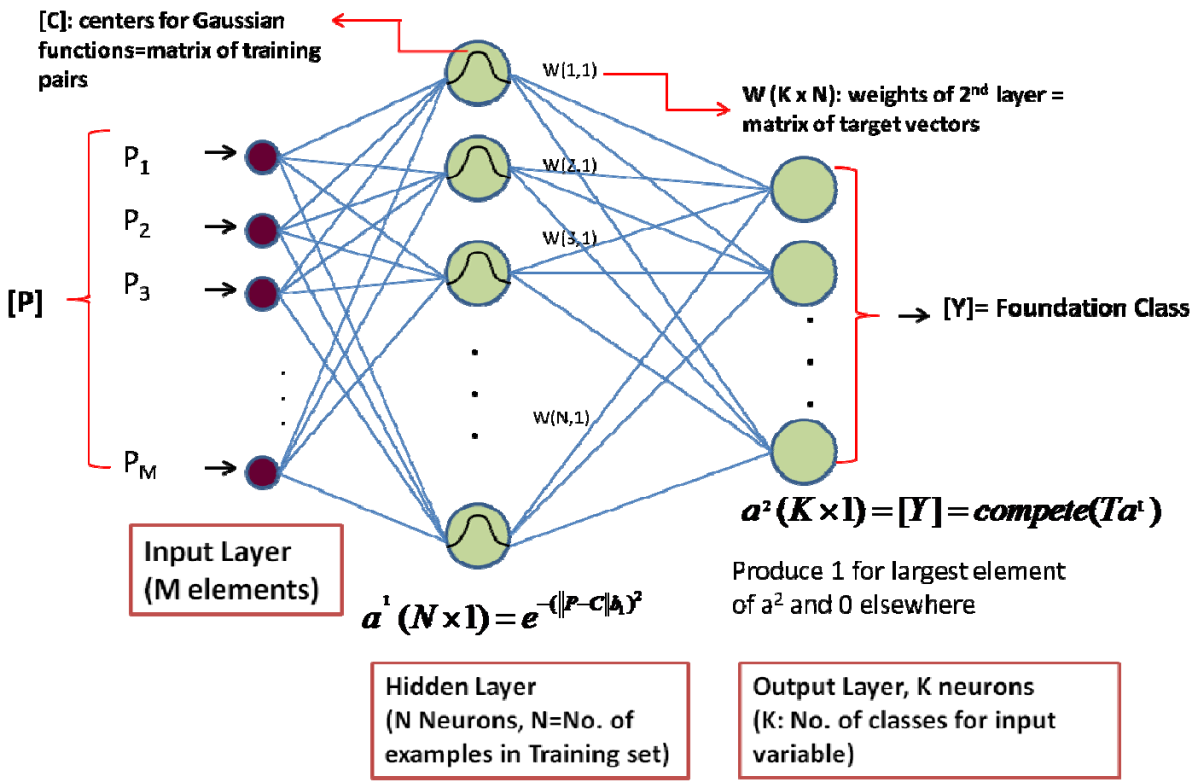

Figure 7-3. Architecture of PNN Network.

FOUNDATION DEPTH PREDICTION

Model Selection Analysis

Finding the best network type and configuration for the purpose of foundation depth prediction required considering different aspects of designing a neural network based model. These aspects are a selection of input parameters, network type and architecture, learning algorithms, hidden units' transfer functions (activation function), and data-sampling methods.

Input Parameters

Selection of input parameters for approximating a target variable using neural networks highly depends on one's knowledge of the problem. The criteria for selecting the relevant input parameters for pile-depth prediction is based on the limit state design method of foundations, which requires foundation load and allowable bearing capacity to be equal.

Several networks with different combinations of parameters were compared to determine the most relevant input parameters. Table 7-1 lists the final selected input parameters.

Table 7-1. ANN Input Parameters for Pile-Depth Approximation.

Input Parameters (Variables)
Load
Dead Load per bent/ per pile (tons)
Live Load per bent/pile (tons)
Geometry
Pile Diameter/Dimension/Cross Section Area (in/in^2)
Item # 51: Roadway Width (ft) when number of piles per bent is not available
Soil Properties
Avg. TCP (Blows/ft)
Skin Friction (tsf)
Time and Location
Item 3: County
Item 27: Year Built
Item 16: Latitude (°)
Item 17: Longitude (°)

Neural Network Type and Algorithm

A preliminary analysis was performed to find the best network type using only a fraction of the database. A number of MLP, RBF, and GRNN networks with different Gaussian function widths (spreads) and also a series of MLP networks were developed using the NN toolbox of MATLAB (MATLAB Neural Network Toolbox, 2009). The evaluation of the networks' performance was based on the root mean square error (*RMSE*) and the correlation coefficient (*R*) for the best linear fit between the measured values (targets) and the predicted values (outputs) of the network. The correlation coefficient is defined as:

$$R = \sqrt{1 - \frac{\sum_{i=1}^{n}(y_i - t_i)^2}{\sum_{i=1}^{n}(t_i - \bar{t})^2}} \qquad \text{(Eq. 7-2)}$$

The root mean square error is defined as:

$$RMSE = \sqrt{\sum_{i=1}^{n} \left(y_i - t_i \right)^2} \qquad \text{(Eq. 7-3)}$$

where y_i is the predicted value (output), t_i is the actual value (target), $RMSE$ is the root mean square error, and R is the correlation coefficient.

MLP networks were trained using two distinct optimization algorithms: Levenberg-Marquardt and Bayesian regularization, where the former is referred to as MLP-LM and the latter is referred to as MLP-BR. Before training, the database was pre-processed, meaning that the duplicated data points and the data points missing the pile depth value were eliminated. Also, both input and output data were normalized regarding the maximum value for each parameter, so that all parameters fell within the range [−1, 1].

For the purpose of training the MLP-LM network, the data set was divided into three parts; 60 percent for training, 20 percent for validation, and 20 percent for testing. The training, validation, and testing were sampled randomly during the training process. The network was trained and monitored using the validation set. When the validation error started to increase, the training was stopped. The performance of the model was examined using the test data set, which had not been presented to the network.

The network was retrained several times using the same procedure, until reaching R greater than 0.8 for both the test data set and the whole data set presented to the network (training plus validation plus test). Each time the network was retrained, the model chose new initial weights and biases. Thus repeatedly retraining the network caused the model to find the optimum value for the initial weights and biases which led to minimizing the error and improving the prediction's accuracy.

The MLP-BR network was generated with the same architecture as the MLP-LM but is trained using the Bayesian regularization algorithm. In this algorithm, weights and biases are assumed to be random variables, and the regularization parameters are associated to the variance of these distributions. Further, there is no validation error in this method, and the network will stop training when the effective number of weights and biases has converged (Demuth et al. 2009).

R for the test data set is close to 0.9 for the MLP-BR network as well as the MLP-LM network, which proves the ability of these networks to generate fairly accurate predictions.

For RBF and also GRNN networks, the working database is divided into training (70 percent) and test (30 percent) subsets. The weights and biases in the network were adjusted using the training set, and the generalization of the network was evaluated using a test set.

Although RBF and GRNN show a good correlation coefficient for training data, the small R2 in the test set (particularly in the case of the RBF) indicates that these networks cannot generalize well in this problem. This could be due to the fact that RBF networks perform well only if they are supplied with a large amount of vectors in the training set, specifically when dealing with several input variables.

Table 7-2 presents a summary of results obtained from different NNs. The best generalization belongs to MLP-LM, followed by MLP-BR. Results show that both of the MLP networks outperform the GRNN and the RBF networks. As expected, GRNN generated far more accurate results compared to RBF, since only a small number of data points were presented to the models in this study.

Table 7-2. Summary of Results for Different Neural Networks.

	RBF		**GRNN**		**MLP-LM**		**MLP-BR**	
Method	training	test	training	test	training	test	training	test
R	1.00	0.33	0.77	0.62	0.87	0.89	0.95	0.81
RSME	0.029	1.8E3	8.29	10.26	7.56	9.99	4.00	8.08

These results helped to define the MLPs with the Levenberg-Marquardt optimization algorithm for approximation of both pile depth and bearing capacity.

Number of Hidden Units

There are several rules of thumb for determining the number of hidden units. For instance, one hidden layer usually suffices, the number of hidden neurons is better between the number of input

elements and number of output elements, and that number should never be larger than twice the number of input elements. However, there is no theory yet which specifies the required number of hidden units for an MLP network.

Fewer hidden neurons increase the prediction error and prevent the model from having enough flexibility to fit the data point. On the other hand, too many hidden neurons make the model too complex and cause the model to be over fitted to the data points and to fail to generalize to new data points.

Trenn (2008) performed a study on the necessary number of hidden units for a multilayer perceptron network. Based on this study, the minimum number of hidden units for a single hidden layer network to reach a certain order of approximation, N, is:

$$n = \frac{\binom{N + n_0}{n_0}}{n_0 + 2} \qquad \text{(Eq. 7-4)}$$

where n_0 is the number of input variables and n is the number of hidden units.

N is the approximation order that refers to the degree of Taylor polynomial which approximates the MLP function. For instance in this case, n_0 is equal to 10, so if considering an approximation order of 3, almost 23 neurons is needed in the hidden layer. This formula gives the minimum required number of hidden units and not the sufficient number of hidden units. It can be shown that more hidden units mean more model parameters and thus more accurate approximation.

This study also shows that the only effective factor on approximation accuracy is the number of model parameters (weights and biases) that are determined by the number of hidden units for a given number of input elements. Thus, the necessary number of hidden units can be included in just one layer, and more than one hidden layer is not necessary. Increasing the number of hidden layers allows having a lower number of hidden units yet the same number of model parameters. Based on the analysis of the number of hidden units, 20 hidden neurons were found to be the optimized number of neurons in this study.

Transfer function

Transfer function, or activation function, maps the input of a neuron to its output in a computational network. Transfer functions can be linear, sigmoidal, Gaussian, or step functions. Multilayer perceptron networks apply either a log sigmoid or tan sigmoid transfer function in the hidden units and linear function in output units.

Log-sigmoid function appears as:

$$f(x) = \frac{1}{1+e^{-x}} \qquad \text{(Eq. 7-5)}$$

Tan-sigmoid function appears as:

$$f(x) = \frac{e^{x} - e^{-x}}{e^{x} + e^{-x}} \qquad \text{(Eq. 7-6)}$$

Figure 7-4 shows the graphical forms of log-sigmoid and tan-sigmoid function.

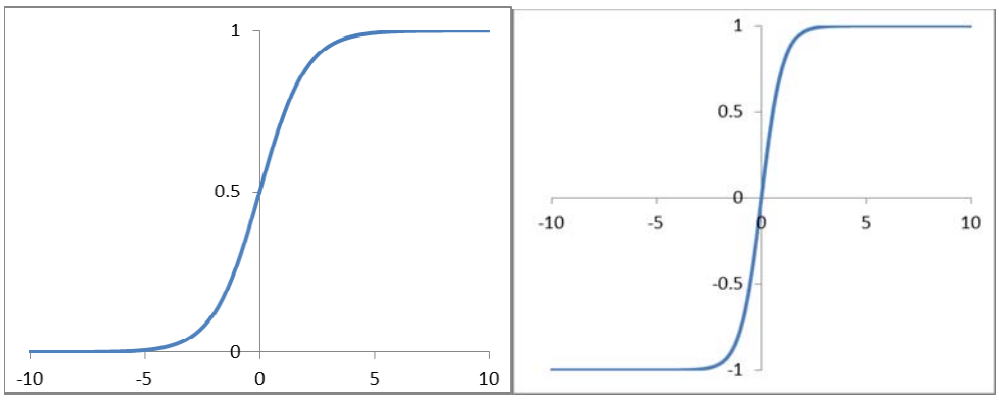

Figure 7-4. Sigmoid Transfer Functions.

An MLP network with log-sigmoid and a similar one with tan-sigmoid for hidden units are trained; however, the R^2 value for training, test, and validation sets was not significantly different. Based on this analysis, ANN models for pile depth and bearing capacity prediction are designed with tan-sigmoid transfer functions for hidden units, which can generate both positive and negative outputs.

Data Split Method

How samples for training, validation, and test data sets are chosen and how the examples for each set are divided can affect perceptions of model performance. The only way to estimate model true error is to test the model error on an entire population, meaning that one would need to have access to an unlimited number of samples. However, this is not possible due to the costly process of data collection.

In order to make a reasonable estimate of model performance (error), different methods of data partitioning are recommended:

- **Holdout method.** In this method, data are divided into two groups, training and test, with a certain proportion (usually 60:40 percent). Data can be selected randomly for each group, or the database can be split into two blocks. The network is trained using a training set, and the network generalization is examined using the test data set. The error rate is computed solely based on one possible test data set, which might happen to be an unfortunate subset and result in underestimating or overestimating the prediction accuracy.
- **Cross validation method—random subsampling.** In this method, data points are randomly selected for a fixed number of examples in training and test data sets (usually 60:40 percent); the network is trained with a training data set and tested with the test data set. This process is performed iteratively for a certain number of times, and the error is computed for each iteration. The model error is the average of error rate for all iterations. This method forms an ensemble of networks that can work in parallel to make predictions for new input data. The best estimation would be the average of predictions by all networks in the ensemble.

The cross-validation method is selected for this study because of its advantages over the hold-out method. The cross-validation method allows for making use of all examples in the database for both training and testing purposes and thus provides a more reasonable estimate of the model's true error. It also helps to reduce the bias of predictions by providing ensembles of networks trained by different subsamples of the same population.

ANN-Predictive Model

The final configuration of the ANN model for pile depth approximation is the MLP network with Levenberg-Marquardt optimization algorithm. This network has one hidden layer with 20 neurons with tan-sigmoid activation function.

For the purpose of training, the working database is split into three groups: training, validation, and test with 3:1:1 proportions. The weight of the network is adjusted using training examples. The network performance is monitored during training using validation examples. The learning process continues until the network error starts to increase for validation data points.

The random subsampling method is used to make use of all data points for the purpose of training and testing. This subsampling runs for 10,000 iterations, and each time a new network is trained from scratch and the performance of the model is measured.

Neural networks are designed to perform interpolation. However, like any other regression methods, they are weak at performing extrapolation. Therefore, they are expected to retrieve more accurate predictions given an input data within the range of the training database.

During the random subsampling, there is the possibility of populating non-uniform subsets, meaning that the test data points might be outside the range of training data points. In order to avoid this problem, ANN networks that perform poorly are removed from the ensemble based on the following selection criteria:

$$R^2 \text{ (All)} > 0.8 \text{ and } R^2 \text{ (Validation)} > 0.7 \text{ and } R^2 \text{ (Test)} > 0.9 \qquad \text{(Eq. 7-7)}$$

This allows for forming an ensemble of best-performance networks to be used as a predictive model. Figure 7-5 shows an example of random subsampling, how test data points vary for each of the networks in the ensemble, and how they cover almost all points in the database.

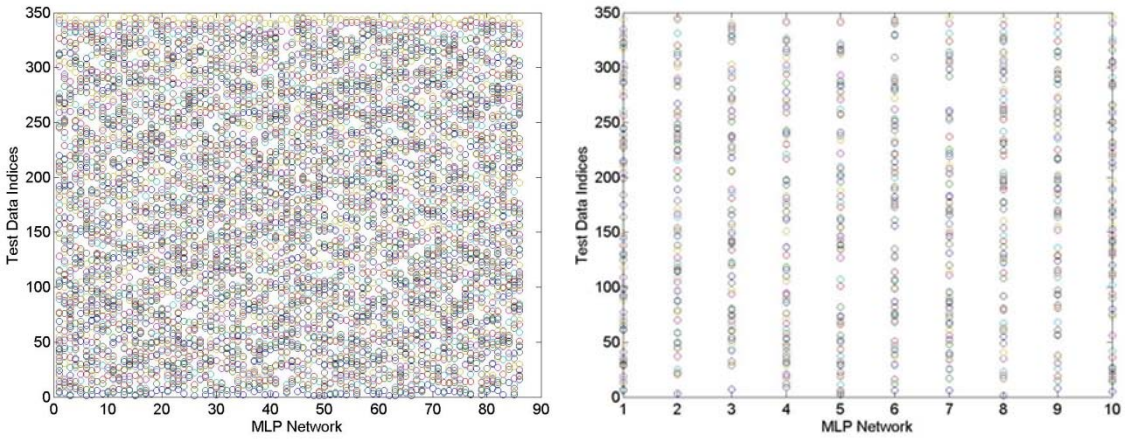

Figure 7-5. Random Subsampling Method Test Set Data Points for Each Network in the Ensemble: (Left) 87 Networks, (Right) 10 Networks.

ANN MODELS FOR FOUNDATION-TYPE CLASSIFICATION

ANN classifiers are powerful tools to classify categorical data. Identifying foundation type can be very helpful for determining the foundation geometry and scour vulnerability. Two ANN classifier models are proposed to classify the foundations based on the bridge-relevant information. One determines the foundation type of bridge among all possible categories of the Bryan District bridges. The other ANN classifier specializes only in determining if the foundation is either deep or shallow because, for the proposed deterministic method in this study, it is important to know if the foundation is deep or not before proceeding with predictions about foundation depth with the ANN models.

Model Selection Criteria

Input Parameters

A preliminary analysis was also performed to identify the most relevant parameters. Table 7-3 shows the model input and target parameters. These parameters are items of NBI that are considered to be the most influential on foundation type.

Table 7-3. Input Parameters for Foundation Classification.

Input Parameter
Item 3: County
Item 27: Year Built
Item 43-1: Main Span Type
Item 44-1: Substructure Type above Ground for Main Span
Item 46: Total Number of Spans
Item 48: Max Span Length
Item 51: Roadway Width
Target Parameter
Item 44-1: Substructure Type below Ground for Main Span

Neural Network Type and Algorithm

PNN and MLP are types of networks that can be used for classification purposes. The architecture and learning algorithm for these two networks were fully described in the Artificial Neural Network section. The only difference between MLP approximator and MLP classifier is in the output layer. MLP classifiers, same as PNN, should have as many neurons as the number of possible categories for target parameter in output layer. These nodes are not linear, as in MLP approximators; rather, they have a function that identifies the neuron with the largest output value and the corresponding category. Figure 7-6 shows the architecture of MLP classifier used in this study.

Herein, the model performance is measured by a factor called classification accuracy (CA), defined as the ratio of the correctly classified examples over total number of examples.

$$CA = \frac{\text{No. of correctly classified examples}}{\text{Total no. of examples}} \qquad \text{(Eq. 7-8)}$$

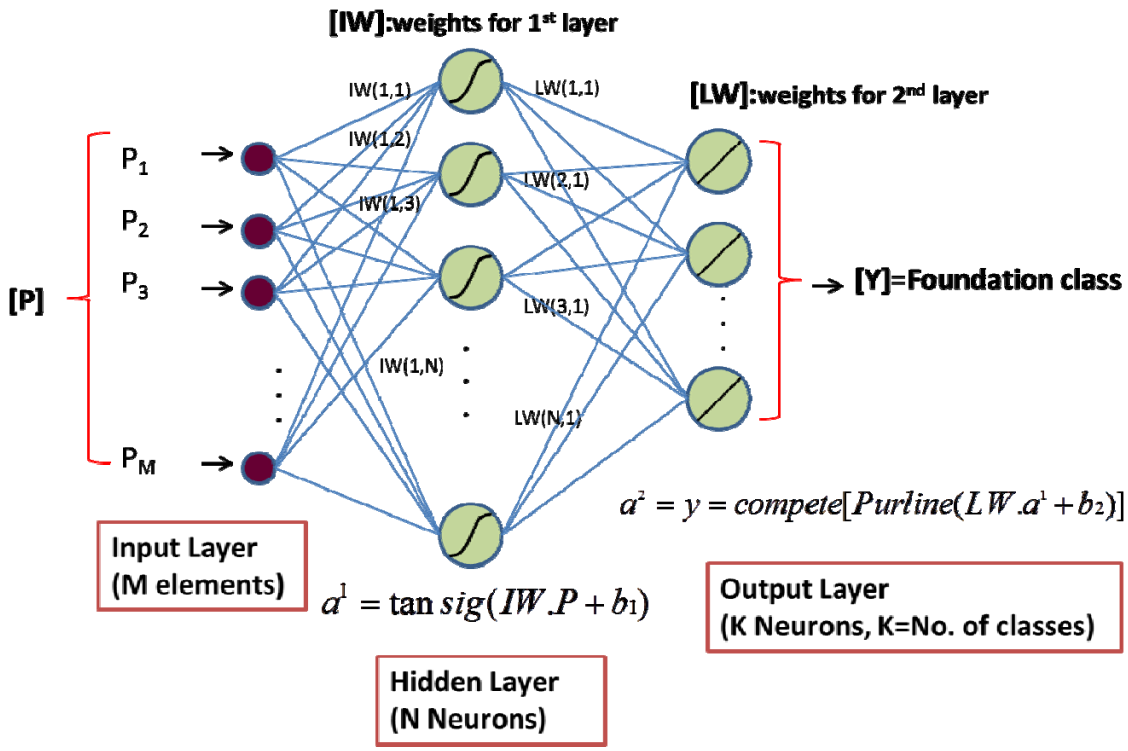

Figure 7-6. Architecture of MLP Classifier.

Preliminary analysis showed that MLP network can classify more numbers of examples compared to PNN. Table 7-4 shows the performance of each classifier.

Hidden Units Number and Transfer Function

Twenty neurons with tan-sigmoid transfer function are considered for hidden layer of the MLP classifier. The same arguments as mentioned in the Number of Hidden Units and Transfer Function sections are also valid for this case.

Table 7-4. Classification Results for PNN and MLP.

Model	PNN		MLP		
	Training	Test	Training	Validation	Test
CA	0.69	0.71	0.9	0.76	0.75

Data Split Method

The random subsampling method is used, and the database is split into three subsets: training, validation and test with 6:2:2 proportion. The data points are randomly sampled for each subset. This is repeated for 1,000 iterations, and the classification accuracy of 1,000 networks is averaged.

The MLP classifier learns the pattern existing in training examples and generalizes to examples in the test subset. The validation set examples are used to prevent the network being overfit to the training examples.

PREDICTION AND VALIDATION

Foundation Type

Figure 7-7 and Figure 7-8 show results of foundation classification. Figure 7-7 presents classification between eight possible foundation types (FT8), and Figure 7-8 gives classification between deep and shallow foundation (FT2). Table 7-5 presents the summary of results for each subset.

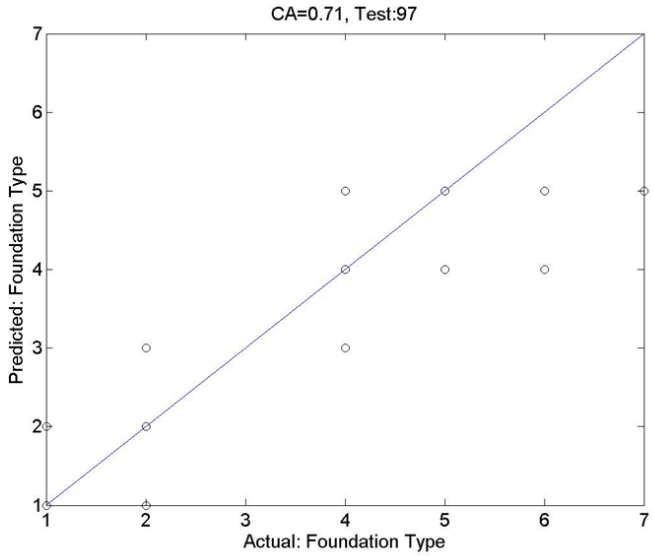

1	Steel Piling
2	Concrete Piling
3	Timber Piling
4	Drilled Shaft
5	Spread Footing
6	Pile Cap on Steel Piling
7	Pile Cap on Concrete Piling
8	Pile Cap on Timber Piling

Figure 7-7. Foundation Classification Using MLP-FT8.

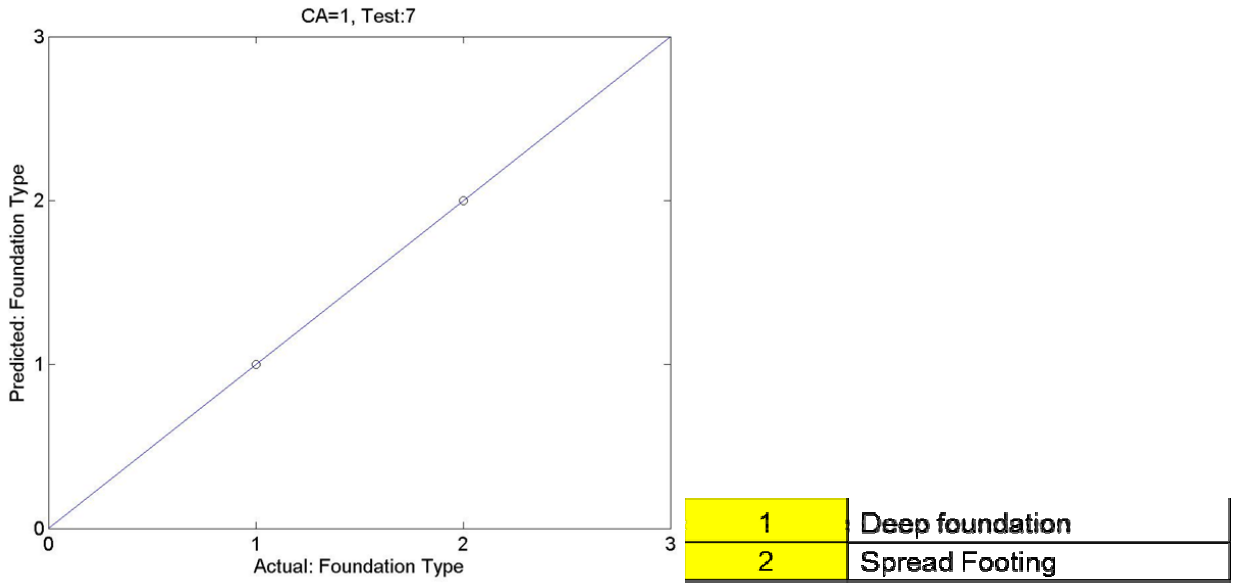

Figure 7-8. Foundation Classification MLP-FT2.

Table 7-5. Results of Foundation-Type Classification.

Model	**MLP-FT2**			**MLP-FT8**		
Subset	**Training**	**Validation**	**Test**	**Training**	**Validation**	**Test**
No. of examples	22	7	7	290	97	97
Ave. CA	1	0.91	0.90	0.9	0.76	0.75

It can be observed that both the MLP-FT98 and MLP-FT2 were able to classify the foundation for both training and test examples with a fairly good accuracy. CA for MLP-FT2 is 0.91 and 0.75 for MLP-FT8, which shows that it is significantly more accurate to classify the foundation as deep or shallow rather than to identify the exact foundation type.

Foundation Depth

Eight different MLP models were developed to predict pile depth based on the availability of soil-boring and foundation type information. The coding of each of these combinations is described below:

- MLP-PL00: Foundation type, dimension, and soil resistance is unknown.
- MLP-PL01: Foundation type and dimensions are unknown; soil resistance is known.

- MLP-PL10: Foundation type is known; foundation dimensions and soil resistance are unknown. Three models are created based on the foundation type:
  - Concrete piling (conc).
  - Drilled Shafts (DrSh).
  - Steel piling (steel).
- MLP-PL11: Foundation type and soil resistance are known; foundation dimensions are unknown; and three models are created based on the foundation type:
  - Concrete piling.
  - Drilled Shafts.
  - Steel piling.

The model performance is measured by the coefficient of determination (R^2), and root mean squared error is obtained from the actual value of pile depth and the predicted pile depth for a given bridge foundation. The coefficient of determination, R^2 is defined as:

$$R^2 = 1 - \frac{\sum_{i=1}^{n}(y_i - t_i)^2}{\sum_{i=1}^{n}(t_i - \overline{t})^2} \qquad \text{(Eq. 7-9)}$$

The root mean square error *(RMSE)* is defined as:

$$RMSE = \sqrt{\sum_{i=1}^{n}(y_i - t_i)^2} \qquad \text{(Eq. 7-10)}$$

where y_i is the predicted value (output) and t_i is the actual value (target).

As the two equations show, *RMSE* and *R* have negative correlation, i.e., when one increases the other decreases.

Figure 7-9 to Figure 7-12 show MLP ensemble prediction for some of the MLP models mentioned earlier in Step 6 of the deterministic approach (see Chapter 4.). These figures show each network and the average prediction over all networks in the ensemble for all examples in the database. R^2 and *RMSE* for average ensemble prediction are also shown in these figures. The same figures for

each of the eight models are presented in the Appendix. Table 7-6 presents the summary of results for different MLP models.

It can be observed that for all eight MLP models, the order of magnitude of average R^2 for the examples in the working data set is above 0.85. This indicates that these models were able to learn from examples in the training set and then successfully generalize to new examples in the test set.

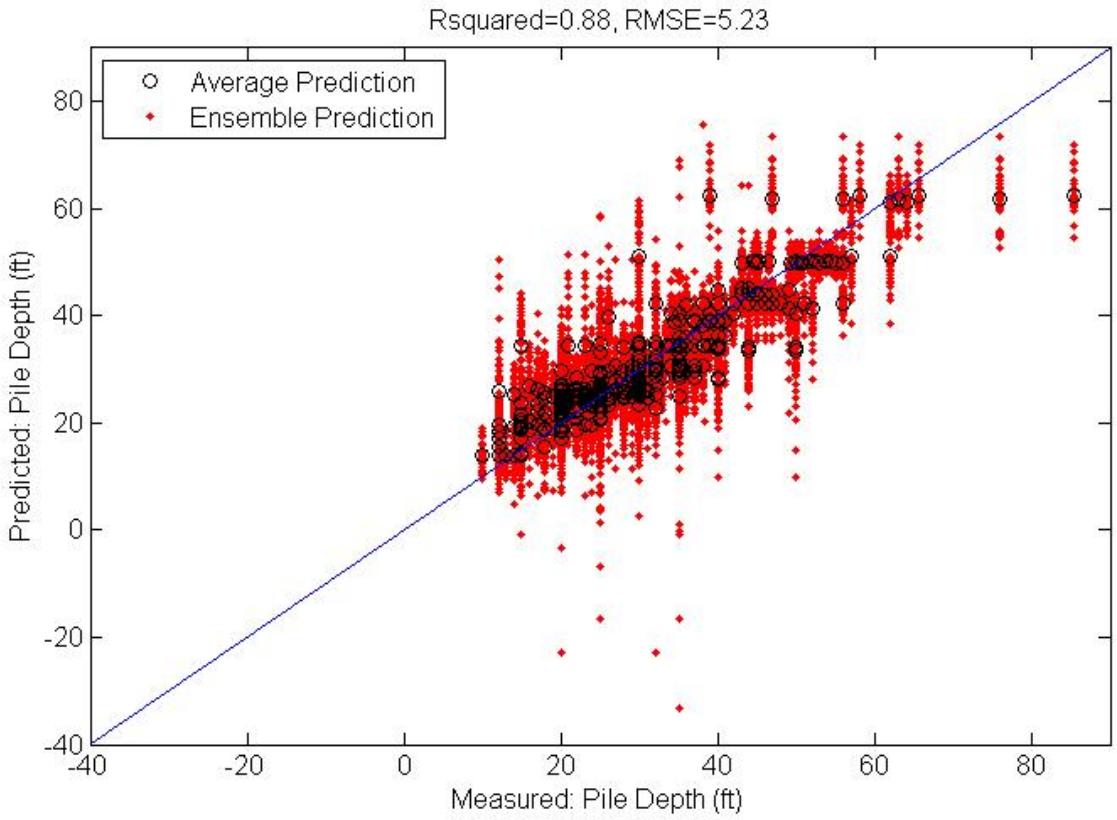

Figure 7-9. Ensemble Prediction for MLP-PL00.

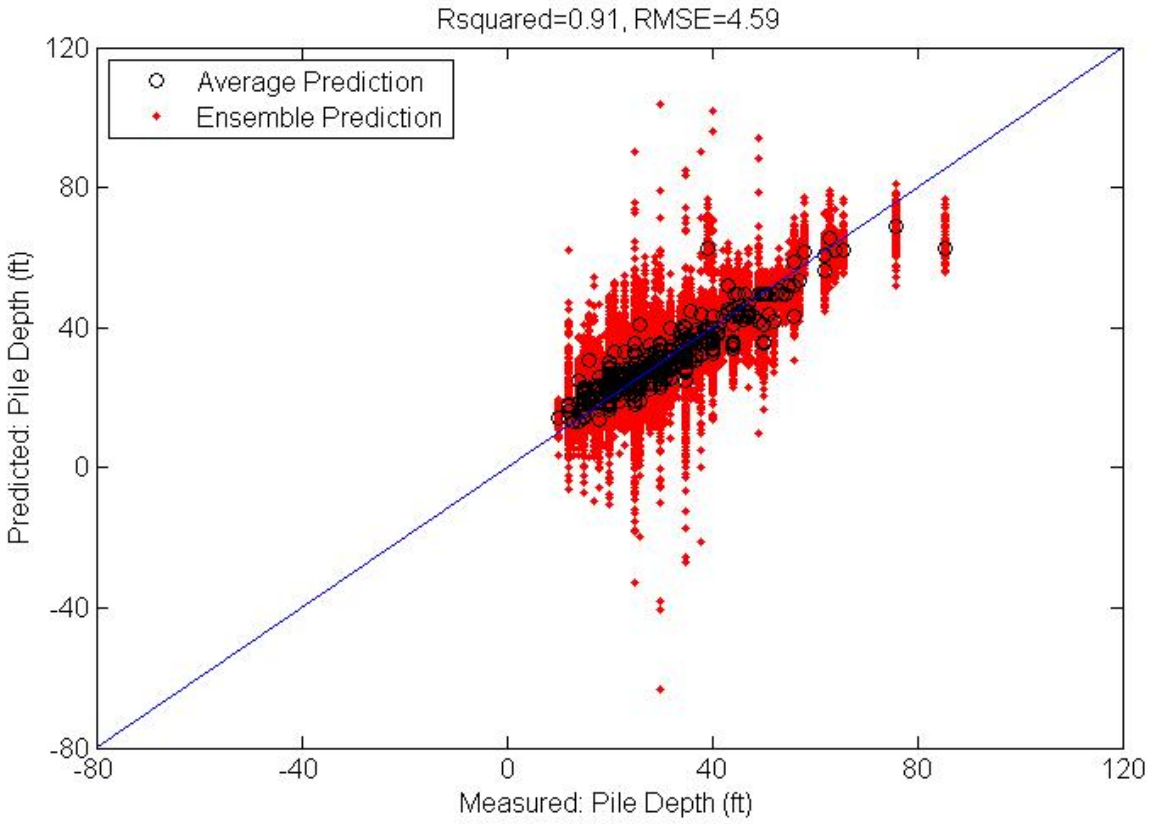

Figure 7-10. Ensemble Prediction for MLP-PL01.

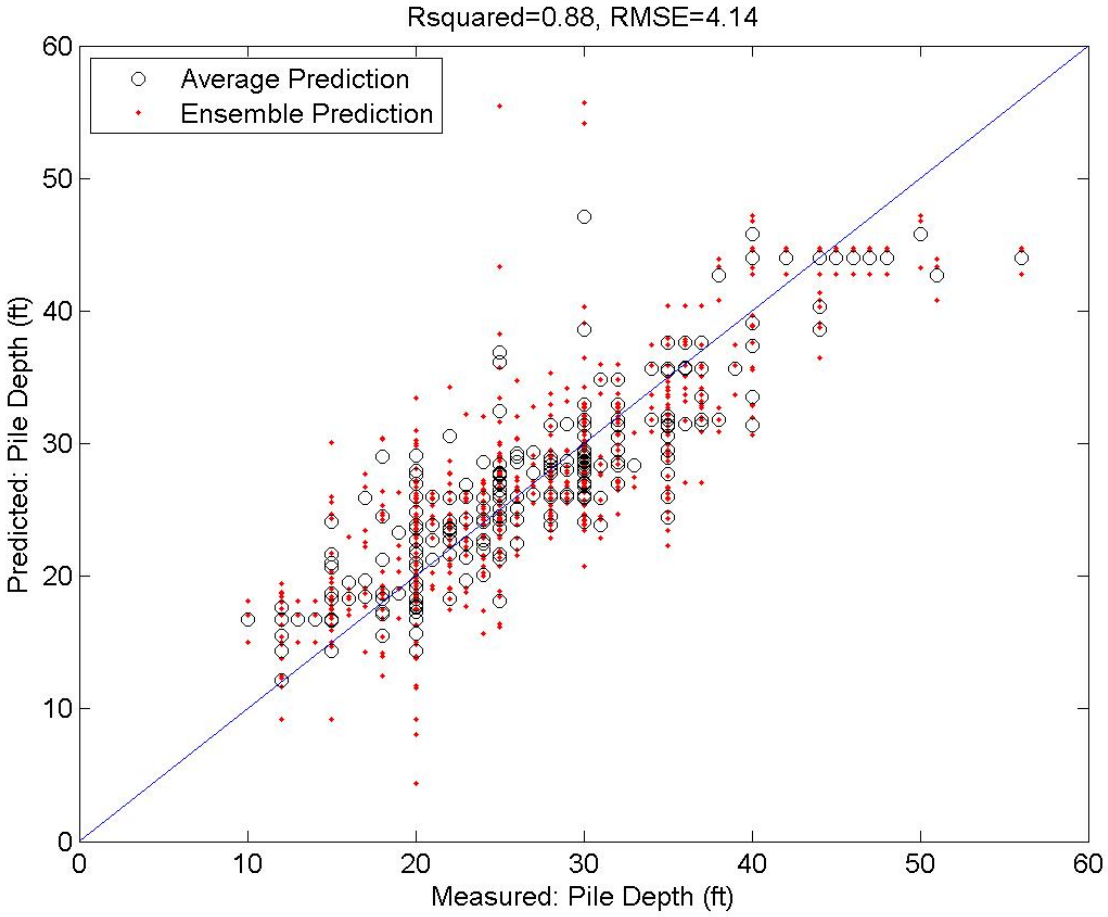

Figure 7-11. Ensemble Prediction for MLP-PL10 for Concrete Piling.

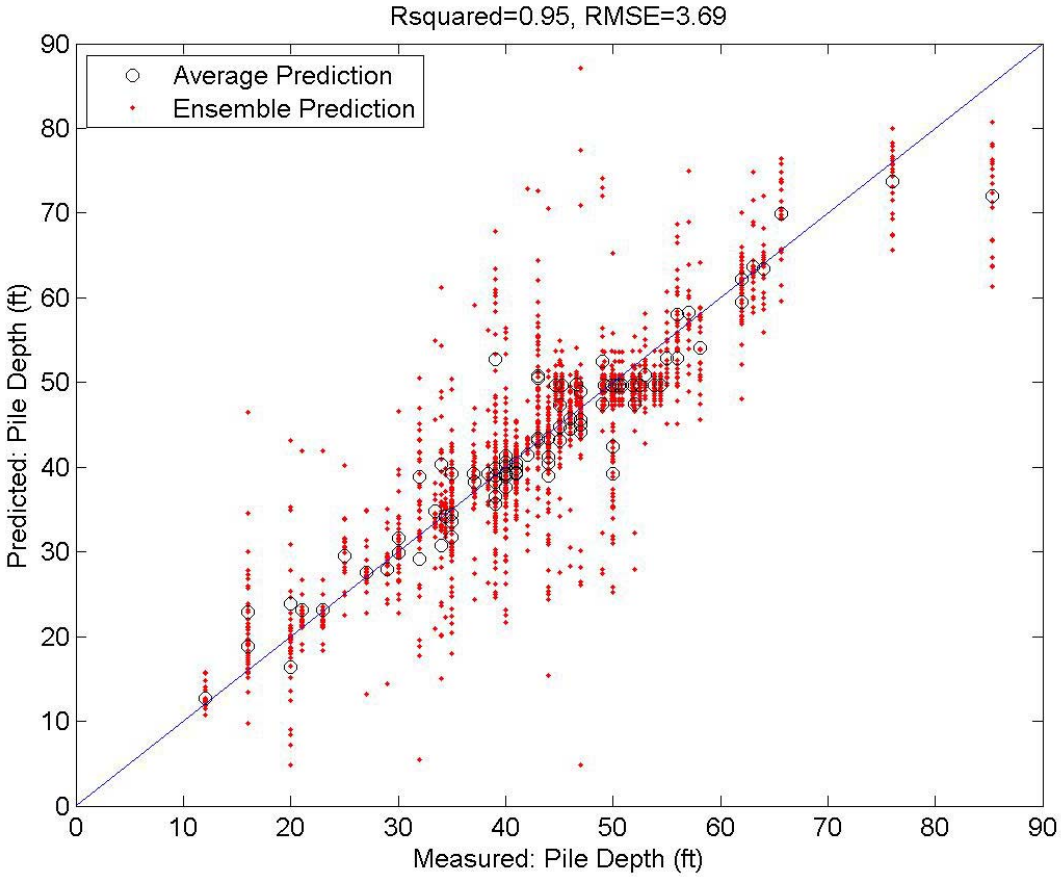

Figure 7-12. Ensemble Prediction for MLP-PL11 for Drilled Shafts.

Table 7-6. Results of MLP Models for Pile Embedment Depth Prediction.

Subset / Model	No of Examples	All		Training		Validation		Test	
		R^2	RMSE	R^2	RMSE	R^2	RMSE	R^2	RMSE
MLP-PL00	378	0.86	6.33	0.88	4.71	0.79	8.90	0.91	7.10
MLP-PL01	378	0.89	6.16	0.91	3.74	0.80	9.45	0.92	7.25
MLP-PL10-Conc	217	0.9	4.76	0.94	2.94	0.79	7.22	0.91	5.87
MLP-PL10-DrSh	80	0.85	7.84	0.84	4.93	0.84	10.45	0.94	10.12
MLP-PL10-Steel	35	0.86	4.08	0.81	2.97	0.79	5.46	0.92	5.03
MLP-PL11-Conc	259	0.91	4.42	0.94	2.08	0.80	7.25	0.91	5.49
MLP-PL11-DrSh	91	0.88	6.42	0.89	1.96	0.81	11.08	0.94	7.91
MLP-PL11-Steel	35	0.87	4.70	0.94	2.52	0.68	8.57	0.82	4.05

Chapter 8.
PROBABILISTIC APPROACH: BAYESIAN INFERENCE

INTRODUCTION

Figure 8-1 depicts the basic components for determining unknown foundations using the proposed probabilistic approach. This method is composed of two stages, where each stage includes two basic procedures.

In the first stage, the dead load, live load, and bearing capacity for known bridge piers are calculated, and then an ANN model is created and trained using relevant information included in the working database defined as the input parameters and aiming at predicting the foundation's bearing capacity as the target parameter. As a result of this stage, an ANN model is generated that is able to predict the bearing capacity for a bridge foundation, according to information collected about its superstructure, load, and location elements.

The MCMC method is implemented for solving the inverse problem, defined as the multidimensional sampling of a foundation's components starting with foundation type, dimensions, and soil resistance, which can target the bearing capacity that is estimated using ANN. The basic procedures for both stages are described in more detail in the following sections and are summarized in the flowchart of Figure 8-2.

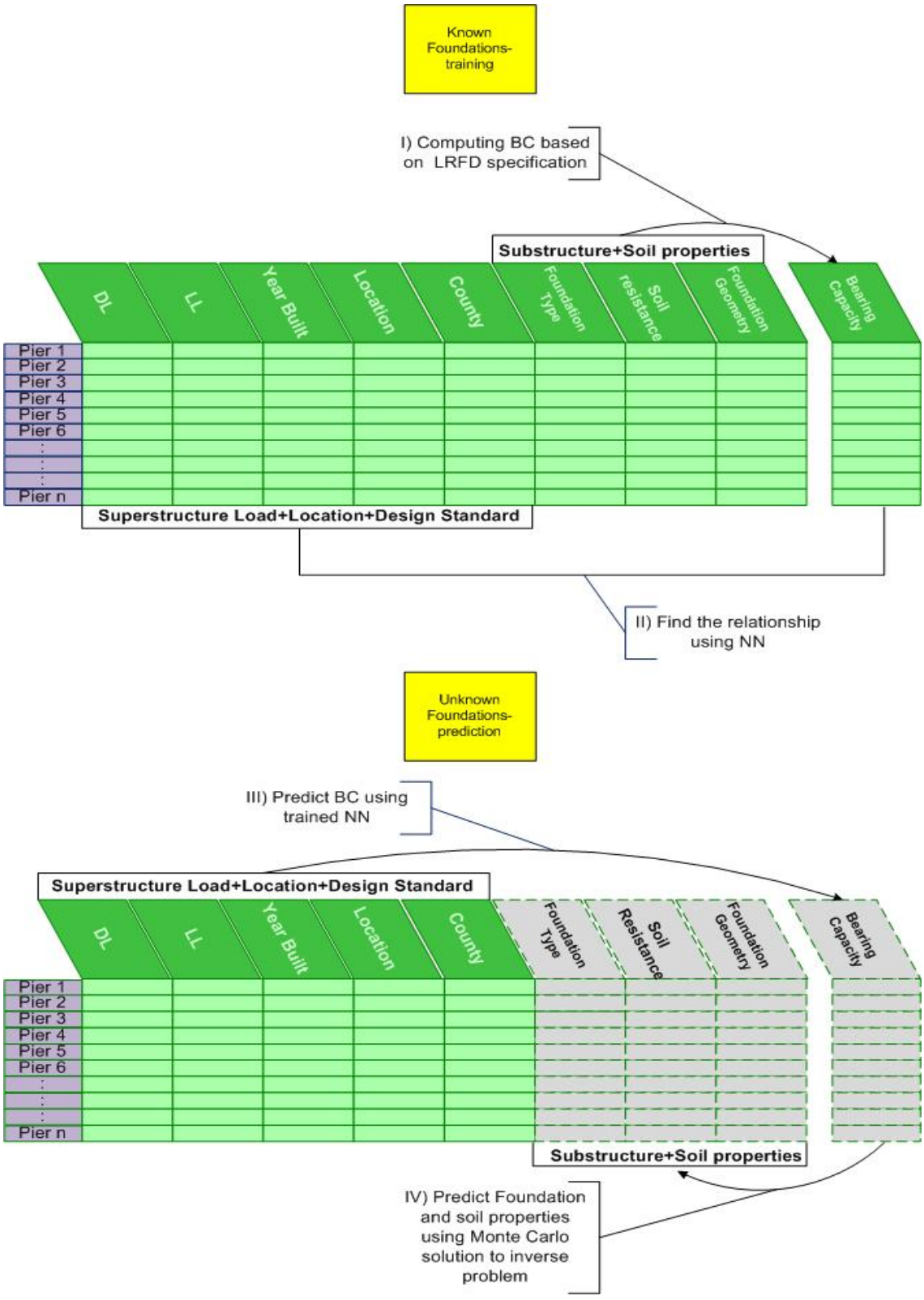

Figure 8-1. Diagram Indicating the Two Main Steps Required for the Probabilistic Determination of Unknown Foundations.

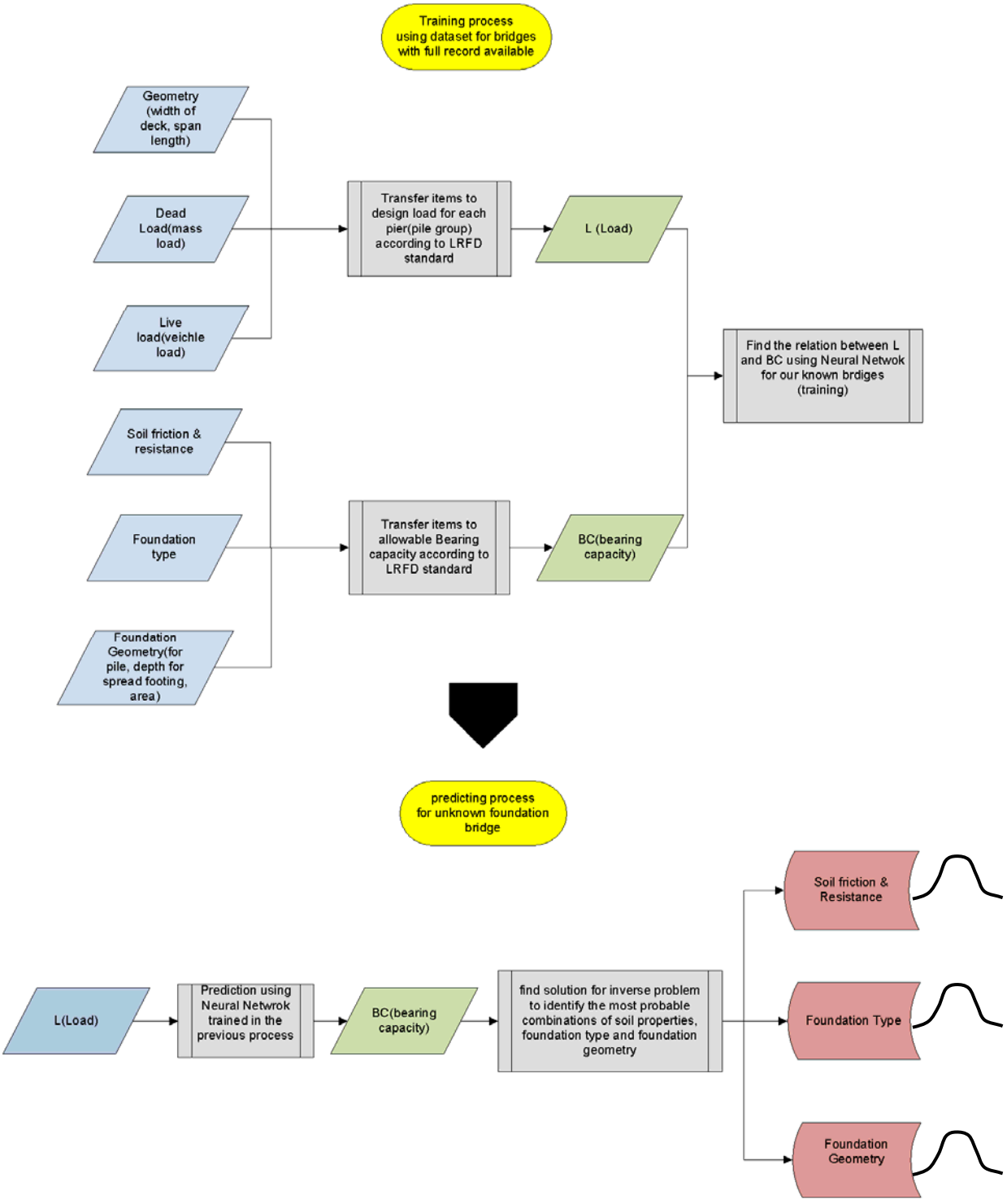

Figure 8-2. Flowchart of the Probabilistic Solution for the Determination of Unknown Foundations.

LOAD AND BEARING CAPACITY ESTIMATION: STEP I

Dead load, live load, and bearing capacity of foundations for all piers of bridges in the database are computed using superstructure, substructure information, and soil properties as described in Chapter 6. Theoretically, dead load and live load should relate to bearing capacity of a foundation following limit-state design, depending on the standard and method used at the time of design:

$$\gamma_D DL + \gamma_L LL = \phi q_{ult} \qquad \text{(Eq. 8-1)}$$

where γ_D, γ_L are the load factors, DL is the dead load, LL is the live load, ϕ is the resistance factor, and q_{ult} is the ultimate bearing capacity. Also, γ_D and γ_L are obtained from AASHTO standards based on the method of design. Table 8-1 shows the corresponding values for two AASHTO standards: LRFD and Highway Bridge.

Table 8-1. Load Factors Based on AASHTO Standards.

Standard	Design method	γ_D	γ_L
Highway Bridges	Allowable Stress Design	1	1
	Load Factor Design	1.3	1.3 × 1.67
LRFD	Allowable Stress Design	1	1
	Load Factor Design	1.25	1.75

The ultimate bearing capacity is reduced by a factor of 0.5 for different foundation types. Figure 8-3 presents the allowable bearing capacity versus estimated total load for foundations in the working database. It is expected that all points will be along the equity line or above; however, as observed in Figure 8-3, there are a few steel and concrete piles for which the points are located below the equity line. This could be due to over-estimation of loads in these cases.

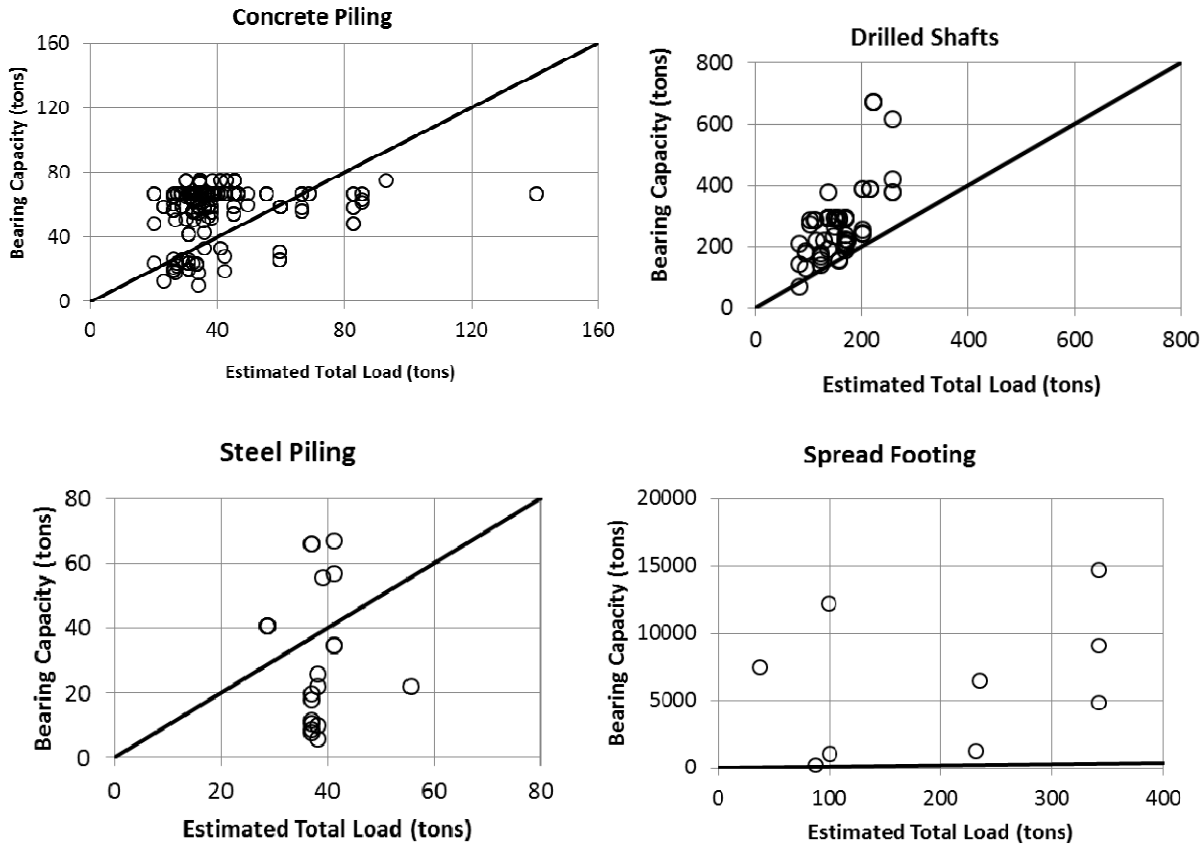

Figure 8-3. Allowable Bearing Capacity versus Estimated Total Load for Foundations in the Working Database.

ANN MODEL DESIGN FOR BEARING CAPACITY: STEP II

The aim is to correlate the relevant features of bridges extracted from the TxDOT inspection database and folders (including superstructure features, load, year built, county, location, etc.), with the bearing capacity of known foundations using ANN. This results in finding the implicit relationship between superstructure, load, and location elements of bridges and the bearing capacity of their foundations. The model selection criteria are described in the following sections.

Input Parameters

Input parameters for bearing capacity (BC) approximation are quite similar to those for pile depth approximation. Table 8-2 presents the input parameters for MLP-BC models. For cases where soil properties are not available, average TCP and skin friction (Su) should be removed from input parameters.

Table 8-2. Input Parameters for MLP-BC Models.

Parameter (variable)
Load Elements
Dead load (tons)
Live load (tons)
Soil Properties
Ave. TCP (blows/ft)
Skin Friction (tsf)
Location and Time
County
Year built
Latitude (°)
Longitude (°)

Neural Network Type and Algorithm

According to preliminary analysis, an MLP network with a Levenberg-Marquardt algorithm is selected as the network type for BC approximation. R^2 and *RMSE* evaluated the network performance.

Number of Hidden Units and Transfer Function

Following the arguments described earlier in the Number of Hidden Units section, one hidden layer including 20 hidden neurons is considered for the MLP-BC models. Tan-sigmoid is selected for the hidden unit activation function based on a preliminary analysis.

Data Split Method

The random subsampling method was performed by iteratively sampling data points for training, validation, and test data sets and training new networks each time. Ten thousand networks were generated using this method to form an ensemble of MLP networks for prediction of BC. The same criteria as described in the ANN Predictive Model section is applied to identify and remove the poor-performance networks from the ensemble:

$$R^2 \text{ (All)} > 0.8 \text{ and } R^2 \text{ (Validation)} > 0.7 \text{ and } R^2 \text{ (Test)} > 0.9 \qquad \text{(Eq. 8-2)}$$

The ratio of database split was 3:1:1, where the networks were trained using examples in the training set and later tested using examples in the test set. The error on validation set examples determined when to stop training the network.

PREDICTING BEARING CAPACITY FOR UNKNOWN FOUNDATIONS: STEP III

After training the ANN model based on information from known foundations in Step II, it follows to use this model for predicting the bearing capacity of unknown foundations (Step III). Ten different MLP models are developed to predict BC based on the availability of soil-boring and foundation-type information:

- MLP-BC00: Foundation type, dimensions, and soil resistance are unknown.
- MLP-BC01: Foundation type and dimensions are unknown; soil resistance is known.
- MLP-BC10: Foundation type is known; foundation dimensions and soil resistance is unknown; four models are created based on the foundation type:
  - Concrete piling.
  - Drilled Shafts.
  - Steel Piling.
- Spread footing.

  MLP-BC11: Foundation type and soil resistance are known; foundation dimensions are unknown; four models are created based on the foundation type:
  - Concrete piling.
  - Drilled Shafts.
  - Steel Piling.
  - Spread footing.

The average ensemble prediction for all bridge piers in the database are shown here for different MLP-BC models (Figure 8-4 to Figure 8-7). The figures corresponding to each of the 10 models are provided in the Appendix.

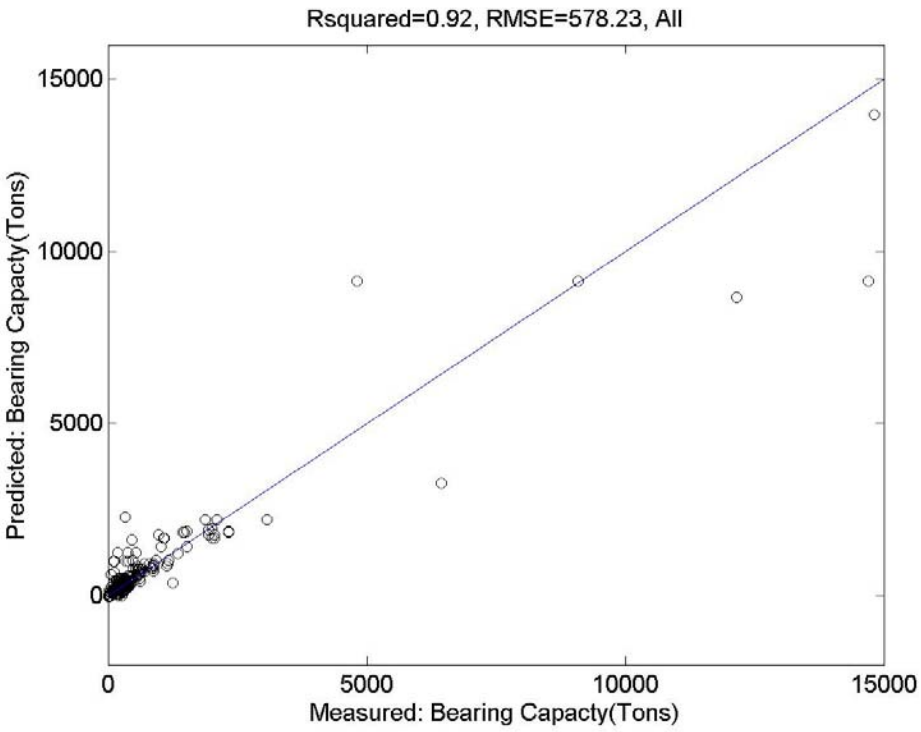

Figure 8-4. MLP-BC00 Predictions.

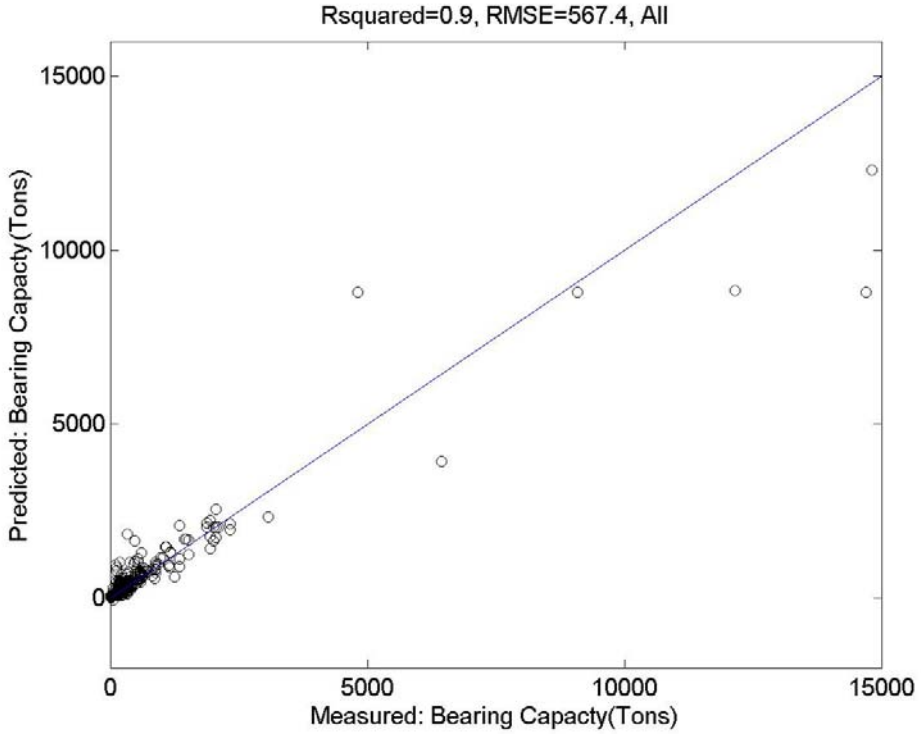

Figure 8-5. MLP-BC01 Predictions.

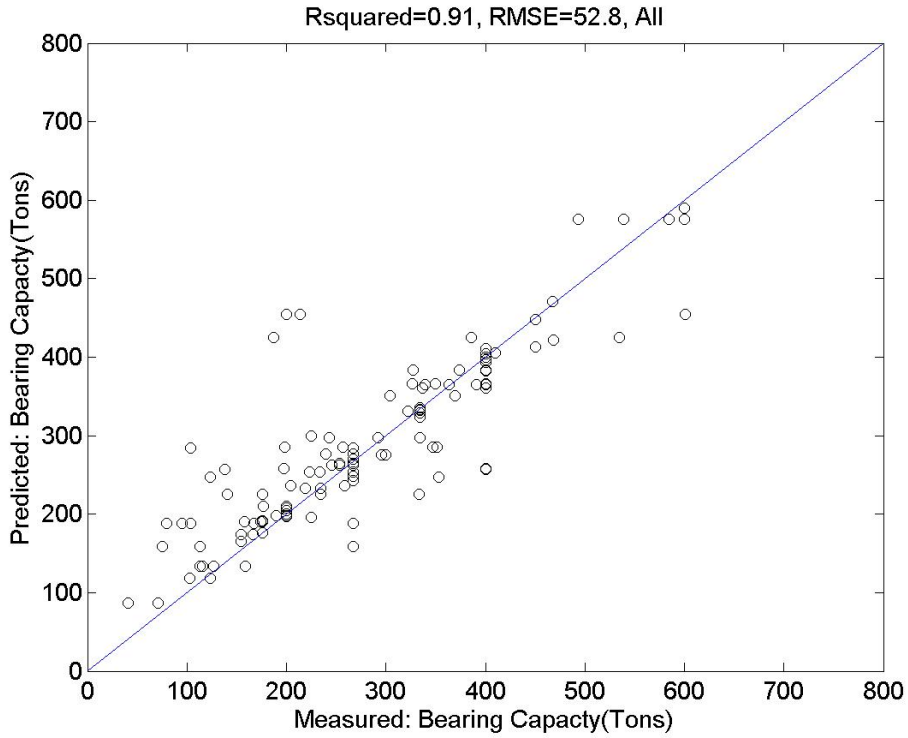

Figure 8-6. MLP-BC10 Predictions for Concrete Pilings.

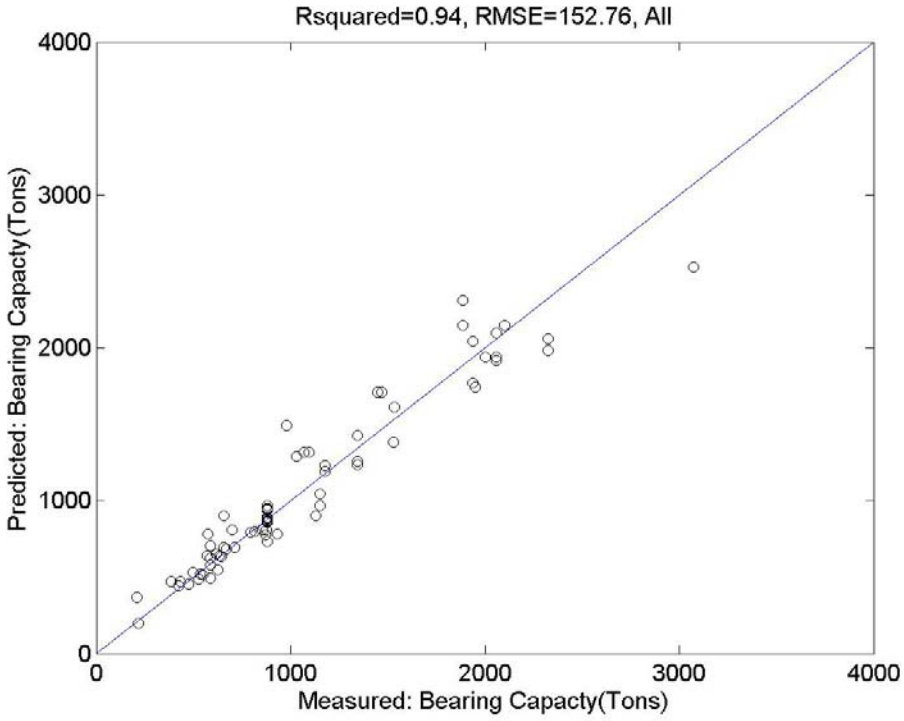

Figure 8-7. MLP-BC11 Predictions for Drilled Shafts.

In order to show how these models work for a set of unknown foundations, a number of bridge examples were randomly selected from the database and their values of BC were predicted using the proposed ANN models.

Ten percent of the examples were randomly selected, and BC was predicted for each of the 10 ANN models. Figure 8-8 to Figure 8-11 show the corresponding predictions for four of the 10 models. Complimentary figures for other MLP-BC model predictions are provided in the Appendix. Table 8-3 summarizes the results of all models for BC prediction.

It can be observed that R^2 is above 0.81 for different models and for different foundation types for all examples in the data set and is above 0.87 for test data set. This indicates that the MLP-BC models are able to predict the bearing capacity of bridge piers fairly accurately.

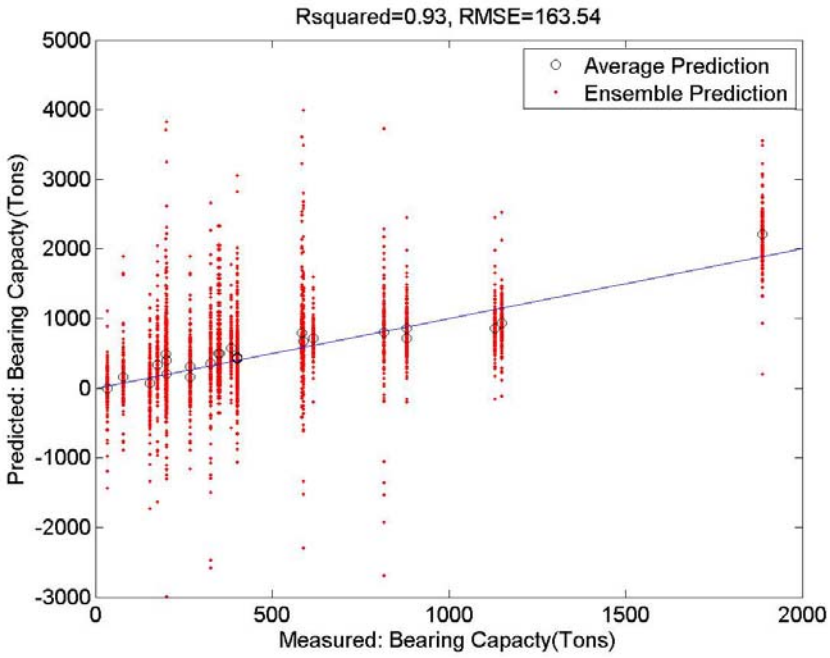

Figure 8-8. MLP-BC00 Predictions for Randomly Selected Bridge Piers.

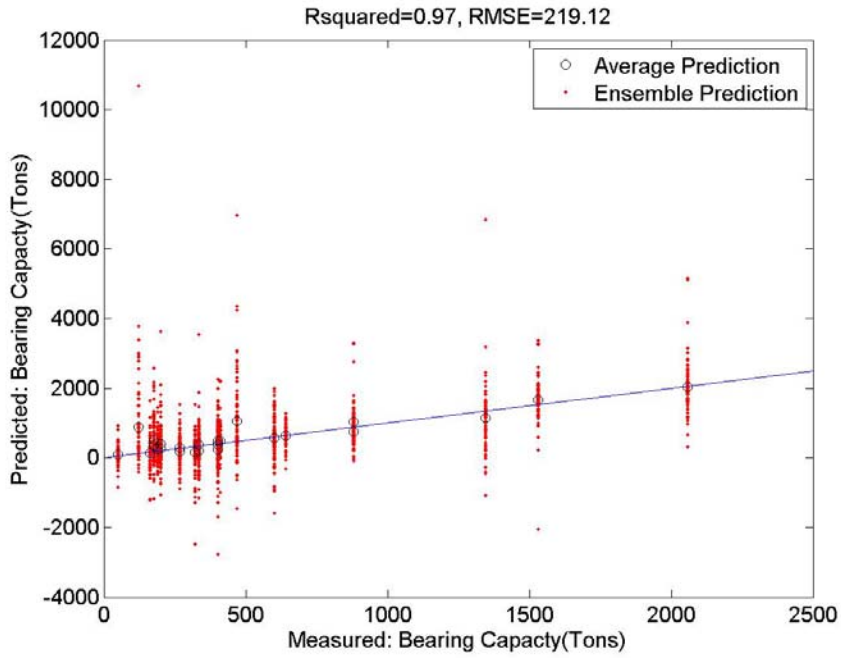

Figure 8-9. MLP-BC01 Predictions for Randomly Selected Bridge Piers.

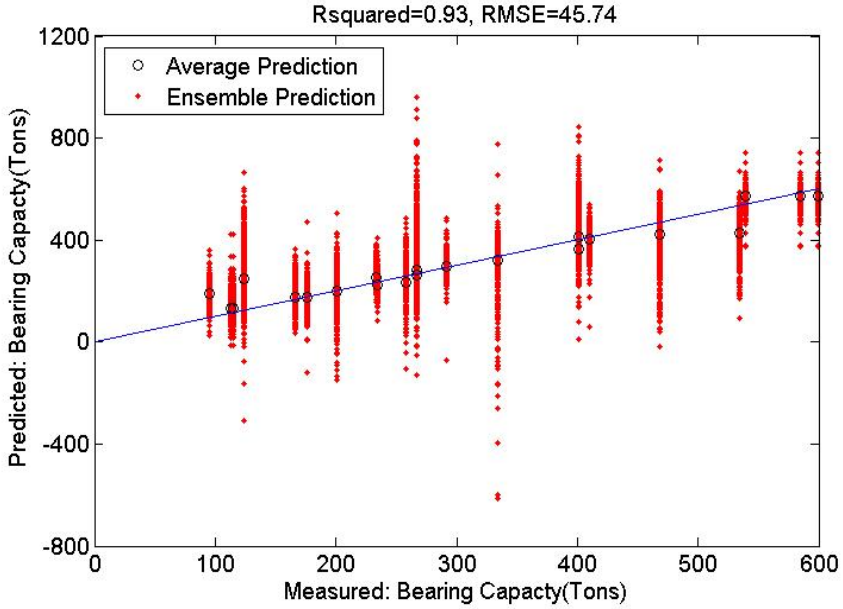

Figure 8-10. MLP-BC10 for Concrete Piling,
Predictions for Randomly Selected Bridge Piers.

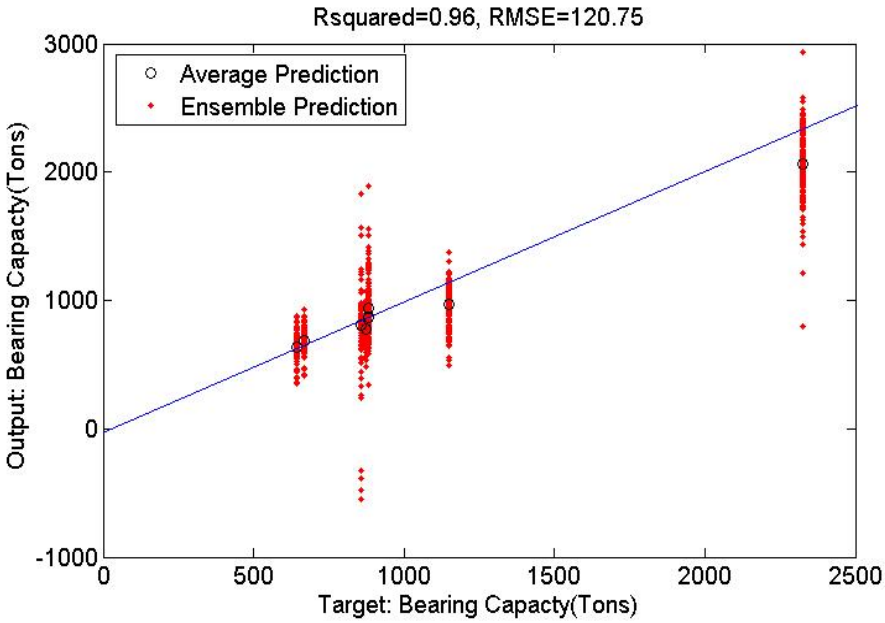

Figure 8-11. MLP-BC11 for Drilled Shafts,
Predictions for Randomly Selected Bridge Piers.

Table 8-3. Results of MLP-BC Models for Prediction of Bearing Capacity.

Subset / Model	No. of Examples in Database	All		Training		Validation		Test	
		R^2	RMSE	R^2	RMSE	R^2	RMSE	R^2	RMSE
MLP-BC00	279	0.94	906.14	0.95	513.54	0.87	1167.48	0.90	1149.73
MLP-BC01	279	0.92	978.86	0.93	523.87	0.84	1399.75	0.96	1155.35
MLP-BC10-Conc	278	0.91	61.41	0.92	48.94	0.83	82.96	0.92	66.58
MLP-BC10-DrSh	79	0.86	278.83	0.88	220.00	0.81	367.39	0.94	298.70
MLP-BC10-Steel	30	0.97	43.44	0.96	19.88	0.88	55.73	0.92	53.58
MLP-BC10-Spread	9	0.85	2533.60	0.85	3128.12	0.85	1978.96	0.71	712.08
MLP-BC11-Conc	278	0.93	54.74	0.97	29.79	0.84	87.63	0.93	65.82
MLP-BC11-DrSh	79	0.94	266.58	0.98	80.68	0.84	411.88	0.87	372.25
MLP-BC11-Steel	35	0.98	35.63	1.00	2.45	0.89	52.36	0.92	49.44
MLP-BC11-Spread	9	0.81	2659.76	0.76	3128.12	0.60	2657.08	0.98	558.15

PROBABILISTIC INVERSION: STEP IV

Bayesian probabilistic inversion is performed by defining a prior probability distribution and a likelihood probability distribution. The prior distribution reflects the state of information about a set of parameters, before introducing additional evidence (i.e., data, model predictions). The

likelihood is a probability density function describing the probability of observed data given the model parameters. The product between the prior and the likelihood, divided by a constant of proportionality, is called the posterior distribution. The posterior distribution represents the updated state of information about the parameters, given the new evidence. It can be integrated with respect to each model parameter, via the implementation of MCMC sampling (Robert 2007).

The probabilistic determination of unknown foundations consists of sampling the most likely combinations of the foundation's parameters (i.e., foundation type, foundation dimensions, and soil resistance), conditioned by the ANN prediction of bearing capacity, which itself is conditioned on the known data characteristics about the load and superstructure.

In Step I described earlier, the bearing capacity was obtained using the foundation type, foundation dimensions, and soil resistance from known foundations, whereas in Step IV, the probabilistic solution to the inverse problem will result in the definition of probability distributions of each of these variables. These will indicate the most likely combinations between the three parameters, as well as their probabilistic confidence measures.

Bayes Paradigm and MCMC Method (Robert 2007)

Bayesian inference is a methodology to estimate the probability of a vector of variables (or hypotheses) when new evidence becomes available (also known as updating process). This is based on the Bayes' paradigm, which refers to the fact that the addition of new evidence may contribute to reducing the uncertainty of a set of parameters to validate a hypothesis.

Bayesian inference assumes at random the parameters of interest, what permits them to operate in the probability state, and any interaction between them, through joint or marginal probability distributions.

If we consider θ vector of model parameters and D vector of new observations about the process of interest, $p(\theta)$ represents the prior distribution, and $P(D|\theta)$ represents the likelihood. Following the Bayesian paradigm:

$$P(\theta|D) = \frac{P(\theta)P(D|\theta)}{\int P(\theta)P(D|\theta)\,d\theta} \qquad \text{(Eq. 8-3)}$$

It is possible to assess the posterior $P(D|\theta)$ distribution, which is the updated version of prior distribution given the new observed data D. The denominator of the above equation is a normalizing constant, which permits to describe the posterior as a proportion of the prior and the likelihood:

$$P(\theta|D) \propto P(\theta)P(D|\theta) \qquad \text{(Eq. 8-4)}$$

When the posterior is not analytical, MCMC allows for sampling of posterior probability distributions, from which it is possible to draw each of the participating parameters' marginal distributions. It is possible also to assess the degree of correlation (linear or non-linear) between the marginal distributions and even identify multiple modes (as opposed to optimization methods where only one set of parameters is selected, thereby leaving no method establishing the correlation between parameters, which provides the possibility of being trapped in local minima/maxima). The success of this numerical methodology is based on the notion that infinite samples can be taken via a Markov Chain converging to a stationary process, irrespective of its previous sampling values. The first samples can be discarded since it takes some time for the chain to converge and become stationary, and the rest of samples can be kept to populate the posterior distribution and each parameter's marginal distribution. The number of samples (*m)* that are discarded is called the "burn-in."

There are several methods to determine if the number of samples (*n*) is enough or to select a proper value for burn-in (*m*). The diagnostic plots are used in this study to ensure the convergence of the chain. This includes the statistic defined by the cumulative mean and standard deviation of each parameter chain.

To select or reject a "point" sample (i.e., a set of parameters) during the sampling of the chain, there exist different rules such as the Metropolis-Hasting's sampler, the independence sampler, and the Gibbs' sampler. The Metropolis-Hasting's type of sampler is used in this study, since it is the most general sampler method.

Problem Definition

In the context of this study, the unknown parameters are the foundation type and foundation dimension for a bridge pier (bent) as well as the soil resistance parameters required for bearing-capacity estimation. The priors for these parameters are obtained from the distribution of parameters based on the collected sample of bridges from the Bryan District of TxDOT (working database). The observed data are the bearing capacity predicted by the MLP-BC models, which is assumed to be deterministic due to its very high accuracy prediction.

The new evidence introduced into the Bayesian paradigm represents the estimate of the bridge bearing capacity, conditioned on the specific characteristics of the superstructure (i.e., for an unknown foundation bridge, what is known are the details of the superstructure, already correlated via ANN with the foundation's bearing capacity).

Four types of problems are defined based on available information about a bridge pier. A similar coding used to describe the ANN models is used here, where the first index in the problem corresponds to the availability of foundation type, and the second corresponds to availability of soil resistance. An index value of 0 implies that the information is unavailable for the corresponding parameter or it is unknown; whereas an index of 1 implies the opposite case.

- **Problem 11** refers to the condition for which foundation type and soil resistance parameters are available but the foundation dimensions are unknown. Depending on the foundation type, four different solution frameworks are developed.
- **Problem 10** refers to the condition for which foundation type is known, but the soil resistance parameters and foundation dimensions are unknown. Again, for each foundation type, the corresponding solution frameworks are developed.
- **Problem 01** refers to the condition for which foundation type and dimensions are unknown but the soil resistance parameters are available or obtainable.
- **Problem 00** refers to the most general condition for which the foundation type and dimensions and also the soil resistance parameters are unknown.

Prior and Model Parameters

For each of the four scenarios defined above, the unknown parameters associated with the bridge foundation and the supporting soil are considered as model parameters and defined as random variables.

Table 8-4 shows different unknown parameters and their corresponding priors. Also, Figure 8-12 to Figure 8-17 present some of the model parameters of prior distributions. These are formulated for each parameter of interest included in the working database. The remaining prior distributions are included in the Appendix. Table 8-5 presents the model parameters associated with each problem.

Table 8-4. Definition of Model Parameters and Their Corresponding Prior Distributions.

Parameter	Explanation	Prior
Foundation Type		
FT	1 = Conc, 2 = DrSh, 3 = Steel, 4 = Spread	Discrete distribution
Concrete Piling		
dpCn (ft)	pile depth for concrete piles	Lognorm (3.26,0.30)
DCn (in)	dimension of pile (cross section)	Lognorm (2.71,0.06)
Drilled Shafts		
dpDr (ft)	pile depth for a drilled shafts	Lognorm (3.72,0.30)
DDr (in)	diameter of drilled shafts	Lognorm (3.48,0.17)
Steel Piling		
dpSt (ft)	pile depth for steel piles	Lognorm(3.16,0.26)
ASt (in^2)	cross section area for steel piles	Lognorm (4.94,0.08)
	Spread Footing	
B (ft)	width of a spread footing	Lognorm (1.64,0.20)
L (ft)	length of a spread footing	Lognorm (3.28,1.13)
Df (ft)	embedment depth for spread footings	Lognorm (1.96,0.86)
Soil Resistance		
Su (tsf)	skin friction	Lognorm (0.57,0.74)
Pb (tsf)	point-bearing capacity	Lognorm (3.02,0.98)
Phi (deg)	friction angle of soil (for spread footings)	Lognorm (3.70,0.21)

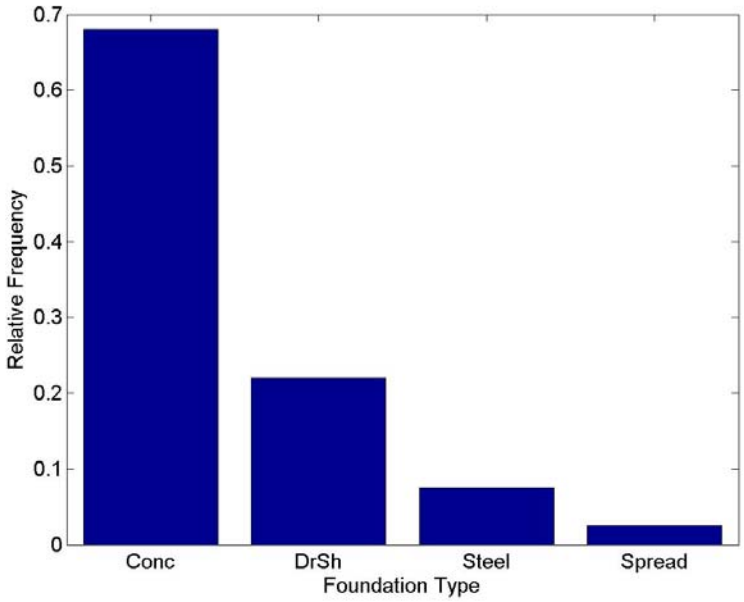

Figure 8-12. Prior Distribution and Histogram for Foundation Type.

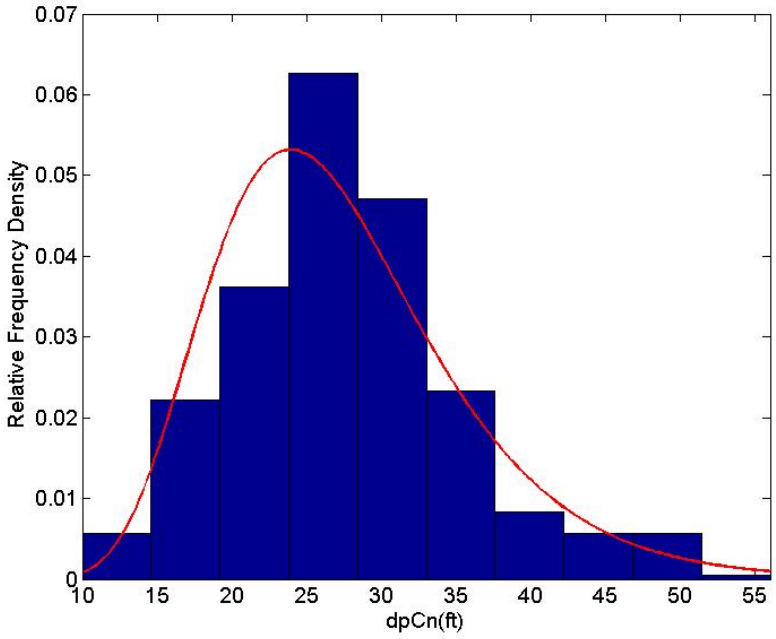

Figure 8-13. Prior Distribution and Histogram for Concrete Piles Depth (dpCn).

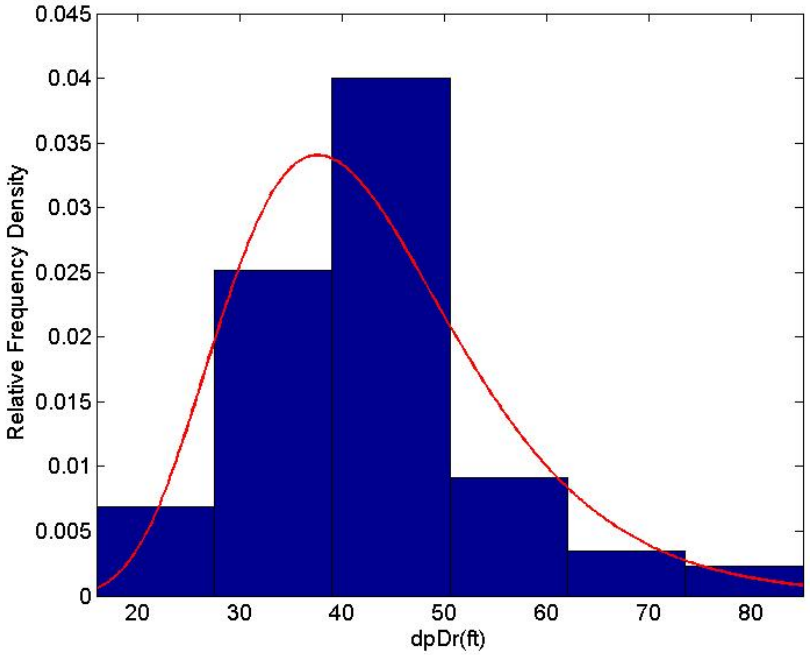

Figure 8-14. Prior Distribution and Histogram for Drilled Shaft Depth (dpDr).

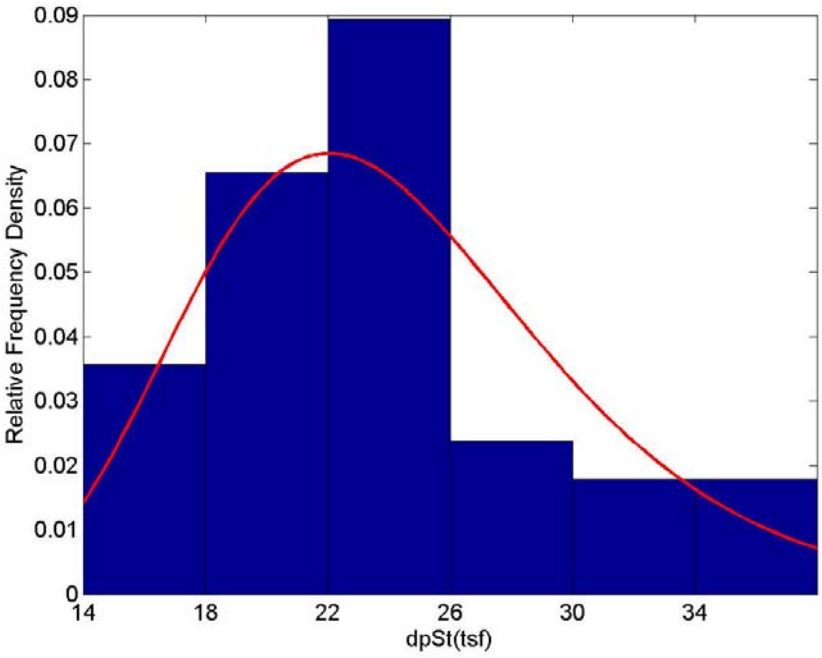

Figure 8-15. Prior Distribution and Histogram for Steel Piles Depth (dpSt).

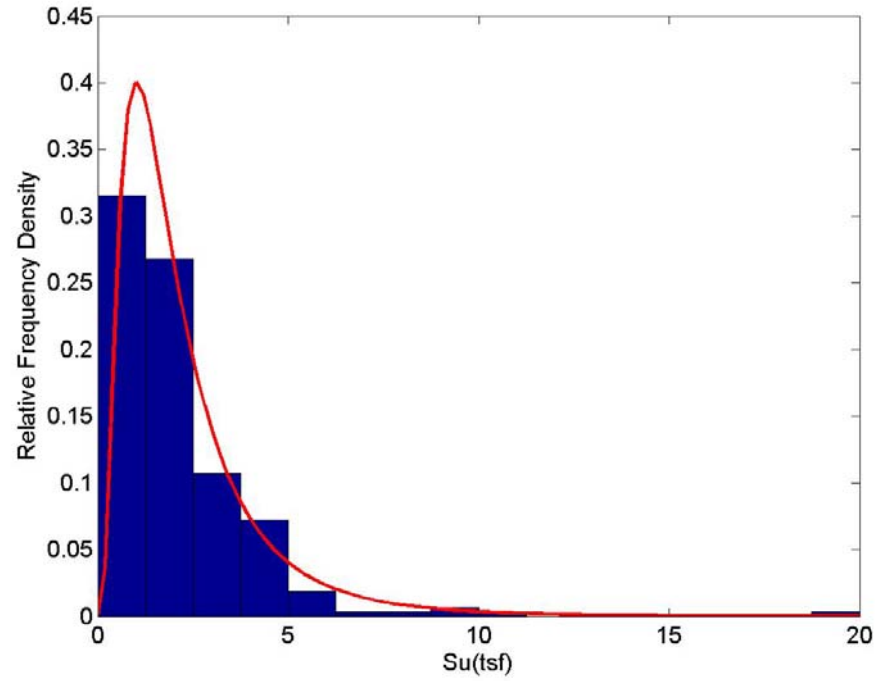

Figure 8-16. Prior Distribution and Histogram for Skin Friction (Shear Strength) (Su).

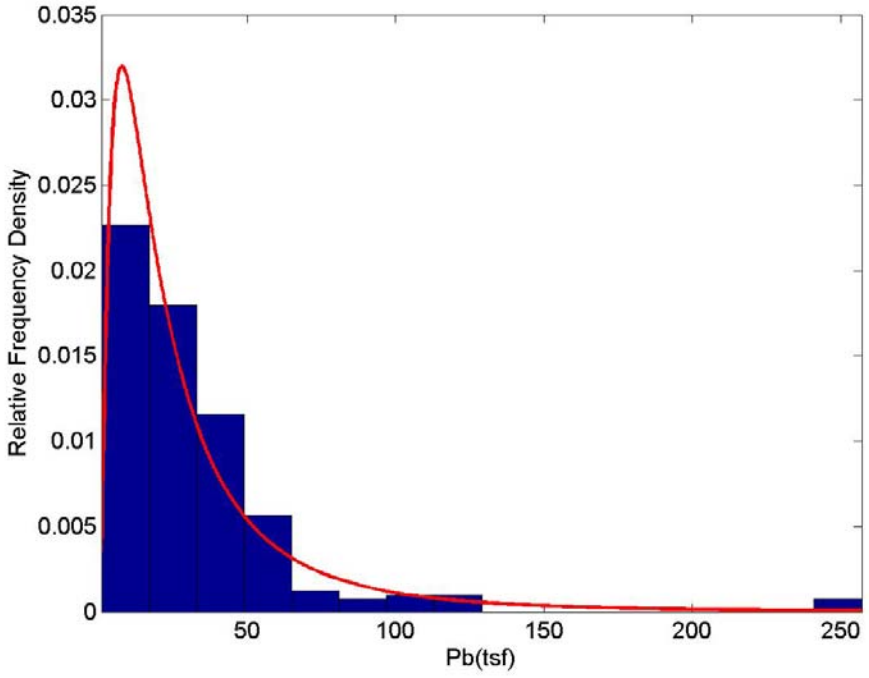

Figure 8-17. Prior Distribution and Histogram for Point Bearing (Tip Resistance) (Pb).

Table 8-5. Coding of Model Parameters for Each Problem Definition.

Problem	Model Parameters
Problem11-Conc	dpCn
Problem11-DrSh	dpDr
Problem11-Steel	dpSt
Problem11-Spread	B, L, Df
Problem10-Conc	dpCn, Su, Pb
Problem10-DrSh	dpDr, Su, Pb
Problem10-Steel	dpSt, Su, Pb
Problem10-Spread	B, L, Df, C=Su, Phi
Problem01	dpCn, DCn, dpDr, DDr, dpSt, ASt, B, L, Df
Problem00	dpCn, DCn, dpDr, DDr, dpSt, ASt, B, L, Df, Su, Pb, Phi

A lognormal distribution is considered prior distribution of model parameters due to their physical nature and data distribution (except for foundation type). Also, for all problem scenarios, unknown parameters are considered independent, so the joint prior distribution is equal to the product of prior distributions for each parameter.

The lognormal probability distribution is denoted as lognorm (μ,σ), where μ and σ are distribution parameters. A lognormal probability density function appears as:

$$\mathrm{P}(x) = \frac{1}{\sqrt{2\pi}\sigma} e^{-0.5\left(\frac{\ln x - \mu}{\sigma}\right)^2} \qquad \text{(Eq. 8.5)}$$

in which $E(x) = e^{\mu + \frac{\sigma^2}{2}}$ is the mean of the distribution and $Var(x) = e^{(2\mu+\sigma^2)}(e^{\sigma^2} - 1)$ is the variance of the distribution.

Likelihood Function

Likelihood is defined as the distribution of model prediction error. Error is defined as the difference between predicted BC and estimated (measured) BC. Distribution of error can be predicted by the corresponding MLP-BC for bridge piers in the database. Error distribution (probability density function) is considered to be normal. Normal distribution, N (μ, σ)appears as:

$$P(x) = \frac{1}{\sqrt{2\pi\sigma}} e^{-0.5\left(\frac{x-\mu}{\sigma}\right)^2} \qquad \text{(Eq. 8-6)}$$

in which $E(x) = \mu$ is the mean of the distribution and $Var(x) = \sigma^2$ is the variance of the distribution. The error of BC estimation can be defined as:

$$Err = BC_p - BC_e \qquad \text{(Eq. 8-7)}$$

where BC_p is predicted by the ANN model and BC_e is the bearing capacity function.

Figure 8-18 shows the cumulative density function (CDF) of prediction error for different MLP-BC models. The error function depends on the equation for BC estimation, and thus it depends on which foundation type we are assuming to have. The BC equation is the same as equations described in Chapter 6 for different foundation types. Thus for four different foundation types, the BCs are:

$$BC_a - Conc = \min\left(GN\,0.5Su\left((dpCn - 10)\left(4 \times \frac{DCn}{12}\right) + 0.5Pb\left(\frac{DCn}{12}\right)^2 \right), GN\left(8.214DCn - 56.429\right) \right) \qquad \text{(Eq. 8-8)}$$

$$BC_a - DrSh = \min\left(GN\left(0.7 \times 0.5Su\left(dpDr - 10\right)\left(\pi \times \frac{DDr}{12}\right) + 0.5Pb\left(\pi \frac{\left(\frac{DDr}{12}\right)^2}{4} \right) \right), GN \times 73.928e^{0.046DDr} \right) \qquad \text{(Eq. 8-9)}$$

$$BC_a - Steel = \min\left(GN\left(0.5Su\left(dpSt - 10\right)\left(\frac{1}{3} \times \frac{ASt}{12}\right) + 0.5Pb\left(\frac{ASt}{12^2}\right) \right), GN\left(0.6 \times 18 \times ASt\right) \right) \qquad \text{(Eq. 8-10)}$$

and

$$BC_a - Spread = 0.5 \times GN \times B \times L(7.5Su\left(1+0.2\left(\frac{B}{L}\right)\right)+\frac{1}{2}(\gamma-0.031)B\times 0.5\times 2\left(e^{\pi\tan\phi_f}\frac{1+\sin\phi_f}{1-\sin\phi_f}+1\right)\tan\phi_f\left(1-0.4\frac{B}{L}\right)$$

$$+(\gamma-0.031)\times 0.5\times Df\times e^{\pi\tan\phi_f}\frac{1+\sin\phi_f}{1-\sin\phi_f}\left(1+\frac{B}{L}\tan\phi_f\right)$$

(Eq. 8-11)

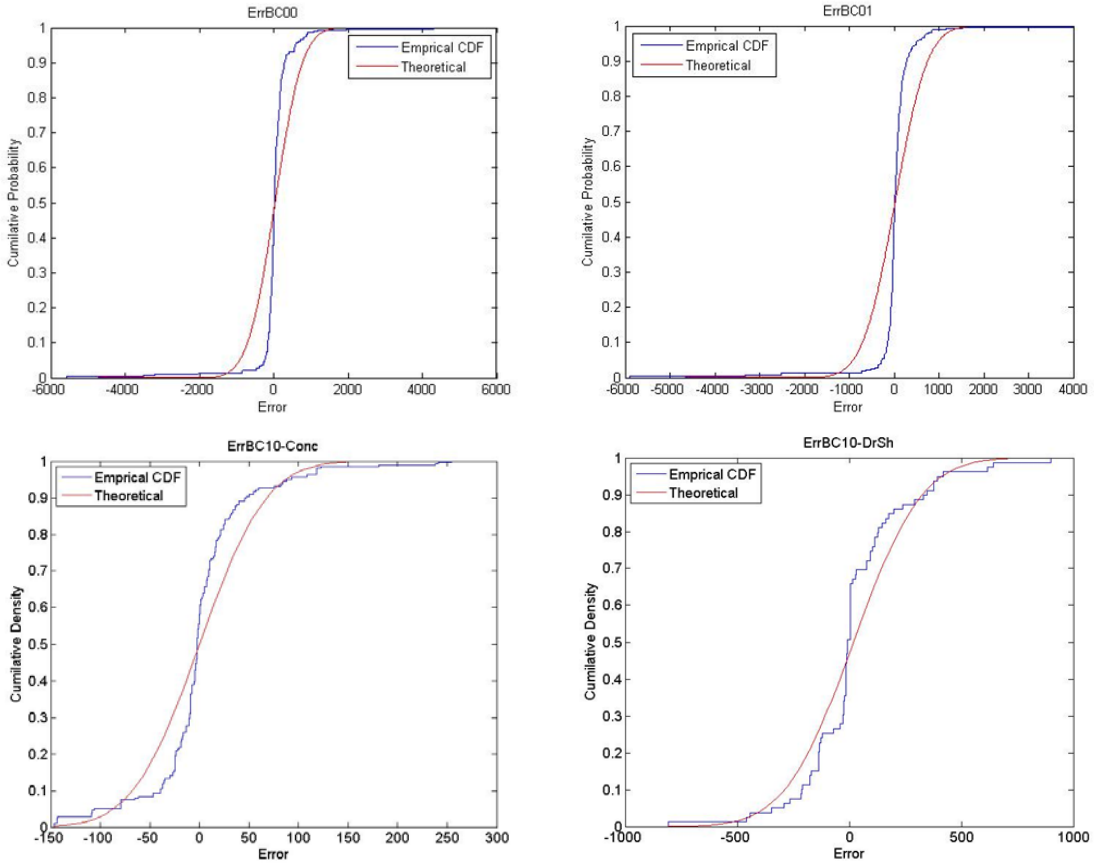

Figure 8-18. CDF for Prediction Error of Different MLP-BC Models.

Recall that the structural bearing capacity is also considered in computing the BC and that the minimum between the geotechnical and structural BC is selected as the foundation bearing capacity. The structural BC equations for concrete piles and drilled shafts are empirical equations derived from the relation between maximum allowable service loads and the size of the pile (shaft).

After performing preliminary analyses, it was found that including the structural BC in the likelihood function generates inconsistency in results because for some of the problem definitions, the structural BC is not a function of model parameters. (It is only a function of pile size.)

Therefore, the predicted embedment depth would be the minimum depth, since the BC predicted by MLP-BC models is based on the minimum between structural and geotechnical BC.

The Cw_1 and Cw_2 are assumed to be 0.5 and C_q; C_γ and dq are equal to one in the BC equation of spread footing. Also, the soil is assumed to be fully saturated. Furthermore, it is assumed that if the soil is sandy, then C (Su) is close to zero, and if the soil is clayey then ϕ_f is zero.

Table 8-6 presents the ANN model for BC prediction, the PDF for error distribution, and the likelihood function associated with each problem and each foundation type.

Table 8-6. Model Parameters for Each Type of Problem.

Problem	ANN Model	PDF of prediction error	Allowable BC
Problem11-Conc	MLP-BC11-Conc	N (-0.79, 35.55)	$\frac{1}{\sqrt{2\pi\times 35.55}}e^{-0.5\left(\frac{BC_p - f(dpCn) - (-0.79)}{35.55}\right)^2}$
Problem11-DrSh	MLP-BC11-DrSh	N (9.81, 153.42)	$\frac{1}{\sqrt{2\pi\times 153.42}}e^{-0.5\left(\frac{\left(BC_p - f(dpDr) - 9.81\right)}{153.42}\right)^2}$
Problem11-Steel	MLP-BC11-Steel	N (0.67,9.74)	$\frac{1}{\sqrt{2\pi\times 9.74}}e^{-0.5\left(\frac{\left(BC_p - f(dpSt) - 0.67\right)}{9.74}\right)^2}$
Problem11-Spread	MLP-BC11-Spread	N (607.16, 5663.93)	$\frac{1}{\sqrt{2\pi\times 5663.93}}e^{-0.5\left(\frac{\left(BC_p - f(B,L,Df) - 607.16\right)}{5663.93}\right)^2}$
Problem10-Conc	MLP-BC10-Conc	N (0.29,52.90)	$\frac{1}{\sqrt{2\pi\times 52.90}}e^{-0.5\left(\frac{\left(BC_p - f(dpCn,Su,Pb) - 0.29\right)}{52.90}\right)^2}$
Problem10-DrSh	MLP-BC10-DrSh	N (18.31, 240.17)	$\frac{1}{\sqrt{2\pi\times 240.17}}e^{-0.5\left(\frac{\left(BC_p - f(dpDr,Su,Pb) - 18.31\right)}{240.17}\right)^2}$

Table 8-6. Model Parameters for Each Type of Problem (Continued).

Problem	ANN Model	PDF of prediction error	Allowable BC
Problem10-Steel	MLP-BC10-Steel	N (2.88,27.42)	$\frac{1}{\sqrt{2\pi}\times 27.42} e^{-0.5\left(\frac{\left(BC_p - f(dpDSt, Su, Pb) - 2.88\right)}{27.42}\right)^2}$
Problem10-Spread	MLP-BC10-Spread	N (502.42, 5663.93)	$\frac{1}{\sqrt{2\pi}\times 5663.93} e^{-0.5\left(\frac{\left(BC_p - f(B, L, Df, Su, Phi) - 502.42\right)}{5663.93}\right)^2}$
Problem01	MLP-BC01	N (21.15, 568.02)	$\frac{1}{\sqrt{2\pi}\times 568.02} e^{-0.5\left(\frac{(BC_p - f(dpCn, DCn, dpDr, DDr, dpSt, ASt, B, L, Df) - 21.15)}{568.02}\right)^2}$
Problem00	MLP-BC00	N (32.44, 578.36)	$\frac{1}{\sqrt{2\pi}\times 578.36} e^{-0.5\left(\frac{(BC_p - f(dpCn, DCn, dpDr, DDr, dpSt, ASt, B, L, Df, Su, Pb, Phi) - 32.44)}{578.36}\right)^2}$

Proposal Distribution

The Metropolis-Hasting sampler obtains samples from a proposal distribution to generate the chain for the parameter. The probability of choosing a candidate point from the proposal distribution only depends on the previous point (state) of the chain.

One of the necessary characteristics of a proposal distribution is its simplicity. For this problem, a multivariate normal distribution is used for all parameters except FT, which is a categorical variable and has a discrete distribution. For foundation type, a discrete uniform probability distribution is used. A multivariate normal distribution function appears as:

$$P(X) = \frac{1}{(2\pi)^{k/2}\left|\Sigma\right|^{1/2}} e^{[-0.5(X-\mu)'\Sigma^{-1}(X-\mu)]} \qquad \text{(Eq. 8-12)}$$

where μ is:

$$\mu = \begin{bmatrix} \mu_1 \\ \mu_2 \\ \vdots \\ \mu_n \end{bmatrix} : mean \qquad \text{(Eq. 8-13)}$$

and $\sum$ is:

$$\Sigma = \begin{pmatrix} \sigma_1^{\,2} & \rho_{12}\sigma_1\sigma_2 & \cdots & \rho_{1n}\sigma_1\sigma_n \\ \rho_{21}\sigma_2\sigma_1 & \sigma_2^{\,2} & \cdots & \rho_{2n}\sigma_2\sigma_n \\ \vdots & \vdots & \ddots & \vdots \\ \rho_{n1}\sigma_n\sigma_1 & \rho_{n2}\sigma_n\sigma_2 & \cdots & \sigma_n^{\,2} \end{pmatrix} : \text{cov} \qquad \text{(Eq. 8-14)}$$

The model parameters are assumed to be independent, thus the covariant matrix is a diagonal matrix in this case.

The discrete uniform distribution function is shown in the following equation. For *N* categories, the probability of any value between 1 to *N is* 1/*N*:

$$P(X|N) = \frac{1}{N} I_{(1,\ldots,N)}(X) \qquad \text{(Eq. 8-15)}$$

RESULTS OF BAYESIAN INFERENCE

The proposed MCMC simulation is performed for the same example bridge for different possible scenarios reflected in different problem definitions. This helps to cross-validate the proposed probabilistic approach. Pier 2 of the bridge with ID 17-166-0209-05-075 is selected for performing the MCMC simulation. Table 8-7 shows the actual values of bridge parameters. Results of each problem's simulations are shown in this section. Note that only sample plots are shown here, and complementary plots are included in the Appendix.

Table 8-7. Actual Parameters Values for Bridge 17-166-0209-05-075 for Pier 2.

Parameter	Value
FT	1 (DrSh)
DDr	30 in
dpDr	37 ft
GN	3
Pb	34 tsf
Su	1.64 tsf
BC_p	746.17 tons
BCe	615.51 tons
γ	0.075 tcf
φ	30 deg

Problem 11 (Known Foundation Type and Soil Resistance Parameters)

The MCMC simulations in this case are performed for 1,000,000 iterations. To illustrate, the sequence of the MCMC sampling, shows the simulations for all model parameters (in this case, pile depth [dp]). Figure 8-19 shows the simulations for all model parameters (in this case, pile depth [dp]). The corresponding convergence analysis plot is shown in Figure 8-20. These figures demonstrate how the samples are randomly selected over the range of the parameters and how the cumulative mean and standard deviation become stationary after some point in the sample sequence. The burn-in point is considered to be at sample 200,000.

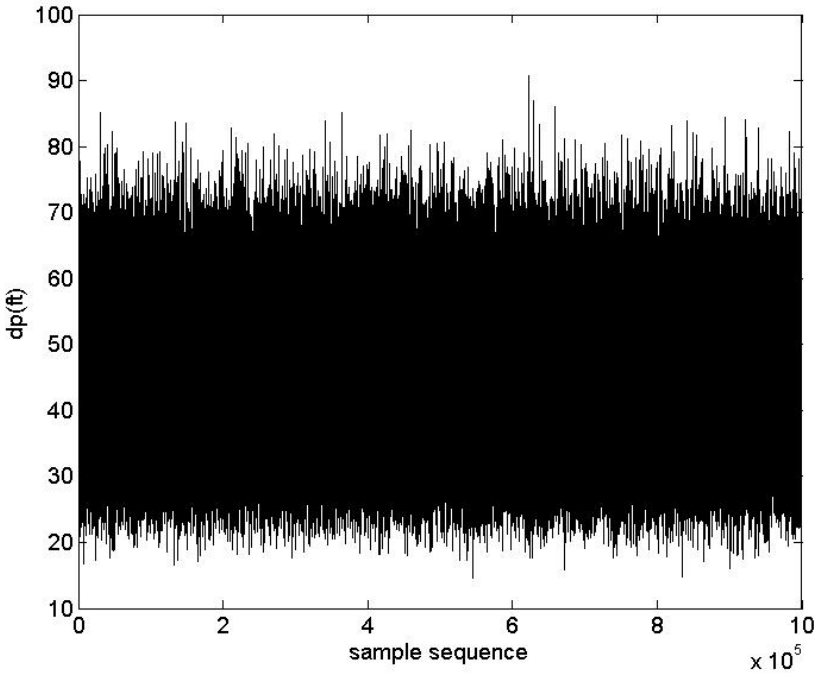

Figure 8-19. Sample Chain for the Model Parameter for Problem 11.

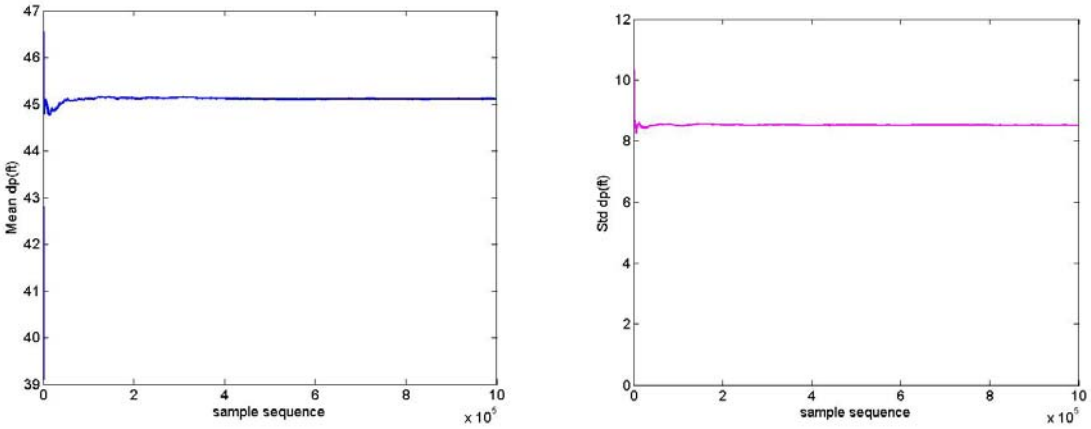

Figure 8-20. Convergence Analysis, Cumulative Mean, and Standard Deviation of Samples versus Sample Sequence for Problem 11.

Figure 8-21 shows the marginal CDF drawn from the posterior. CDFs allow for obtaining quintiles and confidence intervals, and determine the probability of exceeding a specific foundation depth, which is equivalent to the probability that the scour vulnerability of the bridge foundation will be more than what is evaluated using the estimated depth.

In order to emphasize the effect of conditioning the estimate of foundation depth once new details about the superstructure and the foundation bearing capacity are known, Figure 8-22 compares both the prior and the marginal of the posterior for foundation depth. It is remarkable the effect of new evidence in the uncertainty reduction and shift in the distribution's statistics, providing a measure of confidence at the time of making a decision about the assessment of the foundation's depth.

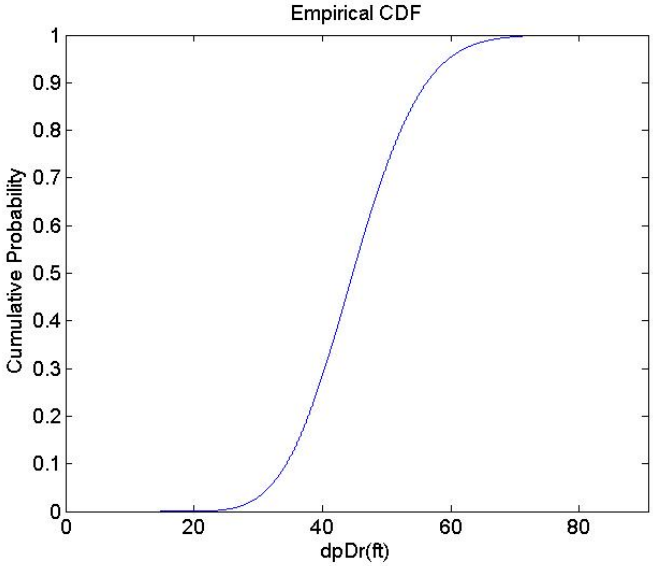

Figure 8-21. CDF Plot of the Posterior for Problem 11.

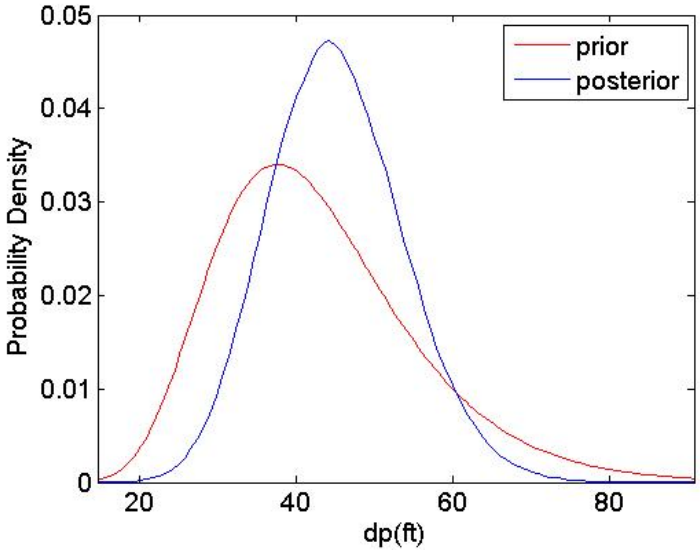

Figure 8-22. Marginal and Posterior for Pile Depth for Problem 11.

The expected value (mean) of the marginal of the posterior is 44 ft, corresponding to a 45 percent chance of having a shallower depth. Considering a pile depth to be around 35 ft will result in an almost 10 percent (or the 10th quantile of the posterior distribution is almost 35 ft) chance of having a shallower depth.

Table 8-8 presents the expected value (exp), standard deviation (stdd), 95 percent confidence interval ($CI_{95\%}$), mode value (i.e., the most frequently occurring value), and the 10th quantile. It is observed that the mode of the marginal posterior distributions for dp are close to the actual pile depth.

Table 8-8. Statistics of Posterior Distribution of the Model Parameters for Problem 11.

Statistics	Value
dp(ft)	
Exp	45.11
Stdd	8.52
$CI_{95\%}$	[45.09 45.12]
Mode	
10^{th} quantile	34.4

Problem 10 (Known Foundation Type and Unknown Soil Resistance Parameters)

In Problem 10, MCMC simulations are performed for 1,000,000 iterations for the same bridge. Figure 8-23 shows the simulations for all model parameters (three in this case). The corresponding convergence analysis plots are shown in Figure 8-24, and the CDF plots for model parameters are presented in Figure 8-25.

As with Problem 11, simulation and convergence diagnostic plots indicate that the sample chain has converged to the target distribution because the mean and standard deviation have become constant after some point in the sample chain. The burn-in point is considered to be at sample 200,000.

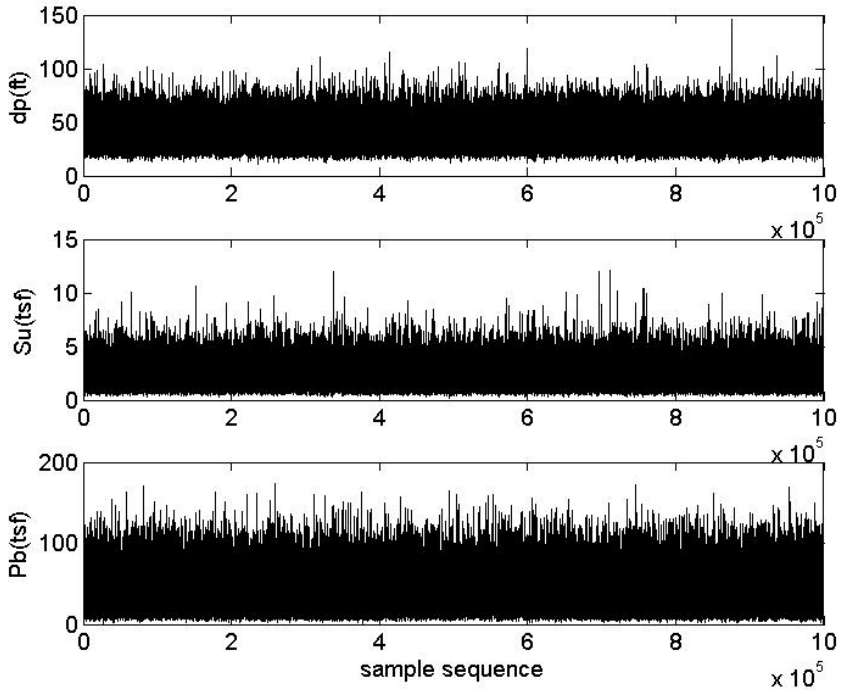

Figure 8-23. Sample Chains for Different Model Parameters for Problem 10.

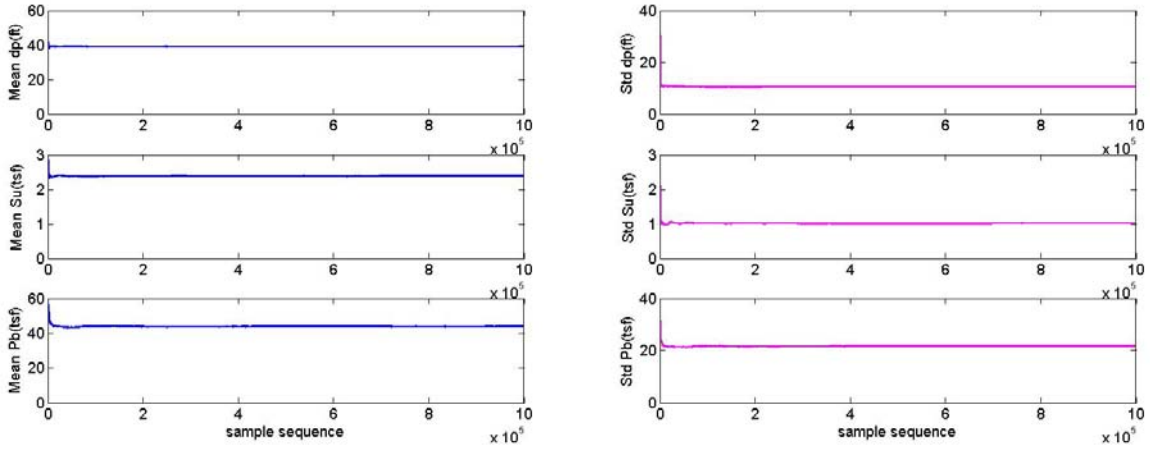

Figure 8-24. Convergence Analysis: Cumulative Mean and Standard Deviation of Parameters for Problem 10.

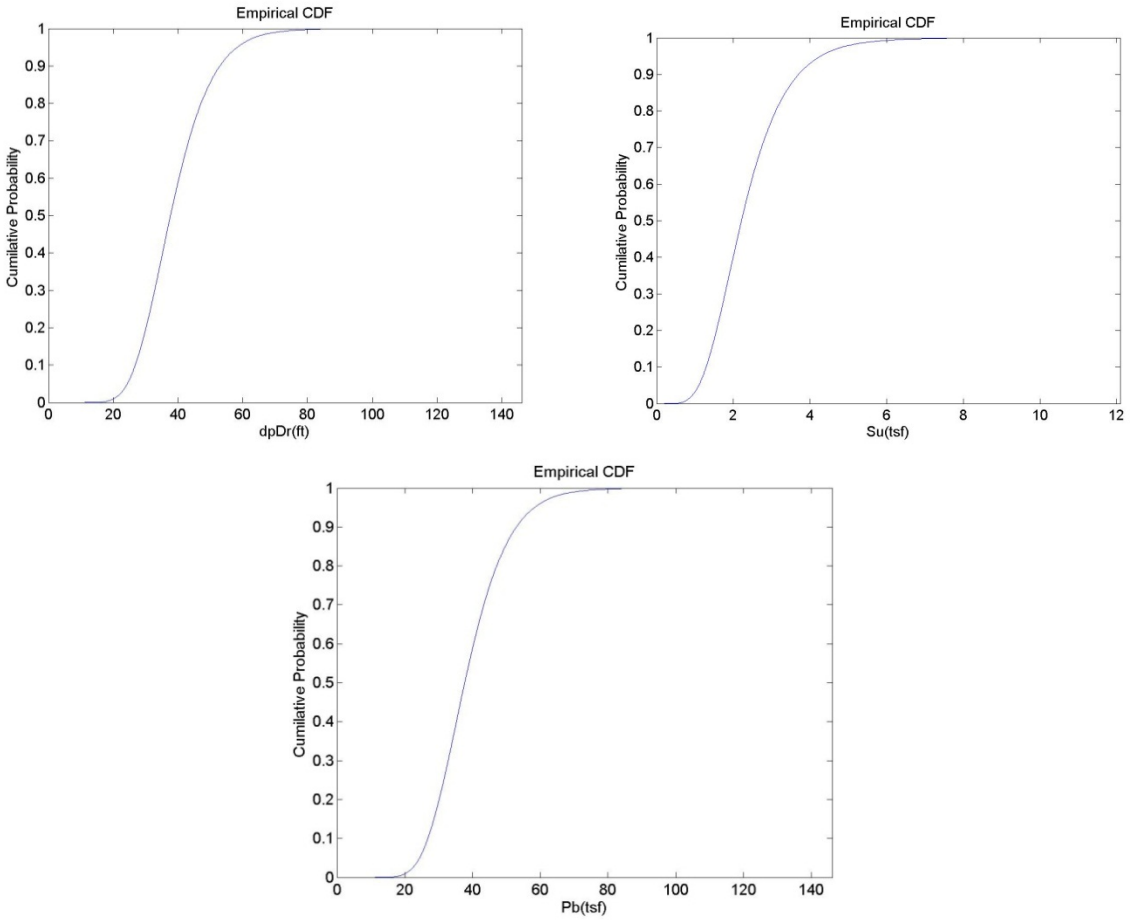

Figure 8-25. CDF of the Marginal Distributions of the Posterior for Problem 10.

A comparison between the prior marginal and posterior distributions of the model parameters are presented in Figure 8-26. It is observed that consistently the posterior distribution is narrower than the prior for each foundation's parameter, which implies the reduction in uncertainty of parameter estimation due to the updating given by information of the superstructure and the estimate of the bearing capacity. Also, the maximum likelihood value (mode of the distribution) becomes closer to the actual value in the posterior for all three model parameters.

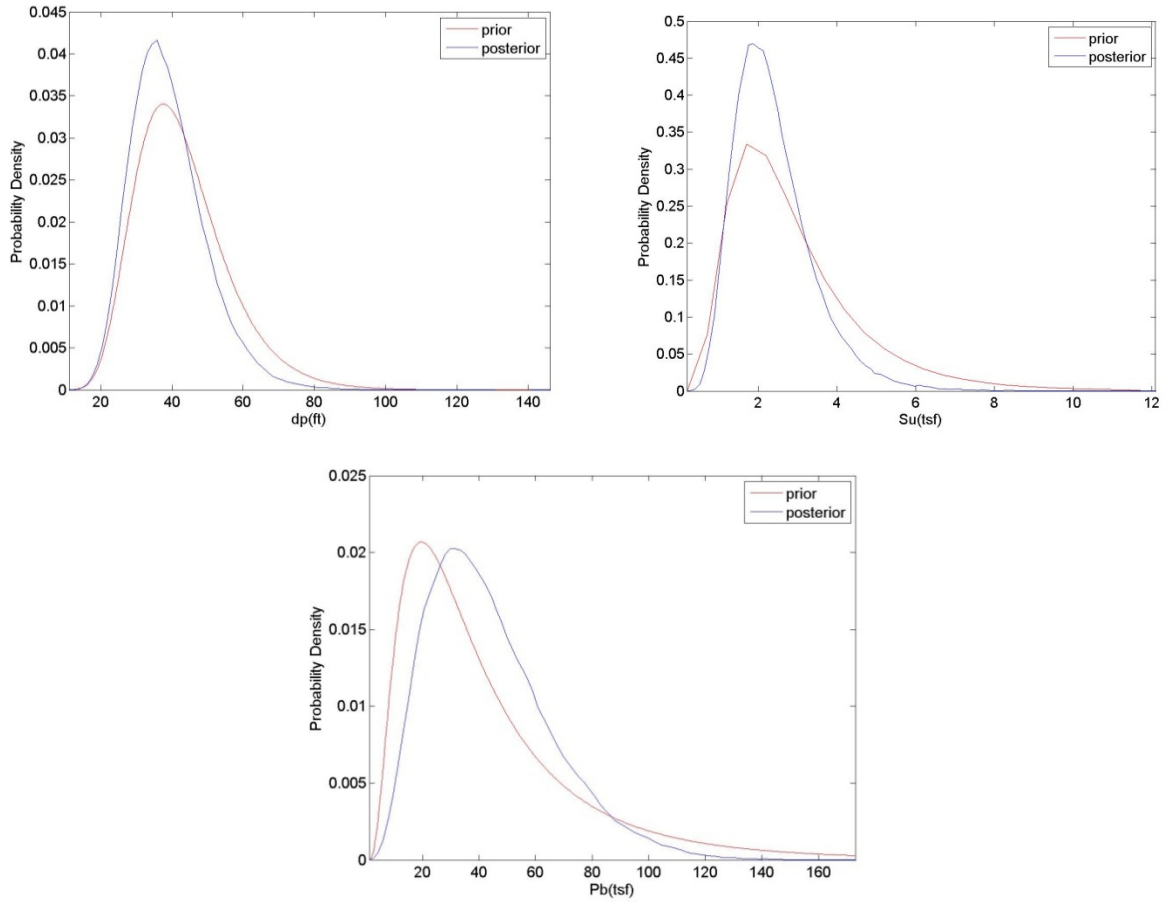

Figure 8-26. Probability Distributions of the Prior and Marginal Posterior Distributions for the Three Model Parameters for Problem 10.

Figure 8-27 shows the prior and posterior joint relative frequency density for two of the foundation's parameters (dp and Su). The prior joint distribution indicates that the two parameters are assumed to be independent, whereas the posterior joint distribution demonstrates that there is a non-linear correlation between them (one increases as the other decreases and vice versa following a non-linear pattern). The joint relative density for the complementary combinations of parameters is presented in the Appendix.

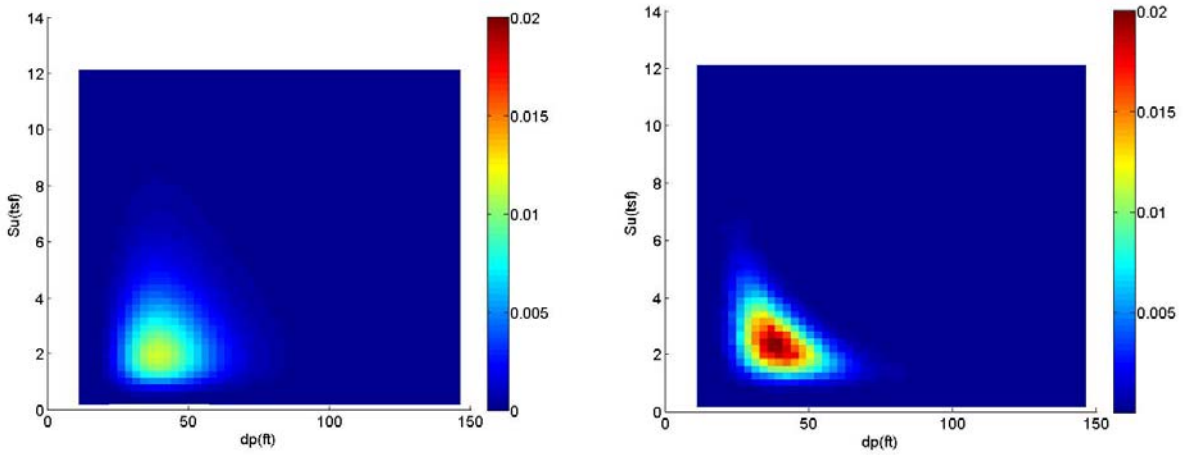

Figure 8-27. Joint Relative Frequency Density of Prior (left) and Posterior (Right) for dp versus Su.

Table 8-9 presents statistics of the posterior, including the expected value, standard deviation, 95 percent confidence interval for the expected value, model value (i.e., the most frequently occurring value), and 10th quantile for the model parameters. It is observed that the mode of the marginal posterior distributions for dpDr, for Su and Pb are close to the actual values.

Table 8-9. Statistics of Posterior Distribution of the Model Parameters for Problem 10.

Parameter Statistics	**dp (ft)**	**Su (tsf)**	**Pb (tsf)**
Exp	39.05	2.39	43.80
Stdd	10.54	1.02	21.80
CI $_{95\%}$	[39.031 39.072]	[2.3874 2.3914]	[43.753 43.838]
Mode	41.88	1.98	34.44
10th quantile	26.84	1.29	19.07

Problem 01 (Unknown Foundation Type and Known Soil Resistance Parameters)

As with Problem 11 and Problem 10, the MCMC simulation is validated using Pier 2 of the bridge 17-166-0209-05-075, considering the scenario of Problem 01. Simulation is performed for 2,000,000 iterations. Figure 8-28 shows the simulations for the model parameters (10 parameters).

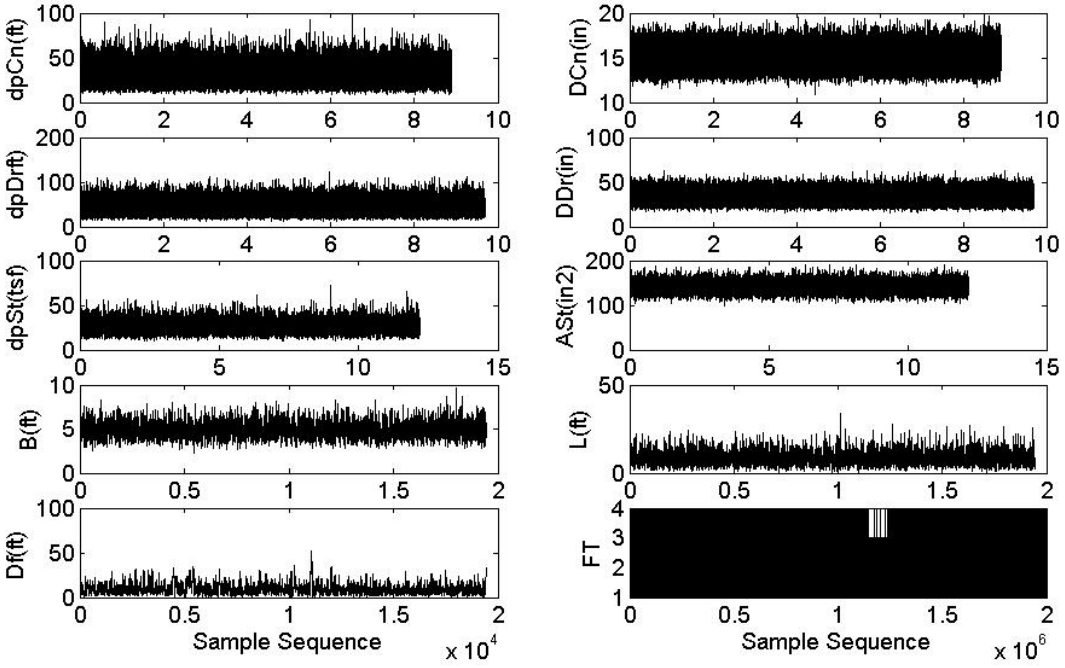

Figure 8-28. Sample Chains for Model Parameters for Problem 01.

Figure 8-29 and Figure 8-30 show convergence analysis plots for the cumulative mean and standard deviation. The burn-in point is considered to be at the 200,000 sample. The CDF plots for different model parameters are presented in Figure 8-31 and Figure 8-32.

Figure 8-33 shows the prior and posterior distributions for FT (foundation type). Notice that the relative frequency for DrSh (which is the actual foundation type) has significantly increased compared to other foundation types.

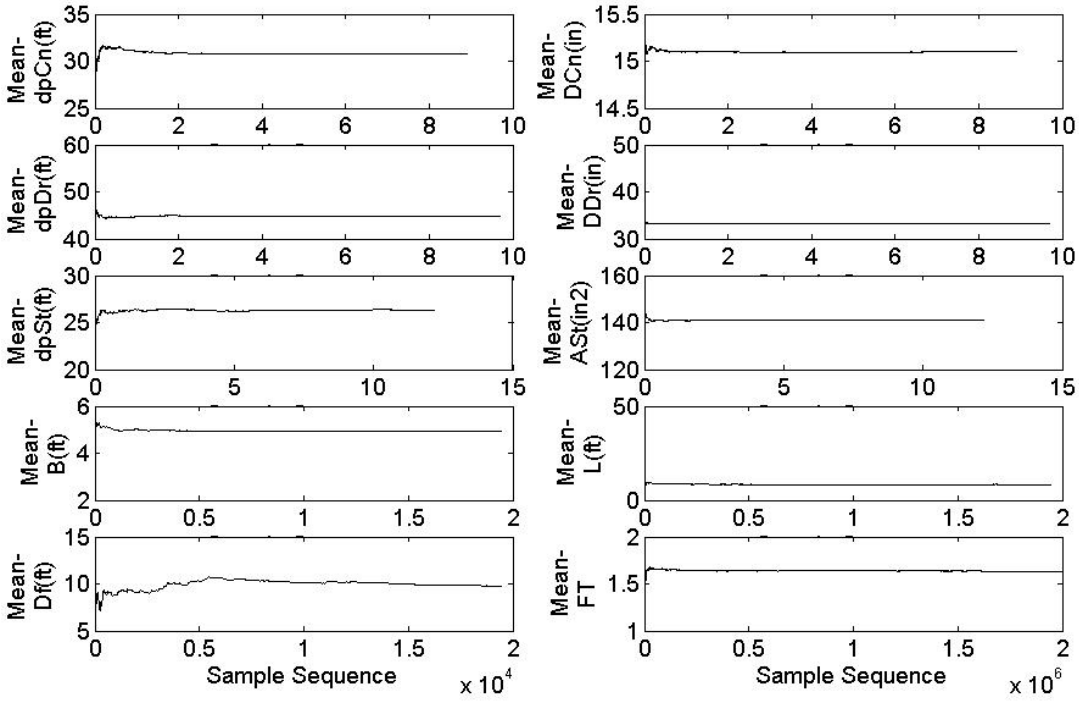

Figure 8-29. Convergence Analysis: Cumulative Mean of Samples versus Sample Sequence for Problem 01.

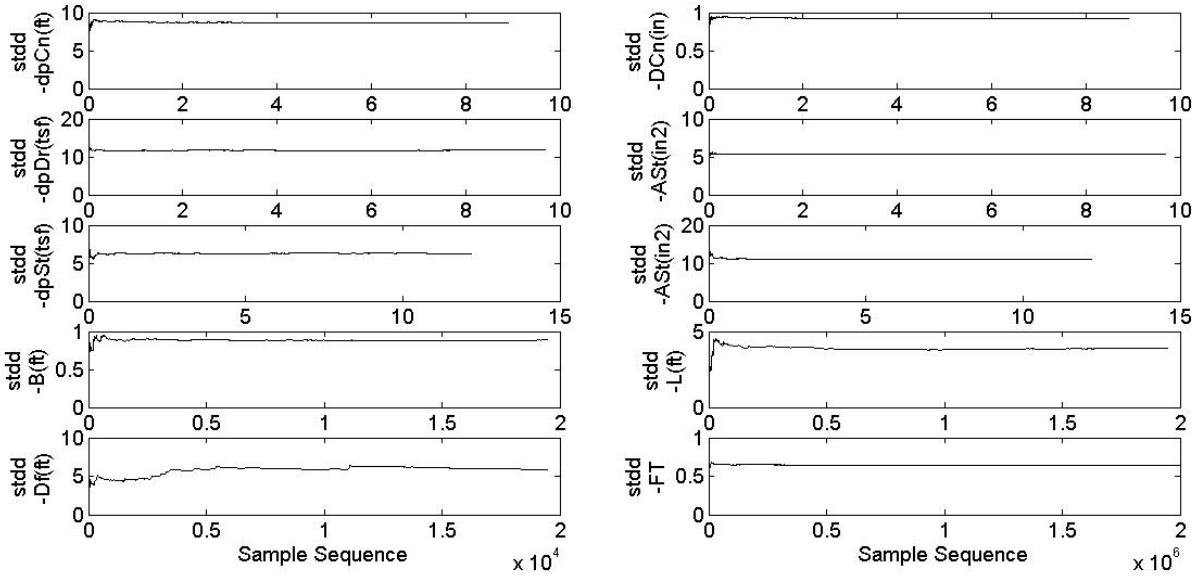

Figure 8-30. Convergence Analysis: Cumulative Standard Deviation of Samples versus Sample Sequence for Problem 01.

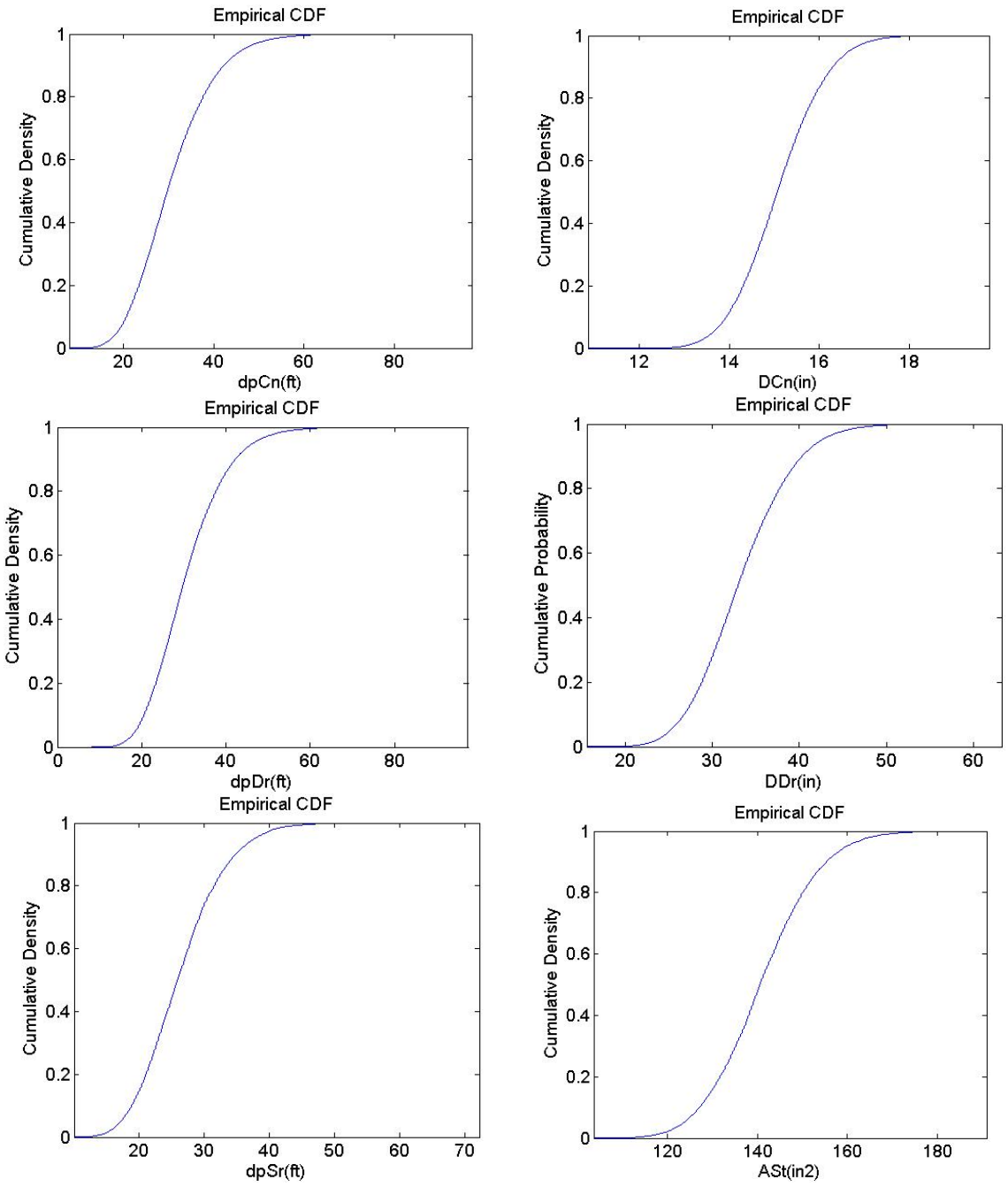

Figure 8-31. CDF Plots of the Posterior Distributions for Different Model Parameters for Problem 01.

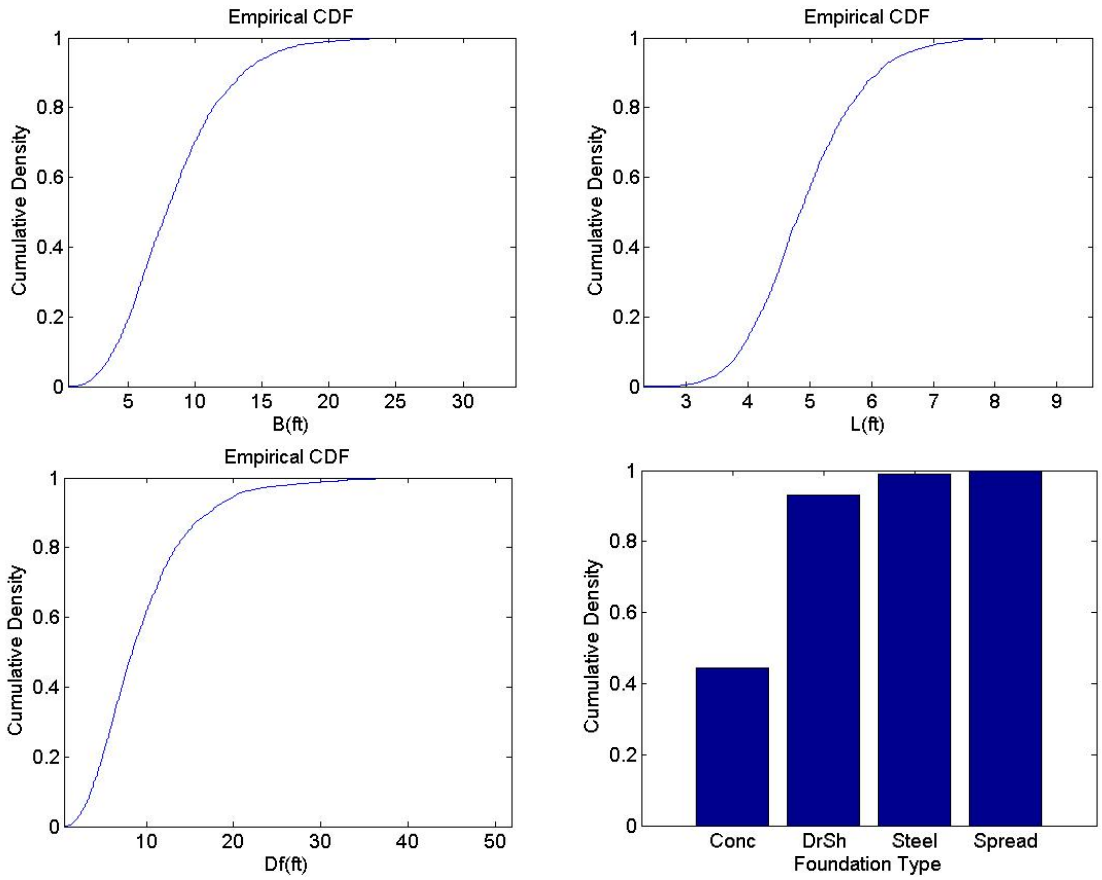

Figure 8-32. CDF Plots of the Marginal Posterior Distributions for Different Model Parameters for Problem 01.

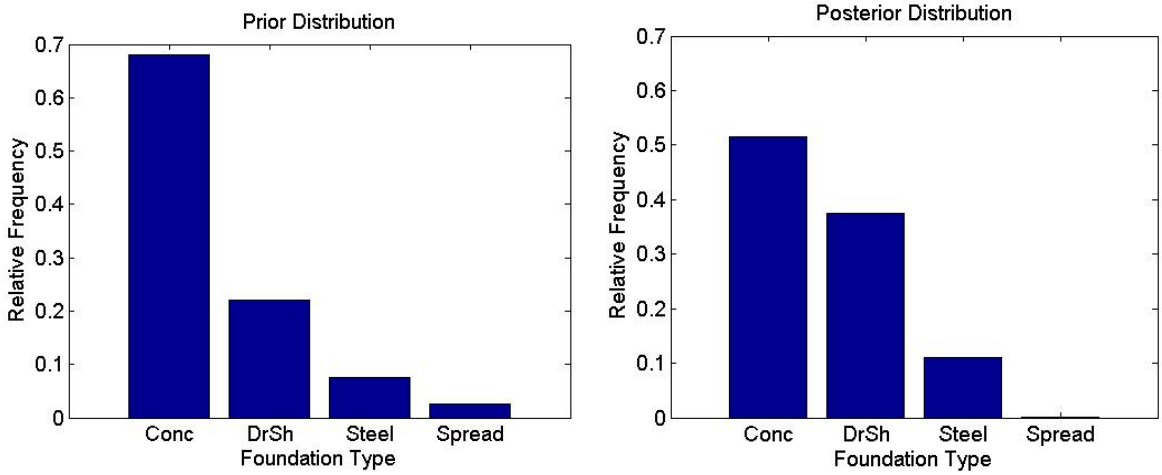

Figure 8-33. Prior and Posterior Distributions for FT for Problem 01.

Figure 8-34 shows the prior and the marginal of the posterior for the depth and size of the drilled shaft. Similar plots are generated for all other model parameters and are provided in the Appendix. Here, it is observed that posterior distribution is more certain compared to its corresponding prior distribution.

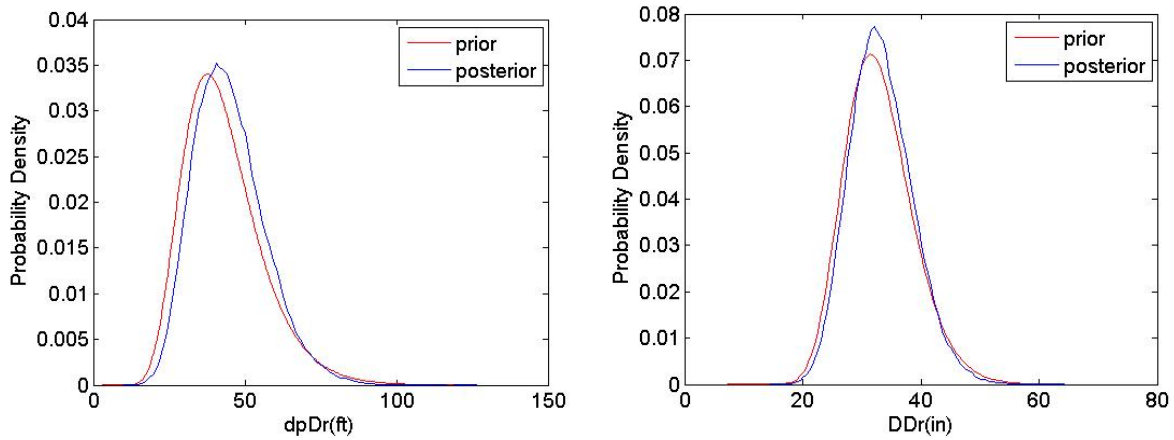

Figure 8-34. Marginal Probability of Prior and Marginal Posterior for dpDr and DDr – Problem01.

Figure 8-35 presents the prior and posterior joint relative distribution for dpDr and DDr. The same plots for other relevant model parameters are presented in the Appendix. The prior joint distribution demonstrates the independency of the two model parameters while the posterior distribution shows a significant reduction in the uncertainty. A slight non-linear negative correlation is also observed between dpDr and DDr.

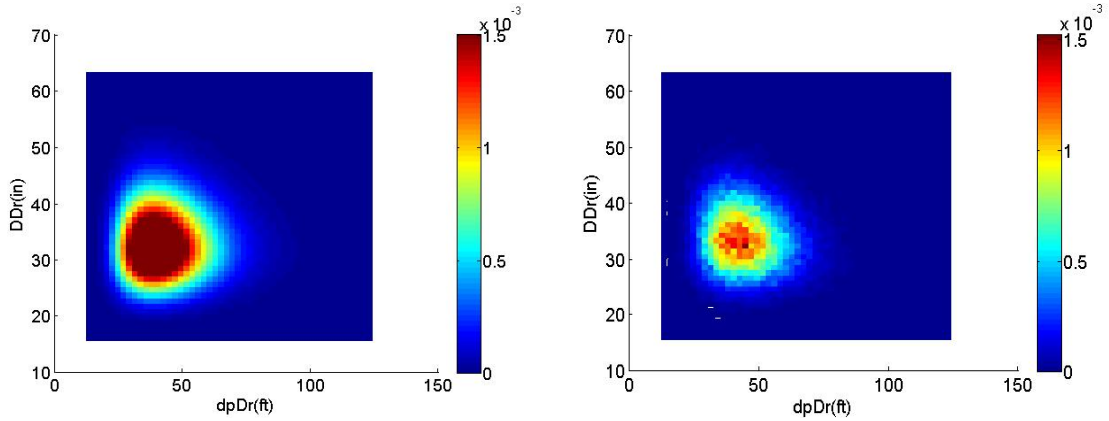

Figure 8-35. Joint Relative Frequency Density of Prior (Left) and Posterior (Right) for dpDr versus DDr.

Table 8-10 summarizes the statistics of posterior distributions for different model parameters. It is observed that the mode of the marginal posterior distributions for dpDr and DDr is close to the actual values.

Table 8-10. Statistics of Posterior Distributions of the Model Parameters for Problem 01.

Parameter / Statistics	dpCn (ft)	DCn (in)	dpDr (ft)	DDr (in)	dpSt	ASt (in^2)	B (ft)	L (ft)	Df (ft)
Exp	30.74	15.10	44.90	33.33	26.44	141.00	4.92	8.42	9.62
Stdd	8.66	0.92	11.77	5.31	6.26	11.03	0.88	3.91	5.92
CI 95%	[30.726 30.764]	[15.096 15.010]	[44.873 44.921]	[33.317 33.338]	[26.394 26.486]	[140.923 141.084]	[4.907 4.936]	[8.353 8.480]	[9.528 9.721]
Mode	32.32	15.11	35.43	31.58	20.82	137.42	5.49	8.55	12.88
10^{th} quantile	20.54	13.93	30.87	26.78	18.87	127.09	3.86	3.91	3.63

Problem 00 (Unknown Foundation Type and Unknown Soil Resistance Parameters)

Pier 2 of the bridge 17-166-0209-05-075 is analyzed this time under the conditions of problem 00. Here, it is assumed that there is no information about foundation type or for soil boring. A million samples are drawn using MCMC simulation.

Figure 8-36 shows the sample chains for different model parameters (14 parameters), and Figure 8-37 and Figure 8-38 demonstrate the convergence analysis plots showing variation of cumulative mean and standard deviation versus sample sequence for the model parameters.

It is observed that the cumulative mean and standard deviation became almost constant after taking a number of samples for most of the model parameters and that the chains are converged to stationary distributions.

It is observed that not enough samples are selected from FT = 4, which is the spread footing due to the value of BC and the very small prior probability of having spread footing. Due to the limited amount of known samples, the chain has not converged for the spread footing model parameters.

CDF plots of posterior distributions for the model parameters are presented in Figure 8-39 and Figure 8-40. Note that Su and Pb plots correspond to FTv=v2 (DrSh), which is the actual foundation type.

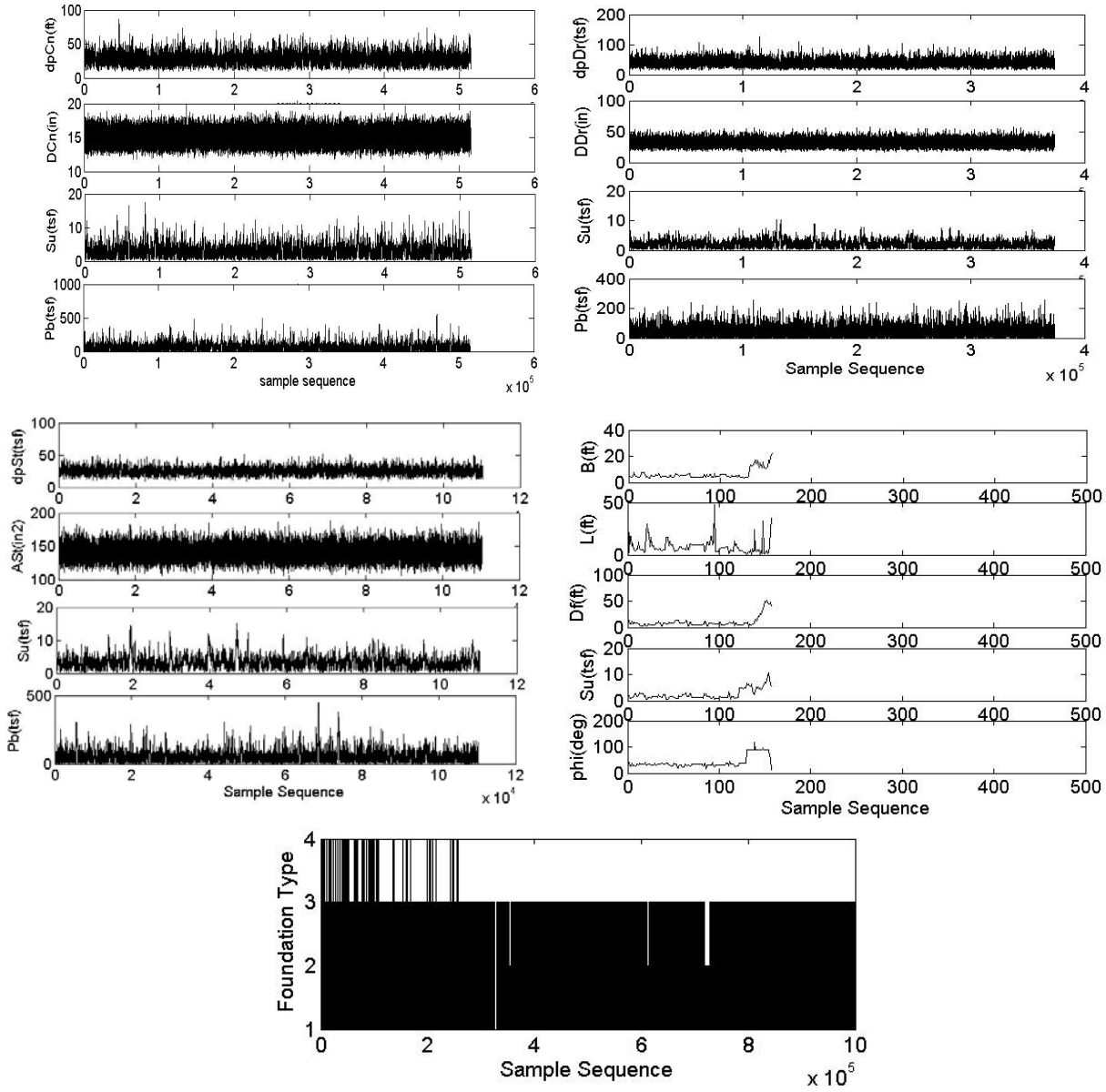

Figure 8-36. Sample Chains for Model Parameters for Problem 00.

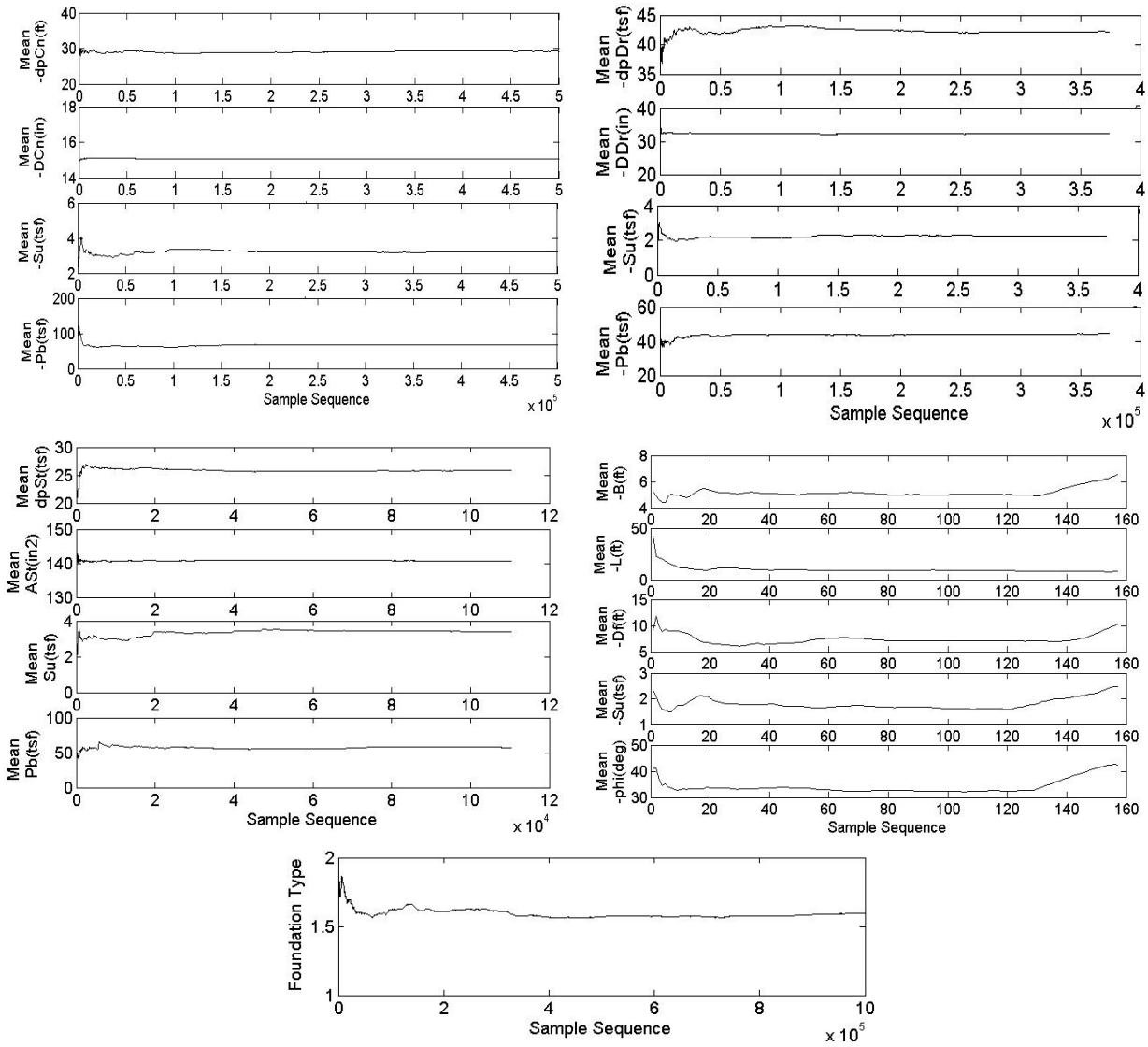

Figure 8-37. Convergence Analysis: Cumulative Mean of Samples versus Sample Sequence for Problem 00.

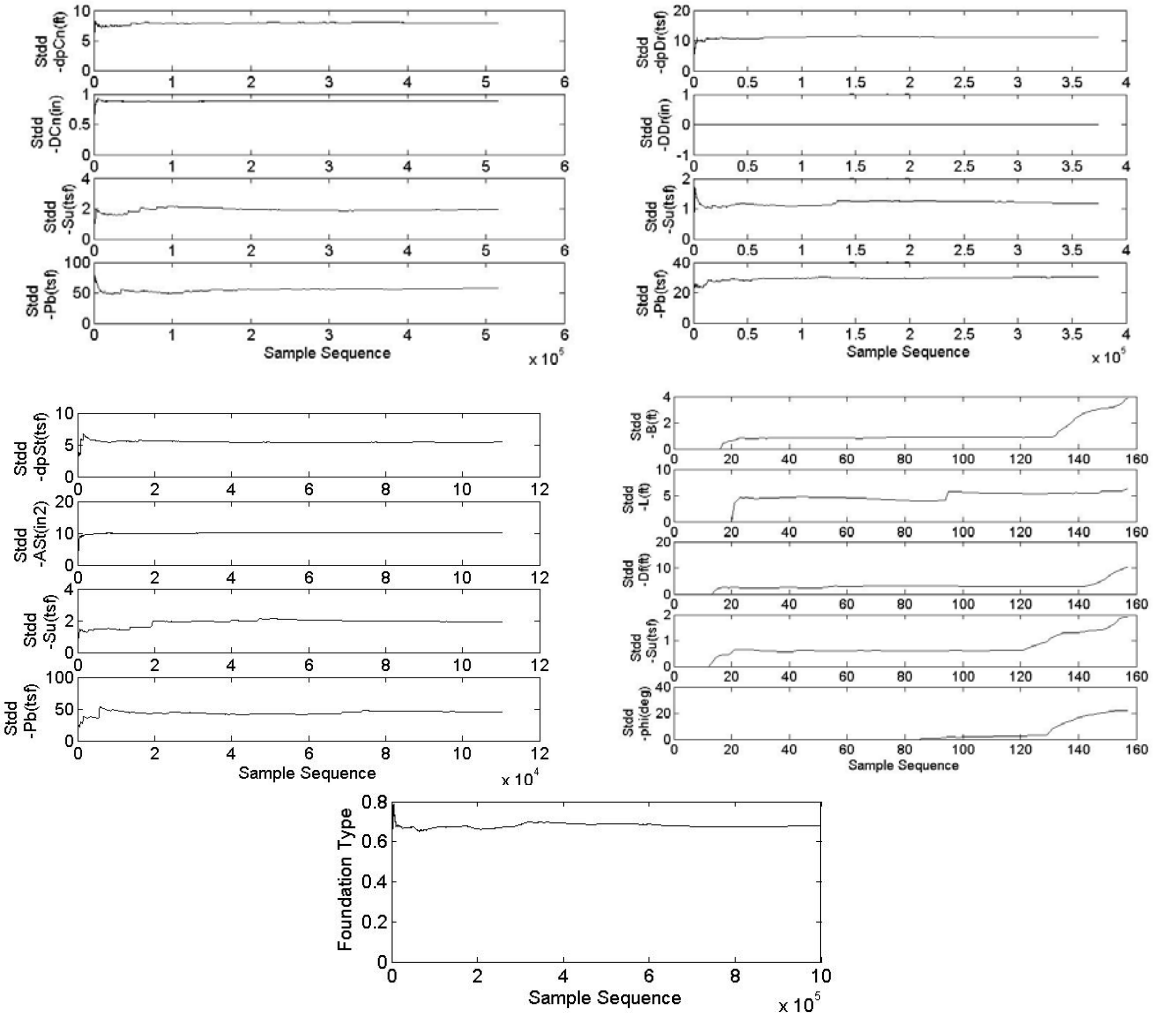

Figure 8-38. Convergence Analysis: Cumulative Standard Deviation for Problem 00.

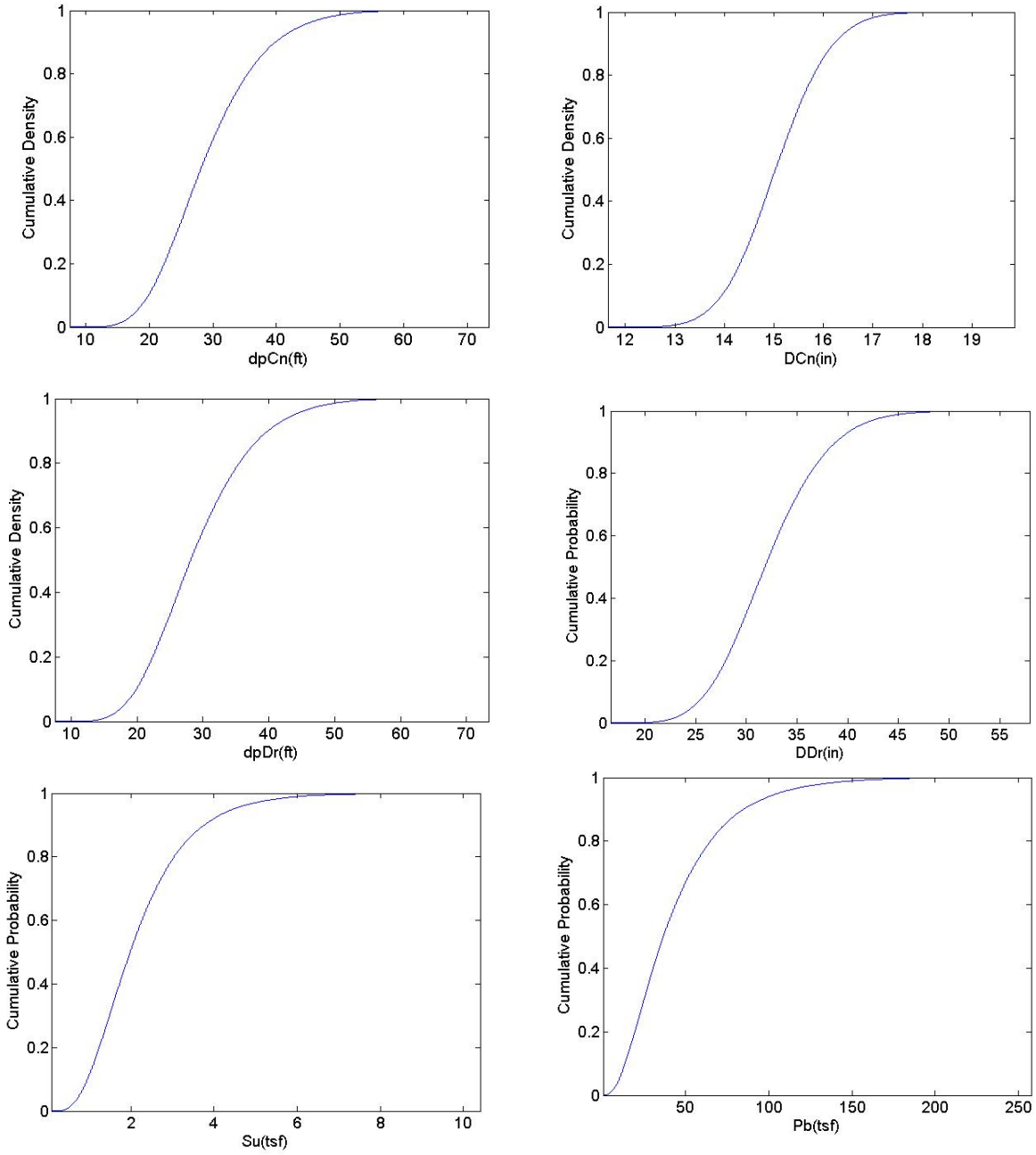

Figure 8-39. CDF Plots of the Posterior Marginal Distributions for Different Model Parameters for Problem 00.

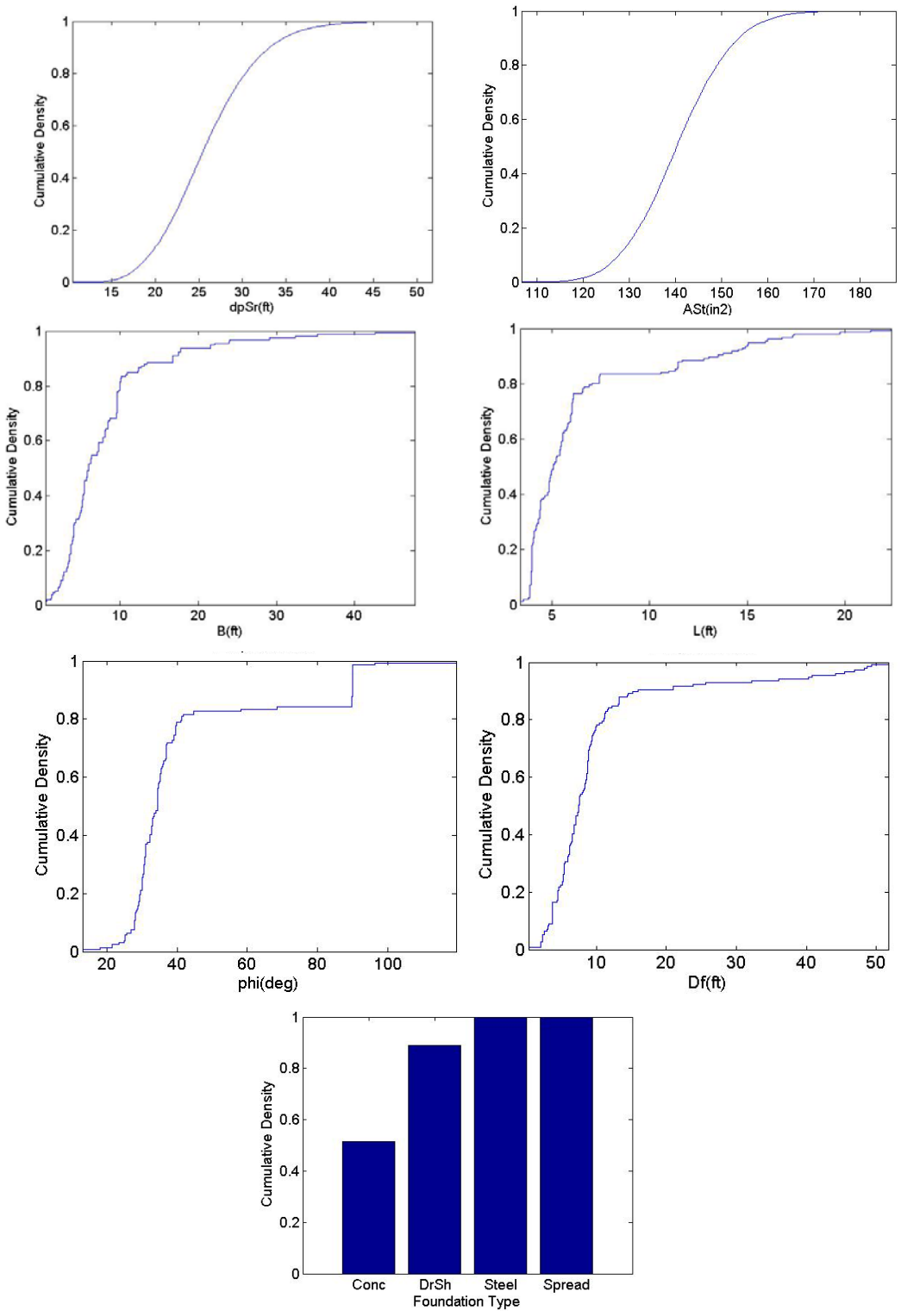

Figure 8-40. CDF Plots of the Posterior Marginal Distributions for Different Model Parameters for Problem 00.

To determine the influence of providing the estimate of the foundation BC, a comparison between the prior and posterior marginal distributions for dpDr, DDr, and FT is shown in Figure 8-41. Complementary plots for other model parameters are included in the Appendix. Results reflect little changes when looking at single parameters, apparently due to the total lack of information about the substructure characteristics of this bridge as compared to previous problem types.

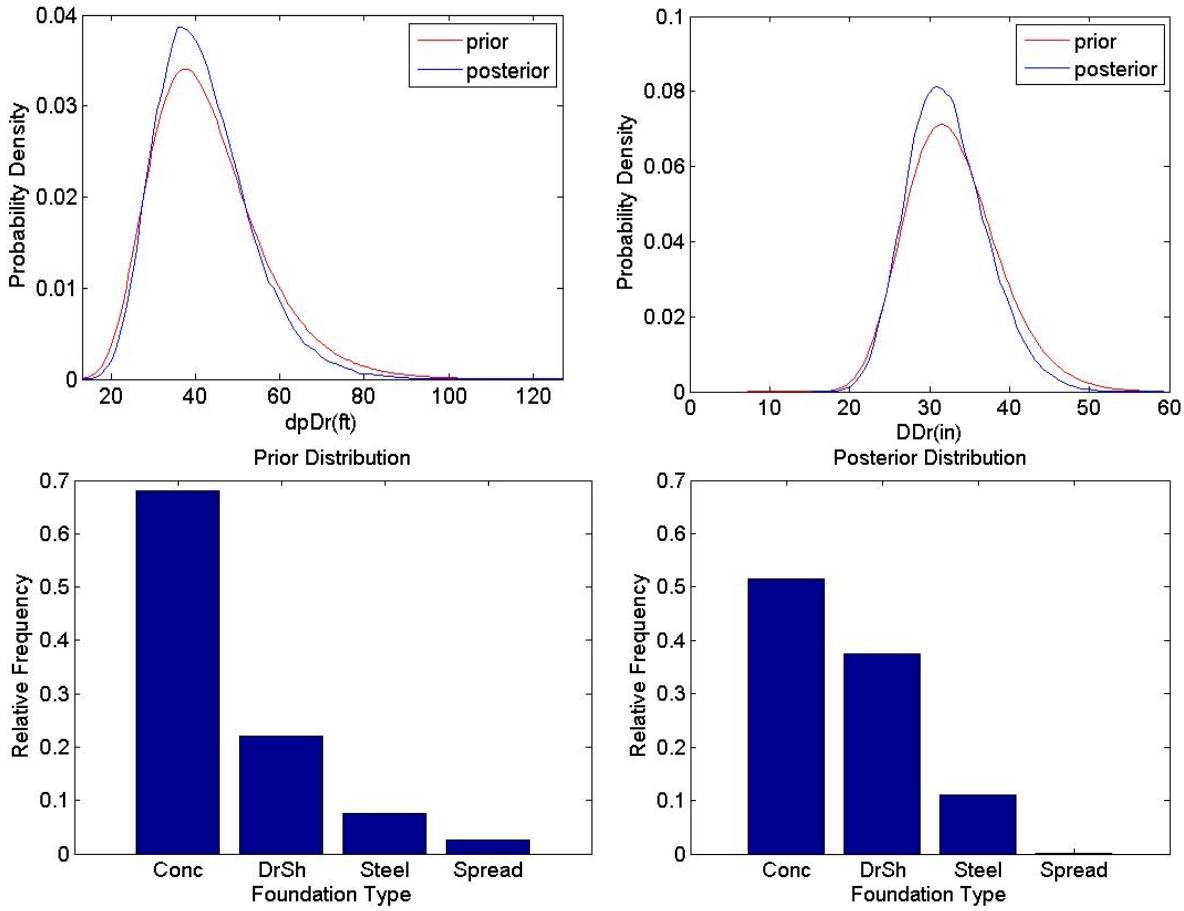

Figure 8-41. Prior Distributions and Marginal Posterior Distributions for dpDr and DDr (Up) and FT (Bottom) for Problem 00.

Also, a comparison of the joint relative frequency distributions (probability) prior and posterior distributions for DDr and dpDr are presented in Figure 8-42. Similar plots for other possible combinations of model parameters are included in the Appendix. It is observed from this figure how the uncertainty in the parameters is reduced in the posterior when compared to the prior distribution. Comparing the prior and posterior of FT, one can see that the probability of DrSh dramatically increased in the posterior, which is an indication of the actual foundation type.

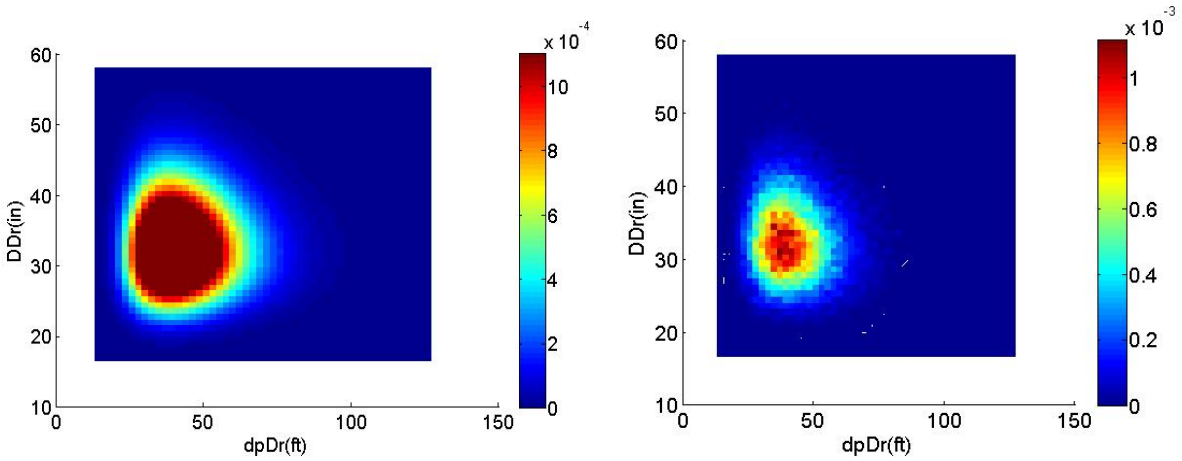

Figure 8-42. Joint Relative Frequency Density of Prior (Left) and Posterior (Right) for dpDr versus DDr.

Table 8-11 provides statistics of different model parameters obtained from corresponding posterior marginal distributions. Notice that the expected value of the dpDr, DDr, Su and Pb are fairly close to the actual known values of the given bridge.

Table 8-11. Statistics of Posterior Distributions of the Model Parameters for Problem 00.

Parameter / Statistics	dpCn (ft)	DCn (in)	Su (tsf)	Pb (tsf)	
FT=1, Conc					
Exp	29.16	15.06	3.24	68.83	
Stdd	7.92	0.89	1.95	58.05	
CI 95%	[29.139 29.185]	[15.058 15.063]	[3.238 3.249]	[68.667 69.000]	
Mode	35.61	14.11	2.40	17.66	
10th quantile	19.89	13.94	1.24	17.02	
FT=2, DrSh					
Parameter / Statistics	**dpDr (ft)**	**DDr (in)**	**Su(tsf)**	**Pb(tsf)**	
Exp	42.24	32.21	2.21	44.50	
Stdd	11.21	4.98	1.18	33.89	
CI 95%	[42.203 42.280]	[32.191 32.225]	[2.211 2.219]	[44.389 44.601]	
Mode	56.46	37.00	1.25	70.34	
10th quantile	29.14	26.10	0.95	13.73	
FT=3, Steel					
Parameter / Statistics	**dpSt (ft)**	**ASt(in^2)**	**Su (tsf)**	**Pb (tsf)**	
Exp	25.93	140.63	3.26	58.90	
Stdd	5.44	10.11	1.68	47.02	
CI 95%	[25.883 25.970]	[140.544 140.706]	[3.246 3.273]	[58.516 59.266]	
Mode	22.47	140.66	2.53	35.03	
10th quantile	19.24	127.74	1.36	16.03	
FT=4, Spread					
Parameter / Statistics	**B (ft)**	**L (ft)**	**Df (ft)**	**Su (tsf)**	**Phi (Deg)**
	B(ft)	L(ft)	Df(ft)	Su	phi
Exp	6.53	8.17	10.18	2.49	42.33
Stdd	3.91	7.185	1018	1.92	22.26
CI 95%	[5.915 7.140]	[7.050 9.298]	[8.576 11.761]	[2.186 2.786]	[38.845 45.808]
Mode	3.98	9.63	3.77	1.24	34.46
10th quantile	3.94	2.67	3.77	0.98	27.84

PART III.
EXPERIMENT-BASED APPROACH

Chapter 9.
VIBRATION METHOD

INTRODUCTION

The use of inducing vibrations for unknown bridge foundation testing is not a new concept. Much research was invested in different ways to excite a bridge using pulse excitation with built-in force transducers (Olson et al. 1998 and Olson 2005). These methods, however, failed to generate enough energy to excite the bridge as desired. For this reason, the research team proposed using Brüel and Kjær 4383 Piezoelectric Charge Accelerometers. The accelerometers were attached to a bridge pier quickly and nondestructively. These sensors measure acceleration in three directions when three are used and send it directly to a data logger. By impacting the pier with a hammer, readings from the sensors were used to calculate the natural frequency of the pier from which the depth of the foundation can be inferred. A numerical simulation employing the finite element method was also created. In this model, shallow foundations were compared to deep foundations, each with different embedment depths. An eigenvalue analysis with frequencies and mode shapes for each system was created to compare the different responses of frequency relative to the foundation depth and type.

LABORATORY CALIBRATION

The accelerometers used for the motion sensor component of this project were calibrated in the Haynes Coastal Engineering Laboratory at Texas A&M University through an experimental modal analysis. Two concrete slabs were buried at different depths in the two-dimensional tow-dredge tank in the Haynes Lab. The two-dimensional tank is a concrete structure that is 45.72 m (150 ft) long, 3.66 m (12 ft) wide, and 3.05 m (10 ft) deep. The bottom of the tank has removable steel sheets that cover the sediment pit filled with sand. The pit is 7.62 m (25 ft) wide by 1.52 m (5 ft) deep. The two 1.83 m (6 ft) long, 0.30 m (1 ft) wide, and 7.62 cm (3 in) thick concrete slabs were buried vertically as shown in Figure 9-1.

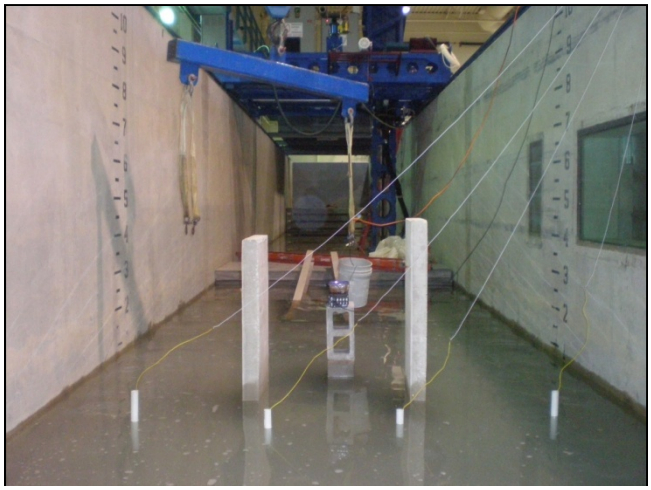

Figure 9-1. Haynes Laboratory Setup.

The left slab was buried 0.76 m (2.5 ft) deep in the sediment pit, and the right was buried 0.91 m (3 ft) deep. After the slabs were in place, approximately 0.3 m (1 ft) of water was pumped into the tank, which can be seen in Figure 9-1.

An accelerometer was attached to the face of each slab, 15.24 cm (6 in) from the edge, in the center of the slab, as shown in Figure 9-2. The other side of the slab was then struck with a rubber impact hammer, creating a pulse excitation.

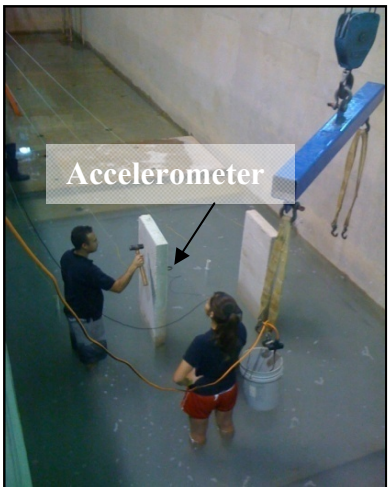

Figure 9-2. Impacting the Slab.

The accelerometer was attached to a signal conditioner and a computer with a Fast Fourier Transform (FFT) analyzer. The output for each impact of the slab was the excitation response of

the slab measured at a constant frequency step. The amplitude of the response versus frequency was plotted for each bridge deck. The slab buried 0.91 m (3 ft) below the soil is a stiffer system, which should result in a higher frequency. This can be mathematically proven by the fundamental equation:

$$\omega = \sqrt{k/M} \qquad \text{(Eq. 9-1)}$$

where ω is the circular frequency, k is the stiffness, and M is the mass. Because the mass of the two slabs are identical, a stiffer system should result in a higher frequency. Figure 9-3 contains the results of the response of the buried slabs.

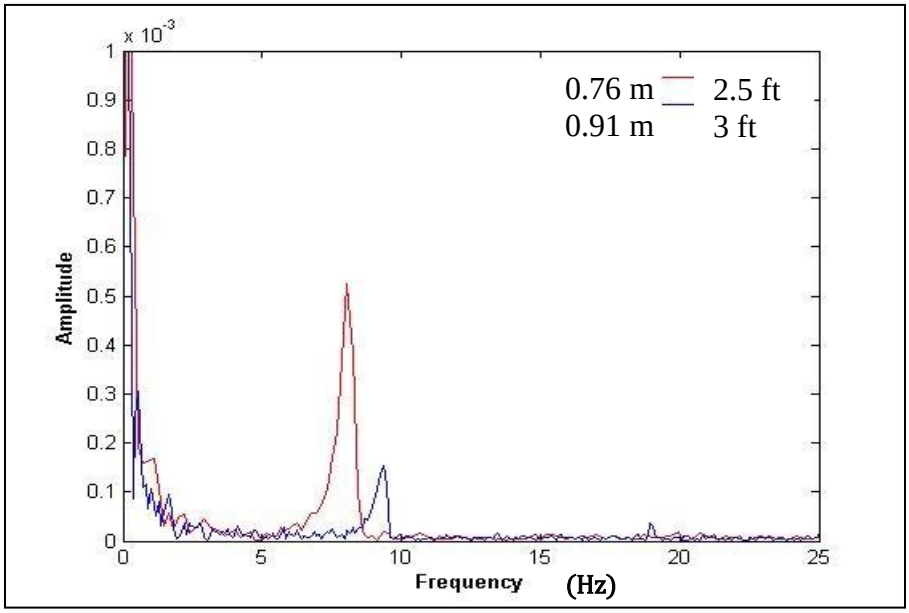

Figure 9-3. Response of the Buried Slabs.

While the amplitude of each response can be neglected because the slabs were not hit with the same force, the results were as expected; the slab buried deeper had a higher frequency response. The laboratory calibration was deemed successful because of the expected results from the experiment explained. Because experiments in the controlled laboratory environment could not be expanded to be more complex further than what was described, the team moved the motion sensor calibration from the lab to bridges in the field for more experimentation.

FIELD CALIBRATION

The accelerometers used for the motion sensor approach of this project were attached to several different bridges in different formations to calibrate them for field use. An advantage of using accelerometers for unknown foundations is that they can be attached to a bridge pier quickly and nondestructively and are capable of measuring the acceleration in three directions and sending the data directly to a data logger. Data from these accelerometers was collected in different ways to determine the optimal approach for determining unknown bridge foundation depth.

Initially, three accelerometers were attached to the face of one side of a pier on the bridge over Kountze Bayou in Burleson County. The bridge is on 15.85 m (52 ft) precast concrete piles. Approximately 1.52 m (5 ft) of the pile is exposed above the ground surface, on which the accelerometers were evenly spaced vertically and placed in the middle horizontally. The locations of the three accelerometers used for this experiment are represented by each square in Figure 9-4.

Figure 9-4. Accelerometers on Kountze Bayou Bridge.

The pier was then impacted with a large rubber hammer on the side perpendicular to the accelerometers. When inspecting the data, it was noted that the force created by an impact hammer was not great enough to generate any significant data. The research team also recorded traffic data as it drove over the bridge. While several trucks drove over the bridge, the vibrations of the pier were still not strong enough to yield measureable data. The intent of these data was to measure the vibration of the individual pier over a given length of time. From this, parameters such as

frequency, damping, vibration amplitude, and phase eigenmodes can be determined. Each accelerometer was attached to a signal conditioner and a computer with a FFT analyzer. The output for each impact of the pier is the excitation response of the pier measured at a constant frequency step. Unlike in the laboratory test, the influencing parameters of the bridge, like its size and additional components, made it too difficult to excite the pier to the level required for valuable results. The results of these tests showed no measurable data from which the depth of the foundation could be inferred. After the negative results from using the excitation response alone, a Time Domain Decomposition (TDD) was done in order to strengthen the weak signal that was not discernible in the frequency domain. After several attempts using a TDD, still no measureable results were found.

Another field test was conducted at the University Drive East bridge over Carter Creek. Three accelerometers were attached to the bridge bent, one in the direction of traffic along the bridge (x-direction), one perpendicular in the direction of the flow of the river (y-direction), and one in the vertical direction (z-direction). The acceleration of the bridge bent was measured in the three directions for 10 sec and 100 sec periods. Using the nearby traffic light to time when the measurements began, 11 different measurements were taken using the traffic. Within these data sets, were periods of light traffic, heavy traffic, traffic with a charter bus, and a four-axle truck alone. For each data set, a Hann window was applied to select the desired data within the set for optimal output. Figure 9-5 shows the acceleration of the bridge bent versus time in the three directions for the traffic with a bus.

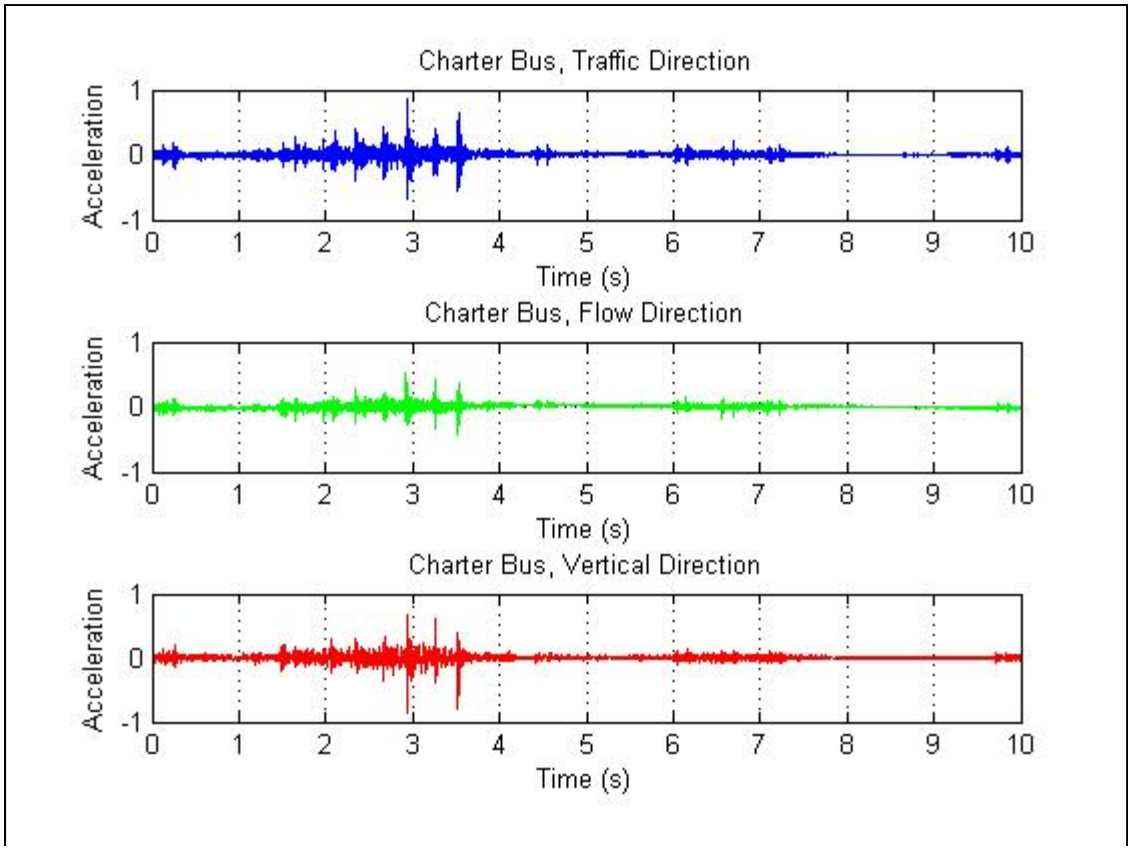

Figure 9-5. Acceleration of Bridge Bent with a Charter Bus.

When looking at these accelerations, the movement of the bent when heavy traffic passed over it can clearly be seen as the large peaks around 3 and 3.5 seconds. An FFT analysis was then applied to these data in all three directions. Figure 9-6 shows the results of the bus traffic in the frequency domain.

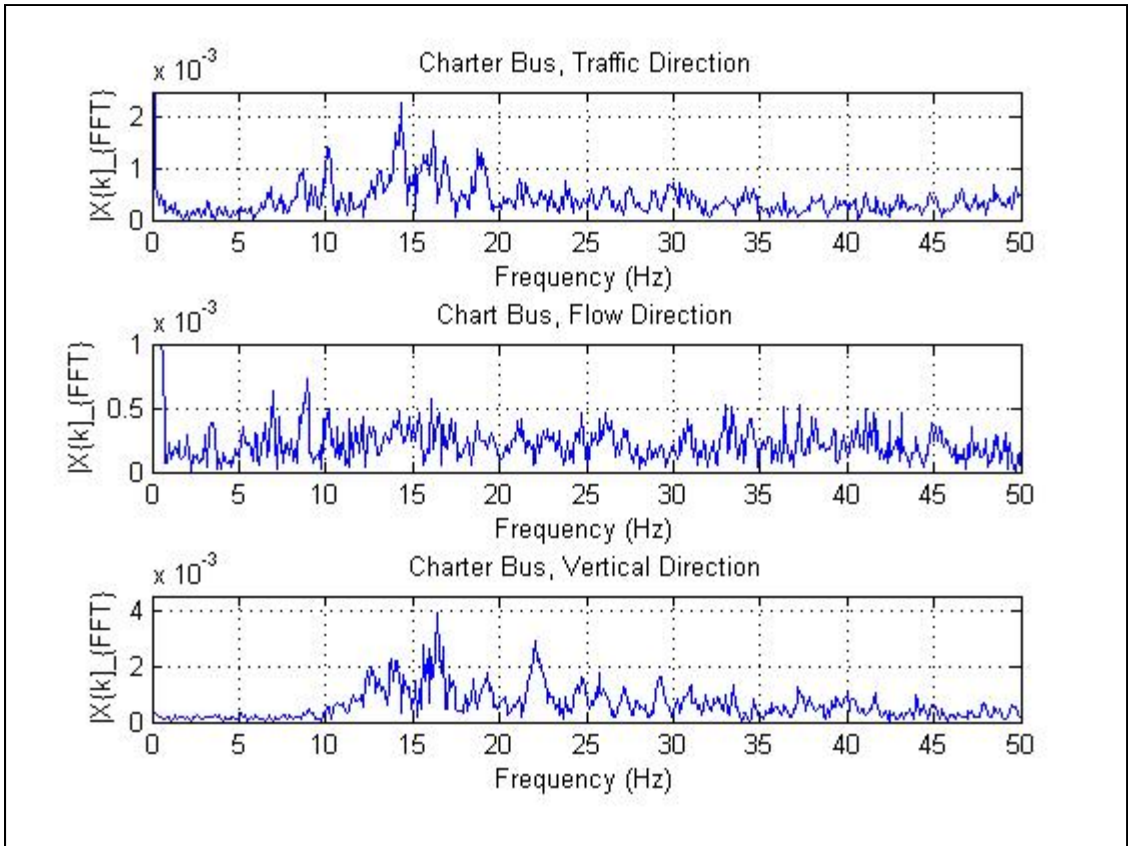

Figure 9-6. Frequency Domain of Bridge Bent with a Charter Bus.

Despite the clear peaks in acceleration, no apparent dominant frequency like what was seen in the laboratory test was noted in any of the three directions. As previously mentioned, one sample was collected when a four-axle truck drove over the bridge. This sample was taken for 100 seconds instead of 10. The increase in accelerations can be seen in Figure 9-7 in all three directions.

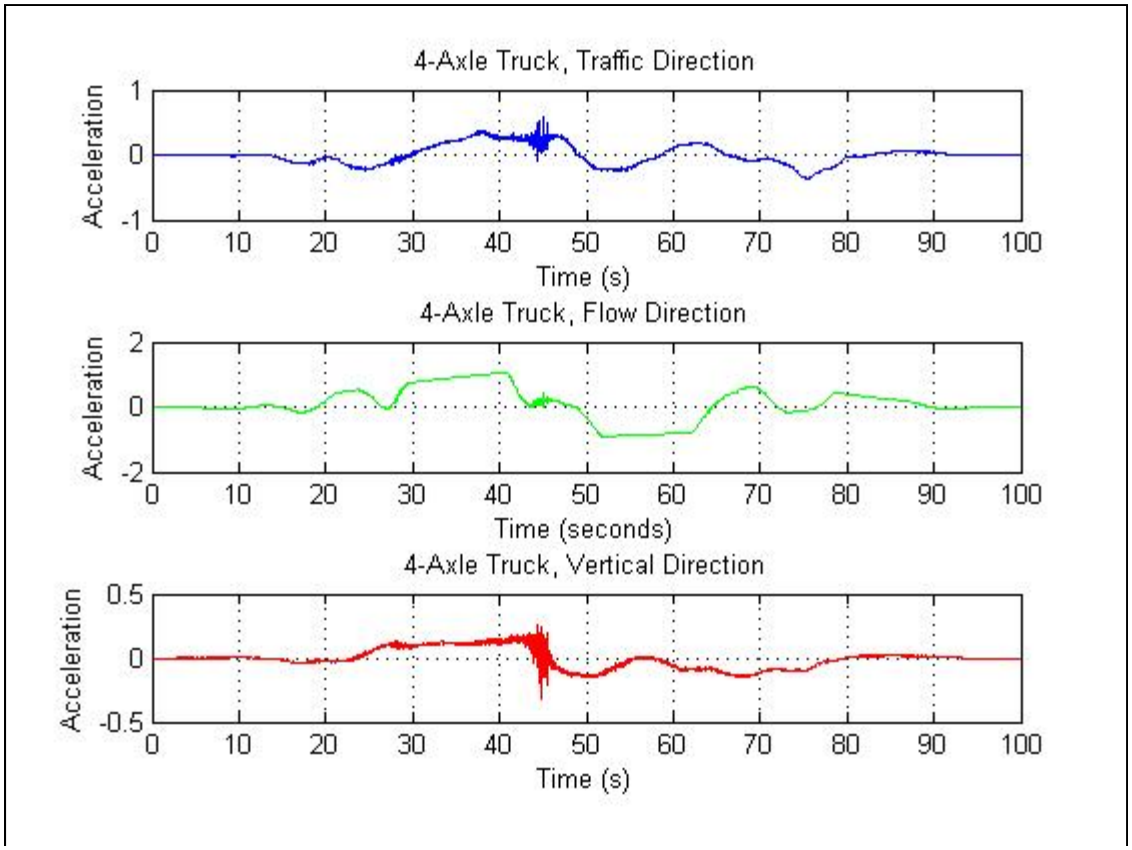

Figure 9-7. Acceleration of Bridge Bent with a Four-Axle Truck.

Again, despite the large jump in acceleration when the truck was over the bent, no dominant frequency was noted in the lower frequencies as expected for large structures. Also, the frequency domain is noisier for the longer 100 sample period than the 10 second sample, as illustrated in Figure 9-8.

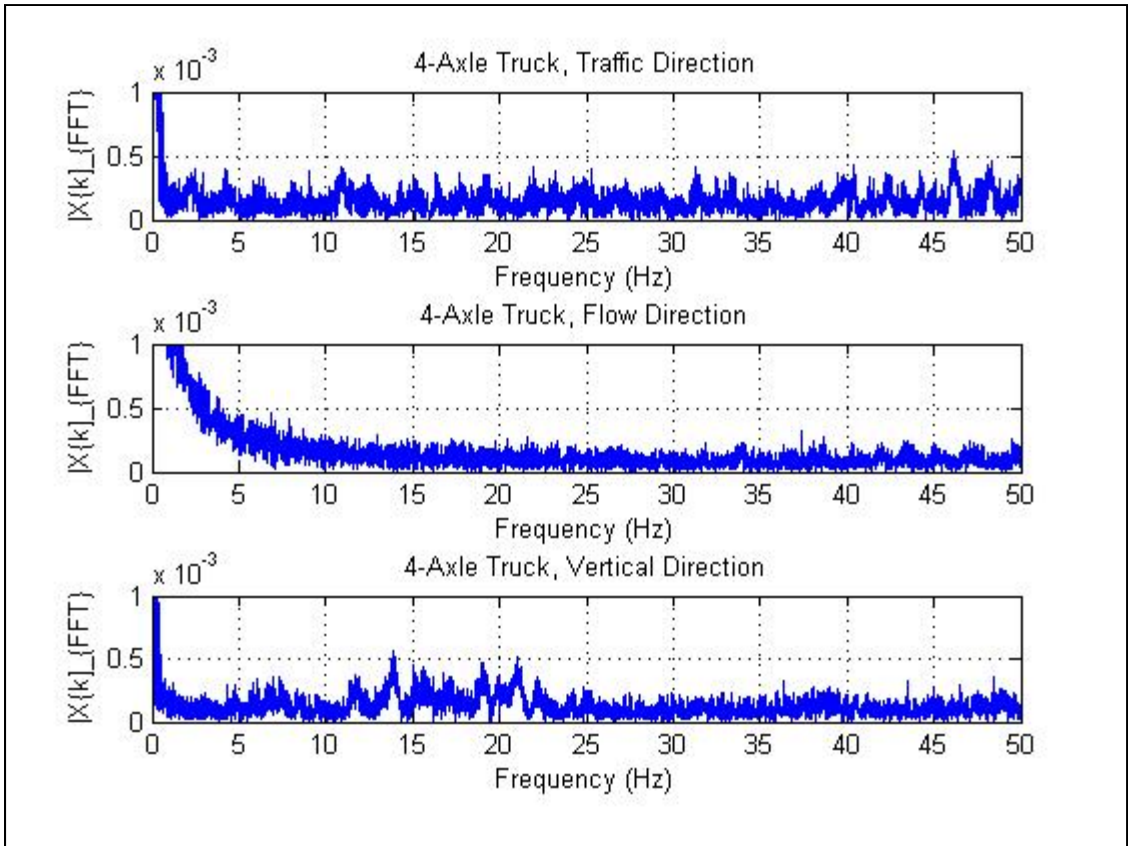

Figure 9-8. Frequency Domain of Bridge Bent with a Four-Axle Truck.

Despite the promising laboratory tests, which were conducted on buried reinforced concrete slabs, due to the difficulties of exciting the large structure with enough force to excite the bridge to the desired frequencies, it was decided that using accelerometers for determining the depth of unknown foundations of bridges was not feasible. The motion sensor team shifted their efforts to helping the resistivity imaging team using another technique, induced polarization.

NUMERICAL SIMULATION

During the field calibration, numerical simulations were also created to determine the feasibility of modeling the field work in order to decrease the time spent in the field. These models were created for a simultaneous project on bridge scour (Briaud et al. 2011). After verifying a numerical simulation could match the field data, more simulations could be created to model different foundation types, while monitoring and identifying various quantities of interest. Using numerical simulation, foundations with varying lengths were generated. Using these different cases, the effects of change in length on quantities of interest were studied. Also, the sensitivity of the

quantities of interest with variation in length could be identified, so a recommendation could be made for the most critical quantity. These parametric studies were used to establish the relationship between the foundation type and the monitored quantities. The change in natural frequency with foundation type was also investigated. A finite element (FE) model of a bridge was made from the drawings and details obtained from TxDOT. The material properties were obtained from both the drawings and were also evaluated at the site. The commercial finite element program LS-DYNA was used for the analysis (LSTC 2003), and the FE models considered in this project were generated by HyperMesh (Altair 2003).

Finite Element Model

Two FE models for a bridge on US 59 over the Guadalupe River were created. Figure 9-9 shows the bridge that was modeled.

Figure 9-9. US 59 over the Guadalupe River.

The first model, the simplified model, was made using the equivalent area and moment of inertia for the bridge. The bridge was modeled using one-dimensional beam elements, and the soil was modeled by a fully integrated quadratic eight-node element with nodal rotations. The second

model, the full scale model, was made using a fully integrated quadratic eight-node element with nodal rotations for the bridge as well as the soil.

Simplified Model

Figure 9-10 shows the simplified model of the bridge with a pile length of 10 m (30 ft). The soil and the concrete were considered elastic. The penalty method was used to model the contacts between the different elements. In this method, normal interface springs were placed between all penetrating nodes and the contact surfaces. The method is stable, does not excite mesh hourglassing, and is capable of handling contacts between dissimilar materials. The material properties were obtained by a combination of field testing and manufacturer specifications. Table 9-1 shows the material properties used.

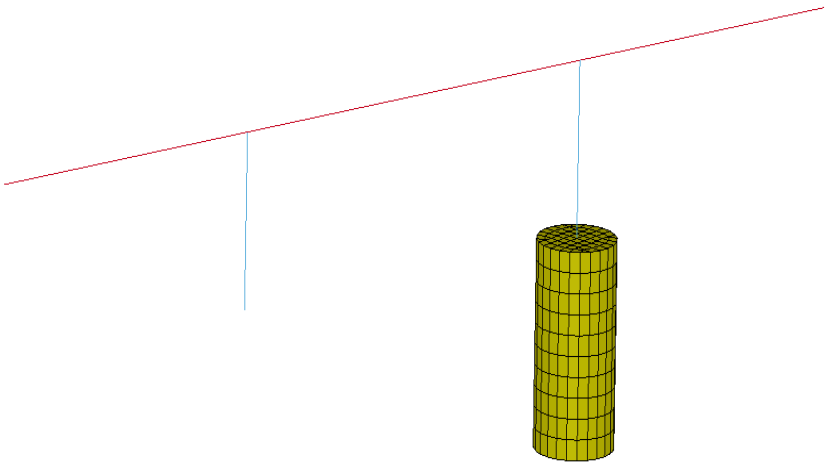

Figure 9-10. Simplified FE Model for Bridge with Full-Pile Length.

Table 9-1. Material Property of Concrete and Soil.

Material	Density ρ kg/m^3 (lb/ft^3)	Modulus of Elasticity E MPa (kips)	Poisson's ratio υ	Unconfined Compressive Strength MPa (kips)
Concrete	2500 (156)	27000 (3916)	0.2	30.0 (4.35)
Soil	1982 (123)	12.0 (1.74)	0.35	-

A parametric study was performed to study the response of the bridge when the depth of the foundation was changed. Two models with different foundation depths were simulated:

- Full pile length (10 m [30 ft]).
- Half pile length (5 m [15 ft]).

Figure 9-11 shows the simplified model with a pile length of 10 m (30 ft) without soil. Figure 9-12 shows the simplified model with a pile length of 5 m (15 ft) without soil.

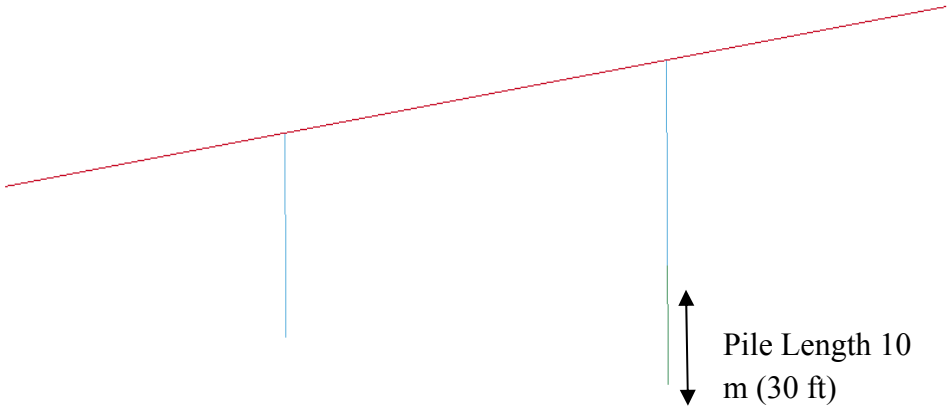

Figure 9-11. Simplified FE Model with Full-Pile Length (No Soil).

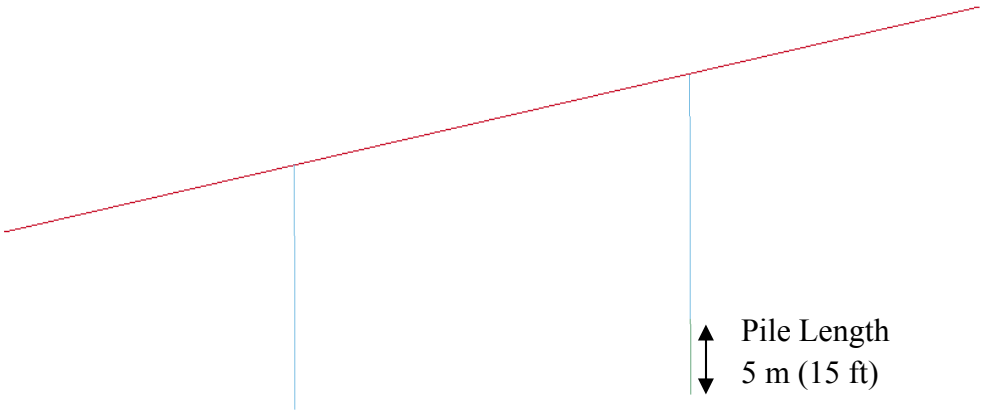

Figure 9-12. Simplified FE Model with Half-Pile Length (No Soil).

Table 9-2 shows the comparison of the natural frequency of the simplified bridge model. Two cases were compared; one with a full-pile length of 10 m (30 ft) and the other with half-pile length of 5 m (15 ft). The relevant modes were compared to study the variation with the change in pile length. The change in the frequency for the corresponding mode shapes was less than 5 percent. The bending mode of the pile in the traffic direction and the axial mode in the vertical direction show change, but the mode in flow direction remained unaffected.

Table 9-2. Comparison of Natural Frequency of Simplified Bridge.

Full Pile Length 10 m (30 ft)			Half Pile Length 5 m (15 ft)			Percentage Change (%)
Mode No.	Type	Frequency (Hz)	Mode No.	Type	Frequency (Hz)	
1	Bending (Flow)	3.691	1	Bending (Flow)	3.689	0.054
5	Bending of Pier (Traffic)	5.437	5	Bending of Pier (Traffic)	5.400	0.680
10	Bending (Flow)	8.051	11	Bending (Flow)	8.049	0.024
17	Vertical Pier	14.250	16	Vertical Pier	13.699	3.866

Full-Scale Model

The full-scale model used a 3D solid model for modeling the elements. The bridge was modeled by a fully integrated quadratic eight-node element with nodal rotations. The gravitational load was transferred using dynamic relaxation. The foundation was also modeled by a fully integrated quadratic eight-node element with nodal rotations. Mesh refinement achieves convergence, so hourglass energy was minimized.

Material Models

A rate-dependent material model was applied for all the materials due to the sensitivity of the material properties with loading rate. For this project, a continuous surface cap model, available in the software, was used to model the concrete. This model also takes into account the strain rate dependency of the concrete strength. The same material properties as the simple model were used for the full-scale model.

Contact Algorithm

The contact between the different parts was modeled using the Contact Automatic Surface To Surface algorithm. In tied contact types, the "slave nodes" are constrained to move with the "master surface." At the beginning of the simulation, the nearest master segment for each slave node was located based on an orthogonal projection of the slave node to the master segment. If the slave node was deemed close to the master segment based on established criteria, the slave node was moved to the master surface. This allowed for the initial geometry to be slightly altered without invoking any stresses. As the simulation progressed, the isoperimetric position of the slave node with respect to its master segment was held fixed using kinematic constraint equations.

Two cases with varying pile length were simulated similar to the simple model previously mentioned. Figure 9-13 shows the model of the full-scale bridge with the full-pile length of 10 m (30 ft) with soil. Mesh refinement was done to achieve convergence. Figure 9-14 shows the model of the full-scale bridge with full pile lengths and without soil.

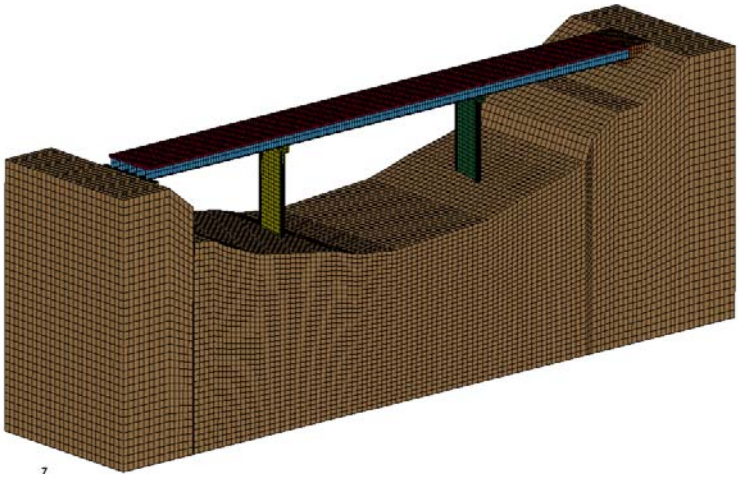

Figure 9-13. Full-Scale Model of Bridge with Soil.

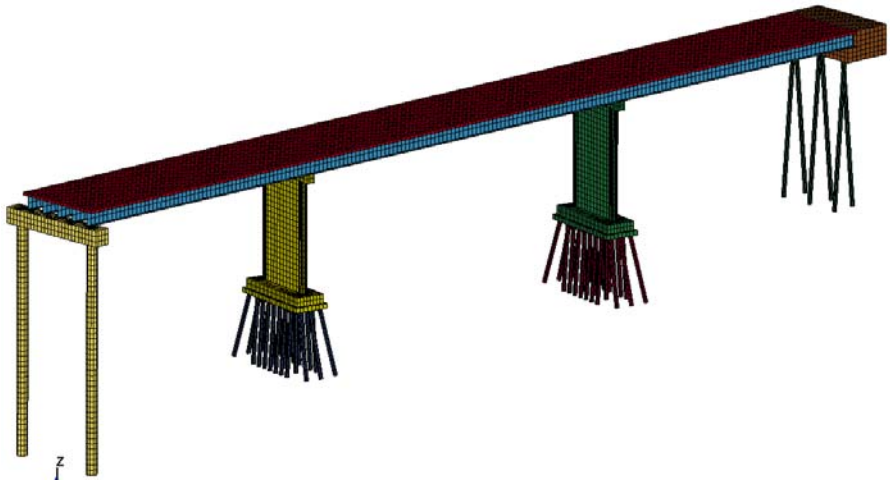

Figure 9-14. Full-Scale Model of Bridge without Soil (Full-Pile Length).

Figure 9-15 shows the model of the full scale bridge with half-pile length of 5 m (15 ft) and without soil.

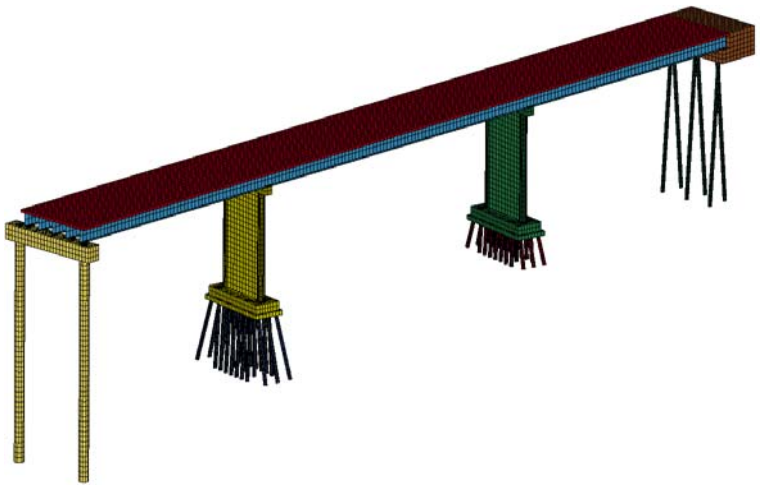

Figure 9-15. Full-Scale Model of Bridge without Soil (Half-Pile Length).

A parametric study was done to analyze the effect of variation of pile length on the natural frequency of the full scale bridge similar to the simplified model. For the parametric study of the variation of the response quantity with the pile length, two models were created. One was with a full pile length of 10 m (30 ft), and other is a half-pile length of 5 m (15 ft).

Figure 9-16 shows the mode shape of the full-scale bridge with full-pile length. The mode is in the flow direction. Figure 9-17 shows the corresponding mode shape of the full-scale bridge with the half-pile length.

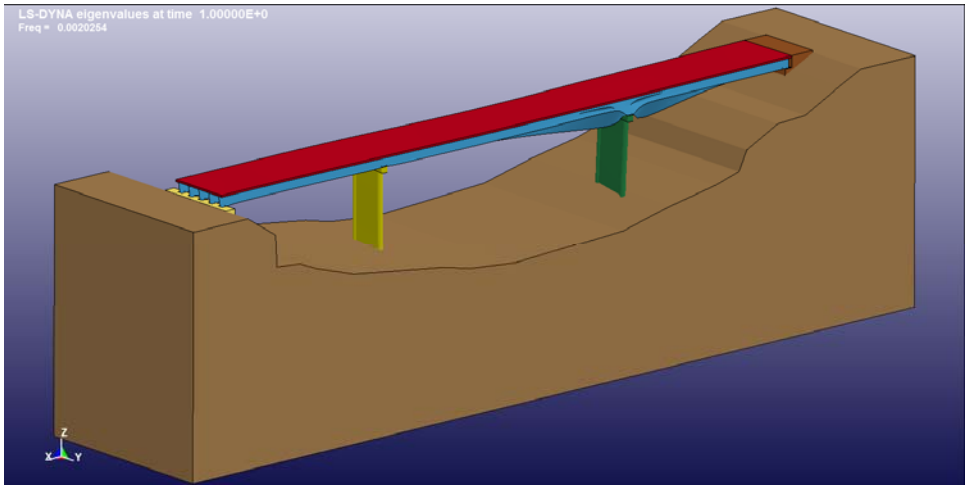

Figure 9-16. Mode Shape of the Full-Scale Bridge (Full-Pile Length).

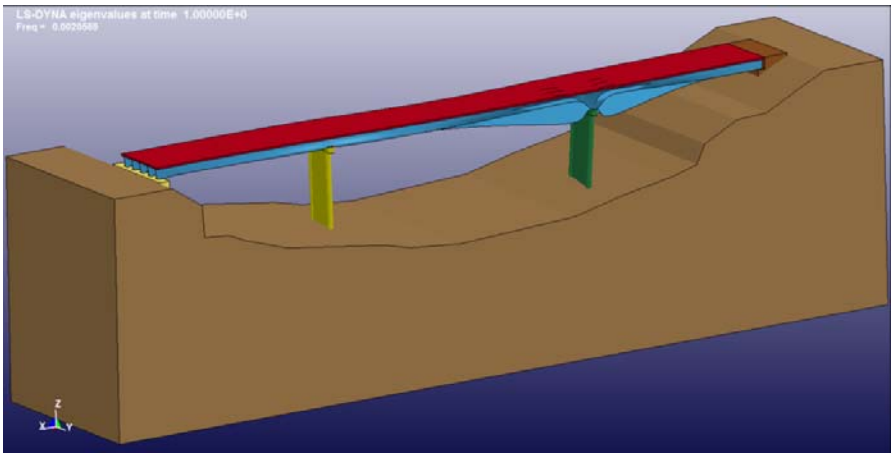

Figure 9-17. Mode Shape of the Full-Scale Bridge (Half-Pile Length).

Table 9-3 presents the comparison of the natural frequency of the full scale bridge in different modes. The modes one, two, and three, which are the bending modes of the pile in the flow direction, did not have a significant change. The fourth mode is the bending of the pile in the traffic direction.

Table 9-3. Comparison of Natural Frequency of Full-Scale Bridge.

Full Pile Length 10 m (30 ft)		Half Pile Length 5 m (15 ft)		Percentage Change (%)
Mode No.	Frequency (Hz)	Mode No.	Frequency (Hz)	
1	2.025	1	2.050	1.23
2	2.368	2	2.368	0.00
3	2.992	3	2.993	0.03
4	3.807	4	3.384	11.1

The fourth mode decreased by 11 percent, which is a significant change in the frequency for the mode in the traffic direction. The bridge was excited more in the traffic direction as compared to the flow direction. Note that the greatest change in the simplified model was in the axial vertical direction, and the second greatest change was in the traffic direction. However, it changed by only 0.68 percent.

Chapter 10.
ELECTRICAL METHODS BACKGROUND

INTRODUCTION

The basics of the electrical resistivity and IP methods, mainstays of near-surface applied geophysics for many decades, are reviewed in this chapter. The techniques have enjoyed resurgence in popularity since the mid-1990s, due to rapid and impressive advancements in data acquisition, forward modeling, and inversion capabilities.

INTRODUCTION TO THE RESISTIVITY METHOD

The fundamental steps involved in the resistivity method may be outlined as follows:

- An electric current I [amperes, A] is directly injected into the ground through a pair of electrodes, and the resulting voltage V [volts, V] is measured between a second pair of electrodes.
- The impedance $Z = V/I \left[V/A \right]$ of the Earth is the ratio of the voltage output at the potential electrodes to the current input at the current electrodes.
- The impedance is then transformed into an apparent resistivity ρ_a [ohm-meters, Ωm], which is an intuitively understood indicator of the underlying electrical resistivity structure $\rho(r)$ of the Earth. Different arrangements of the electrodes permit apparent resistivity to be determined at different depths and lateral positions. A map of the apparent resistivity plotted at these locations is termed a pseudosection (Loke 2000).
- The pseudosection is then inverted to obtain a 2D or 3D resistivity section $\rho(r)$ of the ground.
- Finally, a geological interpretation of the resistivity section is performed incorporating, as far as possible, prior knowledge based on outcrops, supporting geophysical or borehole data, and information gained from laboratory studies of the electrical resistivity of geological materials (see Table 10-1).

Table 10-1. Resistivity of Common Geological Materials.

Geomaterial	Resistivity [Ωm]
Clay	1−20
Sand, wet to moist	20–200
Shale	1–500
Porous limestone	$100–10^3$
Dense limestone	$10^3–10^6$
Metamorphic rocks	$50–10^6$
Igneous rocks	$10^2–10^6$

The electrical resistivity method has a long history in applied geophysics, including the pioneering work of Conrad Schlumberger of France in 1912. A few years prior to that, Swedish explorationists experimented with locating conductive bodies by moving around the potential electrode pair while keeping the current electrode pair in a fixed location (Dahlin 2001).

FUNDAMENTALS

The resistivity technique is founded on basic principles familiar to all scientists and engineers working in the physical sciences. Consider a cylindrical sample of material of length L [m], resistance R [Ω], and cross-sectional area A [m^2]. The resistivity ρ [Ωm] is a material property equal to $\rho = RA/L$. (See Figure 10-1.) The spatially variable resistivity $\rho(r)$ of the subsurface is the physical property that is sensed by the resistivity method. The reciprocal of the resistivity is the electrical conductivity $\sigma = 1/\rho$. Electrical conductivity is a measure of the ability of a material to sustain long-term electric current flow. Thus, electric current can flow readily in low-resistivity zones and is weak or absent in high-resistivity zones.

$$\rho = \frac{RA}{L} \ [\Omega m]$$

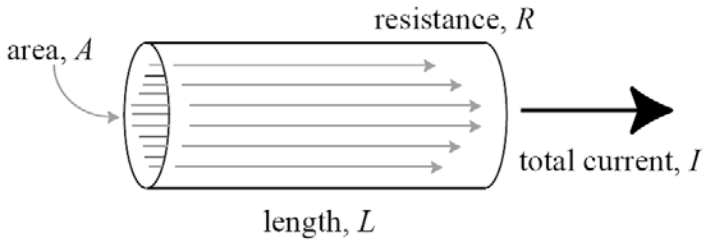

Figure 10-1. Definition of Resistivity, ρ.

Figure 10-2 shows a general exploration scenario, in which a battery is connected to two electrodes that serve as a current source/sink pair. The electric current streamlines, and equipotentials are displayed in the figure for a current injection of $I = 1\ A$ and uniform resistivity $\rho = 1 \Omega m$.

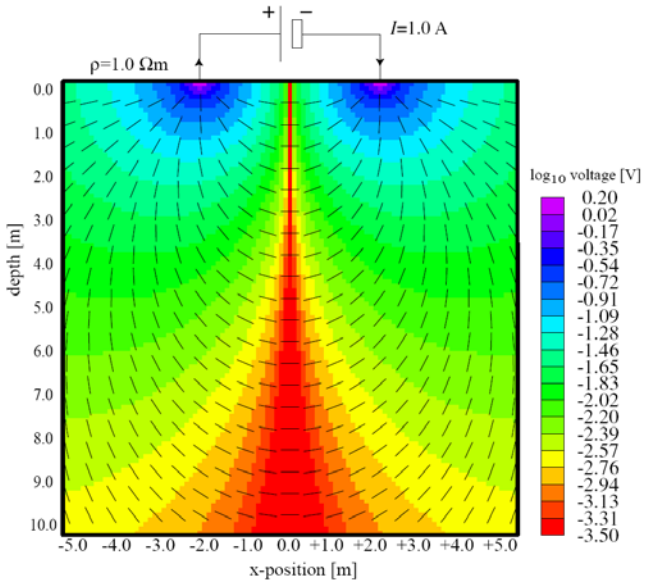

Figure 10-2. Potential and Streamlines of Electric Current for a Point Source and a Point Sink of Current.

The current density **J** is related to electric field **E** by Ohm's law $\mathbf{J} = \sigma\mathbf{E}$ so that

$$\mathbf{E} = \mathbf{J}/\sigma = \rho\mathbf{J} = \frac{I\rho\hat{\mathbf{r}}}{4\pi r^2} \qquad \text{(Eq. 10-1)}$$

Ohm's law for continuous media, as stated in Eq. 10-1, generalizes the familiar circuit law $V = IR$, where V is voltage, I is current, and R is resistance.

To better understand how the resistivity method is used to estimate Earth resistivity, consider an electric current I injected into a hypothetical whole-space of uniform resistivity ρ. Suppose the return electrode is placed at infinity. The situation is depicted in Figure 10-3. In the vicinity of the injection point, the current spreads out symmetrically in all three dimensions. At point P at distance *r* from the injection point, the current density **J** is given by

$$\mathbf{J} = \frac{I\hat{\mathbf{r}}}{4\pi r^2} \qquad \text{(Eq. 10-2)}$$

where $4\pi r^2$ is the area of a spherical surface of radius *r*. The numerator in Eq. 10-2 expresses the magnitude and direction of the current at point P, while the denominator expresses the cross-sectional area through which the current uniformly flows.

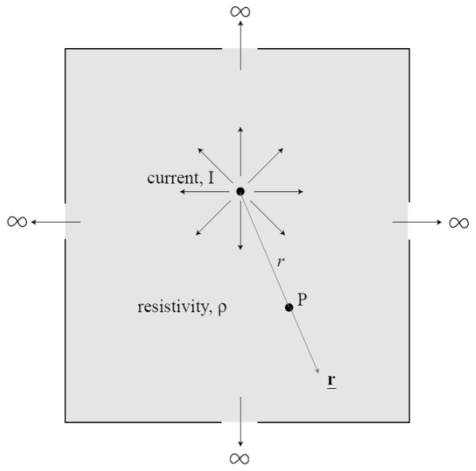

Figure 10-3. Current Injection into a Whole Space of Uniform Resistivity, ρ.

The voltage, *V,* measured at observation point *P* in Figure 10-3 is equal to the work done by a vector field, *F,* to move a test charge from infinity to point P. Work, *W,* is defined as the product of work and distance or more accurately in our case the line integral:

$$W = \int_C \mathbf{F} \cdot d\ \mathbf{s} \qquad \text{(Eq. 10-3)}$$

where C is any path from infinity terminating at point P. The force experienced by a test charge is proportional to the electric field **E**; hence, the voltage at P is defined as the integral

$$V = \int_r^\infty \mathbf{E} \cdot d\mathbf{r} = \int_r^\infty \frac{I\rho}{4\pi r^2} dr = \frac{I\rho}{4\pi r} \qquad \text{(Eq. 10-4)}$$

Now suppose that the injection point is located on the surface of a half-space representing the Earth, as shown in Figure 10-4.

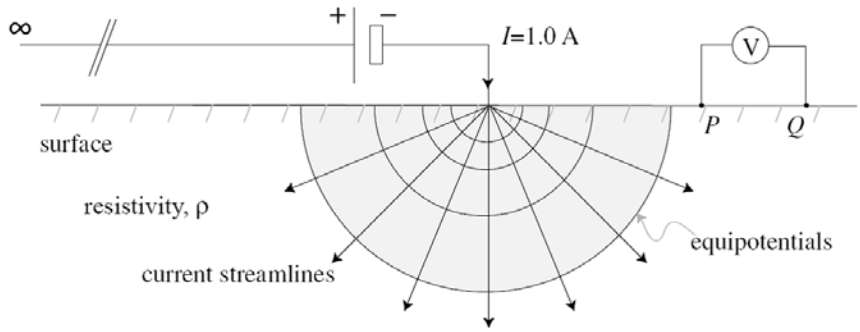

Figure 10-4. Voltage Measured between Points P and Q for a Point Source of Electric Current Injected into a Half Space of Uniform Resistivity, ρ.

The electric current, which cannot flow through the non-conducting air, flows radially outward through a hemisphere of radius r and surface area $2\pi r^2$. Hence, the current density in this case is $\mathbf{J} = \frac{I\hat{\mathbf{r}}}{2\pi r^2}$, so that, using Eq. 10-1 and Eq. 10-4, the voltage measured at point P is $V = \frac{I\rho}{2\pi r_P}$, where r_P is the distance from the current source to the potential electrode P. This is the basic equation of resistivity. The voltage measured across the terminals P and Q of the voltmeter is the difference

$$V_{PQ} = V_P - V_Q = \frac{I\rho}{2\pi}\left[\frac{1}{r_P} - \frac{1}{r_Q}\right] \qquad \text{(Eq. 10-5)}$$

where r_Q is the distance from the current source to the potential electrode Q.

Eq. 10-5 is derived under the assumption that the Earth has a uniform resistivity ρ. In reality, the resistivity distribution inside the Earth is heterogeneous. We therefore rearrange Eq. 10-5 to find an apparent resistivity ρ_a:

$$\rho_a = \frac{2\pi V}{I}\left[\frac{1}{r_P} - \frac{1}{r_Q}\right]^{-1} = \kappa Z \qquad \text{(Eq. 10-6)},$$

which is interpreted to be the resistivity that would have been measured if the Earth were, in fact, homogeneous. Notice that the apparent resistivity can be written as a product of the measured Earth impedance $Z = V/I$ and a geometric factor κ that depends only on the arrangement of the current and potential electrodes. In the configuration shown in Figure 10-4, which is known as a pole-dipole arrangement, the geometric factor is:

$$\kappa = 2\pi\left[\frac{1}{r_P} - \frac{1}{r_Q}\right]^{-1} \qquad \text{(Eq. 10-7)}$$

Although the pole-dipole arrangement has received attention from near-surface geophysicists, a more general exploration scenario is the arbitrary four-electrode configuration shown in Figure 10-5, which includes a point source and the return point sink of current. The geometric factor in this general case is $\kappa = 2\pi\left[\frac{1}{r_{AP}} - \frac{1}{r_{AQ}} - \frac{1}{r_{BP}} + \frac{1}{r_{BQ}}\right]^{-1}$.

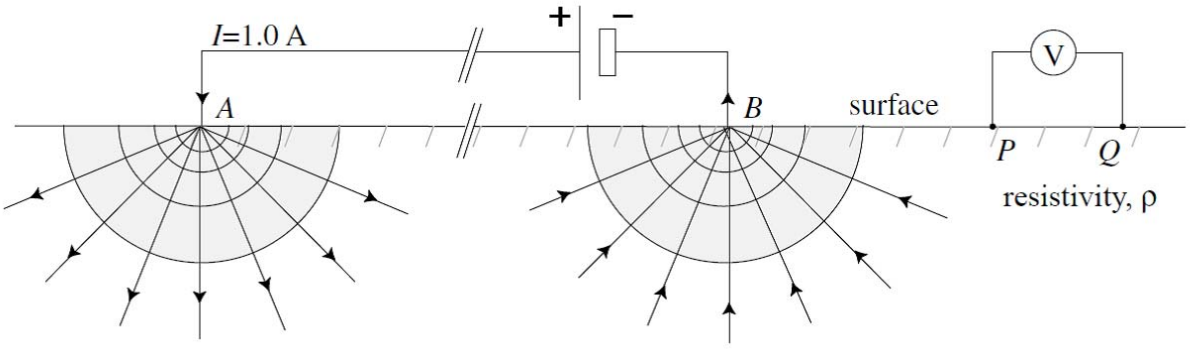

Figure 10-5. Voltage Measured between Points P and Q for a Point Source A and Point Sink B of Electric Current.

Historically, a number of four-electrode configurations have proven popular for a wide range of applications of geophysics. As we describe below, computer-controlled configurations of hundreds of electrodes are now in routine use (Loke 2000). Nevertheless, it remains worthwhile to briefly discuss a few of the traditional four-electrode configurations (Figure 10-6) in order to gain insight into the capabilities of the resistivity method and to explore the advantages and disadvantages of the various electrode configurations in terms of depth penetration, lateral resolution, ease of deployment, and signal-to-noise ratio. Zonge et al. (2005) gave a review of other popular electrode configurations.

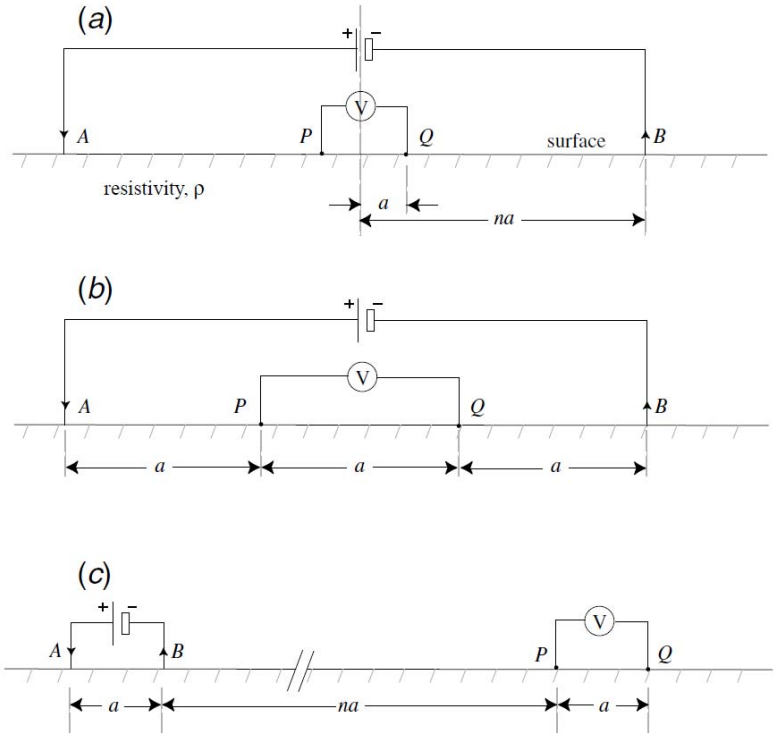

Figure 10-6. Traditional Four-Electrode Configurations: (a) Schlumberger; (b) Wenner; and (c) Dipole-Dipole.

The Schlumberger array (Figure 10-6a) is designed for sounding, that is, determining the Earth resistivity depth profile ρ (z) at a single location. The potential electrodes PQ are kept centered at a fixed location with constant separation 2a. The current electrodes AB are centered at the same location, but voltage readings are made as the separation between them is expanded about the AB midpoint. In this way, apparent resistivity is determined as a function of the current electrode separation. It is traditional to display Schlumberger array data as a graph of the form ρ_a (AB/2),

where AB/2 is half of the current electrode separation. The geometric factor for the Schlumberger array is:

$$\kappa = (n-1)(n+1)\pi a / 2 \qquad \text{(Eq. 10-8)}$$

A Schlumberger sounding can achieve excellent depth penetration with sufficiently large AB separations. However, the array has limited lateral resolution as it is designed for vertical sounding. The Schlumberger array is cumbersome in the field since its deployment requires lengthy wire connections that must be repositioned for each measurement. The signal-to-noise ratio is moderate to good. The voltage reading is taken in the middle of the array, which suggests that a good signal level should be achieved. However, as shown in Figure 10-2, voltages are generally low at the AB midpoint, at least over a uniformly resistive Earth.

The Wenner array (Figure 10-6b) is designed for lateral profiling to determine the Earth resistivity $\rho(x)$ at a roughly constant depth of penetration. There is a fixed separation, denoted a, between adjacent electrodes, with the potential electrodes PQ placed inside the current electrodes AB as in the Schlumberger array. Apparent resistivity is determined as the array is moved along a lateral profile. It is easy to see that the geometric factor for the Wenner array is:

$$\kappa = 2\pi a \qquad \text{(Eq. 10-9)}$$

The penetration depth of the Wenner array depends on the spacing a; the larger its value, the deeper the penetration. The Wenner array is quite effective at mapping lateral contrasts in resistivity within its fixed depth of penetration. The array is moderately easy to deploy as the trailing electrode can be leapfrogged to the front, as the configuration is advanced along the profile. This means that only one electrode movement is required per measurement. Signal-to-noise ratio is generally good since the potential electrodes PQ are located in the central part of the array and are relatively widely spaced compared to the current electrode separation AB.

The dipole-dipole configuration is shown in Figure 10-6c. The current electrodes AB and the potential electrodes PQ have the same spacing a, but the two pairs are widely separated by a distance, na, where $n>>1$. The geometric factor for the dipole–dipole array is:

$$\kappa = \pi n(n+1)(n+2)a \qquad \text{(Eq. 10-10)}$$

The dipole-dipole array offers many of the same advantages as Schlumberger depth sounding and Wenner lateral profiling. However, the signal-to-noise ratio deteriorates at large values of *n* and the voltage measurements across the electrodes PQ are susceptible to distortion by small-scale, near-surface heterogeneities.

RESISTIVITY PSEUDOSECTIONS

A convenient way to display multi-electrode resistivity data is by means of a resistivity pseudosection. As shown in Figure 10-7, the measured apparent resistivity ρ_a associated with a current electrode pair AB and a potential electrode pair PQ is plotted at the intersection of two lines, each making a 45° angle with the ground surface and passing through the center of one of the electrode pairs. This procedure is repeated for each pair of current and potential electrodes. The resulting pseudosection provides a very rough indication of the true earth resistivity since the maximum sensitivity to the ground structure of a given voltage measurement occurs at the midpoint of the four-electrode configuration at a depth of one-half the separation of the current-potential electrode pairs.

To provide an example of resistivity imaging, a data set was acquired using the multi-electrode Sting R8/IP system (www.agiusa.com) illustrated in Figure 10-8. The acquisition protocol involved a computer-controlled sequence of Schlumberger and dipole-dipole electrode configurations, as discussed in more detail below. The measured pseudosection is shown in the top panel of Figure 10-9. The large solid squares at the top of the pseudosection correspond to electrode locations while the smaller symbols that appear in the interior of the pseudosection mark the locations where the measured apparent resistivity is evaluated. The pseudosection is displayed by color contouring the apparent resistivity data. The trapezoidal shape of the pseudosection reflects the fact that the measured data are only minimally sensitive to ground structure in the two triangular regions beneath either the current or the potential electrodes.

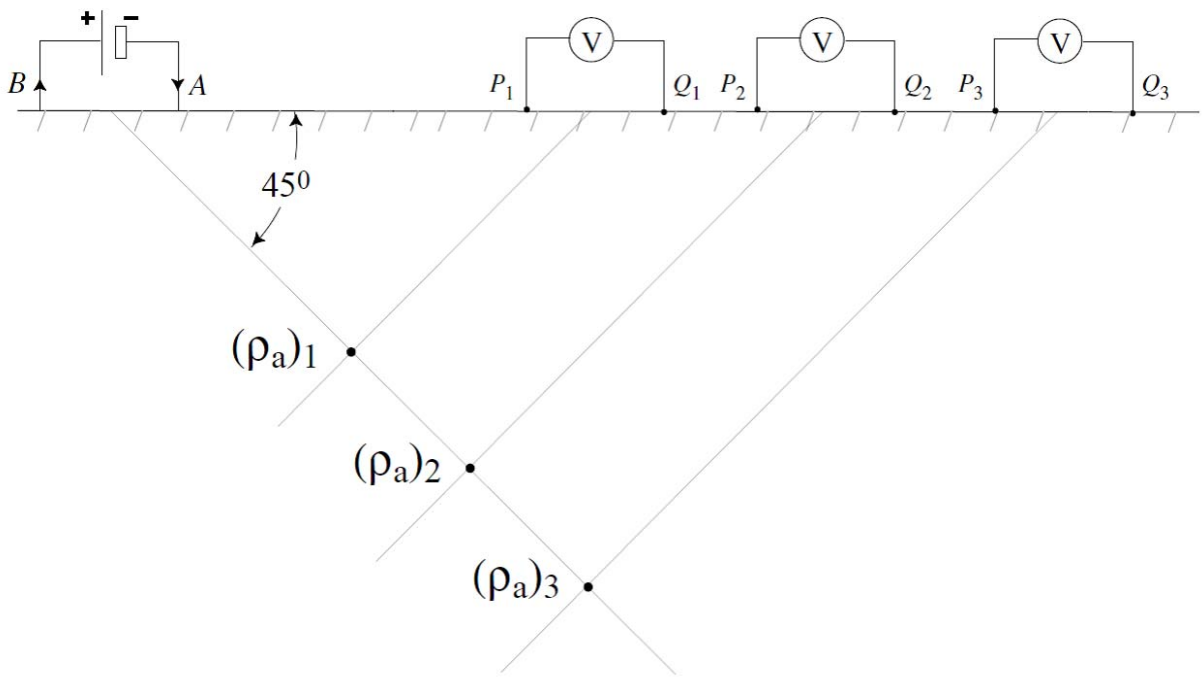

Figure 10-7. Construction of a Dipole-Dipole Resistivity Pseudosection.

Figure 10-8. (Left) Multi-electrode Resistivity System from Advanced Geosciences, Inc.; (Right) Close-up of an Electrode Installation.

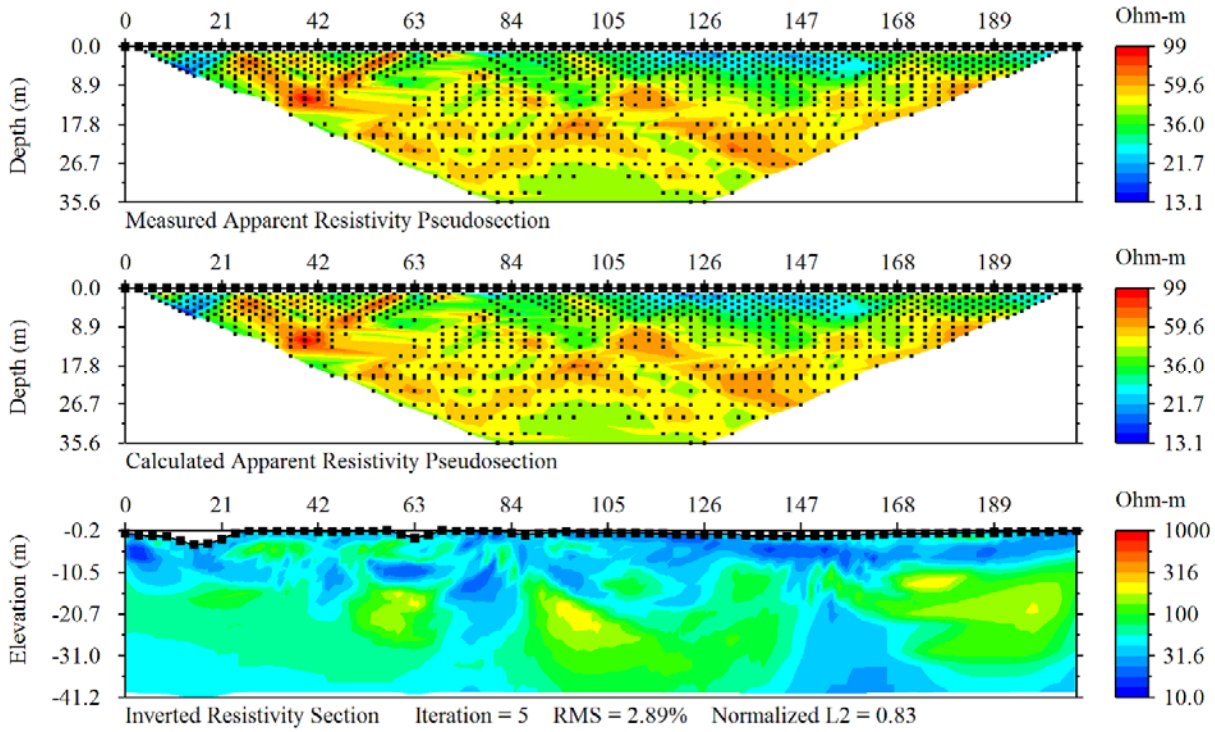

Figure 10-9. Measured Apparent Resistivity Pseudosection (Top) for a Hybrid Schlumberger-DD Electrode Configuration, along with the Inverted Resistivity Image (Bottom).

The Calculated Pseudosection (Middle) is Based on the Solving the Forward Problem for the Resistivity Structure Shown at the Bottom. Note the Good Match Between the Measured and Calculated Pseudosections.

ELECTRICAL RESISTIVITY TOMOGRAPHY (ERT)

Traditional electrical resistivity soundings use a conventional electrode configuration such as Schlumberger, Wenner, dipole-dipole, pole-dipole, or pole-pole. (See Figure 10-6.) A sounding, in which the electrode separation lengths are varied without moving the array midpoint, provides a local 1D electrical resistivity depth model, ρ (z). Alternatively, lateral profiling of ρ (x) over a narrow depth interval can be achieved by traversing the electrode array along a horizontal profile without changing the electrode separations. Neither the sounding nor the profiling method, however, provide an accurate indication of subsurface resistivity distribution in complex geological terrains.

Resistivity imaging of complex subsurface structures has recently been enabled with the development of multi-electrode acquisition systems and 2D and 3D inversions. The resistivity

technique for near-surface applications has surged in popularity due to these advances. Daily and Owen (1991) published pioneering work on electrical resistivity tomography (ERT) that considered a cross-borehole electrode configuration.

ERT imaging is performed by matching the measured apparent resistivity pseudosection to a computed pseudosection that is obtained by solving, for a given earth resistivity structure $\rho(r)$, the governing scaled-Laplace equation. The electric potential distribution $V(r)$ is evaluated at the locations of the electrodes and then transformed into a computed apparent resistivity. The model $\rho(r)$ is then adjusted and the apparent resistivity recomputed, ideally until it matches the measured apparent resistivity to within a predefined acceptable tolerance. The bottom two panels of Figure 10-9 show a resistivity image and its calculated apparent resistivity response. The spatial structure of the resistivity image, in this example, reflects variations in subsurface moisture content.

There is a possibility for interpretation errors to occur if ERT data are acquired on a sparse set of orthogonal 2D lines and then subjected to fully 3D modeling and inversion. Gharibi and Bentley (2000) recommend that, to avoid artifacts, the line spacing should be not more than two to four times the electrode spacing. Furthermore, the electrode spacing should not be greater than the dimensions of the smallest feature to be imaged.

MULTI-ELECTRODE SYSTEMS

The development of direct current resistivity techniques in the last decade has been rapid in both instrumentation and software (Dahlin 2001) and now includes systems comprising a large (>100) number of automatically switched electrodes. The multi-electrode techniques have tremendously improved investigation capabilities. Instead of making individual measurements at various spacings by repeatedly moving the equipment, the multi-electrode technique is now able to rapidly collect thousands of measurements with a stationary apparatus (Hiltunen and Roth 2003).

A 2D multi-electrode ERI survey is carried out using a string of electrodes connected to a multi-core cable. The electrode cable is divided into sections, which are connected end-to-end. Electrodes are inserted into the ground at specified intervals along a survey line. A resistivity meter and electronic switching unit are used to automatically select the combination of four

electrodes for each measurement (Loke 2000). Figure 10-10 shows an example of the electrode arrangement and measurement sequence for a 2D ERI survey.

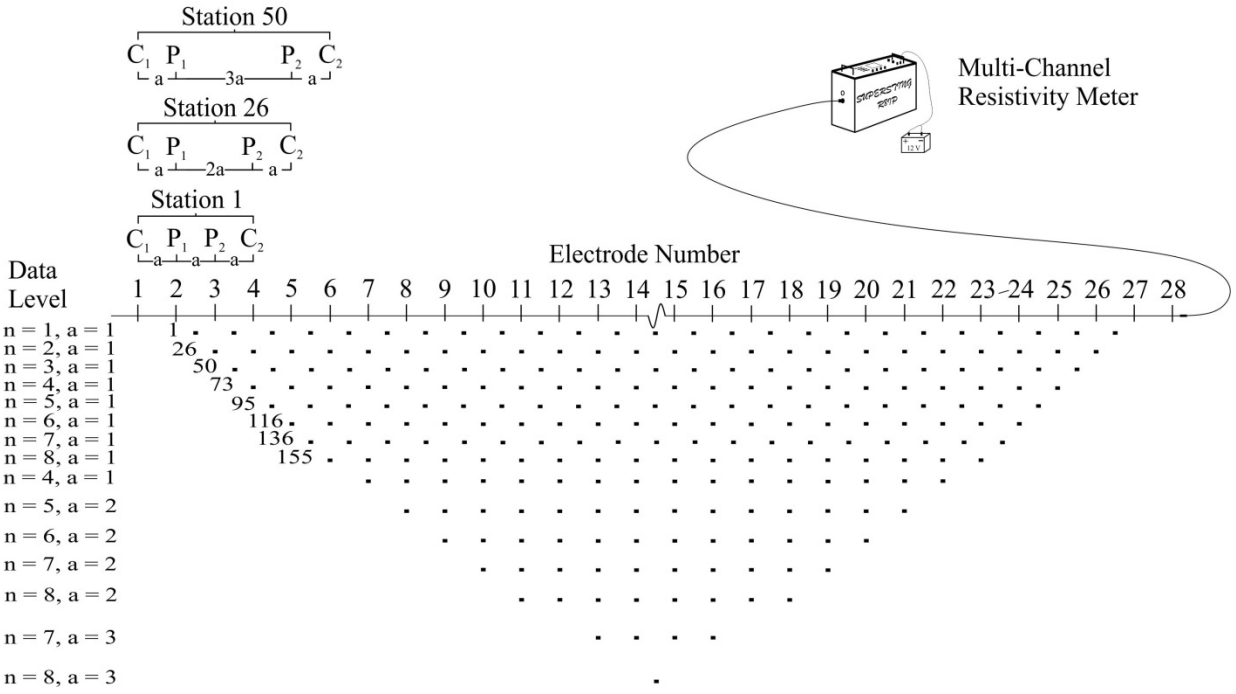

Figure 10-10. The Arrangement of Electrodes for a 2D Electrical Survey and the Sequence of Measurements Used to Build a Pseudo-Section (Loke 2000).

Often the survey line is longer than the available electrode spread. In such cases, after the original data have been acquired, the survey line can be extended or "rolled" by moving the first electrode cable section and electrodes to the end of the last cable. Data for each roll are then recorded and added to the previous data as one complete data file. This procedure is called the roll-along technique. Using this technique, a survey line in principle can be extended indefinitely (AGI (Advanced Geosciences 2006).

The resulting data set from a 2D ERI survey consists of various configurations of transmitting C1 and C2 and receiving P1 and P2 electrode pairs that comprise a mixed sounding and profiling of the subsurface section. The depth of investigation depends on the largest dipole separation during the survey but not on the total length of a survey line. The roll-along technique does not increase the depth of investigation. The actual depth of penetration also depends on the subsurface resistivity distribution (AGI (Advanced Geosciences 2006). In general, a larger

spacing (a) and larger value of n give relatively deep information about the subsurface structure, while a small spacing (a) and small (n) offer relatively good horizontal resolution for the shallower sections of the ground. The 2D electrical resistivity images obtained with the multi-electrode technique are generally used for studying shallow structures located a few tens of meters down to about 100 meters deep, whereas the traditional vertical electrical sounding technique mainly aims at determining the depths of horizontal 1D structures down to depths of several hundred meters.

3D ELECTRICAL RESISTIVITY SURVEYS

Since all geological structures are 3D in nature, a fully 3D ERI survey using a 3D interpretation model should give a more accurate and reliable picture of the subsurface (Loke 2000) than its 2D counterpart. One method of 3D electrical resistivity acquisition is combining data from 2D lines into a single data set for 3D inversion (Gharibi and Bentley 2000), (Samouëlian et al. 2005). However, the best 3D coverage is where current electrodes and potential measurements are made over a large range of azimuths and are not necessarily deployed along straight lines.

A popular quasi-3D surveying method is based on a rectangular acquisition grid. Figure 10-11 shows the electrode arrangement for such a survey using a multi-electrode system with 56 electrodes. The data set is collected with electrodes arranged in square or rectangular grids with constant electrode spacing in both x and y directions.

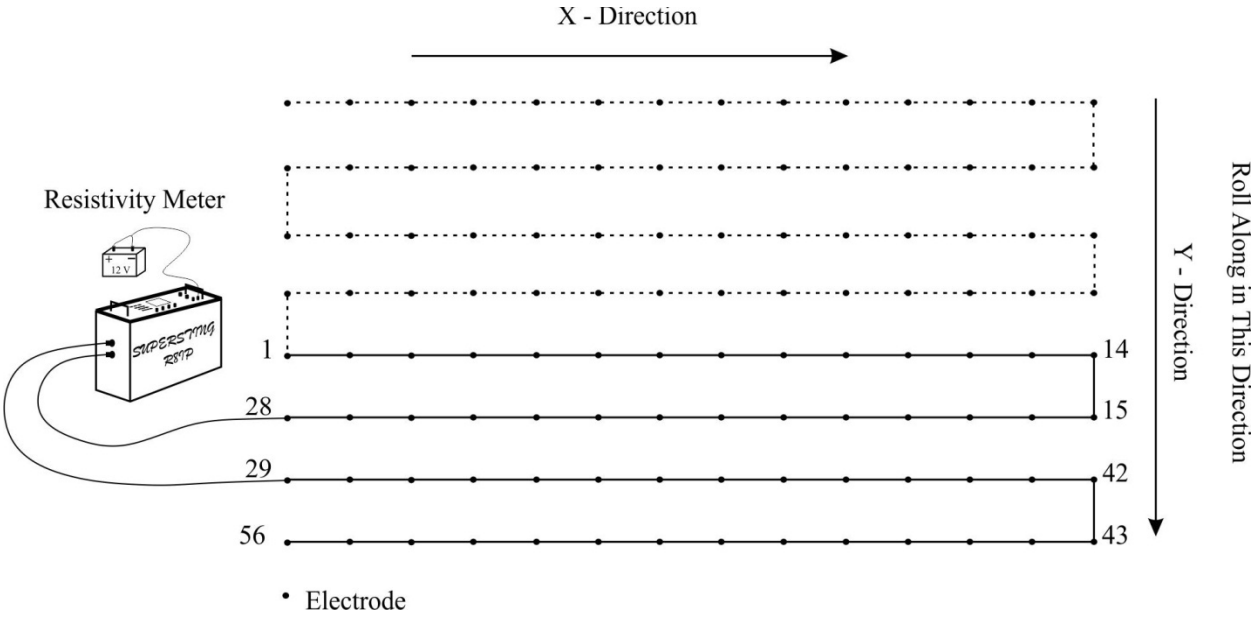

Figure 10-11. The Arrangement of 56 Electrodes and Roll-along Method for a Quasi-3D Survey with a Multi-electrode System (modified from Advanced Geosciences 2006).

UNDERWATER RESISTIVITY TECHNIQUES

The ERI method is widely used for ground surface surveys. Kim et al. (2002), Loke and Lane (2004), Kwon et al. (2005), Castilho and Maia (2008), and others have recently adapted this method for water-covered environments. The use of the electrical resistivity technique to image subsurface structures in water-covered areas is important due to frequent bridge and tunnel construction activities on and under riverbeds. However, it is difficult to image beneath a river bottom (Kwon et al. 2005). ERI carried out in underwater environments often has low signal levels compared to ground surface surveys due to the high resistivity contrast between the water and the earth (Chung et al. 2001).

There are several scenarios for resistivity surveys in water-covered areas:

- A mixed terrain/underwater environment, in which some of electrodes are deployed under the water surface while others are deployed on the ground surface. This configuration is used when the survey line crosses a creek or narrow stream.
- An underwater environment, in which all electrodes are deployed under the water surface on uneven bottom.

- A mobile survey with floating electrodes deployed on the water surface.
- A mobile survey with electrodes towed along the riverbed.

Figure 10-12 illustrates the various electrode scenarios for 2D ERI in water-covered environments.

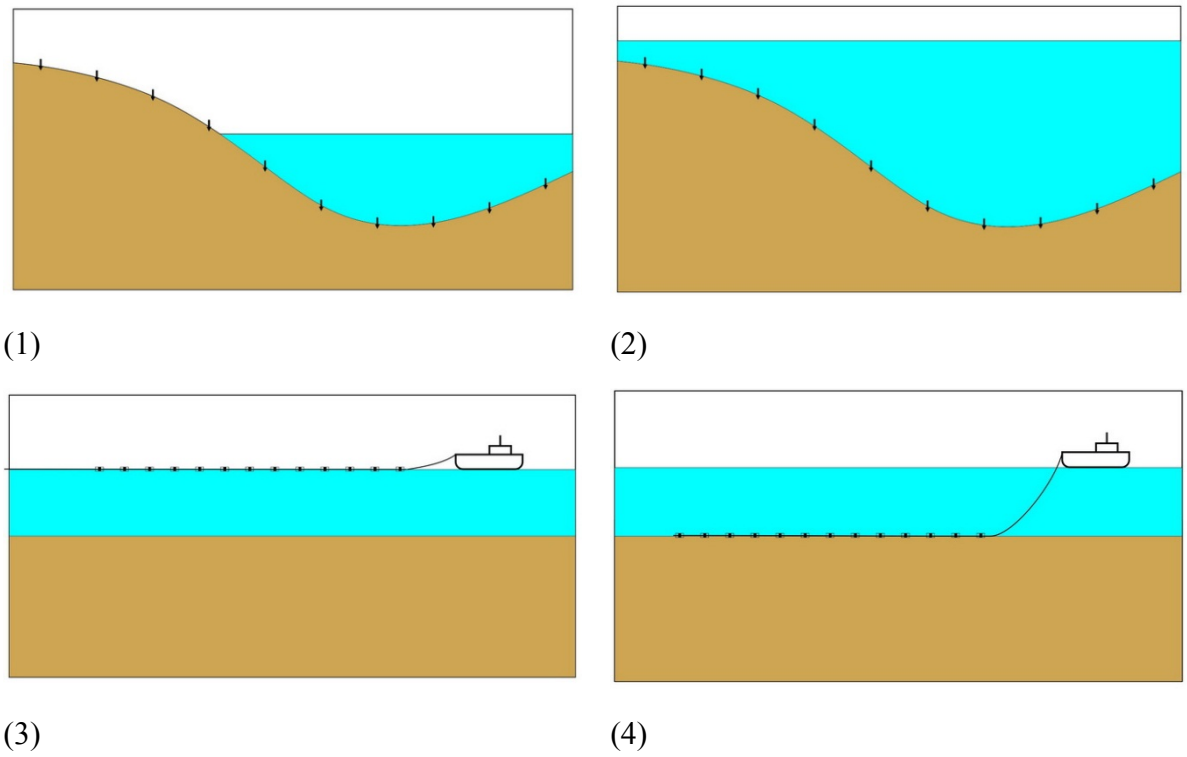

Figure 10-12. Scenarios for ERI Surveys of Water-Covered Areas.

Each type of electrode deployment has advantages and limitations depending on the local conditions (Castilho and Maia 2008). Direct contact of electrodes to the earth increases the current injected, and the resulting sensitivity to subsurface anomalies is much greater than with floating electrodes. However, it requires effort to install electrodes on the water bottom. In practical field surveys, the floating and towed electrode methods are sometimes convenient if a boat is readily available.

ELECTRICAL PROPERTIES OF ROCKS

In the shallow subsurface, the most important geological factor controlling the bulk electrical resistivity is the spatial distribution of pore-fluid electrolytes. The aqueous pore fluids may be contained in pores, fractures, or faults, with ions in the pore fluids being the predominant charge carriers. The solid matrix of grains is typically semi-conducting, with notable exceptions being metallic grains and the surface of certain clay minerals. The pore space in a rock is generally much more conductive than the solid grains owing to the presence of dissolved ions in the pore fluid solution.

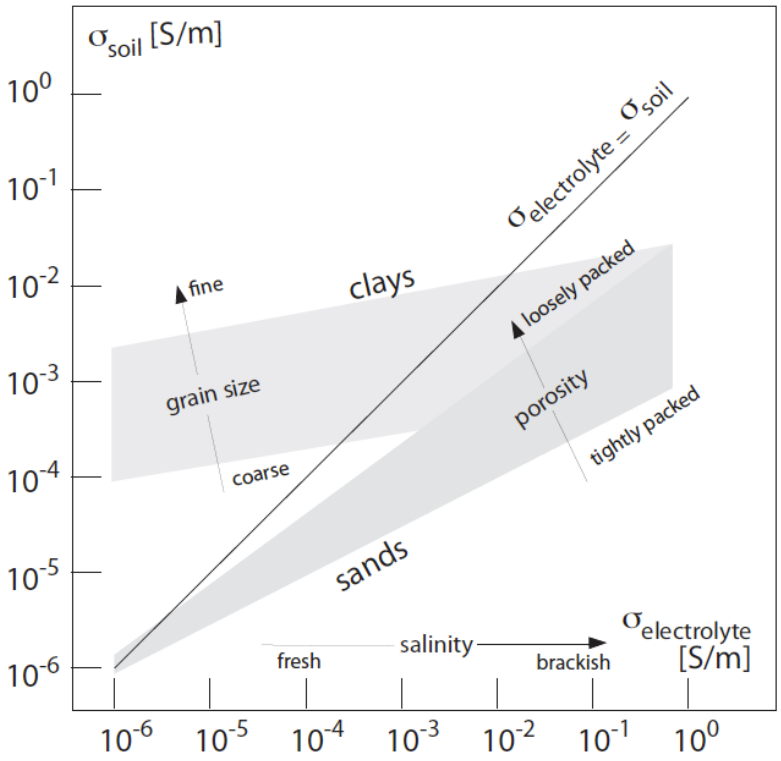

Figure 10-13. Electrical Conductivity of Saturated Soils, after Santamarina et al. (2005).

Electrolytic conductivity increases or equivalently resistivity decreases with increasing salinity, porosity ϕ, and temperature T. A high-salinity pore fluid has a greater concentration of ions available for conduction. A rock with high interconnected porosity often has an abundance of paths for conduction. Higher temperature enhances the mobility of ions. The variation of bulk

electrical conductivity, as a function of salinity for sand-dominated and clay-dominated saturated soils, is outlined in Figure 10-3.

In clean, unfractured sandstones characterized by water saturation S_W and porosity, ϕ, the traditional Archie's law (Archie 1942) gives the bulk electrical conductivity σ [siemens per meter, S/m] as:

$$\sigma = a\sigma_W S_W^n \phi^m \qquad \text{(Eq. 10-11)}$$

Petroleum geoscientists and, more recently, hydrogeophysicists have long used this empirically based relationship with saturation exponent n~2 to describe the bulk electrical conductivity σ of hydrocarbon reservoirs and aquifers. The parameter *m*, historically known as the cementation exponent, depends on the grain shape and generally lies within the range m~1.2–2.2 for sandstones (Worthington 1993). The leading coefficient *a* can vary widely depending on the pore cementation, tortuosity, grain size and shape, fluid wetability, clay content, and numerous other factors.

The quantity σ_W~0.3−1.0 S/m (Keller and Frischknecht 1966) in Eq. 10-11 is the electrical conductivity of the pore electrolyte, which is controlled by the salinity, or more generally, the total dissolved solids in the pore water. Commonly, an intrinsic formation factor $F=\sigma_W/\sigma$ for a fully water-saturated ($S_W=1$) rock unit is defined. Since pore fluids are electrically conductive relative to the solid rock matrix, we have $\sigma_W>\sigma$ and hence F>1. From Archie's law (Eq. 10-11) for a fully saturated rock, we see that the formation factor is related to porosity by $F\sim\phi^{-m}$.

Clay minerals originating from secondary diagenetic processes can coat the sand grains and clog the pore throats, reducing the porosity and permeability. A general rule of thumb is that high-porosity sandstones are clean while low-porosity sandstones are shaly. Clay minerals also have an inherent negative surface charge which contributes an additional electrical conduction pathway that is not found in clean sandstones. Thus, clay-bearing formations generally have a considerably higher bulk electrical conductivity than clean sandstones.

Carbonate rock units commonly exhibit secondary porosity, such as moldic vugs caused by anhydrite dissolution of fossil remains, which develop after the rock is formed. The secondary

porosity can carry a considerable fraction of the permeability. The bulk permeability depends strongly on whether the vugs are separate or touching each other. Furthermore, the range of intergranular textures found in carbonate rocks varies greatly from coarser grain-dominated to finer mud-dominated fabrics.

In carbonates, the relationship between electrical resistivity and porosity is quite complicated (Summers 2006). Archie's law has limited predictive value in carbonates, as the *m* value can vary widely and is difficult to ascertain for a given formation. Asquith (1995) has noted that large values of *m* are associated with higher separate-vug porosities, while a lower *m* value is associated with touching-vug porosity, such as fractures.

The resistivity of igneous and metamorphic rocks is greatly dependent on the degree of fracturing: as a rule, the more fractured a rock and the higher its water content, the higher the conductivity. Sedimentary rocks normally have lower-resistivity values compared to igneous and metamorphic rocks since they usually have more porosity and higher water content. There are many geological processes such as dissolution, faulting, shearing, columnar jointing, weathering, and hydrothermal alteration, which can alter a rock and significantly lower the resistivity of the rock.

Unconsolidated sediments generally have much lower resistivity values than consolidated rocks. The electrical resistivity of soils varies across a large range of values from 1 Ωm for saline soil to about 10^5 Ωm for dry soil. Electrical current in soils vary with the amount of water in the connected pores and on the quantity of dissolved salts (Samouëlian et al. 2005).

ELECTRICAL RESISTIVITY OF CONCRETE

The electrical resistivity of concrete is related to the microstructure of the cement matrix, the porosity, and the pore-size distribution. The mobility of ions in the pore solution plays an important role in determine bulk conductivity (Humkeler 1996). As concrete is manufactured, water becomes trapped in pores. When resistivity is measured, electric current is carried by the ions in the pore water. Moreover, the electrical resistivity of concrete has been used as an indirect index to evaluate the corrosion of embedded steel (Su et al. 2002). The electrical

resistivity of reinforced concrete may vary over a wide range from 10^1 to 10^5 Ωm, depending on degree of corrosion, the moisture content, and the material composition (Tuutti 1982).

Browne (1982) reports that concrete resistivity should be in the range of 500 to 1,000 Ωm to prevent corrosion of the reinforcement steel. Gonzalez et al. (1993) added that the corrosion rate is negligible when concrete resistivity is higher than 10,000 Ωm. Concrete structures with low risk of corrosion generally have high resistivity values whereas concrete structures with high risk of corrosion have lower resistivity values. The resistivity of concrete also increases as the concrete dries out (Polder 2001).

In an ERI survey, the presence of rebar in a concrete foundation can cause interference with the foundation resistivity determination, especially if the rebar are in direct contact with the ground. The concrete foundation in this case would have high bulk conductivity, and the resistivity contrast of the foundation with its surrounding materials might be small. If the geological materials surrounding a concrete foundation are high in resistivity relative to that of the concrete, an ERI inversion may not be able to distinguish between the concrete foundation and its surrounding materials (Conrad 2010).

INTRODUCTION IN THE IP METHOD

Consider the hypothetical situation shown in Figure 10-14 in which electrical charges are distributed unevenly within the subsurface. Charge accumulations are portrayed schematically in the figure as positive and negative "charge centers." The charges may be volumetrically distributed, or they may reside on mineral surfaces and other interfaces. In either case, the regions where charge is concentrated can be viewed as the spatially extended terminals of a kind of natural battery, or geobattery. The sketch shown in the figure greatly simplifies the realistic charge distributions that occur within actual geological formations, but it is instructive for the present purpose. Electrical energy supplied from an external source can maintain the "out-of-equilibrium" charge distributions shown in Figure 10-14. Without an energy input, they would rapidly neutralize in the presence of the conductive host medium, and the geobattery would soon discharge. The IP method of geophysical exploration is based on measurements normally made at the surface of the Earth of electric potentials that are associated with subsurface charge distributions.

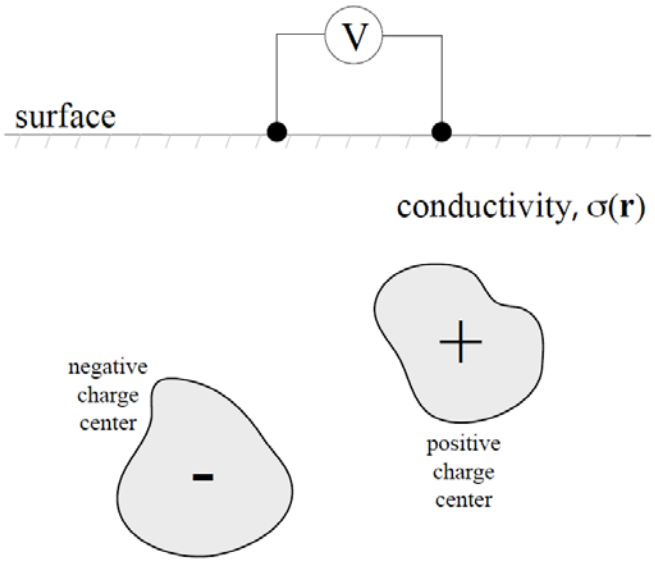

Figure 10-14. Generic Subsurface Charge Polarization.

Suppose a standard resistivity experiment is performed in which the current I is suddenly switched off at time t=0. The voltage across any pair of potential electrodes does not instantaneously drop to zero if the ground is polarizable. Rather, the voltage drops rapidly from its initial value V_0 to V_1 and thereafter decays slowly, often with a characteristic stretched exponential shape of the form $\sim t\exp\left(-at^{\beta}\right)$ with $0<\beta<1$, as shown in Figure 10-15. This transient behavior is known as the time-domain IP effect. Notice that the IP decay curve cannot simply be explained by an effective capacitance C in series with an effective resistance R in an equivalent RC circuit of the Earth. The discharge of such a capacitance after current switch off generates a transient voltage that decays purely exponentially as $\sim\exp\left(-t/RC\right)$ (Tipler 1982) not according to a stretched exponential law.

There are many ways to measure the time-domain IP effect in field studies, and a number of different expressions have appeared in the literature. Let $V(t_0)$ be the voltage measured at some fixed time t_0 after switch off. The polarizability, η, of the ground has been defined as:

$$\eta=\frac{V\left(t_0\right)}{V_0}\ [\text{mV/V}] \qquad \text{(Eq. 10-12)}$$

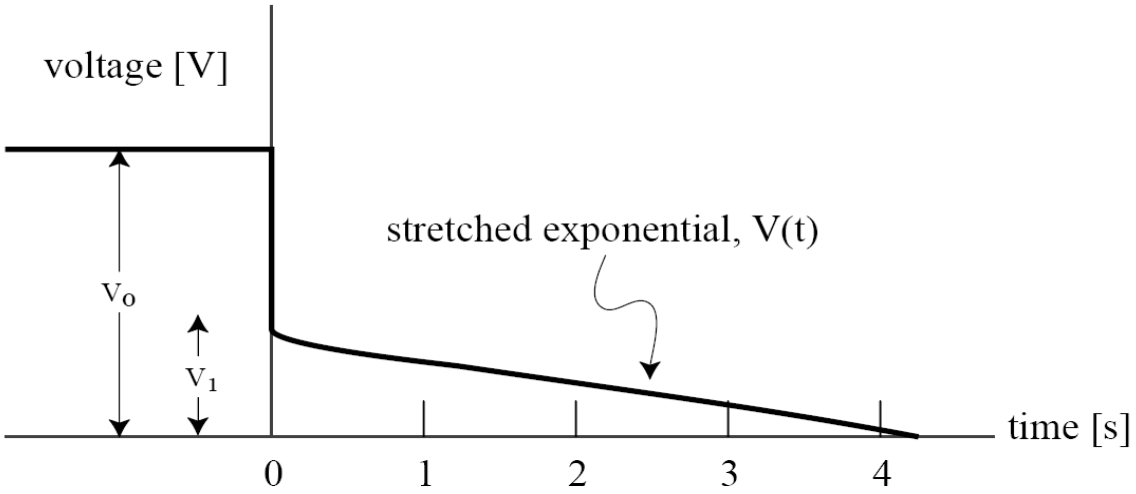

Figure 10-15. A Typical IP Decay Curve.

The partial chargeability M_{12} of the ground is its polarizability η averaged over a predefined time window $[t_1,t_2]$ during the stretched exponential decay:

$$M_{12} = \frac{1}{V_0}\int_{t_1}^{t_2} V(t)\mathrm{d}t \ \text{[ms]} \qquad \text{(Eq. 10-13)}$$

There is a considerable amount of inconsistency throughout the geophysical literature with respect to the exact definitions of η and M_{12}. Equations 10-12 and 10-13 are commonly used, but other definitions and nomenclature have been adopted by different authors.

NON-POLARIZING ELECTRODES

The difference in electric charge transport mechanism between the soil pore-fluid electrolyte and the metal electrodes staked into the ground results in an electrochemical impedance mismatch at the metal/electrolyte interface. If electric current passes in one direction between the soil and the electrode for an extended period of time, charge accumulates at the interface manifesting itself as an electrode polarization. The result is a spurious DC voltage. It is easy to misinterpret the spurious DC voltage as an apparent chargeability of the subsurface. The polarizability of a metal electrode depends on the type of metal employed, as shown in LaBrecque and Daily's (2008) study.

Non-polarizing electrodes reduce the electrochemical mismatch, and hence mitigate the spurious contribution to electrode polarization. Essentially, a non-polarizing electrode is one whose potential does not change upon the passage of an electric current (Bard and Faulkner 1980). Typical materials used in the fabrication of non-polarizing electrodes are $Pb/PbCl_2$ and $Cu/CuSO_4$. The metal electrode is enclosed within a porous medium or a hard gel that is infused with a solution containing a salt of the same metal. The salt solution buffers the transition from electronic conduction in the metal electrode to ionic conduction in the soil electrolyte. The non-polarizing electrodes used for this project contain a copper rod that is surrounded by $Cu/CuSO_4$ with a porous stone at the tip. Figure 10-16 shows the non-polarizing electrode and the core.

The potential of carefully made $Pb/PbCl_2$ non-polarizing electrodes, such as those described by Petiau (2000), remain stable over time frames lasting months to years.

Figure 10-16. Non-polarizing Electrode and Copper Core.

Chapter 11.
ELECTRICAL RESISTIVITY IMAGING

INTRODUCTION

In this chapter, the ERI field equipment is described, and data acquisition and imaging results from a number of bridges and test sites are reviewed. The experimental sites span a range of conditions, including both small and large foundations, both known and unknown foundations, and both land surface and mixed terrain/underwater environments.

EQUIPMENT

Resistivity imaging data were acquired with the AGI SuperSting^{TM} R8/IP multi-channel imaging system (www.agiusa.com). Voltages are measured simultaneously across eight pairs of potential electrodes for a single current injection, resulting in rapid data acquisition. Each of four cables is equipped with 14 electrode connection points, or takeouts, spaced at 2 m (6.56 ft) intervals. The 56 steel electrodes are 45 cm (17.72 in) in length and 1 cm (0.39 in) in diameter. Figure 11-1 shows the equipment and field setup.

The imaging system is powered by a 12-V deep-cycle battery. A rugged field laptop is used to upload command files and download the resulting data files. A tape measure is used to locate the positions of electrodes. A hammer is used for inserting electrodes into the ground. A total-station surveying instrument is used to measure site terrain variations to ~1 cm (0.39 in) accuracy.

Underwater electrode stakes were designed and built for the surveys conducted in water-covered areas. The upper half of each electrode is waterproofed by sealing inside a PVC pipe, leaving the lower half exposed. A wire is inserted into the PVC pipe and connected to the electrode. In this way, electrodes planted into a riverbed are electrically insulated from the water. A successful test of the underwater electrodes was conducted at a small lake at Texas A&M University's Riverside Campus.

Figure 11-1. (Upper Left) AGI SuperSting™ R8/IP Meter; (Upper Right) Electrodes Connected to the Cable Takeouts; (Lower Left) Underwater Electrodes; (Lower Right) Field Setup.

A command file is uploaded to the imaging system console prior to data acquisition. The command file prescribes the sequence of electrodes to be used for current injection and voltage measurements. An acquisition protocol is selected that provides the desired penetration depth and spatial coverage. The total number of measurements is reported to help the user ensure that the survey is completed within the allotted time.

The SuperSting imaging system automatically switches the various electrodes during acquisition. Electrodes are planted into the ground as firmly and deeply as possible to ensure good electrical contact. The electrodes are fastened to the cable takeouts via spring assemblies. The roll-along technique is used, as required, to extend the length of a survey profile by 14 electrodes at a time.

Once the field setup is complete, prior to data acquisition, coupling tests are conducted to check electrode contact resistances. These should be in the range 0.5−5 kΩ. Errors are reported if the system detects poor ground contacts or, alternatively, loose connections at the cable takeouts. If the

ground surface is highly resistive, salt water is added at the point of ground contact. During acquisition, repeat measurements are made and those with a variation greater than 5 percent are rejected as noise.

Mainly 2D electrical resistivity imaging (2D ERI) surveys are carried out in this study. The vertical extent of the subsurface targets, i.e., the bridge foundations, is of greater interest here than their horizontal extent. The dipole-dipole array is used since it is known to be sensitive to horizontal resistivity variations at depth (Loke 2010).

FORWARD MODELING

Forward modeling is employed to predict responses from typical bridge foundations embedded in typical geological backgrounds. Accordingly, the subsurface resistivity structure is divided into two zones: the background geology and the concrete foundation embedded within the geology. Generally, bridge foundations rest upon firm, highly resistive bedrock while the earth material surrounding the columns is typically less resistive alluvium or soil.

A portable resistivity meter is used to estimate *in situ* soil resistivity. For example, at one test site it is found to be ~120 Ωm. The *in situ* resistivity of the concrete is more difficult to measure, so a wide range of values must be explored by forward modeling. Concrete foundations in good condition are expected to be highly resistive, whereas extensively corroded foundations should be much more conductive.

Forward modeling is used to explore the impact of concrete foundations on resistivity imaging. Bridge foundations are modeled here in 2D using various sizes and depths. In 3D they are modeled at 1×1 m^2 (3.28×3.28 ft^2) horizontal extent and 9 m (29.53 ft) depth (for deep foundations) and at either 3×3 or 5×3 m^2 (9.84×9.84 or 16.40×9.84 ft^2) horizontal extent and 5 m (16.40 ft) depth (for shallow foundations). The forward modeling assumes a homogeneous geological background of 116 Ωm.

3D-forward modeling is performed here using the RES3DMOD finite element code. A dipole-dipole inline configuration on land is specified with 1 m (3.28 ft) electrode spacing and 2 m (6.56 ft) line spacing. A single foundation of specified resistivity is placed at the center of the

electrode array, embedded within the homogeneous background. The electrodes are assumed to be laid out on flat ground surface.

The RES3DMOD program allows the user to examine the synthetic pseudo-section and to alter the resistivity model as desired. The computed apparent resistivity values are perturbed by 5 percent Gaussian noise to simulate realistic field conditions. After the calculation, 2D apparent resistivity profiles along the *x*-direction are extracted.

Synthetic apparent resistivity pseudo-sections, calculated directly in 2D or extracted from 3D calculations, are inverted using the RES2DINV blocky least-squares optimization code with the vertical resistivity variations preferentially weighted. The inverted resistivity section is termed a resistivity image. The validity of 2D imaging in an actual 3D environment is evaluated.

TEST SITES AND DATA ACQUISITION

Laboratory experiments and field ERI surveys were carried out between 2009 and 2011. Figure 11-2 shows the project flowchart. The bridges are located in Brazos and Burleson counties in Texas. The Bryan TxDOT District granted access to the bridges. Data were acquired in non-flood seasons when sites were easily accessible. Figure 11-3 shows maps of the five study areas.

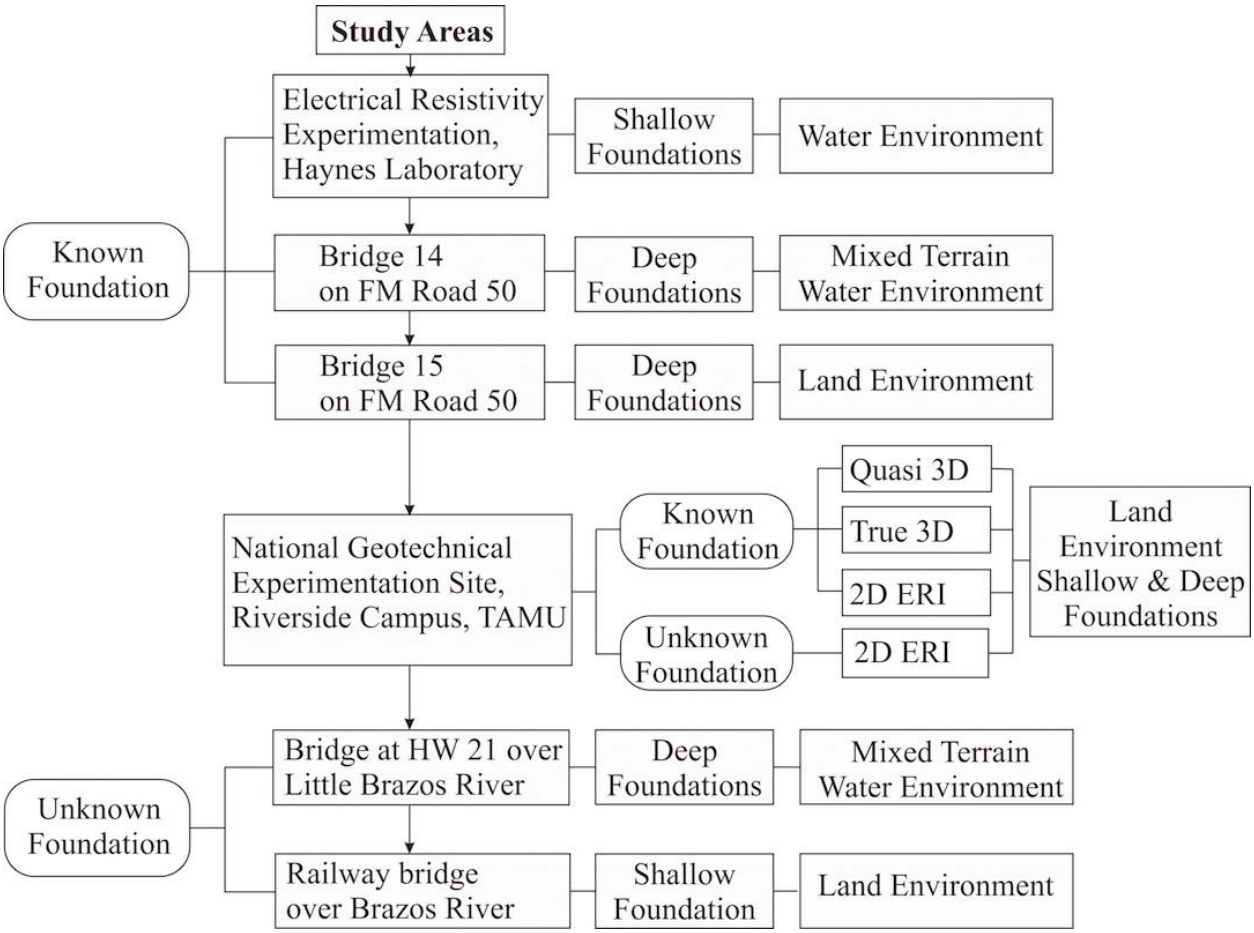

Figure 11-2. Flow of ERI Experimentation and Data Acquisition.

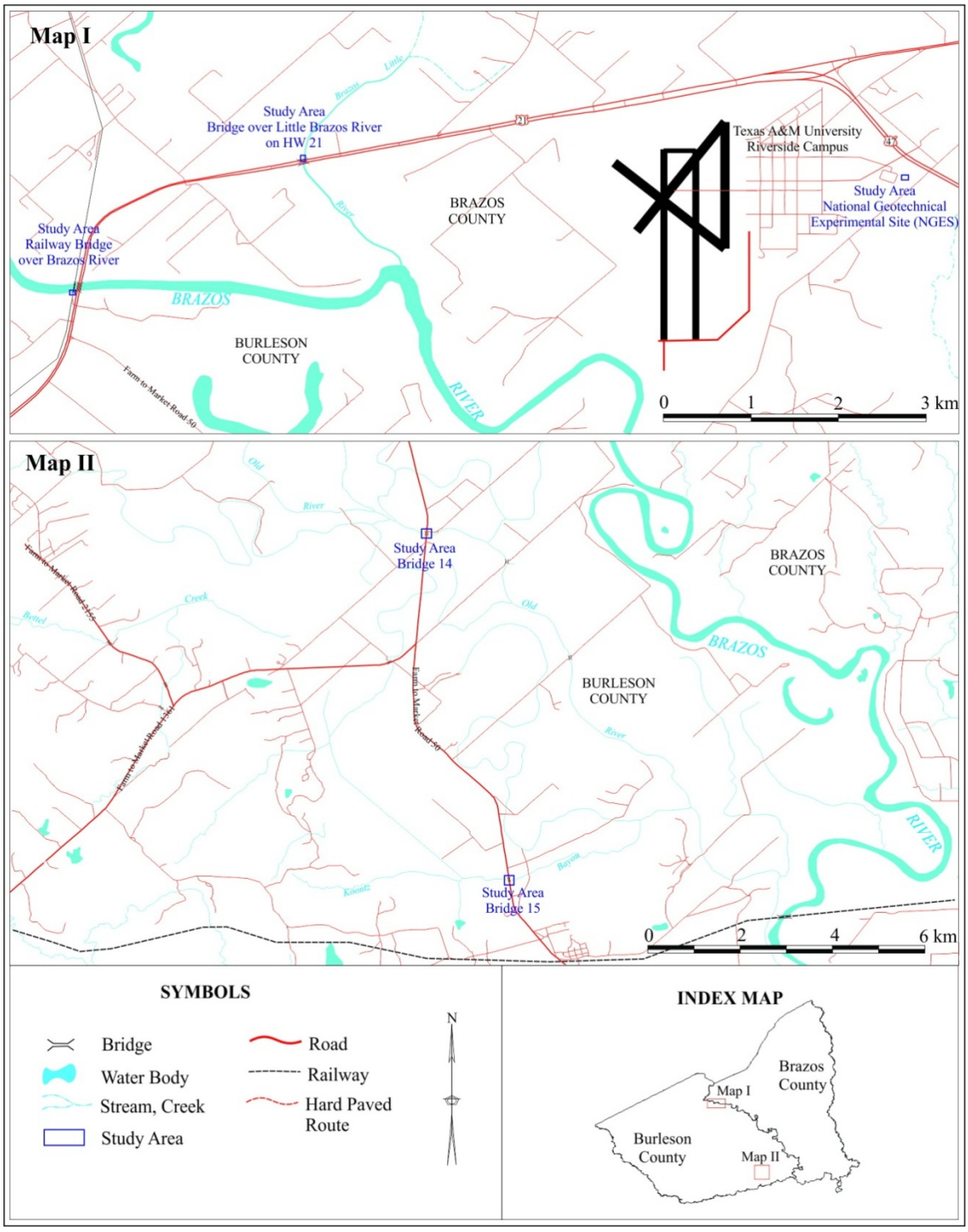

Figure 11-3. Locations of the Five ERI Study Areas.

Haynes Laboratory

Initial evaluation of ERI testing of concrete foundations using underwater electrodes was conducted at Haynes Coastal Engineering Laboratory on the Texas A&M campus. The electrical resistivity imaging system was evaluated in a water tank of length 45.72 m (150 ft), width 3.66 m (12 ft), and depth 3.35 m (11 ft).

In the first test, two concrete slabs were buried in sediment to 0.76 and 0.91 m (2.5 and 3 ft) depths below 0.3 m (1 ft) of water. Four underwater electrodes were deployed in the orientation shown in Figure 11-4, initially with 0.25 m (0.82 ft) spacing. Measurements were made for several values of electrode spacing.

Figure 11-4. Electrical Resistivity Experiments at the Haynes Laboratory.

Stable apparent resistivity values were successfully measured. While a large resistivity contrast exists between the foundations and the water-saturated sediment, the resistivity of the tank walls and floor is comparable to that of the foundations. The ERI testing was curtailed, however, since the tank walls and floor greatly distorted the measurements. A more useful field test of the underwater electrodes was conducted at a lake at the Riverside campus of Texas A&M University. Again, excellent stable readings of apparent resistivity were found. The experiments then shifted to actual bridge sites and the National Geotechnical Test site on the Texas A&M campus.

Bridge 14 on FM 50

Bridge 14 spans Old River on FM 50 in Burleson County, roughly 20 km southwest of College Station (see Figure 11-3.) The TxDOT layout shows concrete pile foundations of 0.39 m (1.28 ft) square cross-section and 10.1–15.8 m (10.1–51.84 ft) burial depth. At the time of survey, the river was ~6 m (19.69 ft) wide with maximum water depth ~1 m (3.28 ft). The area beneath the bridge is of moderate topographic relief with occasional boulder-sized concrete fragments. The soil lithology consists of reddish clay ~7.3 m (24 ft) thick underlain by clayey sand depth of 10.4 m (34.12 ft), below which lies coarse sand and gravel to 14.6 m (50 ft). Silty and clayey sand is present to 21 m (68.90 ft), the bottom of the hole. Visual inspection of the piles revealed the presence of exposed metal hooks, some in contact with the ground.

The site is a mixed terrain/underwater environment, as shown in Figure 11-5 and Figure 11-6. Profile BG14 consists of 56 electrodes spaced at 0.5 m (1.64 ft); it is aligned parallel to the roadway and centered on the river. Underwater electrodes were used as needed. ERI data were acquired November 30, 2009, on wet ground caused by overnight rain. Equipment setup time was ~1 hr with an additional 20 min for each of six roll-alongs. Data measurement time was 1.5 hr plus 45 min for each roll-along.

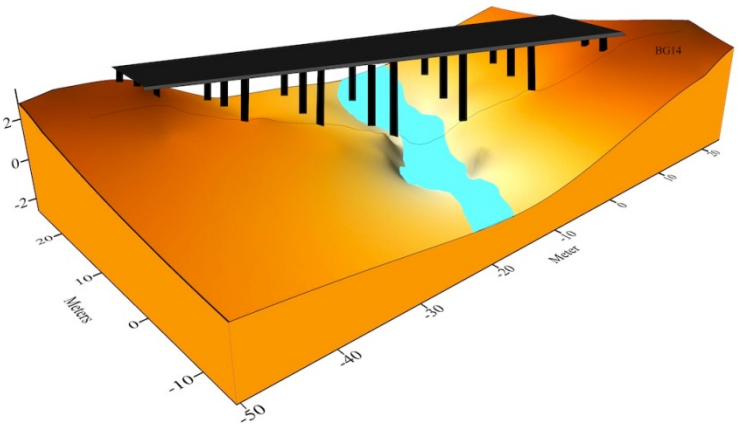

Figure 11-5. Bridge 14 Illustration Showing ERI Profile and Foundations.

Figure 11-6. Bridge 14 ERI Fieldwork.

Bridge 15 on FM 50

Bridge 15 spans Koontz Bayou Creek on FM 50 in Burleson County roughly 35 km (21.75 mi) southwest of College Station (Figure 11-3). The TxDOT layout shows the same concrete pile foundations as Bridge 14. The ERI surveys lie in the flooding area, but the water level was low at the time of the survey. The site has low relief with occasional concrete cobbles. The soil lithology consists of red and grey clay to 16.7 m (54.80 ft) depth underlain by gravel to 19.2 m (63 ft).

Initially, three ERI profiles of length 33.5 m (109.91 ft) shown in Figure 11-7 were run parallel to the river with 0.61 m (2 ft) electrode and 0.5 m (1.64 ft) line spacing. Profile B15A is closest to the row of concrete piles, and B15C is furthest. A second survey consisting of two profiles of length 55 m (180.45 ft) (BG15A and BG15B) was performed in roughly the same locations and orientation as the first survey, with 1 m (3.238 ft) electrode spacing and 1 m (3.28 ft) line spacing. Underwater electrodes were not required.

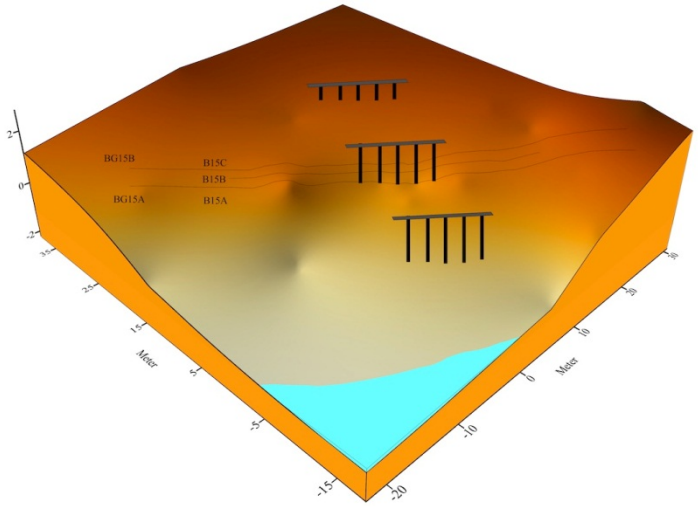

Figure 11-7. Bridge 15 Illustration Showing ERI Profiles and Foundations.

Figure 11-8. Bridge 15 ERI Fieldwork.

ERI data were acquired January 27, 2010, and January 29, 2010, on moist ground a few days after a rainfall event. Profile B15A, nearest the foundations, was expected to provide the best images of them. All profiles were expected to have similar geological background.

National Geotechnical Experimentation Site (NGES)

NGES, located on Texas A&M Riverside Campus ~16 km (9.94 mi) west of College Station (Figure 11-3), has been used for civil engineering research projects over the past 20 years. The site includes a number of groups of buried, steel-reinforced concrete structures such as spread footings and drilled shafts with square and cylindrical cross-sections. Metal and rebar debris is scattered over the site.

The unknown and known foundations at NGES are used here as proxies for actual bridge foundations since their depths are well documented, and the site is more accessible for testing geophysical methods than a river site. The terrain is a mix of undulated and flat due to previous excavations and earth shaping. The stratigraphy consists of fine silty sand to 3.6 m (11.81 ft) depth, underlain to 9.1 m (29.86 ft) depth by a layer of fine clean sand and further to 13.4 m (43.96 ft) by silty sand and clay seams. Below the sand lies clay to at least 33 m (108.27 ft) (Ballouz et al. 1991). Five known drilled shaft foundations constructed in December 1991 contain planned defects such as necking, bulbs, soft bottoms, mud cake, and cave-ins. Their dimensions range from 10.4−15.7 m (34.12−51.51 ft) in length and 0.8−1.1 m (2.62−3.61 ft) in diameter.

A group of five spread footings and five reaction shafts were built at NGES in December 1995 to test their stability in sand. One small, intact 0.9 m (2.95 ft) square footing proved suitable for resistivity experimentation; the others were unsuitable due to severe cracking. The intact footing is of known height 1.2 m (3.94 ft), embedded 0.76 m (2.49 ft) in the ground. There are three PVC pipes containing rebar embedded into this footing. Other drilled shafts and spread footings at NGES of unknown provenance are intact and appear to have been built after the previous group. They are categorized as unknown foundations. Two drilled shafts have 0.91 m (2.99 ft) and 0.3 m (0.98 ft) diameters while a spread footing is 3 × 3 m (9.84 × 9.84 ft) square. The locations of the drilled shafts (*circles*), the footings (*squares*), and the resistivity profiles (*lines*) of the quasi-3D geophysical survey are shown in Figure 11-9.

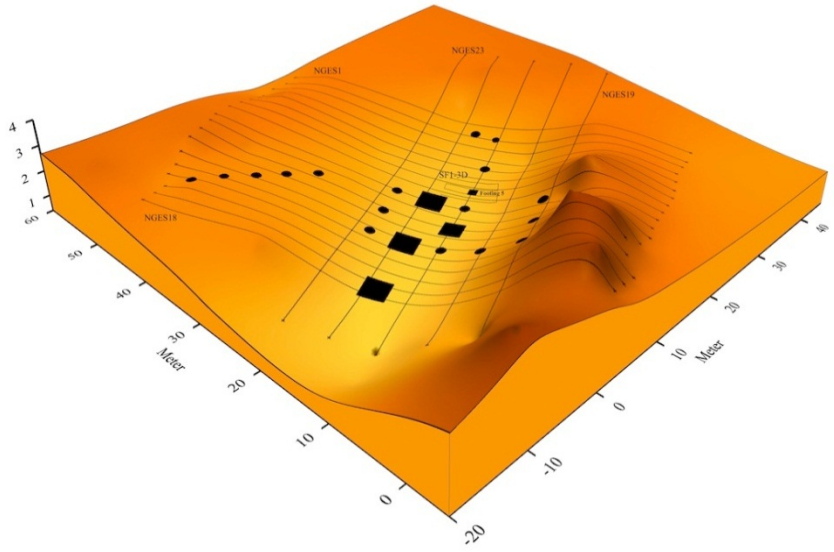

Figure 11-9. NGES Illustration Showing 3D ERI Profiles and Foundations.

Several ERI surveys with different objectives were performed at NGES. The first survey was conducted in two stages, May 24−28, 2010, and June 3−5, 2010, with the goal of exploring the full capabilities of quasi-3D resistivity imaging for evaluating concrete foundations. Data were acquired as a series of dipole-dipole profiles of length 55 m (180.45 ft) and electrode spacing 1 m (3.28 ft), including 18 E-W profiles (NGES1-18) spaced 2 m (6.56 ft) apart and crossed by 6 N-S profiles (NGES19-23) spaced 5 m (16.40 ft) apart. Reciprocal measurements were made on all survey profiles. Electrodes intersecting concrete were covered in wet clay to ensure good electrical coupling.

A fully 3D ERI survey was conducted on February 25, 2011, over the shallow footing SF-5. Mixed arrays of dipole-dipole, Wenner, Schlumberger, equatorial, and dipole-dipole configurations were used to test advantages over conventional arrays. Profiles were laid out in a 14 × 4 m (45.93 × 13.12 ft) rectangular grid with 0.5 m (1.64 ft) electrode spacing and 1 m (3.28 ft) line spacing, as shown in Figure 11-10.

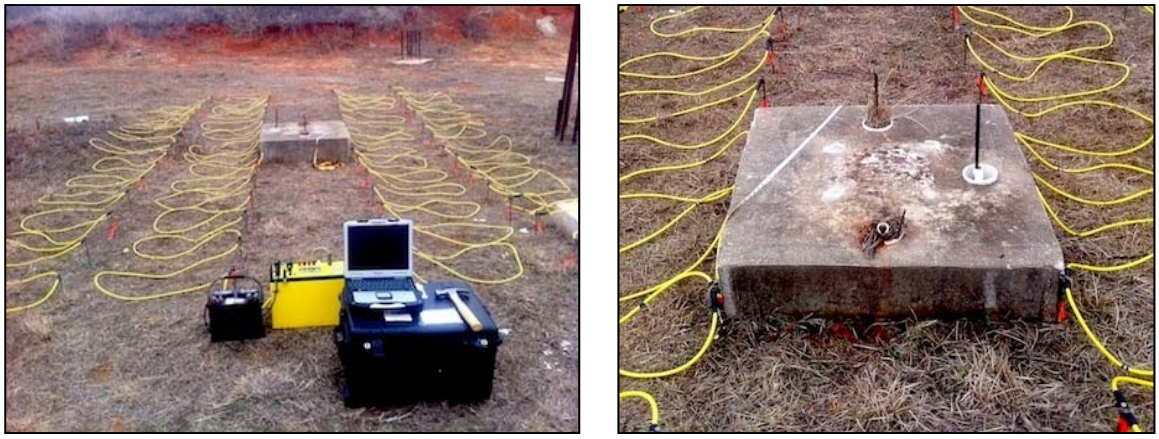

Figure 11-10. 3D ERI Layout at Footing SF-5.

A number of 2D ERI profiles employing 28 or 56 electrodes, at 1 m spacing, targeted individual foundations at NGES between December 10 and February 2011. Data were acquired directly over small foundations and alongside larger foundations in a "side-scanning" mode. The latter is preferred since it can be applied at actual bridge sites. Figure 11-11 shows the 3D survey profiles.

ERI data were acquired on six profiles over three known drilled-shaft foundations: three at TS2; two at TS4; and one at RS5. At drilled-shaft TS2, profile TS2A was conducted directly across the foundation while TS2B and TS2C were side-scanning (see Figure 11-12). Similarly, as shown in Figure 11-13, profiles TS4A and RS5A directly crossed the foundation while profile TS4B was side-scanning. Profiles SP1A and SP1B at spread footing SF-5, employing 28 electrodes at 0.5 m (1.64 ft) spacing, were also side-scanning, as shown in Figure 11-14.

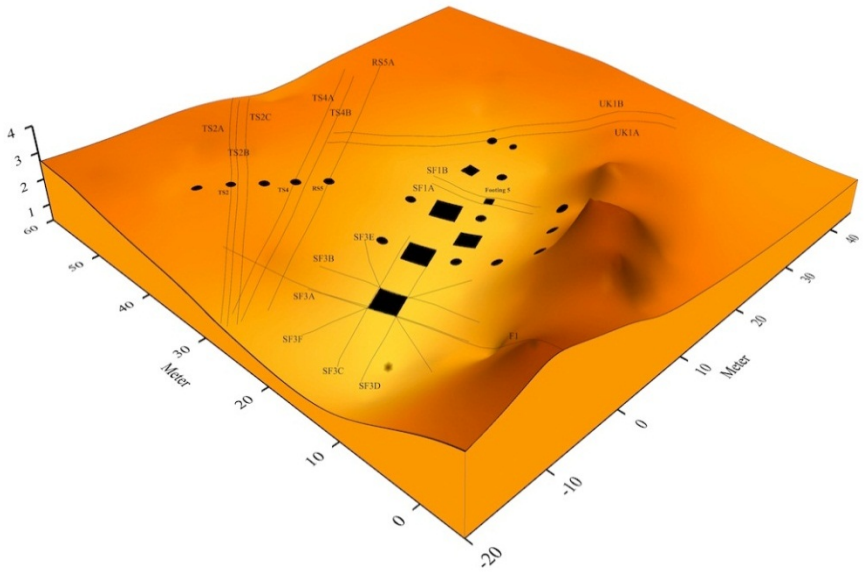

Figure 11-11. NGES Illustration Showing 3D ERI Profiles and Foundations.

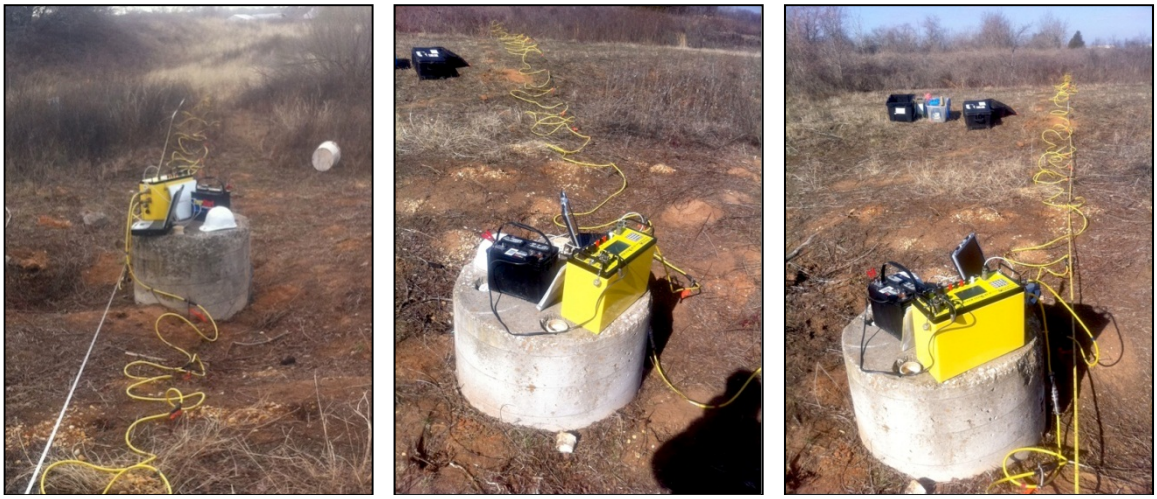

TS2A TS2B TS2C

Figure 11-12. 2D ERI Profiles TS2A, TS2B, and TS2C.

TS4A TS4B RS5A

Figure 11-13. 2D ERI Profiles TS4A, TS4B, and RS5A.

SF1A SF1B

Figure 11-14. 2D ERI Profiles SF1A and SF1B.

At NGES, data were also acquired over the unknown drilled-shaft foundation. Profile UK1A directly crossed the drilled shaft while profile UK1B is side-scanning, as shown in Figure 11-15. Both profiles used 56 electrodes with 1 m (3.28 ft) electrode spacing. Four side-scanning profiles (SF3A, SF3B, SF3C, and SF3D) at 1 m (3.28 ft) electrode spacing were deployed along the four sides of the 3 m (9.84 ft) square footing shown in Figure 11-16. A further two profiles (SF3E and SF3F) ran directly across opposite corners of the footing. A final 2D-ERI profile F1 with 56

electrodes at 1 m (3.28 ft) spacing was conducted directly across the spread footing to provide confirmation.

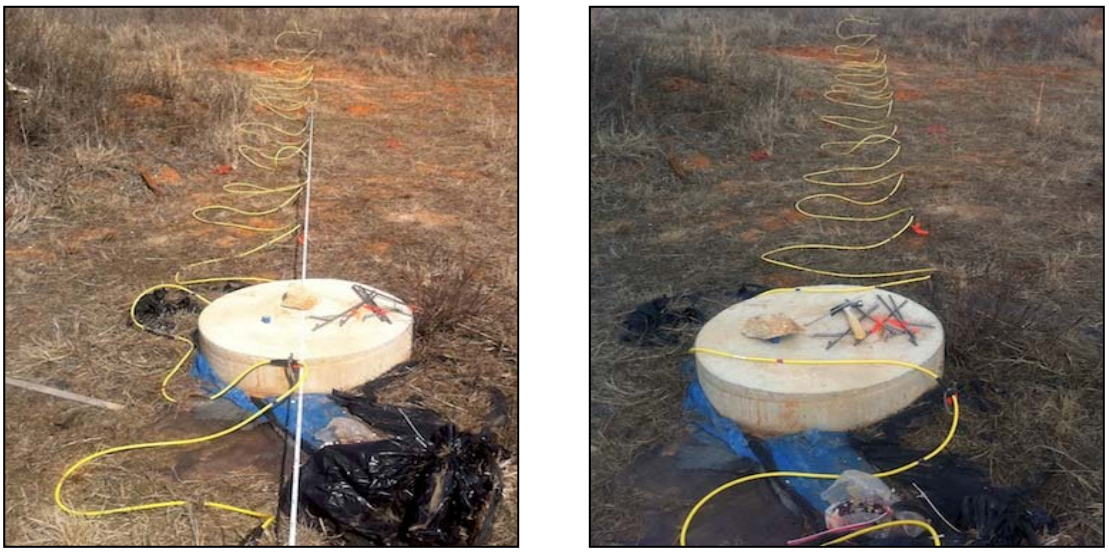

UK1A UK1B

Figure 11-15. 2D ERI Profiles UK1A and UK1B.

SF3A SF3B

Figure 11-16. 2D Profiles SF3A and SF3B.

Bridge over Little Brazos River, HW 21

2D-ERI profiles were acquired in a mixed terrain/underwater environment beneath the Highway 21 (HW21) westbound bridge spanning the Little Brazos River in Brazos County ~20 km (12.42 mi) NW of College Station (Figure 11-3). The TxDOT layout is not available, but the available layout of the adjacent eastbound bridge should be a good indicator of subsurface conditions.

The heavily vegetated terrain around the bridge has high relief, with the steepest slopes on the west bank. The north-south flowing river was ~25 m (82.02 ft) wide and ~1.4 m (4.59 ft) deep at the time of the survey. Brown and grey shale to 3.1 m (10.17 ft) depth is exposed in outcrops on the riverbed and along the bank and is underlain by siltstone to 12.2 m (40.03 ft) depth.

The foundations at the eastbound bridge are drilled shafts of 0.91 m (2.99 ft) diameter and 22.55 m (73.98 ft) total length, embedded 10.36 m (33.99 ft) into the riverbed (Figure 11-17). At the westbound bridge, six foundations reside in the water-covered area, three on each of two bents. Visual inspected found significant erosion of the foundation with corroding rebar exposed, some of which are in contact with water. Reinforced concrete rubble from a previously demolished bridge is present in the water and on the bank.

Two ERI profiles using 56 electrodes at 1 m (3.28 ft) spacing were acquired at this site (Figure 11-18) in a mixed terrain/underwater environment. Profile BHW21A acquired on April 7, 2011, oriented north-south parallel to water flow, targeted a drilled-shaft foundation on the north bank. Profile BHW21B oriented northeast-southwest was carried out on April 26, 2011, and targeted a foundation in the river near the south bank. The resistivity of the water was measured with a portable meter. Water depth was measured at the underwater electrodes. Due to dry soil conditions, water was used to improve electrical contact of the electrodes. Electrode and cable setup time was ~3.5 hr due to the difficult working conditions. Reciprocal measurements were recorded on both profiles.

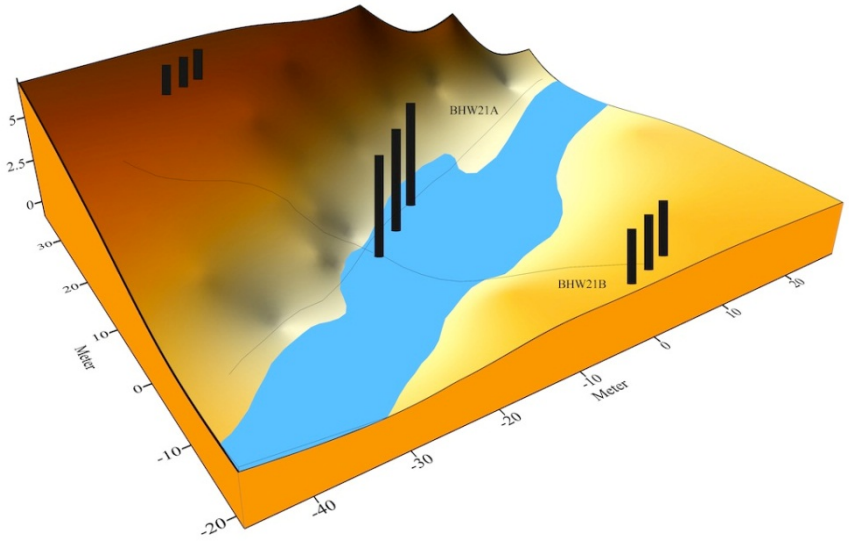

Figure 11-17. Little Brazos River Site Showing ERI-2D Profiles and Foundations.

(1) (2)

Figure 11-18. Field Setup at Little Brazos River.

Railway Bridge over Brazos River, HW 21

ERI-2D profiles were acquired in a moderately vegetated land environment beneath a railway bridge adjacent to the HW 21 roadway bridge spanning the Brazos River in Brazos County ~25 km (15.53 mi) northwest of College Station (Figure 11-3). The targeted foundation has a hexagonal cross-section with 8, 3, and 3 m side lengths and an unknown depth. The terrain is undulating with steep banks sloping toward the river as shown in Figure 11-19. The site is underlain by weathered

grey and brown shale rock exposed as outcrops along the riverbank and reddish brown fossiliferous sandstone exposed on the steep slopes. Two ERI profiles were acquired (Figure 11-20) under very dry conditions at this site on July 6, 2011, using 28 electrodes with 2 m (6.56 ft) spacing. It was difficult to deploy the electrodes in a straight line due to the hard bedrock. Bankside profile RWB1 was deployed east-west, parallel to the river, on rugged terrain of weathered shale. Profile RWB2 runs perpendicular to the river up the slope. The two profiles intersected near their centers. Reciprocal measurements were carried out for both profiles.

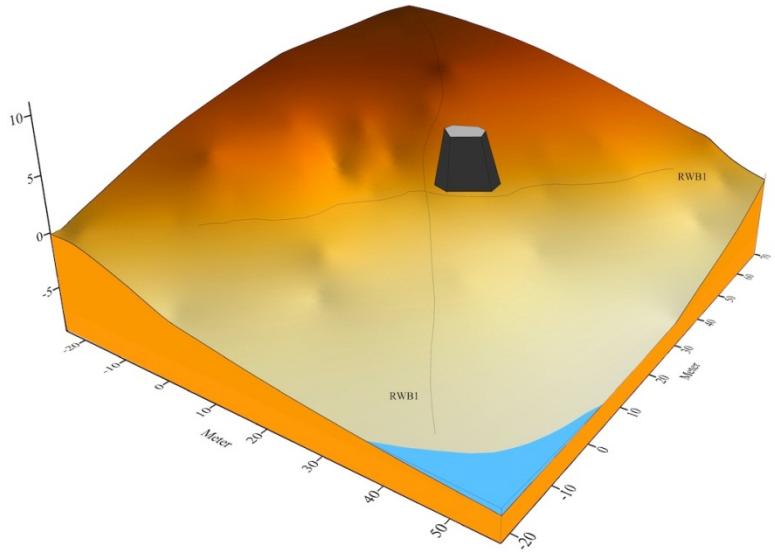

Figure 11-19. Brazos Railway Bridge Site Showing ERI-2D Profiles and Foundation.

(1) (2)

Figure 11-20. Field Setup at Railway Bridge over Brazos River.

ELECTRICAL RESISTIVITY IMAGING RESULTS

In this section, 2D and 3D inversion results are presented and discussed. For surveys conducted at bridge sites with known foundations, the interpretation of each profile is validated using TxDOT-provided bridge layouts. The ERI geophysical method is well-understood and well-established. However, a limitation of the ERI technique is that the interpretation of ERI images becomes difficult in the presence of complex subsurface features. The ERI method applied to bridge sites is straightforward if the foundations are known and geological background structures are relatively simple. When the lateral position of the foundation on the survey profile is known, ERI interpretation (including an estimation of foundation depth) can be performed by qualitative examination of the subsurface anomalies at the known foundation position. ERI image quality depends on a number of factors including data quality, data coverage, and robustness of the inversion algorithm. However, one of the primary determinants of image quality is the resistivity contrast between the foundation and the background geology, which of course is not under the control of the experimenter.

Application of the ERI method to image long, slender bridge foundations is challenging. Bridge foundations, being man-made, have different characteristics compared to natural geological structures of similar shape such as igneous dikes. Moreover, it is well-known that the geological

interpretation of geophysical data is inherently ambiguous. A number of distinct subsurface geometries can produce the same resistivity image. Resolving ambiguities is based somewhat on the expected subsurface geology and wherever possible should include comparison with auxiliary data such as drill core, geophysical logs, and other types of geophysical data.

The bulk resistivity of a reinforced concrete foundation may be higher or lower than that of the surrounding geological materials, depending on its physical condition. For example, a zone of low resistivity in an ERI image could be caused by the presence of a conductive rebar cage embedded in a deteriorating foundation. On the other hand, a zone of high resistivity could be caused by an intact foundation with no cracks or exposed rebar. Careful interpretation of resistivity imaging results is necessary, although not sufficient, to estimate the physical condition of the foundation.

3D-Forward Modeling Results

A number of 3D ERI synthetic responses were evaluated by varying the depth and lateral dimensions of deep and shallow foundations and also varying the resistivity contrast of the foundation relative to the surrounding geological medium.

Figure 11-21 shows a vertical slice through 3D ERI images of a 9 m (29.53 ft) deep foundation of lateral dimensions 1 × 1 m^2 (3.28 × 3.28 ft^2). In the upper image, the resistivity of the foundation is 0.01 Ωm, and it is embedded in a homogeneous geological medium of 50 Ωm. The image shows a low resistivity anomaly, due to the foundation, in the middle of profile. However, the shape of the low-resistivity zone is distorted, and the bottom of the foundation cannot be clearly discerned. In the lower image, the resistivity of the foundation is 10,000 Ωm. Although the image does contain a zone of high resistivity close to surface, the foundation at depth is not detected.

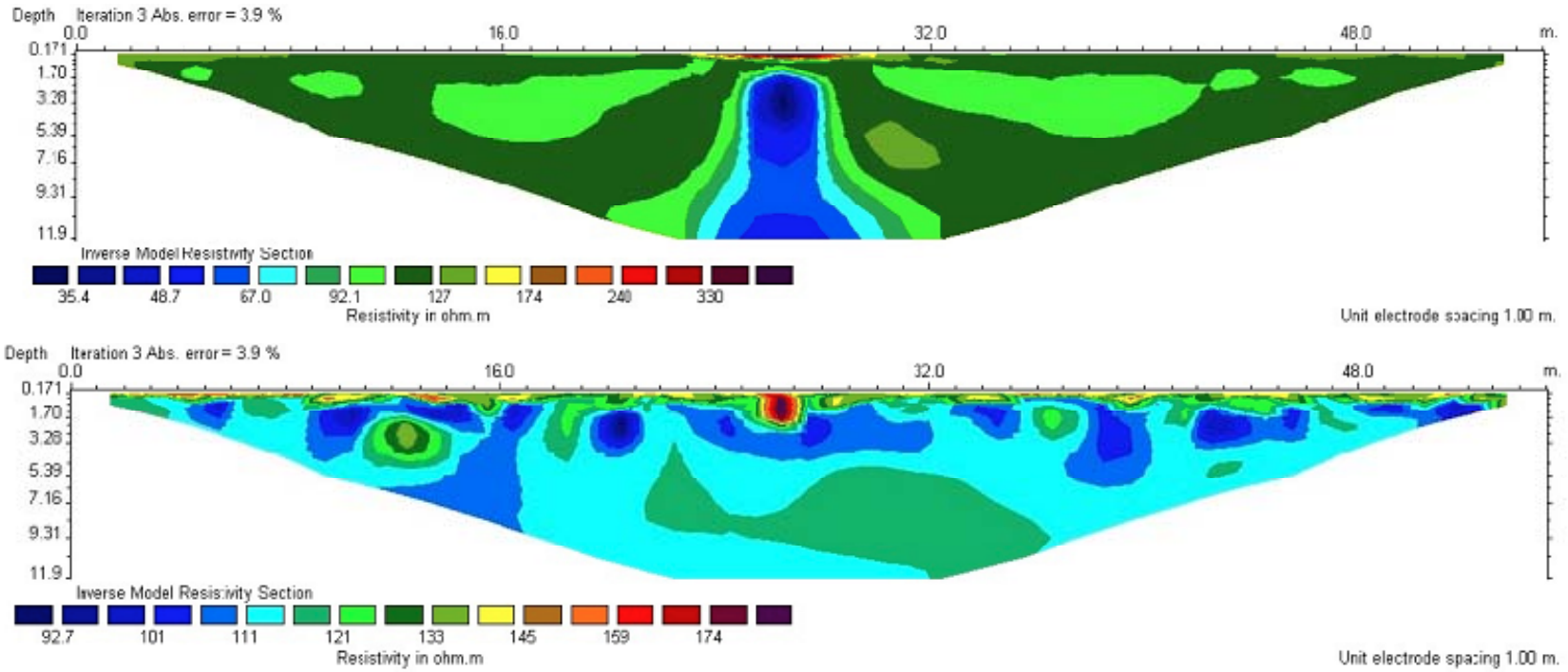

Figure 11-21. Synthetic ERI-3D Response of a 9 m (29.53 ft) Deep Foundation of Lateral Dimensions 1 × 1 m^2 (3.28 × 3.28 ft^2). The Resistivity of the Foundation Is Less (Top) and Greater (Bottom) than That of Geological Background.

Figure 11-22 shows a vertical slice through 3D ERI images of a 5 m (16.40 ft) shallow foundation of lateral dimensions 3 × 3 m^2 (9.84 × 9.84 ft^2). The resistivity of the foundation in the upper and lower images is 50 and 200 Ωm, respectively. In the upper image, a well-defined zone of low resistivity approximately 5 m (16.40 ft) in vertical extent is found at the location of the foundation. In the lower image, the location, shape and vertical extent of the high-resistivity anomaly can be identified but overall it is poorly focused.

Figure 11-23 shows a vertical slice through 3D ERI images of a 5 m (16.40 ft) shallow footing of lateral dimensions 5 × 3 m^2 (16.40 × 9.84 ft^2). The resistivity of the foundation in the upper and lower images is 50 and 200 Ωm, respectively. In both cases, the foundation is clearly and accurately imaged. The bottom and sides of the anomalies are well defined.

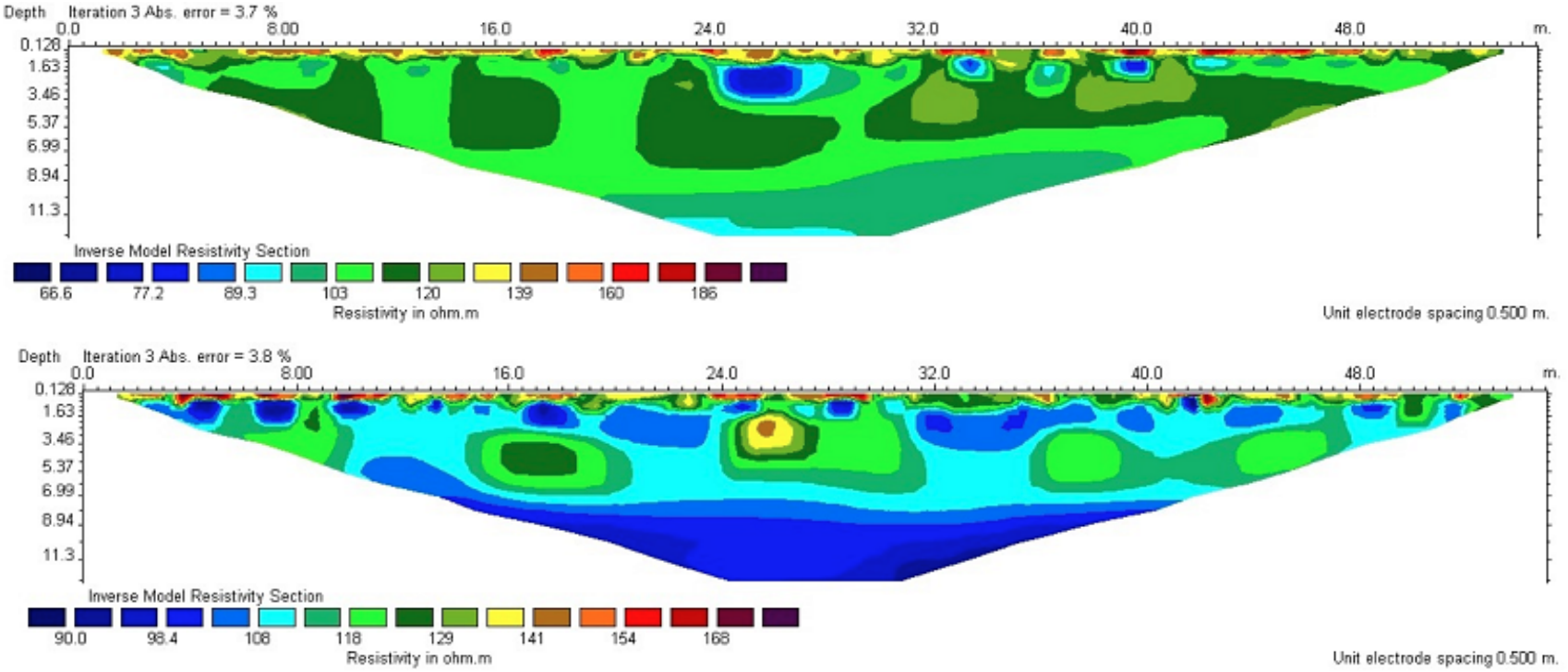

Figure 11-22. Synthetic ERI-3D Response of a 5 m (16.40 ft) Shallow Foundation of Lateral Dimensions 3 × 3 m^2 (9.84 × 9.84 ft^2). The Resistivity of the Foundation Is Less (Top) and Greater (Bottom) than That of Geological Background.

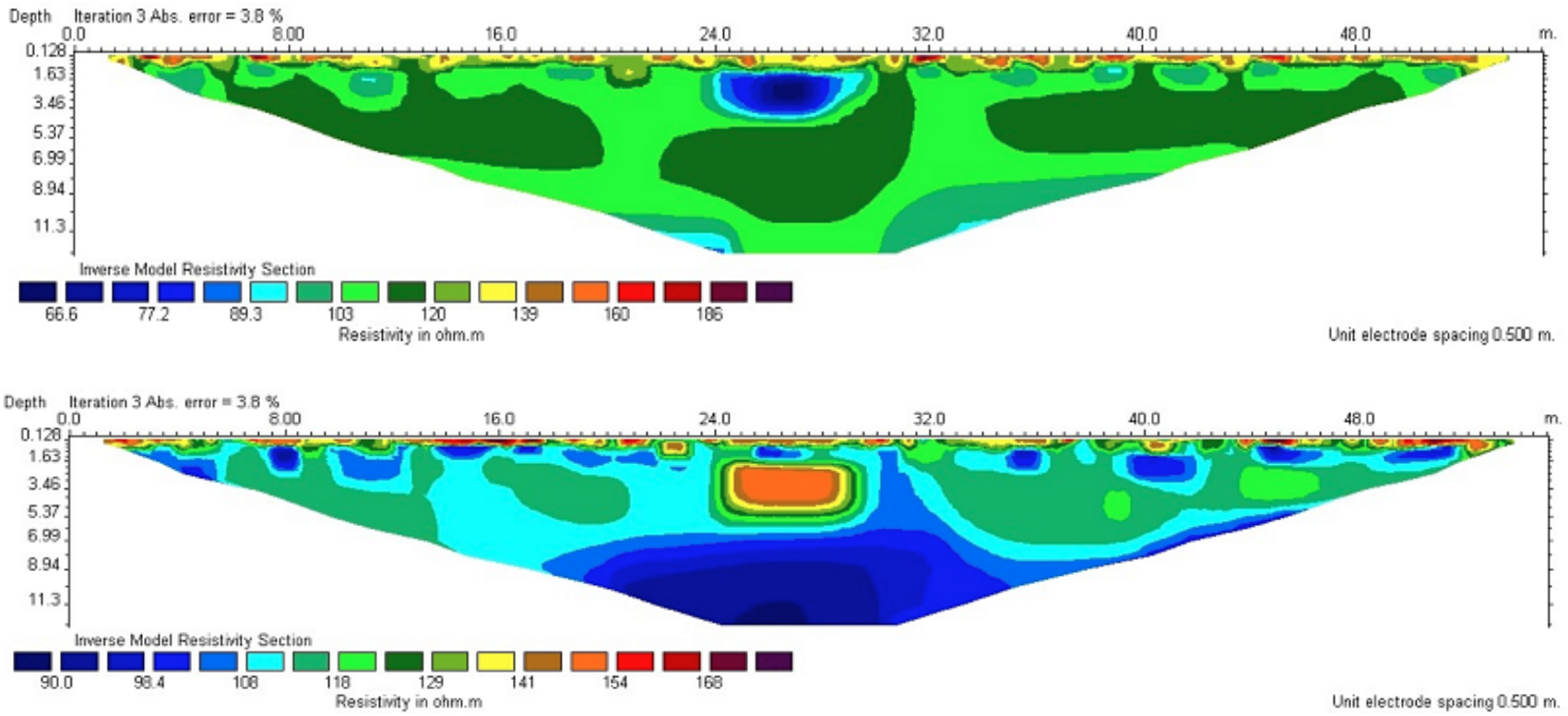

Figure 11-23. Synthetic ERI-3D Response of a 5 m (16.40 ft) Shallow Foundation of Lateral Dimensions 5 × 3 m^2 (16.40 × 9.84 ft^2). The Resistivity of the Foundation Is Less (Top) and Greater (Bottom) than That of Geological Background.

The 3D model studies suggest that ERI imaging is able to detect the presence of a bridge foundation, especially one that is conductive relative to the geological background. While it is always difficult to resolve the precise shape and depth, increasing the lateral size of the foundation offers better images. These 3D model studies are clearly not complete. The electrode spacing and configuration should be tuned to optimize the spatial resolution of the foundation. Moreover, in real-data acquisition, noise can vary significantly depending on several factors not under control of the experimenter. Although the bottom of the foundation cannot always be located precisely, an important goal that can be met in most cases is the determination of whether the foundation is deeper or shallower than the depth of critical scour, which is typically 5 m. These 3D model studies led the way for a series of field investigations on foundations at actual bridge and test sites.

Bridge 14 Results

Figure 11-24 shows the ERI image from profile BG14 at Bridge 14. The underwater segment of the profile is marked by the blue zone above the ground surface. Small tick marks on the ground surface are half the electrode spacing of 0.5 m (1.64 ft). The depth of investigation is ~6 m (19.69 ft). The survey profile intersected eight concrete pile foundations. Several possible foundation bodies are outlined in the resistivity image based on their relatively low resistivity zones (< 3 Ωm). There does not appear to be a low resistivity anomaly corresponding to the third foundation located at 28 m (91.86 ft). The geology is interpreted to be consolidated sediments based on its resistivity between 5 and 45 Ωm. A relatively high resistivity body (> 100 Ωm) below the river section is interpreted to be slightly weathered bedrock. A thin high resistivity layer near the surface at the beginning of profile is supposed to be the consolidated material of an asphalt road.

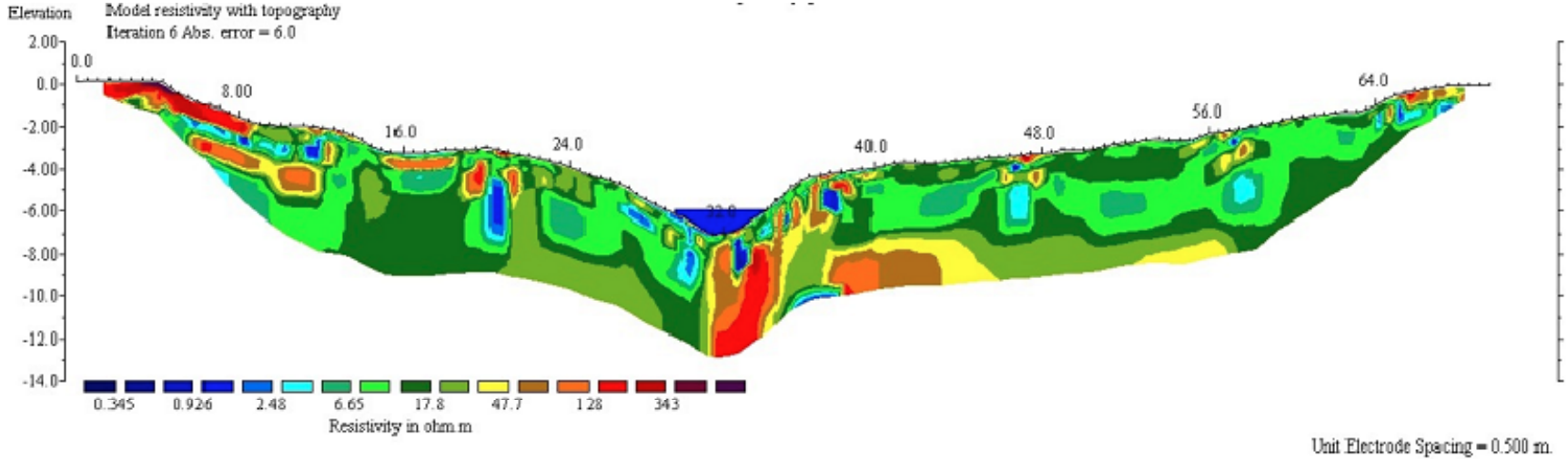

Figure 11-24. ERI Image from Profile BG14 at Bridge 14. Vertical Exaggeration 1:1.

The inversion result can be compared to the TxDOT bridge layout. The piles are 0.39 × 0.39 m^2 (1.28 × 1.28 ft^2) in cross-section, and the length embedded into the ground varies from 10.1 to 15.8 m (33.14 to 51.84 ft). From the resistivity image, however, there is not a strong indication of a long and slender anomaly that represents accurately the shape of the concrete pile foundations. However, a visual inspection at the concrete piles supports their appearance as low-resistivity zones. All concrete piles at Bridge 14 are in good condition. However, a hooked metal sling is found in contact with the ground. These metal cables are used for holding or lifting the piles up and down during bridge construction.

At this site, small electrode spacing was used, but the depth extent of the concrete piles is not clearly detectable. Decreasing the electrode spacing increases the spatial resolution. If the electrode spacing was to be reduced below 0.5 m (1.64 ft), a better defined foundation anomaly might be obtained, but it would remain challenging to determine the depth of the long and slender foundations since the depth of investigation would also be reduced. The roll-along technique is not useful since increasing the number of electrodes does not increase the depth of penetration.

Bridge 15 Results

Figure 11-25 shows the ERI images from profiles BG15A, BG15B, and BG15C at Bridge 15. Recall that the first profile is coincident with a row of five regularly spaced concrete pile foundations, while the other profiles are parallel to the first one at 0.5 m (1.64 ft) line spacing. Topography is not included here due to the relatively flat ground surface. The electrode spacing is 0.61 m (2 ft), the total length of the profiles is approximately 33.5 m (109.91 ft), and the depth of penetration is about 7 m (22.97 ft). After five iterations, the inversion process converged with an RMS misfit of 2.8, 1.96, and 1.37 for profiles B15A, B15B, and B15C, respectively.

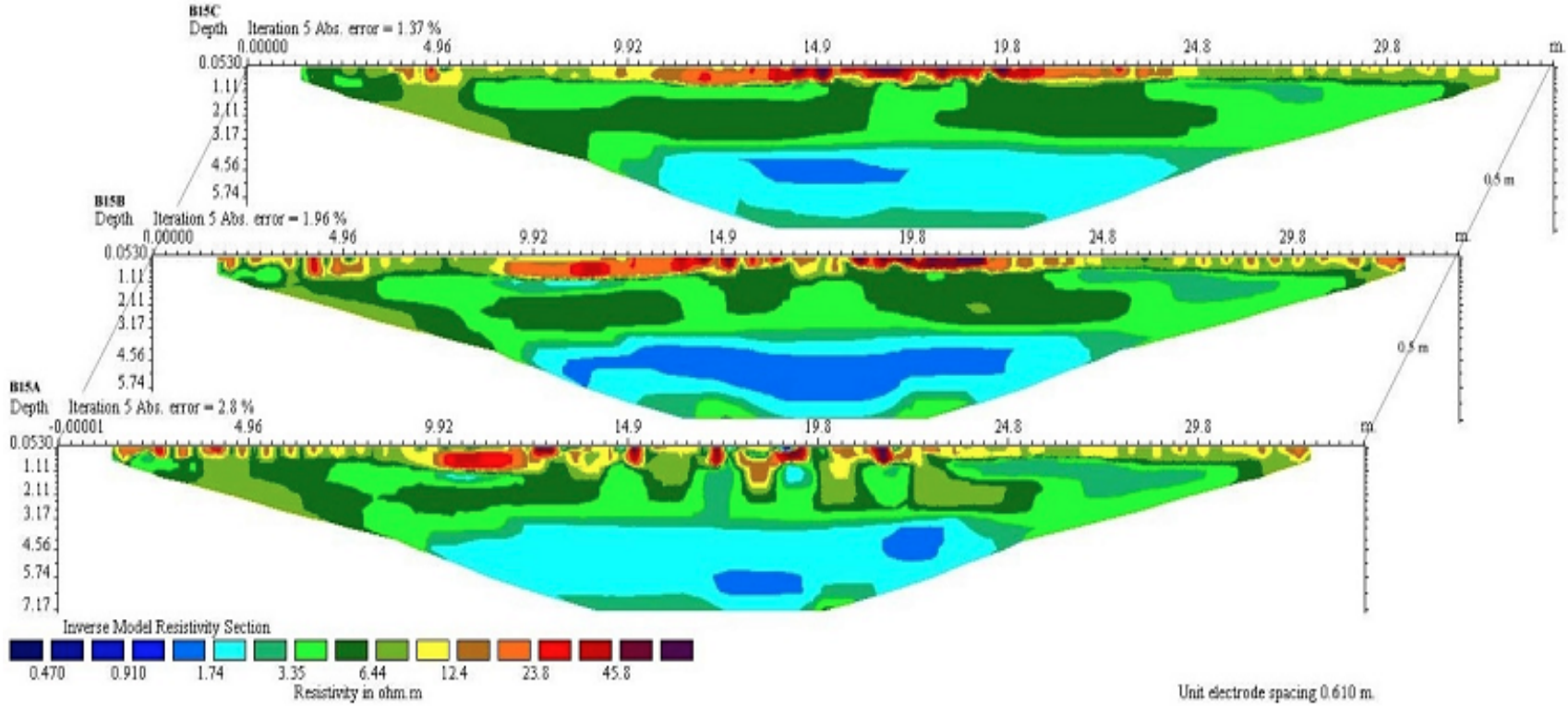

Figure 11-25. ERI Images from the First Test at Bridge 15. Vertical Exaggeration 2:1.

The inversion result from profile BG15A shows the locations of foundations marked by regularly spaced, high-resistivity bodies near the ground surface. The resistivity values are > 35 Ωm and extend to ~1 m (3.28 ft) depth. The inversion result from profiles B15B and B15C do not show clear indication of concrete pile anomalies. Rather a thin continuous layer of high resistivity > 35 Ωm is found near the surface. This could be due to concrete boulders exposed under the bridge. All profiles show a low-resistivity layer at 3 m (9.84 ft) depth that is interpreted as the saturated zone.

Figure 11-26 shows ERI images from the second survey at Bridge 15. The electrode spacing has been increased to 1 m (3.28 ft) yielding a total length of the profiles of 55 m (180.45 ft). The depth of penetration is now about 11 m (36.09 ft). Somewhat similar results to the first survey are obtained, but the concrete pile foundations are not imaged as clearly. A discontinuous thin layer of resistivity > 20 Ωm is found near the surface. The low resistivity zone of about 2 Ωm is interpreted as the zone of groundwater saturation.

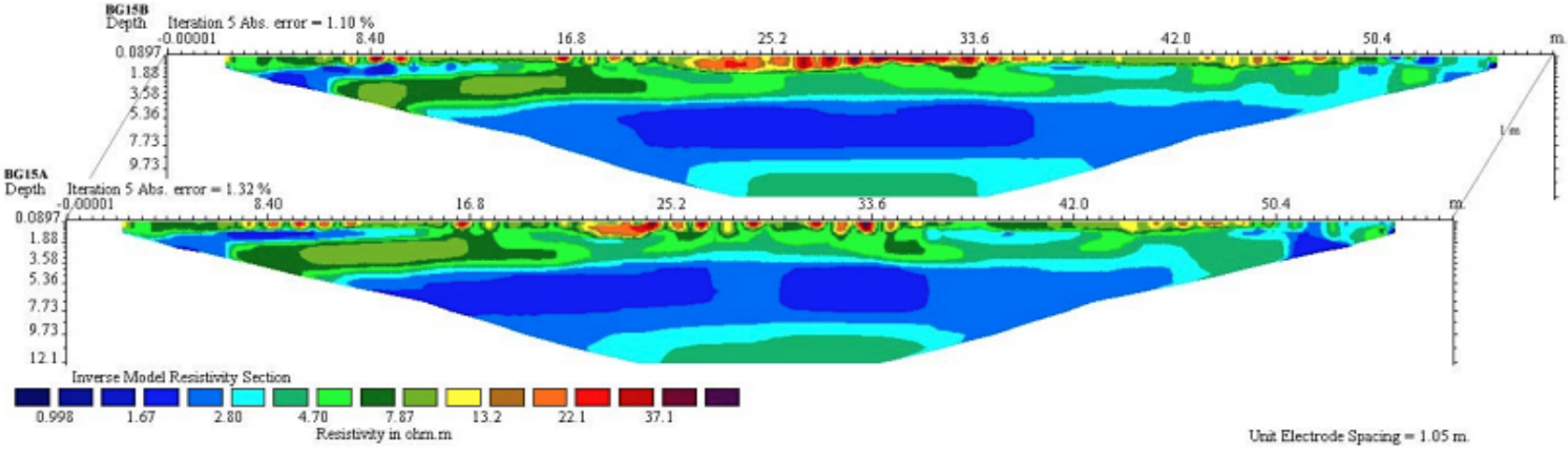

Figure 11-26. ERI Images from the Second Test at Bridge 15. Vertical Exaggeration 2:1.

The TxDOT bridge layout shows small concrete piles 0.39 × 0.39 m^2 (1.28 × 1.28 ft^2) in cross-section with a length embedded into the ground of 13.1 m (42.98 ft). The ERI images reveal small, high-resistivity bodies near the surface but do not capture the shape and length of the concrete piles. The concrete piles have sufficient resistivity contrast, but they are too slender to be accurately imaged by the resistivity method.

NGES 3D Results

Figure 11-27 presents horizontal depth slices at 0−3 m (0–9.84 ft) depth from the 3D resistivity image at NGES. It is of interest to match zones of anomalous resistivity with the known positions of foundations. Scattered high-resistivity bodies are found near the surface, but there is no clear indication of the foundations. Cultural interference from metal fences and discarded metal such as rebar may be responsible for many of the anomalies. A distinct, localized high-resistivity zone is found at depth 1–3 m (3.28−9.84 ft) in the middle to south portion.

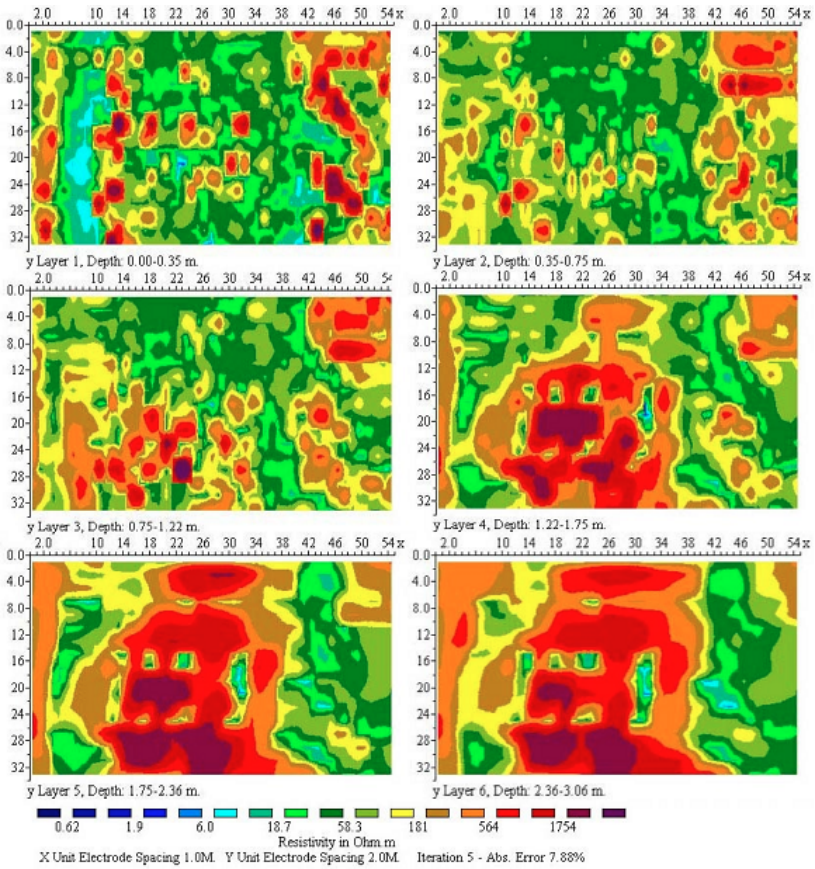

Figure 11-27. Horizontal Slices through the NGES 3D Image at 0−3 m (0−9.84 ft) Depths.

Better results are found at the deeper slice, 3−6 m (9.84−19.69 ft), shown in Figure 11-28. This central anomalous zone of low resistivity coincides with a group of drilled shafts and a spread footing. However, the inferred depths are greater than expected, and the precise shape of the foundations cannot be determined.

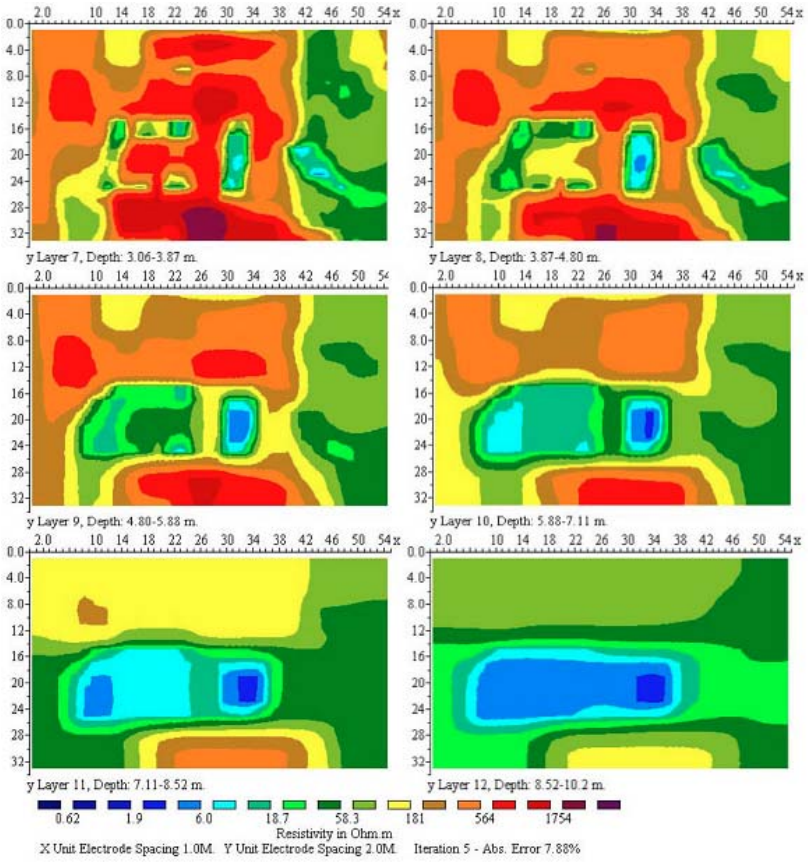

Figure 11-28. Horizontal Slices through the NGES 3D Image at 3−6 m (9.84−19.69 ft) Depths.

Figure 11-29 and Figure 11-30 present vertical slices extracted from the NGES 3D resistivity image. Distinct low resistivity zones are found in (x/z) planes 8, 9, 10, 11, and 13. These zones are in locations that are consistent with positions of reaction shafts. Zones of high resistivity interpreted as spread footings have greater depth than expected and are of larger size. The extracted 2D images from the 3D inversion may be compared directly with the 2D inversion results from individual profiles. The images from 2D inversion and the sliced 2D images at the same location are rather different. The 2D inversion images are much more consistent with the site layout. The 2D images sliced from the 3D inversion result are distorted. The distortions and artifacts present in the sliced 2D images may cause misinterpretation. Fully 3D experimentation was carried out over Footing 5, but the data set SF1-3D was discarded due to very poor data quality.

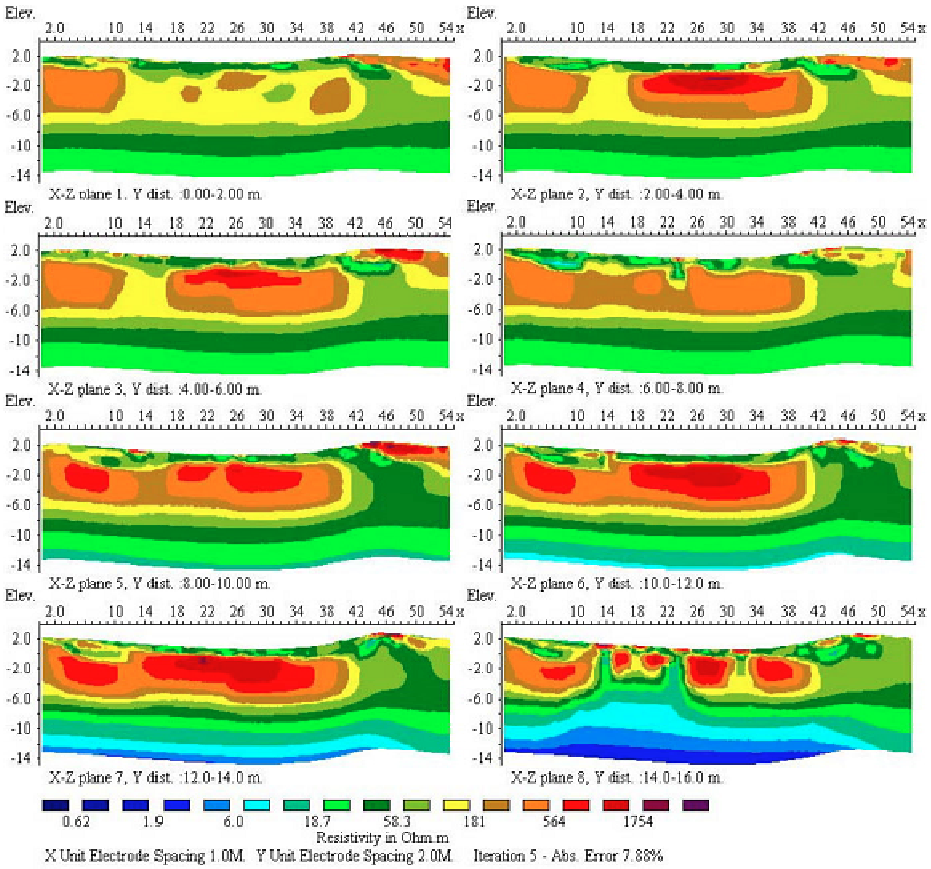

Figure 11-29. Vertical Slices of the NGES 3D Resistivity Image.

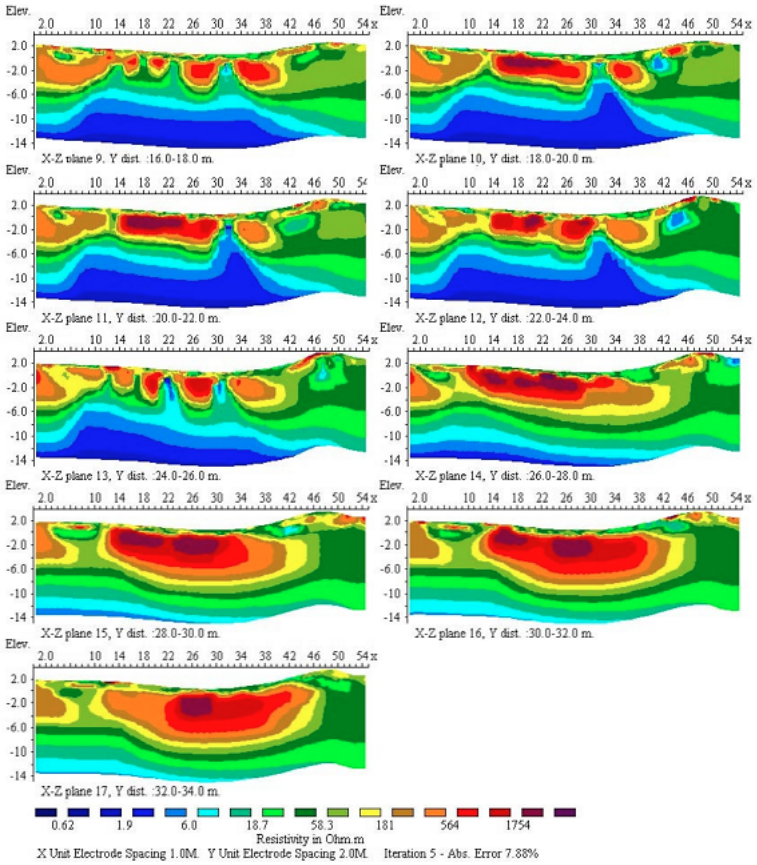

Figure 11-30. Vertical Slices of the NGES 3D Resistivity Image.

The 3D-ERI method in principle should provide the most accurate images of 3D subsurface structures. In the case of foundation determination at NGES; however, it was found that the quasi-3D inversion procedure does not provide clear, accurate images of known foundations. A possible explanation is that the survey profiles did not sufficiently cover all major clusters of spread footings and drilled shafts. Moreover, the various foundations are not all elongated, vertical structures, so that the 3D images provide a wide range of anomaly shapes that are difficult to interpret. One important limitation of the 3D survey is the need to have a sufficiently large electrode layout. The number of electrodes must be greater than conventional 2D electrode deployments to ensure adequate vertical and horizontal data coverage. The ERI method for bridge foundation determination is usually conducted in an undulated terrain, and accessibility may limit surveys to one direction. For these reasons, the 3D-ERI technique is not likely to be a useful practical technique for bridge engineering geophysics investigations.

NGES 2D Results

Figure 11-31 shows the ERI-2D inversion results for profiles TS2A, TS2B, and TS2C conducted over drilled shaft TS2. The length of the profile is 55 m (180.45 ft), and depth of penetration is ~12 m (39.37 ft). A low-resistivity zone (< 20 Ωm) corresponding to the drilled shaft appears at the middle of each profile. The width of the low resistivity zone gradually increases from 1.5 m (4.92 ft) near the surface to 4 m (13.12 ft) at the bottom. A high resistivity body appears close to the surface, while the surrounding geological materials dominantly show high resistivity values. From the NGES site layout, the length of the drilled shaft is 10.8 m (35.43 ft), so that the zone of low resistivity is wider and longer than the actual structure.

Figure 11-32 shows the inversion results for profile TS4A and TS4B at Drilled Shaft TS4. Figure 11-33 shows the inversion results for profile RS5A conducted over drilled shaft RS5. These inversion results show similar images to those for drilled shaft TS2.

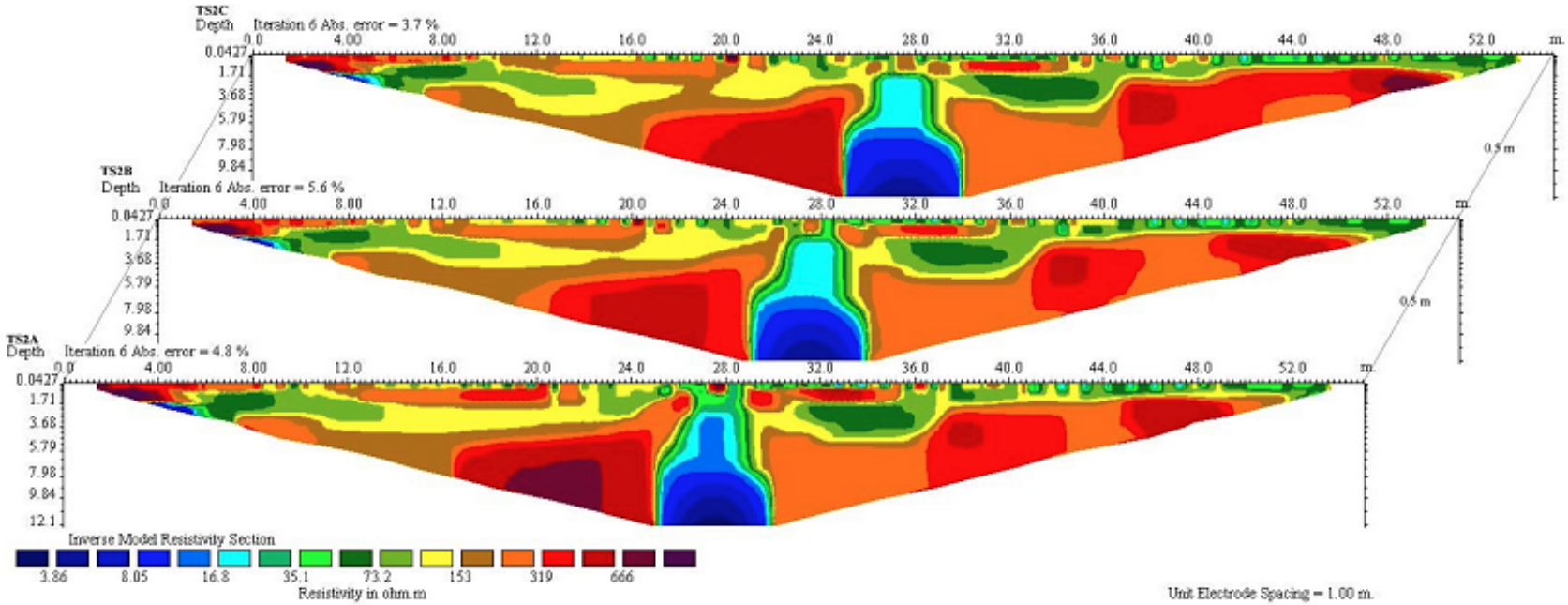

Figure 11-31. ERI-2D Images: Profiles TS2A, TS2B, and TS2C at Drilled Shaft TS2.

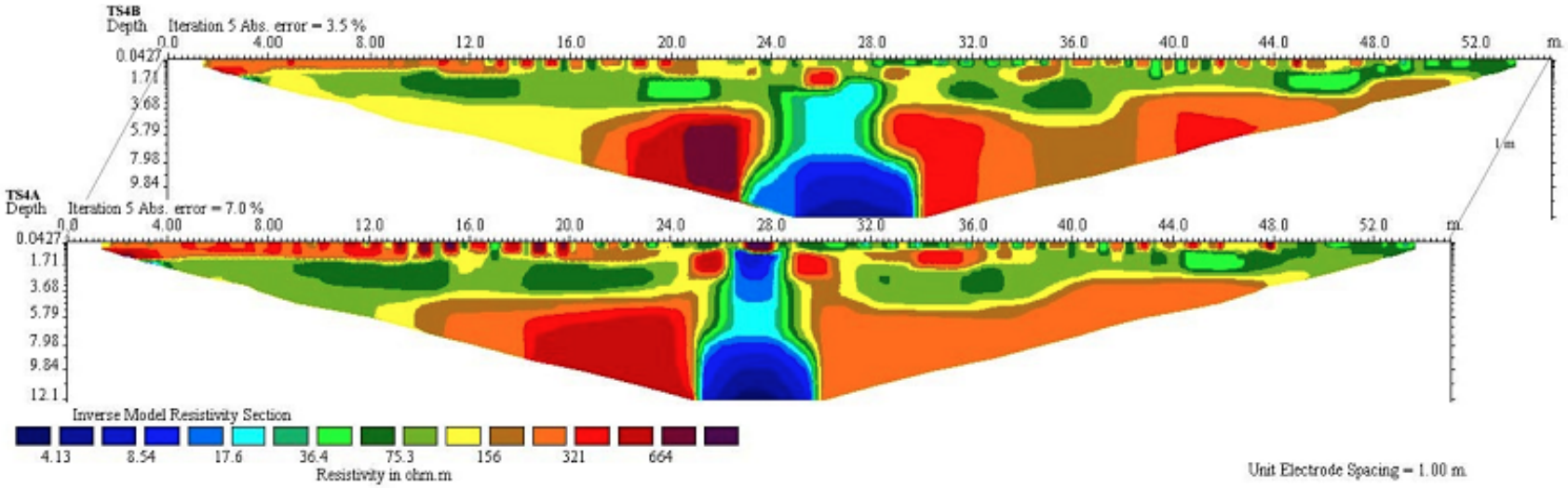

Figure 11-32. ERI-2D Images: Profiles TS4A and TS4B at Drilled Shaft TS4.

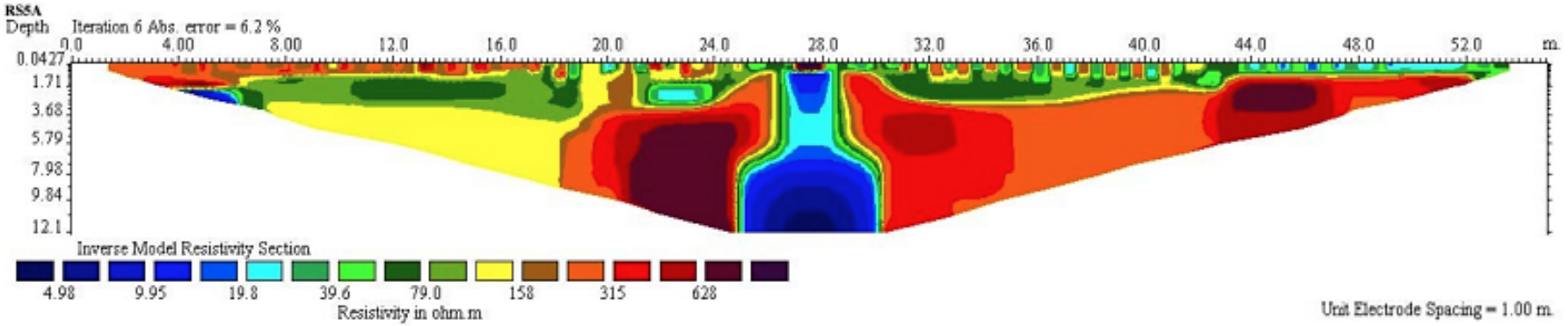

Figure 11-33. ERI-2D Image: Profile RS5 at Drilled Shaft RS5.

The accuracy of the results may be verified using the site layout. A vertical zone of low resistivity extends from the surface to the bottom of each image. However, the depth of the drilled shaft cannot be estimated from the resistivity images. Moreover, 3D effects might cause distortions at depth in the lower sections of the image, and the presence of conductive rebar might affect background resistivity. The images are consistent with the hypothesis that as the drilled shaft was being constructed, the rebar cage was exposed along and at the bottom of the hole, and has made contact with the ground.

Figure 11-34 shows ERI-2D images for profiles SF1A and SF1B conducted over a 1×1 m^2 (3.28×3.28 ft^2) spread footing. The length of the profiles is 13.5 m (44.29 ft), with penetration depth ~3 m (9.84 ft). The profile SF1A shows a body of low resistivity of 20 to 40 Ωm located between 6.5 and 7.5 m (21.33–24.61 ft). This zone represents the footing buried to a depth of about 1 m (3.28 ft) from the ground surface. A somewhat similar result is found for profile SF1B. The accuracy is verified according to the site layout and visual inspection. The zone of low resistivity of ~1 m (3.28 ft) width and 1 m (3.28 ft) depth is the approximate size of the spread footing. Again, the presence of rebar exposed to ground strongly affects the results of a resistivity survey and likely causes the low resistivity values associated with the spread footing.

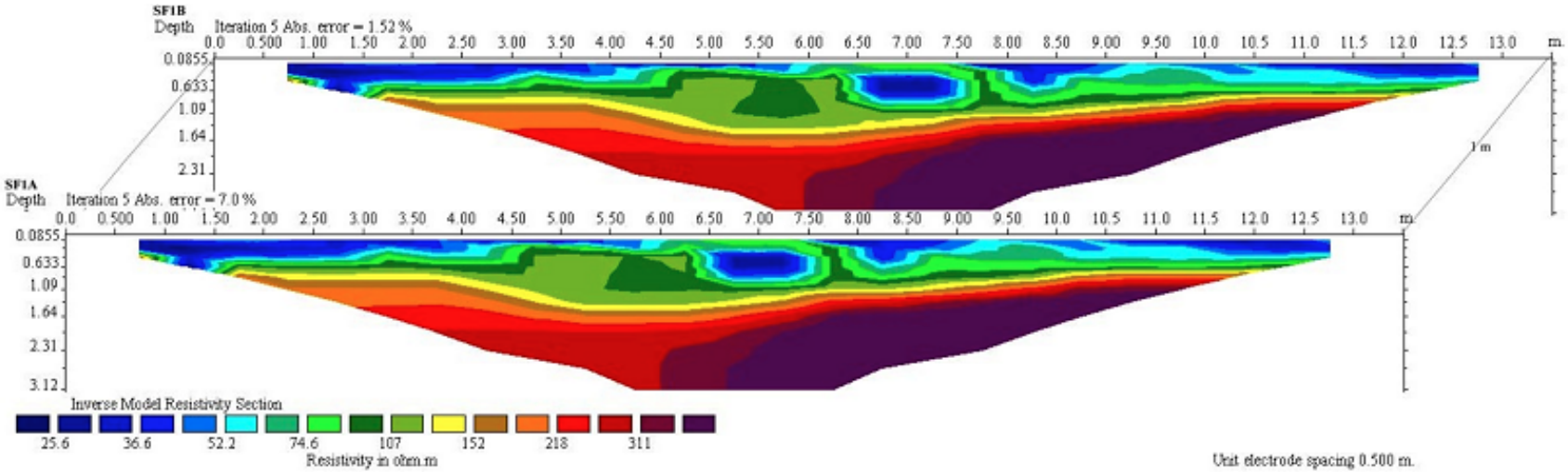

Figure 11-34. ERI-2D Images: Profiles SF1A and SF1B at a Shallow Spread Footing.

Further experimentation was conducted over a drilled shaft and a 3 × 3 m^2 (9.84 × 9.84 m^2) shallow spread footing that are categorized as unknown foundations. Figure 11-35 shows inversion results for profiles UK1A and UK1B conducted over the drilled shaft. The length of the profiles is 55 m (180.45 ft), and the depth of penetration is about 12 m (39.37 ft). The UK1A images show a high resistivity zone (> 250 Ωm) at the location of the foundation. The zone is 1 m (3.28 ft) wide and 3 m (9.84 ft) deep. The UK1B image shows a smaller zone of high resistivity. The central anomaly is interpreted as an unreinforced concrete drilled shaft or solid concrete of 0.9 m (2.95 ft) diameter embedded ~3 m (9.84 ft) in the ground. According to forward modeling, slender vertical foundations are difficult to image. For this reason, the actual foundation might be longer than its ERI-interpreted length.

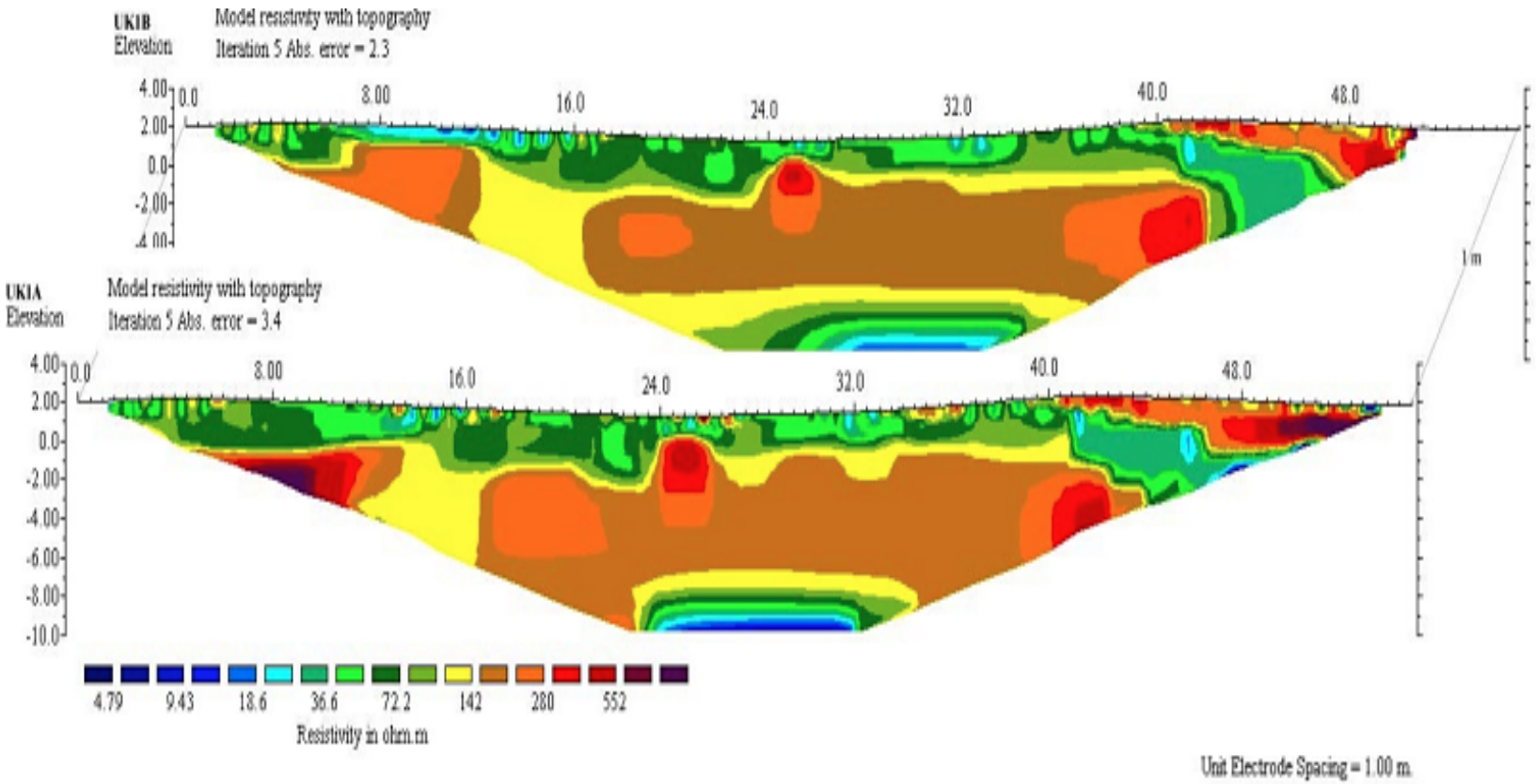

Figure 11-35. ERI-2D Images: Profiles UK1A and UK1B at a Drilled Shaft.

Four profiles (SF3A, SF3B, SF3C and SF3D), were carried out along the four sides of the footing, and two profiles (SF3E and SF3F) were conducted across opposite corners of the footing. Only the first two inversion results (SF3A, SF3B) are illustrated here because other two profiles (SF3C, SF3D) provide an identical result. Moreover, the profiles carried out across opposite corners are of very poor quality data, so they were discarded. Figure 11-36 shows inversions results of profiles SF3A and SF3B conducted over the 3 × 3 m^2 (9.84 × 9.84 ft^2) spread footing. The depth of penetration is 5 m (16.40 ft). Both profiles give a similar result, showing very high resistivity zones (> 1500 Ωm) at the location of the footing. The high resistivity zones of depth are ~3 m (9.84 ft) from ground surface and of width ~6 m (19.69 ft), indicating that the anomaly shape is considerably larger than the actual footing size. The thin low-resistivity zone at the top of the SF3B image is caused by wet ground during the survey.

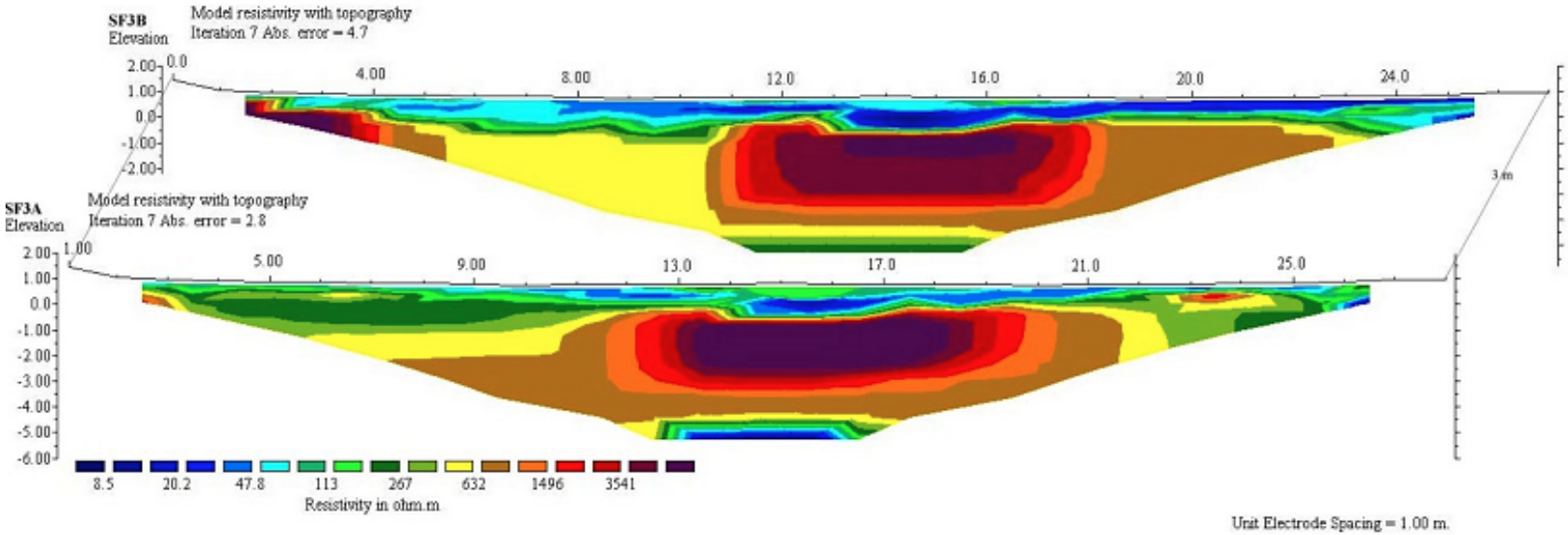

Figure 11-36. ERI-2D Images: Profiles SF3A and SF3B at a Shallow-Spread Footing.

Figure 11-37 shows the inversion result for profile F1 conducted over the 3 × 3 m^2 (9.84 × 9.84 ft^2) spread footing. The length of the profile is 55 m (180.45 ft) with depth of penetration ~12 m (39.37 ft). Topographic information is included in the inversion process. At the position of the spread footing, the image shows a very high resistivity zone > 2000 Ωm. A low resistivity zone appears on the top of the image as in the previous experimentation. The design layout of this spread footing is 3 × 3 × 1 m^3 (9.84 × 9.84 × 3.28 ft^3). A picture of the footing before the concrete was poured is shown in Figure 11-38. The lack of correlation between the images and the actual footing may be due to a low contrast in resistivity between the foundation and the soil. Also, 2D side-scanning profiles are subject to a significant distortion of the images of an actual 3D structure.

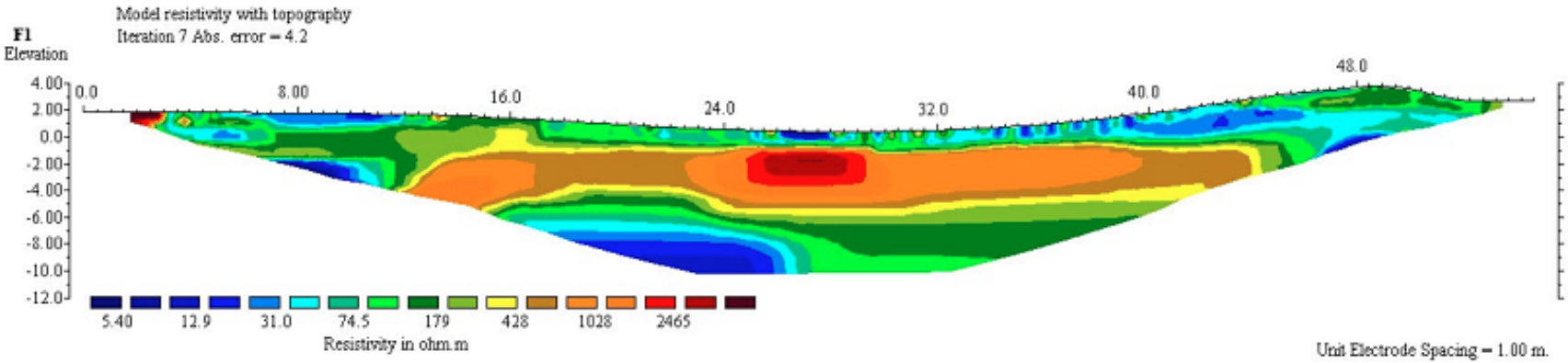

Figure 11-37. ERI-2D Image: Profile F1 at a Shallow-Spread Footing.

Figure 11-38. 3 × 3 × 1 m^3 (9.84 × 9.84 × 3.28 ft^3) Foundation during Construction (Dunn 2010).

The work at NGES and Bridge sites 14, 15 indicate that using electrode spacing < 1 m (3.28 ft) for detecting a foundation smaller than 1 m (3.28 ft) diameter is not recommended. Due to loss of resolution with depth, imaging a slender foundation to depth > 10 m (32.81 ft) is not feasible. The smallest advisable electrode spacing is 1 m (3.28 ft). The lessons learned from resistivity imaging at NGES were applied to additional bridge sites.

Bridge over Little Brazos River

The ERI-2D images for profiles BHW21A and BHW21B at Little Brazos River are shown in Figure 11-39. The length of the profiles is 55 m (180.45 ft) and depth of penetration is ~11 m (36.09 ft). The water in the river where electrodes are underwater is marked by the thin blue zone above the ground surface. The foundation anomaly is clearly outlined as relatively low resistivity zone.

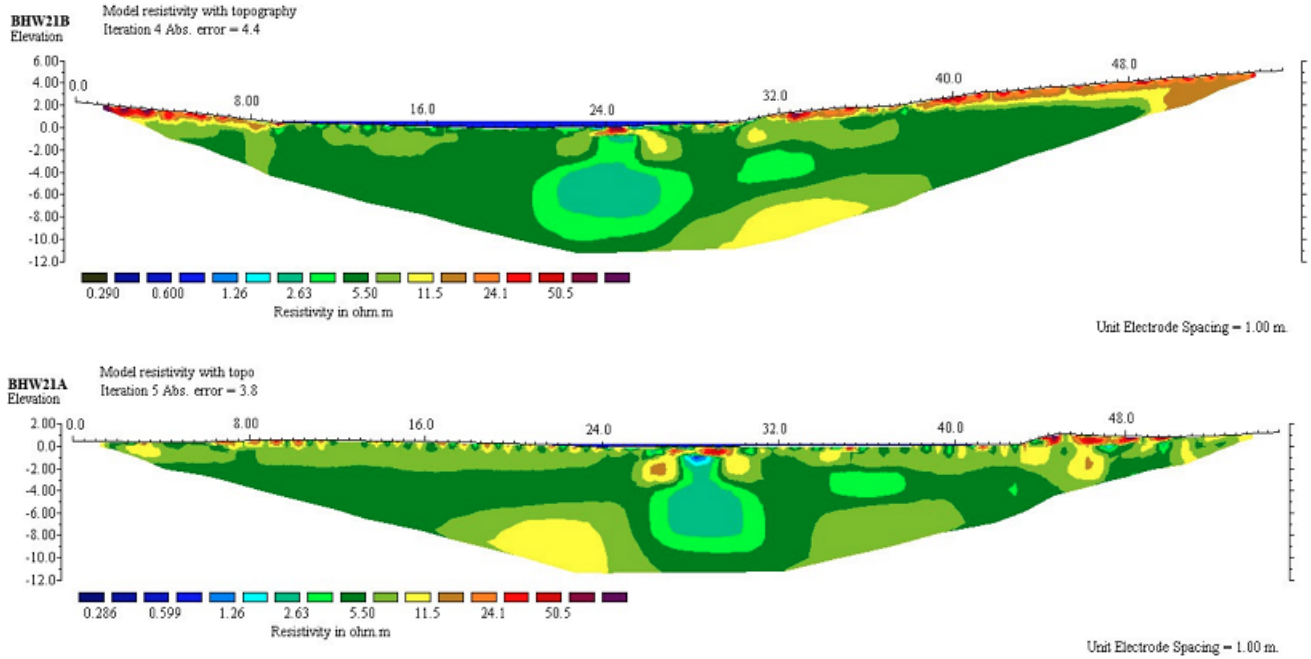

Figure 11-39. ERI-2D Images: (Top) Profile BHW21A; (Bottom) Profile BHW21B at Highway Bridge, Little Brazos River. Vertical Exaggeration 2:1

The inversion result BHW21A (top) spans a small range of resistivity values (5−23 Ωm) indicating little heterogeneity in the subsurface geology. This is consistent with prior information from the TxDOT layout. Near-surface heterogeneities with high resistivity values >23 Ωm are located between 44 and 49 m (144.36−160.76 ft). Field investigation shows an association with debris from a previous demolished bridge. The central anomaly has a width that is much greater than the actual foundation diameter of 1 m (3.28 ft). The bottle-like shape is about 2 m (6.56 ft) wide near the surface and widens to 4.5 m (14.76 ft) at depth. The interpreted depth of the foundation is ~10 m (32.81 ft).

The inversion result BHW21B (Figure 11-39 bottom) provides consistent results to the previous profile BHW21A. The low resistivity body associated with the foundation contrasts with the higher resistivity values of the surrounding geological materials. The interpreted depth of the foundation is ~10 m (32.81 ft).

Visual inspection of the drilled shaft foundations supports the inversion results. The foundation is corroded with rusting rebar exposed and in contact with water. Broken concrete boulders and rebar from the previous bridge were found scattered under the bridge in water and on the bank. The inversion result shows a lower resistivity for the foundations than the surrounding geological materials. It is assumed that cracks or corrosion has degraded the reinforced concrete foundation and caused the iron rebar to come into contact with the ground, resulting in an efficient transport of ions through the concrete and the surrounding materials.

The images are compared with known information from the TxDOT layout of the eastbound bridge of the same construction. The drilled shaft foundation at the eastbound lane is known to be 0.91 m (2.99 ft) in diameter and 22.55 m (73.98 ft) in total length. The foundations are located in water-covered areas, with a 10.36 m (33.99 ft) long section embedded into the ground. The resistivity image is consistent with this layout. Although the resolution of the 2D ERI in a mixed terrain underwater area is generally lower than 2D ERI performed over a land surface area, these inversion results clearly show the existence of low-resistivity anomalies at the known foundation position. Although the images do not indicate the precise shape of the foundation, the horizontal and vertical extent of the anomaly is sufficient to estimate the size and depth of the foundation. From this inversion result, it may be concluded that the 2D-ERI method used widely for land

surveys can be adapted effectively for unknown bridge foundation investigations in water-covered environments.

Railway Bridge over Brazos River

The ERI-2D images for the two orthogonal profiles RWB1 and RWB2 at the Brazos river railway bridge are shown in Figure 11-40. The length of the profiles is 54 m (177.17 ft), and the depth of penetration is ~10 m (32.81 ft). The inversion results clearly indicate a strong contrast in resistivity of the large spread footing and the surrounding geological materials. The inversion results show lower resistivity values of geological materials and higher resistivity values of the foundation.

At RWB1, the footing is imaged as the high resistivity anomaly > 80 Ωm between 20 and 31 m (65.62−101.71 ft). Its shape is somewhat rectangular with a width of 11 m (36.09 ft) and depth of 5 m (16.40 ft). A thin zone of high resistivity anomaly close to the footing is caused by outcropping boulders and discontinuous bedrock. Lower resistivity values correspond to weathered rock materials. The low resistivity value <10 Ωm underlying the spread footing is typical of weathered materials in the area. This zone of low resistive anomaly also appears toward both end sections of profile where clay particles and elevated moisture act to increase electrical conductivity. The shallowest bedrock is found close to the foundation, with resistivity values ranging between 10 and 40 Ωm. This layer represents weathered to moderately weathered shale, as observed on the surface.

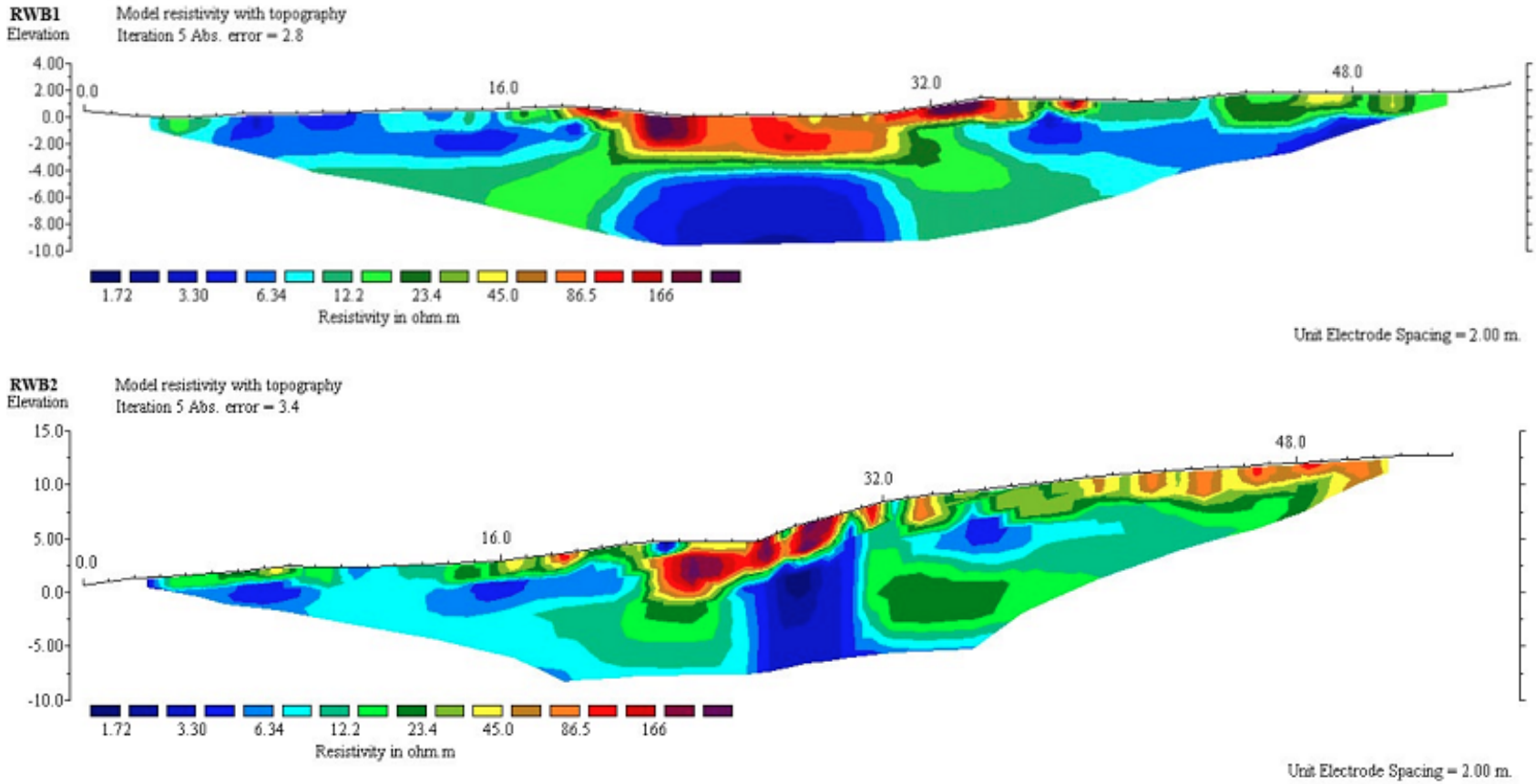

Figure 11-40. ERI 2D Images: (Top) Profile RWB1; (Bottom) Profile RWB2 at Railway Bridge, Brazos River. Vertical Exaggeration 2:1

The RWB2 image provides important additional information. The center of this profile was placed a few meters away from the foundation due to lack of access. A high resistivity anomaly > 80 Ωm corresponds to the footing. It is located between 22 and 25 m (72.18–82.02 ft) with a somewhat rectangular shape of width 3 m (9.84 ft) and depth 5 m (16.40 ft). Discontinuous bedrock underlies the foundation, as in the previous profile. The sloping section between 25 and 32 m (82.02−104.99 ft) reveals discontinuous high resistivity bodies > 80 Ωm. This location marks the occurrence of exposed sandstone outcrops. Conversely, a low resistivity zone (< 5 Ωm) beneath the high resistivity bodies is interpreted as a highly weathered zone and is perhaps also high in water content. A near-surface thin layer from 37 m (121.39 ft) at the end of profile with a comparatively high resistivity value is interpreted as hard ground.

Both railway bridge images show a foundation anomaly that is consistent with the actual size of the foundation (11 × 3 m^2 [36.09 × 9.84 ft^2] in lateral dimensions and 5 m [16.40 ft] in vertical extent). The foundation has high resistivity in accordance with the visual observation that iron rebar is not in contact with the ground. The foundation footing is intact. The inversion results demonstrate that the 2D-ERI method is an effective tool for delineating shallow bridge foundations that are much larger than the electrode spacing. Unfortunately, the bridge layout showing the original design of the footing is not available, so the interpretation cannot be verified. The two orthogonal profiles increase the image reliability relative to a single profile in any direction.

Chapter 12.
INDUCED POLARIZATION

INTRODUCTION

Induced polarization is a unique approach to determining the unknown foundations of bridges primarily because current methods, when successful, do not show the type of the foundation, only the depth. Also, because the test is conducted alongside the structure and does not physically use it, the complexity of the substructure will not hinder its results. Induced polarization is widely used for archaeological surveys looking for buried artifacts (Meyer et al. 2007) and for distinguishing between coarse and fine-grained materials in landfill explorations (Leroux et al. 2007). IP is also used to characterize waste dumps, distinguishing between reinforced concrete at the bottom of the dumps and the garbage on top of it (Bavusi et al. 2006). It is used for aquifer explorations and locating unexploded ordnances and land mines (Pellerin 2002) and is increasingly used for contaminant-plume mapping (Sogade et al. 2006).

While IP has been proven in several subsurface applications, it has not yet been used for unknown foundations. However, it has been used for laboratory measurements of corrosion of reinforcing bars in concrete. IP measurements were taken in the frequency domain with electrodes placed on the concrete surface, successfully measuring a change in the IP response as corrosion occurred in the reinforcement (Hubbard et al. 2003). These results are important because they show that although IP has not previously been used for unknown foundation measurements, reinforced concrete does, in fact, possess a measureable IP response.

INDUCED POLARIZATION MEASUREMENTS

For IP, the dipole-dipole array introduced in Chapter 10 is primarily used; however, other arrays were investigated to ensure that the dipole-dipole is the optimal array for this application. Figure 12-1 shows how the arrays look in the field. Arrays similar to this are set up alongside bridges with unknown foundations.

Figure 12-1. Field Setup.

Figure 12-2 shows the two types of electrodes used. The electrodes on the left are stainless steel electrodes while the electrodes on the right are non-polarizing (NP) electrodes discussed in Chapter 10.

Figure 12-2. Electrodes.

These electrodes are manufactured by AGI along with the SuperSting system that was used for this project. However, using two types of electrodes is time-consuming and more expensive, so research has been conducted on the feasibility of using only the steel electrodes for IP measurements and later correcting for the additional polarization potentials (Dahlin et al. 2002). Dahlin et al. took measurements at two different locations and gathered similar data when comparing the NP electrodes and the stainless steel electrodes after a correction for the additional

noise was applied. They also used a specific data collection sequence. When using stainless steel electrodes only after an electrode has been used to transmit current, even when a cyclic positive and negative current is used, a charge can remain in the electrode for over 600 sec. This additional charge is one of the reasons NP electrodes are used; however, Dahlin (2002) notes that if a data collection sequence does not use electrodes as potential electrodes immediately after they transmit current, the amount of noise can be minimal.

When looking at Figure 12-1, one can assume that the SuperSting system appears to be designed primarily for investigations only on dry land; however, AGI also manufactures marine cables that are capable of gathering data under fully saturated conditions. Sogade et al. (2006) noted that resistivity measurements alone are more sensitive to fluctuating groundwater conditions than IP measurements. When testing during a period of rain, "the IP measurements…were barely affected by the wet-dry conditions, as shown by the much smaller RMS [Root Mean Square] error of the wet-dry measurements" (Sogade et al. 2006). This lower sensitivity to fluctuating ground water conditions is another advantage of IP.

While the equipment available for this research measures chargeability in the time domain exclusively, it can also be measured in the frequency domain. The percent frequency effect (PFE) is measured in the frequency domain. Related to frequency domain measurements is the apparent frequency effect (AFE), which is the difference between apparent resistivity and the frequency excitation of a conducting target (Apparao et al. 2000). When using AFE, researchers noted that if a highly conductive target cannot be detected using resistivity, it cannot be detected using IP unless it contains conducting materials that cannot be detected by resistivity. While materials that cannot be detected by resistivity but instead by IP were not identified, the importance of the coupling between resistivity and IP should be noted. This coupling is imperative when normalized chargeability is used instead of apparent chargeability. Slater and Lesmes (2002) noted that the typical parameters for IP, chargeability, PFE, and the phase angle yield a poor measurement of the surface polarization, which is what often interests geophysicists. Similarly, the IP response that is most useful for bridge foundations is also the surface polarization. Normalized chargeability, MN, is the apparent chargeability, M, divided by the resistivity magnitude, ρ.

$$MN = \sigma'_{rock} M = \frac{M}{\rho} \qquad \text{(Eq. 12-1)}$$

Normalized chargeability better quantifies the surface polarization. Slater and Lesmes (2002) conducted laboratory and field experiments to study the dependence of apparent chargeability and normalized chargeability on salinity and clay content. It was illustrated that normalized chargeability improves interpretations of IP data in both the laboratory and the field. For this reason, normalized chargeability was used for the field work in this research by doing simple preprocessing of the raw data in MATLAB.

FORWARD MODELING

While IP is a technique widely used for locating cavities as well as other underground objects like minerals, it is not generally used for civil engineering applications. A parametric study was, therefore, conducted to identify the most influential factors for using IP for foundations.

Model Background

Before a parametric study could be conducted, field tests were necessary to obtain a range of values of chargeability for reinforced concrete. These tests were conducted at one of the NGES on the Texas A&M Riverside campus, which was sponsored by the National Science Foundation and the Federal Highway Administration in 1997. This site contains a sand site, shown below, which consists of five spread footings and five reaction shafts. There are two $3 \times 3 \times 1.2$ m^3 ($9.84 \times 9.84 \times 3.94$ ft^3) footings; one $2.5 \times 2.5 \times 1.2$ m^3 ($8.20 \times 8.20 \times 3.94$ ft^3) footing (shown in Figure 12-3); one $1.5 \times 1.5 \times 1.2$ m^3 ($4.92 \times 4.92 \times 3.94$ ft^3) footing; and one $1 \times 1 \times 1.2$ m^3 ($3.28 \times 3.28 \times 3.94$ ft^3) footing; along with four 21.3 m (70 ft) long, 0.91 m (3 ft) diameter drilled shafts with underreamed bells and one 5 m (16.40 ft) long, 0.91 (3 ft) diameter drilled straight shaft.

Figure 12-3. Large Footings at the Sand Site.

The general soil layering at the sand site consists of a medium dense, tan, silty, fine sand to 3.5 m (11.48 ft) below the surface; medium dense, silty sand with clay and gravel from 3.5 to 7 m (11.48 to 22.97 ft), medium dense, silty sand to sandy clay with gravel from 7 to 11 m (22.97 to 36.09 ft); and very hard, dark gray clay from 11 to 33 m (36.09 to 108.28 ft). The water table at the sand site is located 4.9 m (16.08 ft) below the surface (Gibbens 1995). Several trial experiments were conducted at the sand site to ensure that reinforced concrete does, in fact, possess a measureable chargeability. From these field tests, it was determined that the chargeability of reinforced concrete is 80–100 mV/V. It was also determined that concrete without reinforcement does not possess a measureable IP response with the field setup used for this research. This band of data was used to generate the forward models to simulate various field conditions to lessen the time consuming field work. An example of one of these field tests on the 1 ×1 × 1.2 m^3 (3.28 × 3.28 × 3.94 ft^3) footing with its corresponding inversion is shown in Figure 12-4. Note that the foundation does not appear to be embedded 1.2 m (3.94 ft) because approximately 0.4 m (1.31 ft) is exposed above the ground surface.

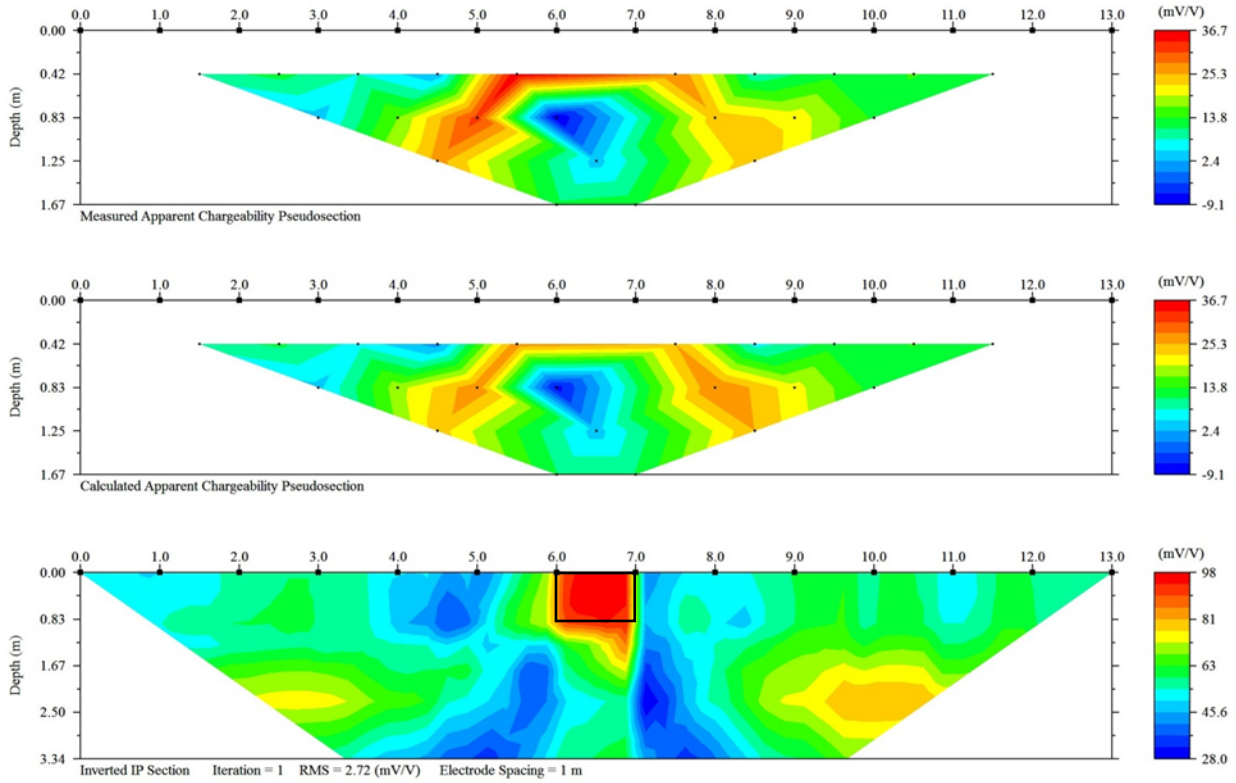

Figure 12-4. Field Results of a Small Footing at the Sand Site.

Because the depth of the foundation is known at Riverside Campus, the depth of the foundation is shown on the figure. This field test was conducted using a dipole-dipole array with 14 stainless steel and 14 non-polarizing electrodes. Several other field tests were conducted on other known foundations at the sand site from which the band of 80–100 mV/V was determined.

Single Foundation Models

All models in the parametric study are simulated using *EarthImager 2D*™, which is the program accompanied with the *SuperSting* equipment that AGI created. The forward modeling program within *EarthImager 2D* is a finite element approach with user-prescribed starting models that use the Cholesky Decomposition for its forward equation solver. Within the forward model settings is a program called Survey Planner. Survey Planner first allows the user to input synthetic material properties into an interactive workspace in which the dimensions of the different materials can also be inserted as shown in Figure 12-5.

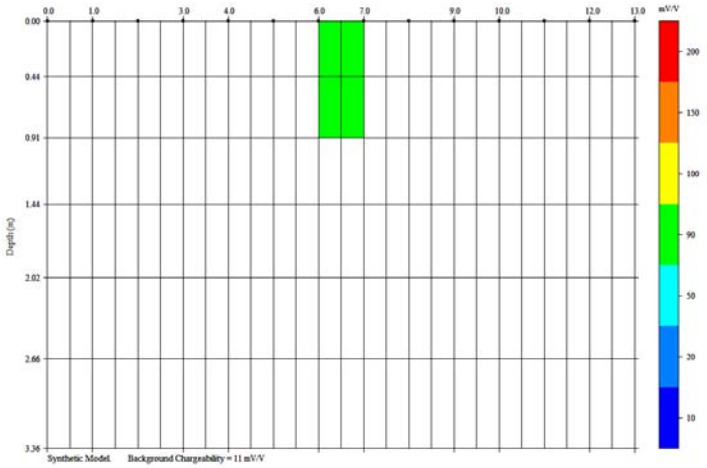

Figure 12-5. Synthetic Chargeability Model.

Survey Planner then employs a forward model to generate the raw data that would be gathered in the field should these conditions exist as shown in Figure 12-6.

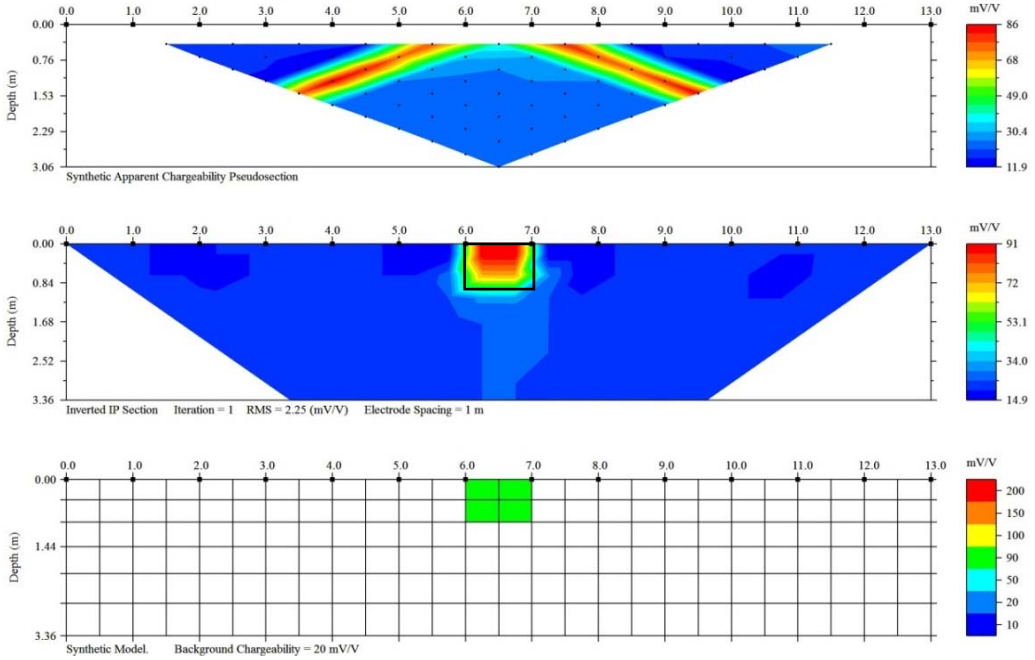

Figure 12-6. IP Survey Planner Results.

The bottom image is the synthetic model (Figure 12-6), input by the user from which the top image is generated showing the synthetic raw data. The final step (the middle image) is an inversion of the synthetic pseudosection. When the inversion is run, the top image looks like what the raw data collected in the field will look like, and the middle image is an example of what the final product

will be. Overlays of the synthetic models have been drawn on the inversions, so the accuracy can easily be seen for each case. Ten models were created to evaluate the feasibility of using IP for bridge foundations that vary in material, size, and depth. Because the IP model is coupled with a resistivity model, base values were assumed for the foundations and backgrounds of both inputs. It was also determined in the field, using this equipment, that reinforced concrete foundations possess a resistivity of 30−40 Ωm. Also, when the field tests were conducted, the background resistivity of the field location, at the National Geotechnical Testing Sand Site, was measured from 100−115 Ωm and the background chargeability was measured from 5 to 15 mV/V. A background resistivity of 100 Ωm and a background chargeability of 11 mV/V were assumed for each model.

Beginning with the simplest model, below is a 0.5 × 3 m^2 (1.64 × 9.84 ft^2) spread footing embedded 0.25 m (0.82 ft) (Figure 12-7).

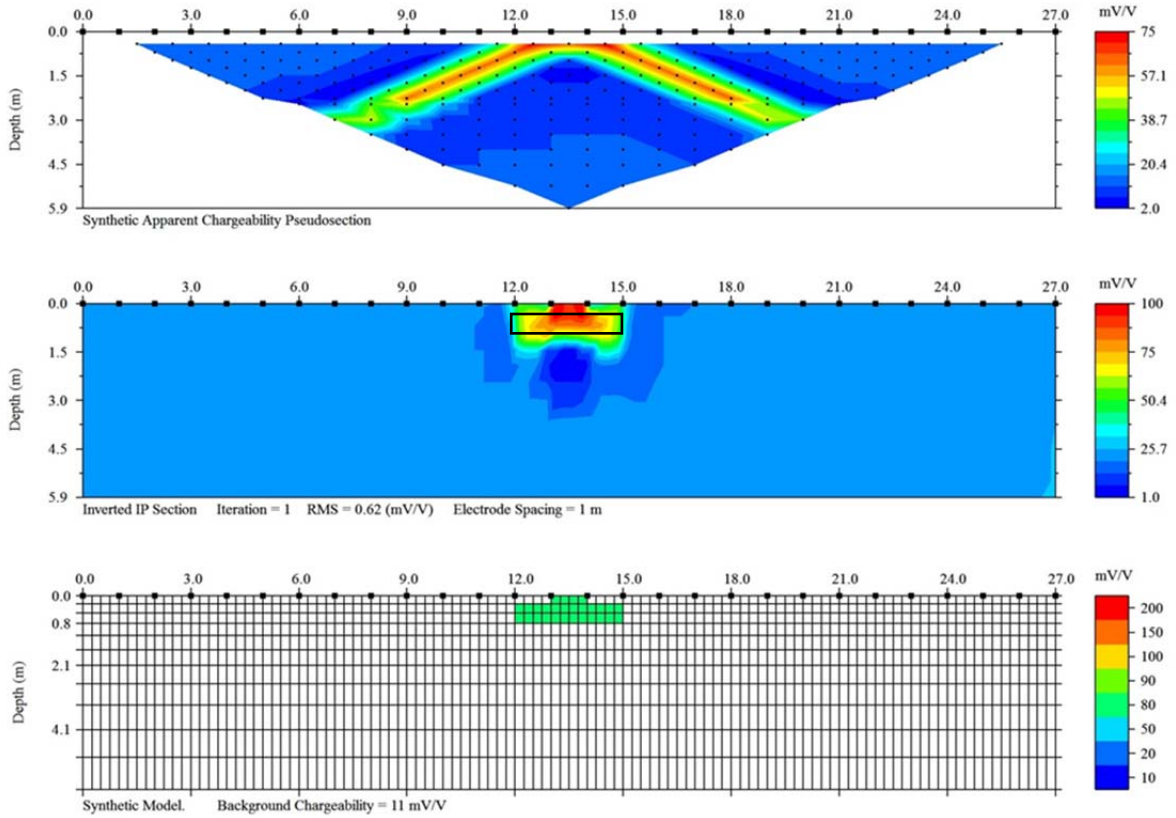

Figure 12-7. 0.5 × 3 m^2 (1.64 × 9.84 ft^2) Spread Footing Buried 0.25 m (0.82 ft).

The strong correlation between the synthetic model and the inverted IP section was expected because the foundation was near the surface where data are more easily collected. From this image, the foundation type and depth can be easily identified; however, the strong chargeability of 100 mV/V does not extend to the full width of the foundation. This could be attributed to the soil coverage over the edges of the foundation.

Next, a 1 × 4.85 m^2 (3.28 × 15.91 ft^2) straight shaft foundation with a chargeability of 90 mV/V was generated. Figure 12-8 shows a strong correlation with the input model down to 3 m (9.84 ft).

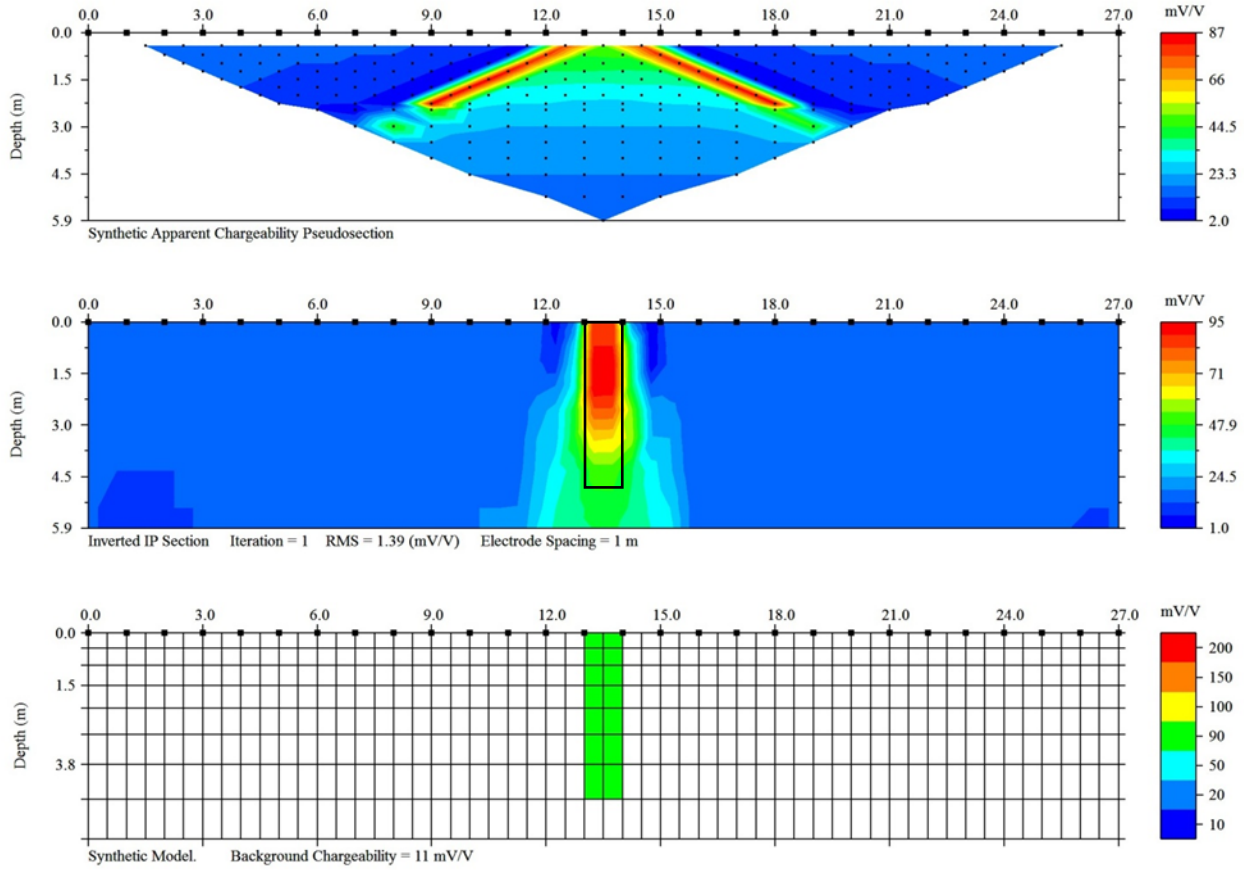

Figure 12-8. 1 × 4.85 m^2 (3.28 × 15.91 ft^2) Straight Shaft Foundation.

The inverted IP section does not, however, show a strong response to the full depth of the model. This lack of full-depth correlation between the synthetic model and final inversion is due to the fact that, with only 28 electrodes spaced 1 meter (3.28 ft), data only is collected to 5.9 m (19.36 ft). These data are shown in the synthetic apparent chargeability pseudosection above, and there is only one data point generated at the bottom and center of this model. In order to gather data deeper

to yield a stronger IP response for more electrodes, more electrodes must be used, making a longer array in the field. To investigate this reasoning, next a 1 × 5.5 m^2 (3.28 × 18.04 ft^2) straight shaft foundation was created using a 56 electrode array instead of a 28 electrode array, still spaced at one meter (3.28 ft). Figure 12-9 demonstrated that using more electrodes in the field will, in fact, generate an IP effect on a foundation to a greater depth of penetration, which was expected. With a 1 meter (3.28 ft) wide foundation and electrode spacing and 56 electrodes, this model gathered a strong IP response to approximately 4.45 m (14.60 ft). It does not, however, gather data to twice the depth of the previous models despite the fact that two times as many electrodes were used.

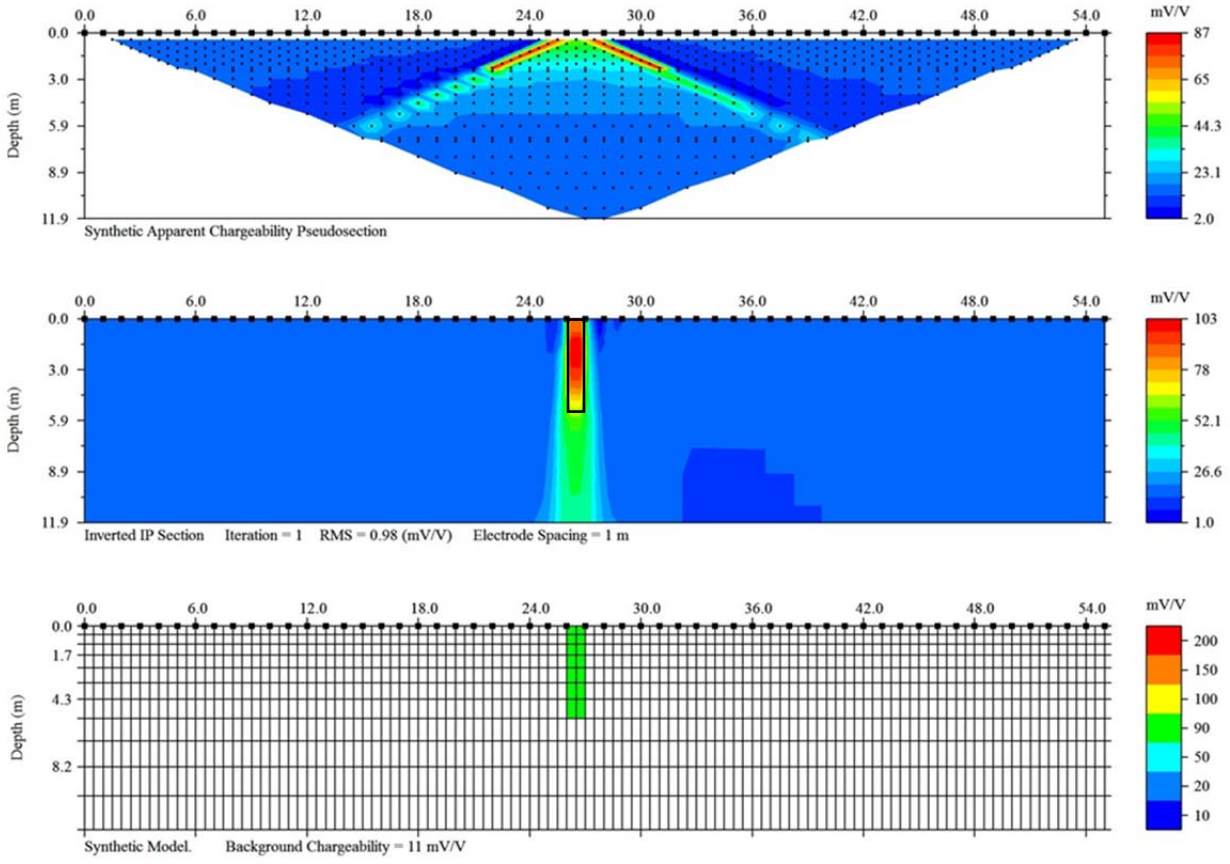

Figure 12-9. 1 × 5.5 m^2 (3.28 × 18.04 ft^2) Straight Shaft Foundation with 56 Electrode Array.

Next, to investigate the influence of the width of the foundation relative to the length of the array, without changing the electrode spacing, a foundation of equal depth, 5.5 m (18.04 ft), was created with a width of 4 m (13.12 ft) as shown in Figure 12-10.

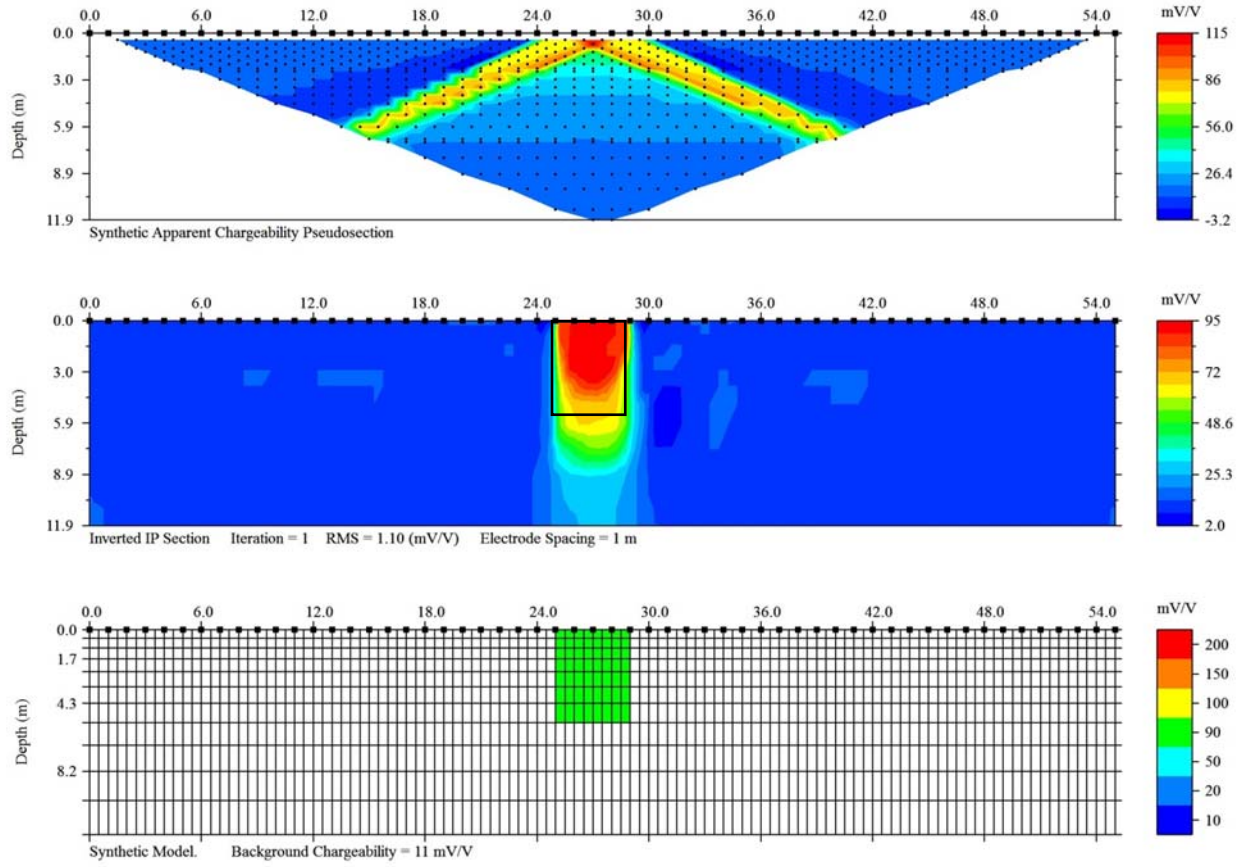

Figure 12-10. 4 × 5.5 m^2 (13.12 × 18.04 ft^2) Straight Shaft Foundation with 56 Electrodes.

The correlation between the synthetic model and the inverted IP section matched much more closely for the larger foundation with less variation in the chargeability on the surface than the smaller foundations.

While deep foundations can be simple straight shaft piles, some bridges also use a pile cap with driven steel H-piles that are much deeper (greater than 10 m [32.81 ft]). For this reason, a forward model of a pile cap with steel piles was also created. The value of chargeability that was assumed for the H-piles, 150 mV/V, was assumed from a brief field test conducted on a galvanized steel pipe that yielded a chargeability of around 200 mV/V (see Figure 12-11). This field test is discussed in the Riverside Campus section within this chapter. Note that, in the deep foundation model, a clear boundary between the reinforced concrete pile cap and the steel piles exists.

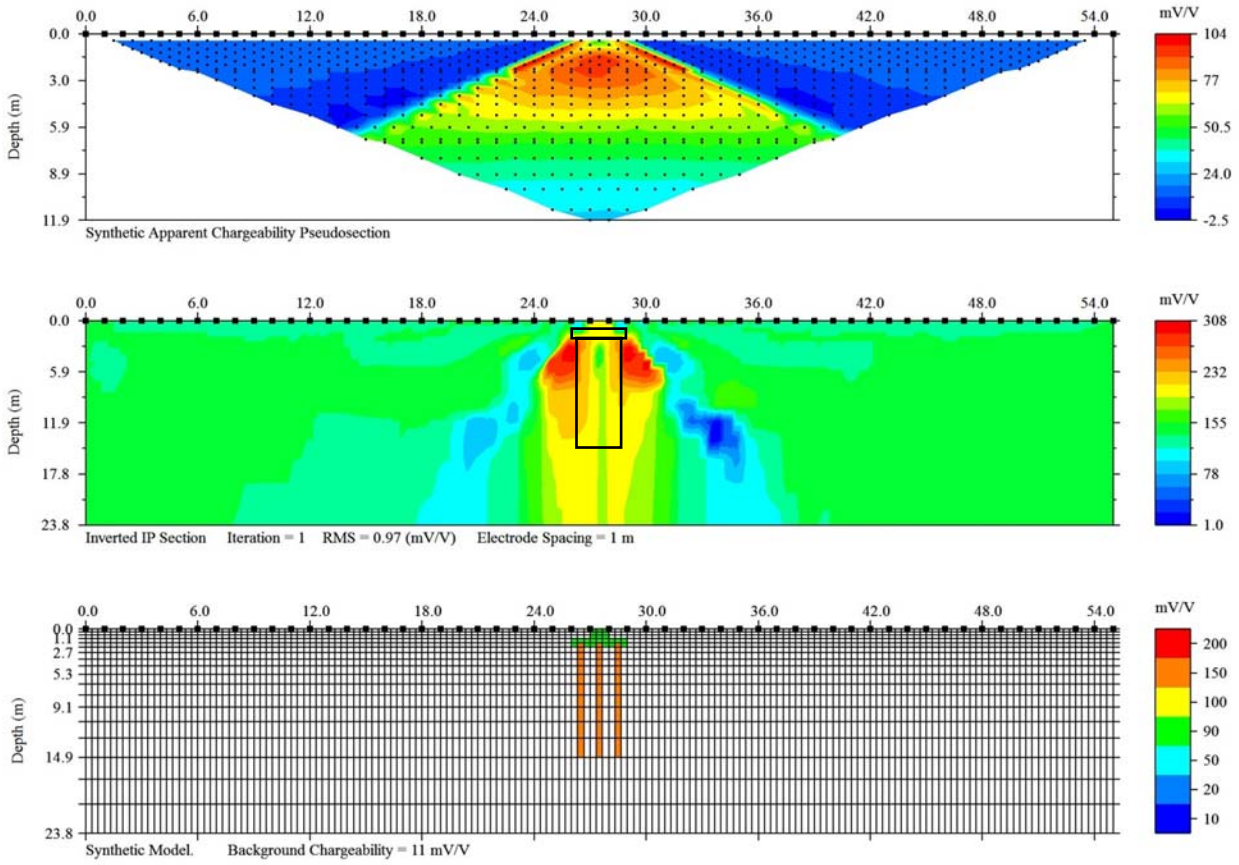

Figure 12-11. Reinforced Concrete Pile Cap with Three 12.5 m (41.01 ft) H-Piles.

Despite the dissimilarities between the synthetic model and the inverted IP section, the inversion showed the clear start of the pure steel versus the reinforced concrete. Steel possesses a much higher chargeability than reinforced concrete. The strong IP response for steel is expected, as previously mentioned. Induced polarization is often used for iron ore exploration (Sumi, 1959). Because the IP effect in steel is much stronger than that of reinforced concrete, the pile cap is much harder to discern despite how close it is to the surface. Yet, because the shaft, which is attached to the cap, will be exposed above the surface in the field, investigators will be able to infer that steel exists below the surface if a strong reaction like this is seen after a field test. This will most likely be in the form of a pile group below a pile cap because of the great increase in chargeability. Also, despite the fact that three piles were included in the synthetic model, only the buildup of the charge is shown on the exterior piles. This is not greatly troubling, however, because knowing the minimum depth of the exterior piles is sufficient information for classifying an unknown bridge foundation to a degree of certainty.

Despite the fact that more data can be collected deeper with more electrodes, currently only 28 non-polarizing electrodes are available for field work at Texas A&M University, so more models were investigated with only 28 electrodes in attempt to optimize field work. While the smaller 28-electrode data collection system yields results that look like the synthetic model, it loses resolution with depth around 4 m (13.12 ft). A solution to this problem was to use more electrodes. However, while the larger array does penetrate deeper, it was not significantly greater than the 28 electrode array, and resources were limited. For this reason, the 28-electrode system was again used but with an electrode spacing of two m (6.56 ft) instead of one m (3.28 ft). The farther the electrodes are spaced, the greater the depth from which the data will be collected. A tradeoff was that resolution of the data was lower.

Compared to Figure 12-8, which had an electrode spacing of 1 m (3.28 ft), Figure 12-12 penetrates deeper, by over 1 m, (3.28 ft). Figure 12-9, which used 56 electrodes, showed an IP response down to 4.45 m (14.60 ft), the same as Figure 12-12, below; however, having the electrode spacing greater than the foundation width caused the resolution to be of lower quality. The inversion appeared to be wider than the model, and data were lost at the top of the foundation. For this reason, the next model (Figure 12-13) was created with both a 2 m (6.56 ft) wide electrode spacing and foundation.

The inversion in Figure 12-13 shows that again the data penetrates with a strong IP response to 4.45 m (14.60 ft) as in Figure 12-12; however, the width of the foundation now also matches the width of the synthetic model. For this reason, it was decided that the electrode spacing should always be equal to or less than the width of the foundation for higher data quality.

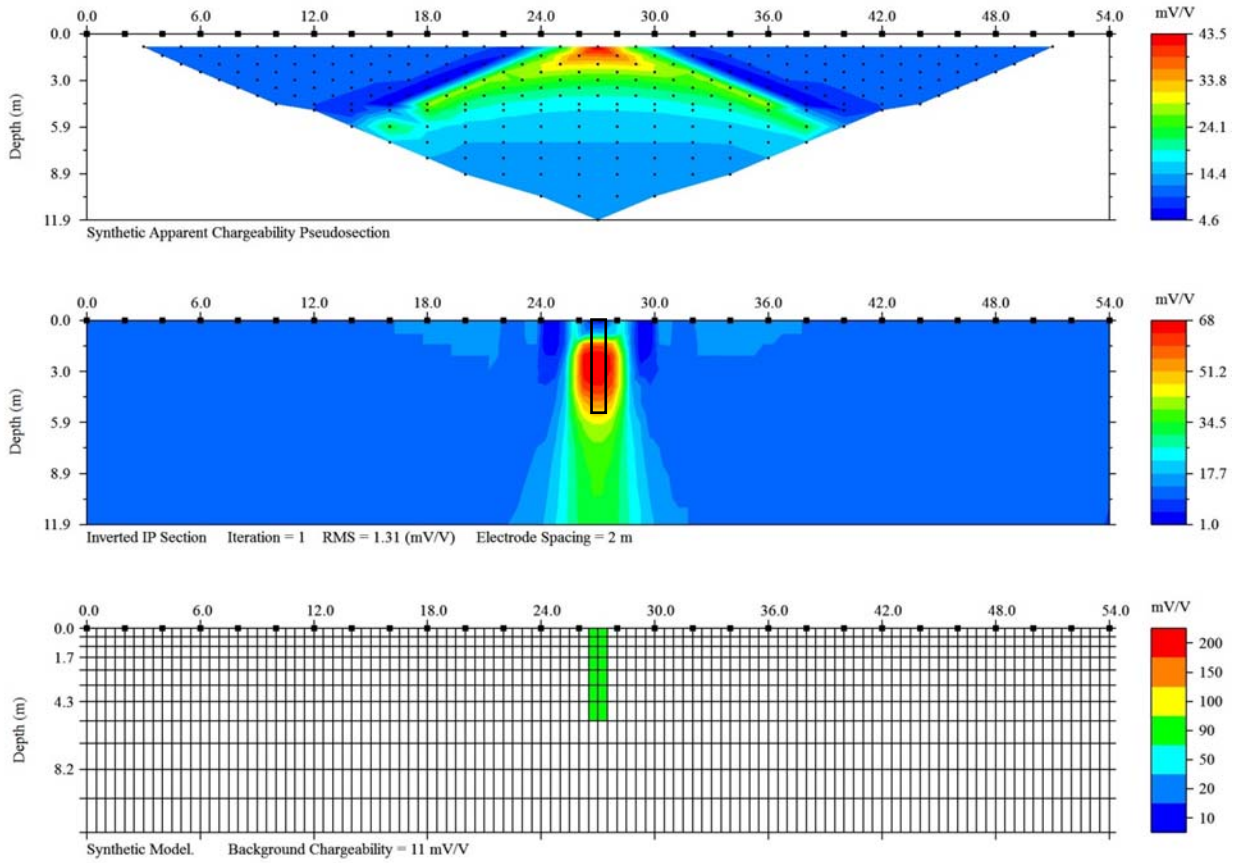

Figure 12-12. 1 × 5.5 m^2 (3.28 × 18.04 ft^2) Straight Shaft with 2 m (6.56 ft) Electrode Spacing.

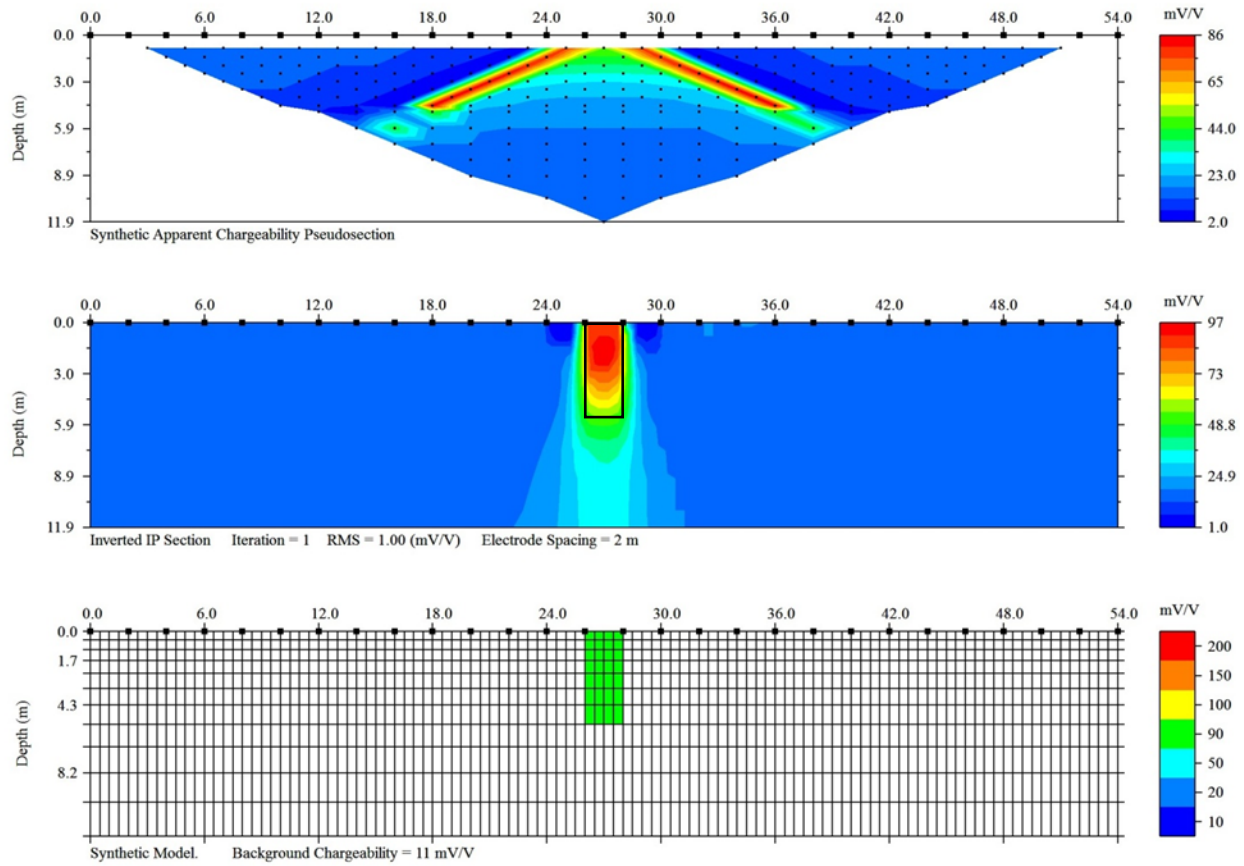

Figure 12-13. 2 × 5.5 m^2 (6.56 × 18.04 ft^2) Straight Shaft with 2 m Electrode Spacing.

Multiple Foundation Models

The shallow foundation that was tested in the field in order to obtain base values for chargeability was modeled in a more complex system. Three spread footings that did not have any soil cover as in Figure 12-7, were modeled to ensure the same results as the field test and to infer on the influences they will have on one another (see Figure 12-14). Because the depth of embedment is small, 1 m (3.28 ft), they did not draw chargeabilities from one another.

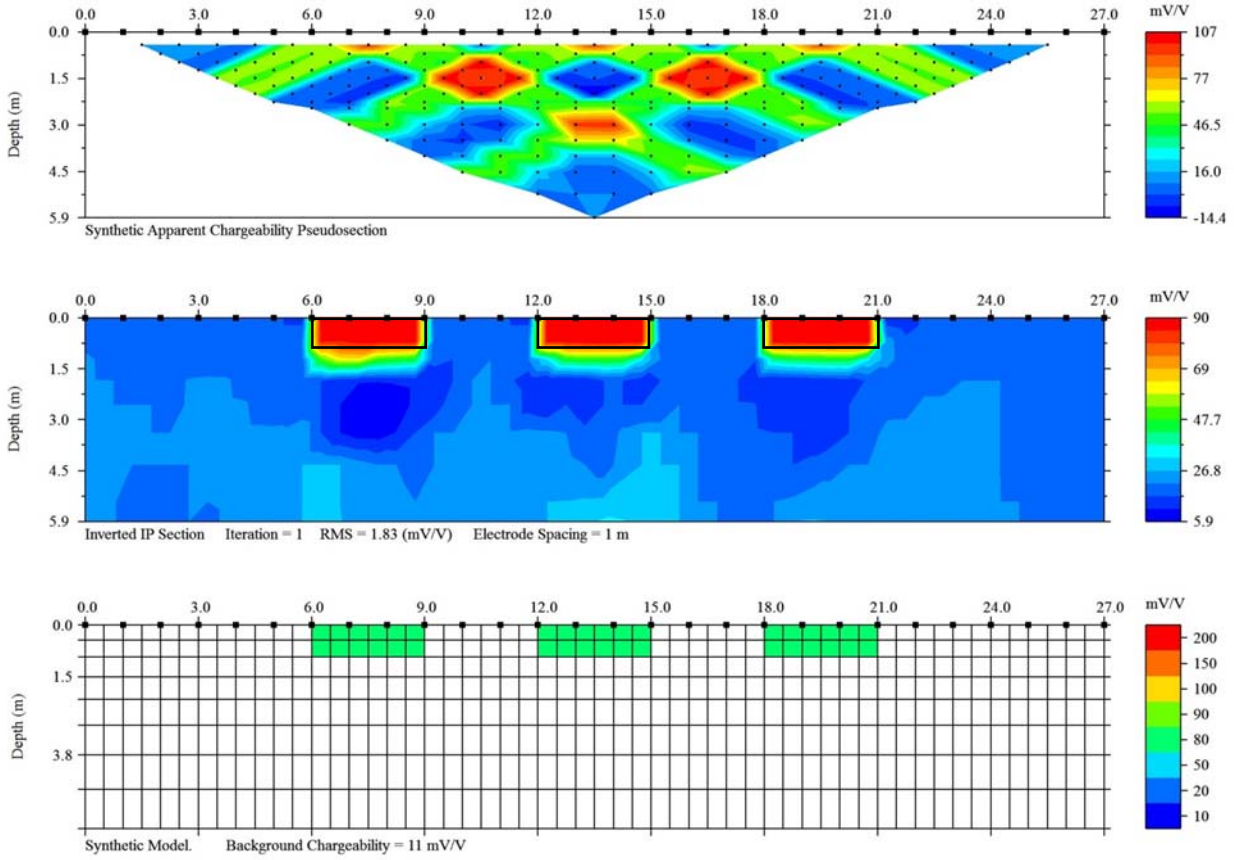

Figure 12-14. Three 3 × 1 m^2 (9.84 × 3.28 ft^2) Footings Spaced at 3 m (9.84 ft).

The strong correlation between these three foundations and the inverted IP section again shows the strength of IP on shallow foundations. For this reason, the foundations were lengthened to 5 m (16.04 ft) and reduced in width to 1 m (3.28 ft), leaving a spacing of 5 m (16.04 ft) between the foundations (see Figure 12-15).

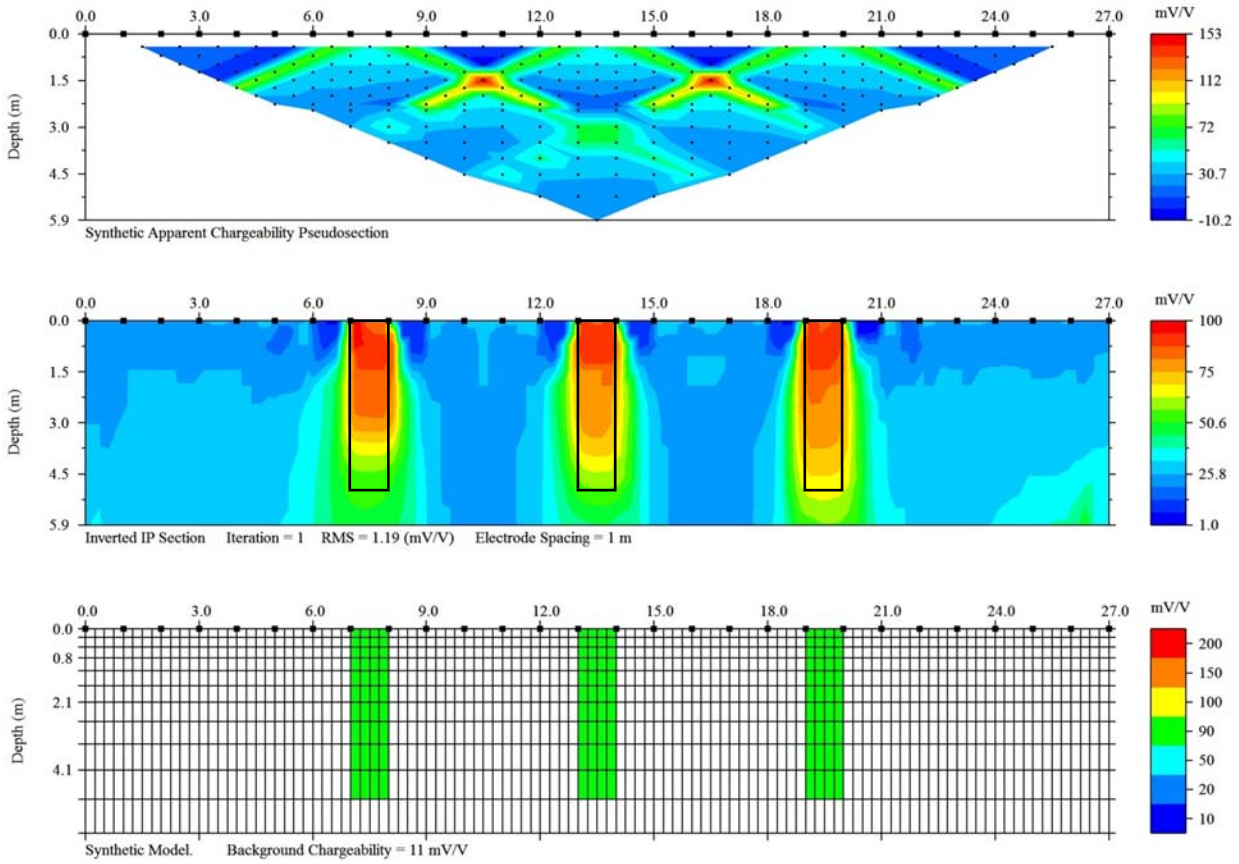

Figure 12-15. Three 1 × 5 m^2 (3.28 × 16.40 ft^2) Straight Shafts Spaced at 5 m (16.40 ft).

With the foundations spaced at 5 m (16.04 ft), some influence can be seen from the surrounding foundations. The high chargeability value does not extend to the bottom of the predicted model as for the single pile deep foundations, but a minimum depth prediction of 3 m (9.84 ft) could still be made with these data. For this reason, it is more advantageous if each pile can be isolated as discussed in the Single Foundation Models section. Alternatively, the farther the piles are spaced apart, the less influence they have on each other. If space was available for a larger array and foundations were spaced far apart, they could be tested as shown below where 56 electrodes are again used instead of 28. With 56 electrodes, 1 × 5.5 m^2 (3.28 × 18.04 ft^2) piles were modeled 10 m (32.81 ft) apart (see Figure 12-16.)

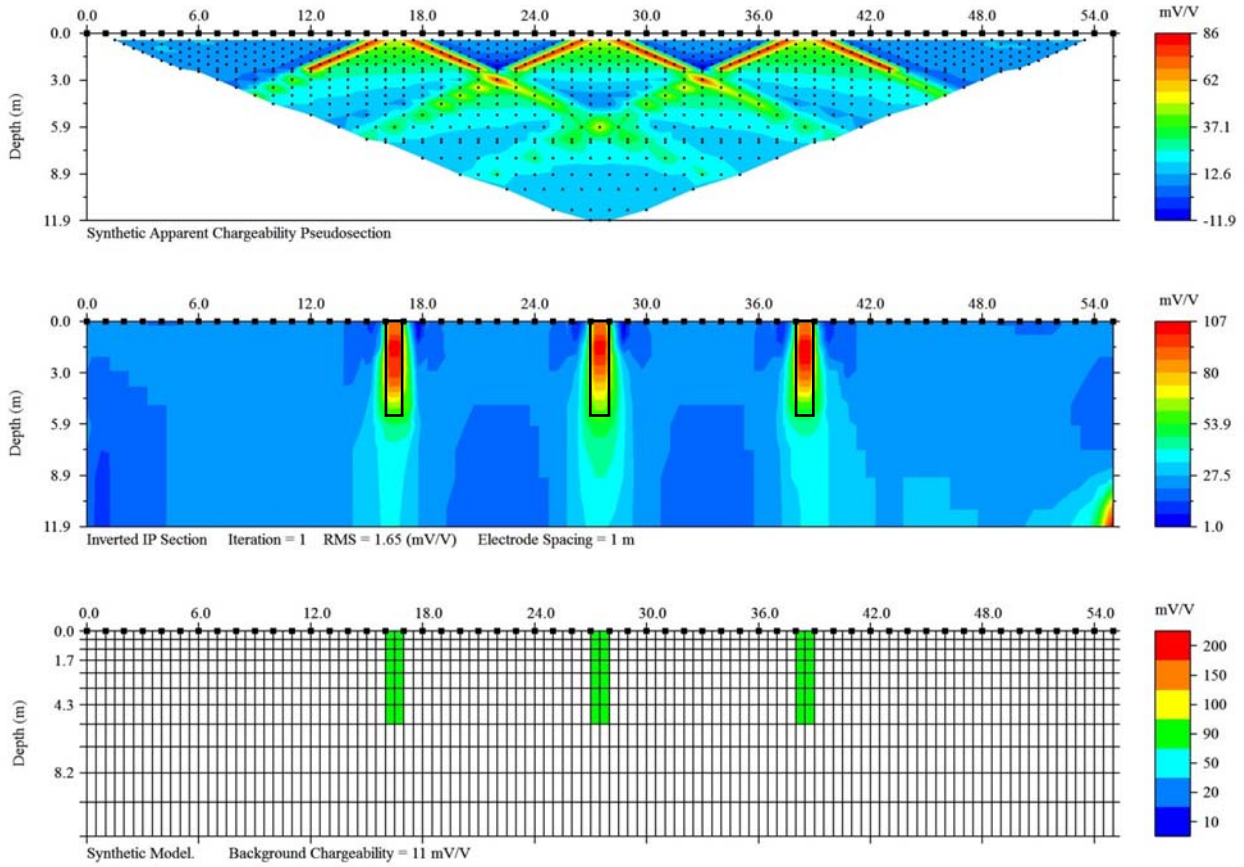

Figure 12-16. Three 1 × 5.5 m^2 (3.28 × 18.04 ft^2) Straight Shafts Spaced at 10 m (32.81 ft).

Using the larger array with 10 m spacing allowed for less influence of each pile on one another. Also, because the array is larger, the inverted IP section shows the piles to a greater depth than the 28-electrode array. For this reason, when the substructure is larger and spaced over 10 m apart, the 56 electrode array is advantageous.

RIVERSIDE CAMPUS TEST

As introduced in the forward model section, Texas A&M University has a NGES at the Riverside Campus on the outskirts of College Station, Texas. The Riverside campus was used as a replacement for the laboratory phase for IP for this project. This was done because there are only foundations at the test site, and they were all installed on level ground. This simplified the testing by eliminating a bridge super structure, unlevel ground that requires surveying, and the possibility of water. Four different foundations, one buried pipe, and one H-pile were tested several times at the Riverside campus to optimize the field setup for bridges. The depths of five

of these materials were known and one, the large 3 × 3 × 1 m^3 (9.84 × 9.84 × 3.28 ft^3) foundation, was identified after testing and data processing was complete.

One Cubic Meter Foundation

Testing began with the smallest known foundation at the sand site, an unreinforced 1 × 1 × 1.2 m^3 (3.28 × 3.28 × 3.94 ft^3) spread footing. The foundation contains a reinforcement cage slightly elevated from the bottom of the footing with #11 rebar spaced 150 mm (5.91 in) center-to-center in both directions. The three PVC pipes that can be seen in Figure 12-17 were set in place to allow the drilling of three telltales after the construction. The telltales were used to measure vertical displacements during loading in another project.

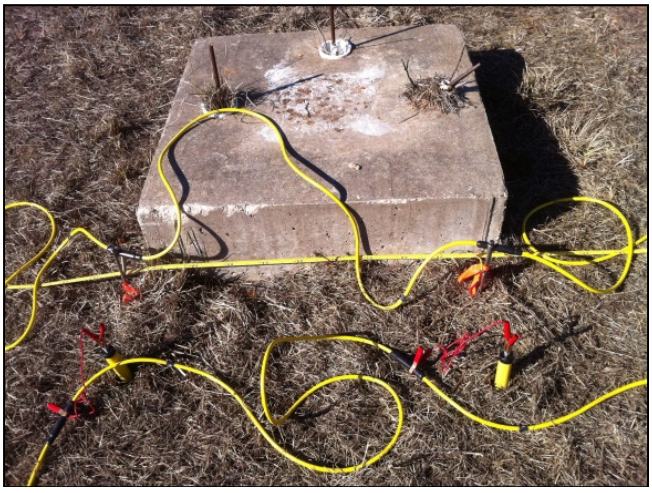

Figure 12-17. Small-Spread Footing.

The initial results from testing the small spread footing were shown in Figure 12-4; however, this foundation was tested several times as a base test for checking the equipment and optimal field setup. Normalized chargeability was applied to each model presented in this section. Because the entire output from one field test has already been shown (Figure 12-4), each model in this section will only be the final IP results. The full results have been included in the appendix for each model along with extra data that have not been presented within the text. Figure 12-18 shows the normalized chargeability results with the actual foundation dimensions overlaid by a black box.

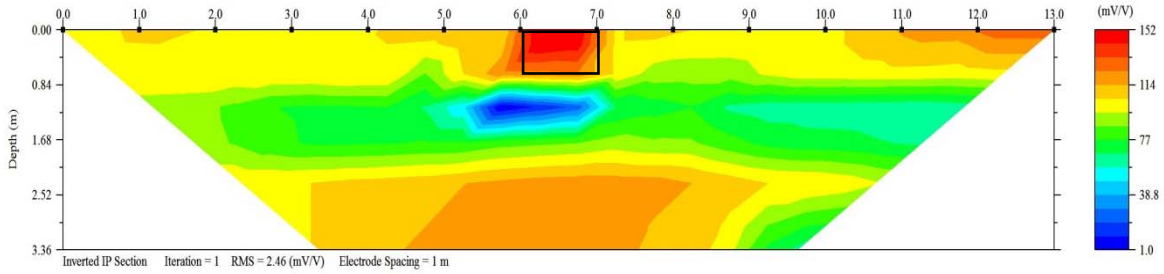

Figure 12-18. Normalized Chargeability Results for Small Footing.

This test, which was repeated several times, shows the strong correlation between the inverted IP results and the actual foundation for a small footing. The strong correlation may be attributed to the mat-like steel cage that is located at the bottom of the foundation.

Once the small foundation was tested several times to validate that the results were repeatable, optimal arrays for testing bridge foundations were investigated. Using the same field setup each time, five different command files were investigated: a Wenner-Schlumberger array, a dipole-dipole array, a pole-pole array, a dipole-dipole array with reciprocal measurements, and a vertical sounding. The dipole-dipole array was recommended for IP surveys, and after investigation it yielded the best results with the least amount of noise. The vertical sounding was the simplest to set up; however, the results were not as clear to interpret as the dipole-dipole array and required more data processing along with more effort to generate the array file.

Similarly, once the optimal array was determined, the dipole-dipole, the optimal setup of the array was investigated. The electrodes were set up so that the foundation was in the middle of the array; however, where the foundation was located relative to the electrodes was changed. Note that in Figure 12-17 the stainless steel electrodes are next to the foundation, and the NP electrodes are farther away. The NP electrodes were also placed next to the foundation with the stainless steel electrodes farther away. Both electrodes were placed next to the foundation, so that the signal was forced to go through the foundation at shallow depths. The latter can be seen in Figure 12-19.

Figure 12-19. Deep Foundation with Optimal Electrode Placement.

Foundation without Reinforcement

After the optimal array was determined from testing on the shallow foundation, a deeper foundation that the resistivity team also investigated was tested. The resistivity team noted that this foundation is approximately 4 m (13.12 ft) deep. The foundation posed a new challenge; however, because it is surrounded by a tarp at the top of the foundation that is thought to go the full length of the foundation. Also, it is believed that the foundation is not reinforced.

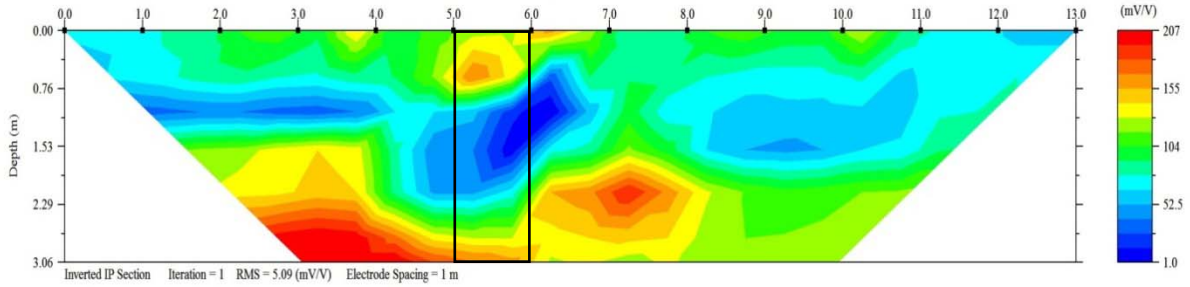

Figure 12-20. Results from Unreinforced Pile.

The lack of any high chargeability expected from foundations supports the hypothesis that this foundation does not contain any reinforcement. The extremely low chargeability in the middle of the foundation may be due to the tarp, which most likely contains non-chargeable plastics. Because no more intermediate length piles exist at the NGES sand site, the research group then tested a deep pile.

Deep Pile

In addition to the small spread footings that have been put in place at the NGES, five deep foundations were installed on a nearby embankment. These 0.9 m (2.95 ft) in diameter foundations were installed to depths varying from 15.8 m (51.84 ft) to 10.4 m (34.12 ft) below the ground surface for a previous project at the experiment site. Once the 1 m (3.28 ft) shallow foundation was tested successfully and following the identification of the failure for the intermediate foundation due to the tarp or lack of reinforcement, the research team moved on to testing one of the deep piles to more closely simulate field conditions. Most bridges have deep foundations, not shallow. Several of these foundations have deteriorated over time as shown in Figure 12-21. An exposed reinforcing cage can be seen in the third and fifth foundation, and the foundation closest to the photographer shows deep cracks along the side of the exposed top. For this reason, the least deteriorated of the five foundations was chosen for the deep foundation testing.

Figure 12-21. Five Straight Shaft Foundations at the NGES.

Figure 12-19 shows the field setup for the test run for the deep foundation where 14 stainless steel and 14 NP electrodes were used spaced at 1 m (3.28 ft) intervals. Only 14 electrodes were used at this time because of limited space available. The results are disheartening because they do not show a clear foundation as in the small foundation; however, a strong charge up can be seen at the bottom of the figure. It is known that the foundation is over three times deeper than the depth of penetration in the image shown in Figure 12-22.

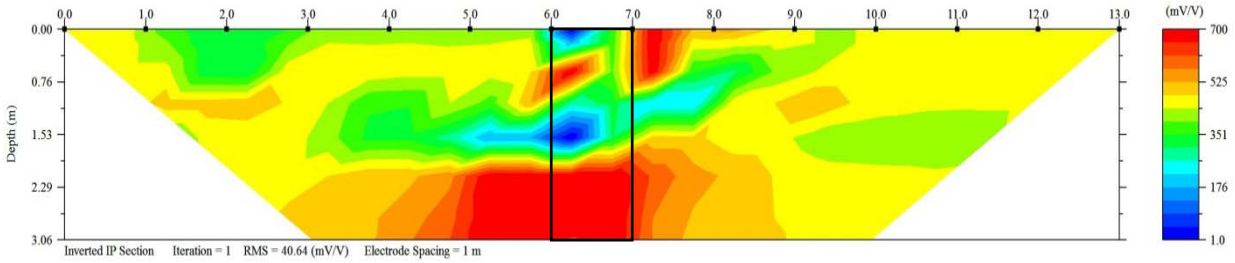

Figure 12-22. Deep Pile.

Despite the little correlation between the inverted section and the actual pile, the array was not rerun with more electrodes. Space was limited, and with 28 electrodes, the depth of penetration is less than 6 m (19.69 ft). This depth is still less than half the depth of the pile, which is 10.8 m (35.43 ft). The strong charge up at the bottom of the inversion still provides the researchers with some information. While the finite depth of the foundation cannot be determined from this test, a minimum depth can be estimated. Also, should more electrodes (the full 28) be used, this minimum depth would be deeper, proving more useful. Note that the chargeability for this foundation was much higher than previous and later foundations that were tested. This high chargeability may be due to deterioration of the pile. As previously discussed, the other four piles at the site show significant deterioration of the pile above the ground. It is a reasonable assumption that this deterioration continues down the piles in various locations. They were designed for dynamic and static testing, and each pile contains intended defects.

Pipe

As previously mentioned, a galvanized steel gas line imbedded at a known depth was also tested in order to obtain an estimate for steel, to use in a forward model (Figure 12-23). The depth of this pipe is known from numerous tests. The array was set up perpendicular to the direction of the pipe, so the pipe and line crossed at the middle of the array.

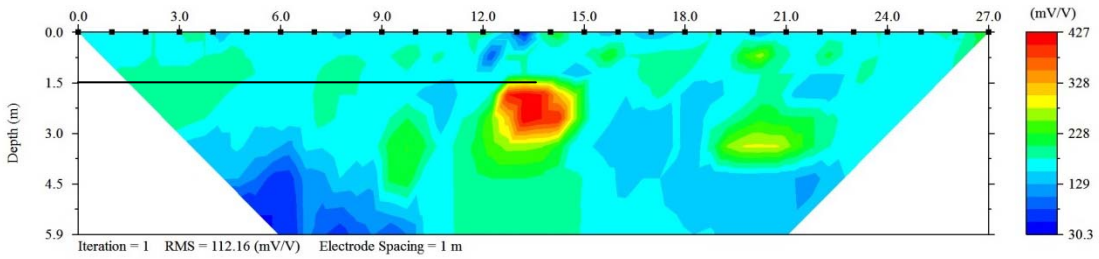

Figure 12-23. Gas Line Test.

While the exact dimensions of the pipe are not known because as-built plans were not located, numerous nondestructive tests have indicated that the pipe is located 1.5 m (4.92 ft) below the ground surface, which is where the strong IP response appears. While the diameter of the pipe may be exaggerated, the depth can be easily identified from this test.

Large Foundation

The large foundation at the experiment site was constructed for a research project on dynamic impedance functions of shallow foundations. A 3 × 3 × 1 m^3 (9.84 × 9.84 × 3.28 ft^3) fully embedded footing was constructed, fully reinforced with #6 reinforcing steel every 12.7 cm (5 in).

The results, as shown below in Figure 12-24, indicate that the foundation is approximately 1.22 m (4.00 ft).

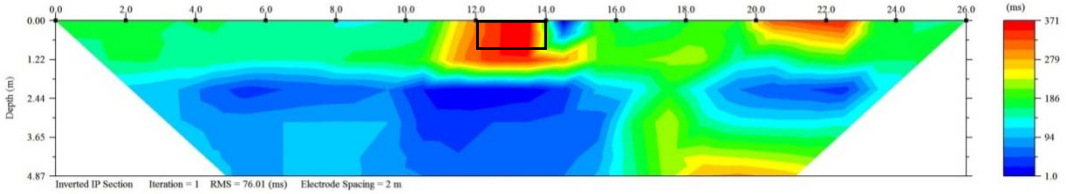

Figure 12-24. 3 m × 3 m × 1 m (9.84 ft × 9.84 ft × 3.28 ft) Foundation.

Note that the results shown appear to be a 2 m (6.56 ft) wide foundation even though the foundation is in fact 3 × 3 m^2 (9.84 × 9.84 ft^2). This is because the spacing between the take outs on the SuperSting cables are spaced at 2.5 m (8.20 ft), so the array could not be set up to fully span the foundation. For this reason, electrodes were spaced at 2 m (6.56 ft) intervals, and the array crossed the foundation on a bias. The results show a foundation depth of approximately

1.22 m (4 ft), 0.22 m (0.72 ft) deeper than the actual foundation. The additional strong chargeability between the electrodes at 20 m (65.62 ft) and 22 m (72.18 ft) down the line on the right side is due to another foundation at the sand site that the array side scanned.

H-pile

A final field test was conducted at the Riverside campus because several bridges across Texas have driven steel H-pile foundations. Texas A&M University has 17 driven H-piles at the NGES, which were tested before a steel H-pile bridge was considered. The pile tested can be seen in Figure 12-25.

Figure 12-25. H-Piles at the NGES.

Preliminary tests were necessary because IP produces a much stronger response for steel than concrete. While concrete does hold a surface charge, it is not as easily charged as steel or other metals. For this reason, initial testing of steel leads to chargeabilities too high for the post processing to handle, so adjustments in the testing procedure had to be made. All other tests have been run at the maximum current that the equipment allowed: 2000 mA; however, when this was done for steel, the chargeabilities greatly exceeded the maximum IP. Another test was run with the maximum current lowered to 700 mA, and the results were better. However, the best results, which can be seen in Figure 12-26, were achieved with a maximum current of 500 mA.

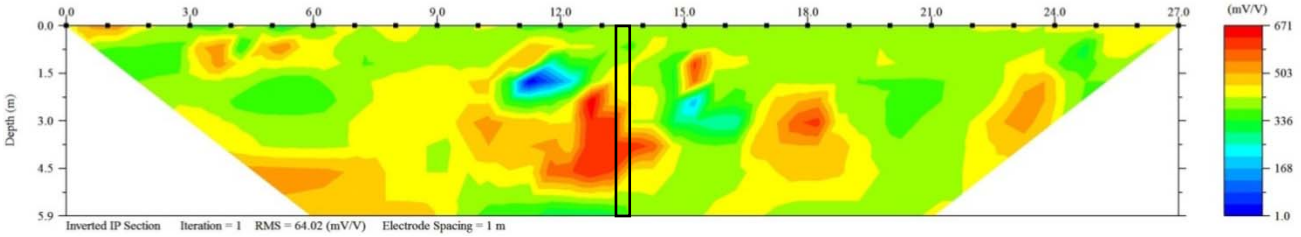

Figure 12-26. H-Pile Results with 500 mA Max Current.

The strong response from the steel H-pile can be seen around built up near the 13th and 14th electrodes. The H-pile is not 1 m (3.28 ft) wide like the array, so the results are not as sharp as with previous tests. The large 1 m (3.28 ft) spacing was used over the width of the H-pile because of the depth to which the H-pile is buried. Closer electrode spacing would lead to a shorter depth of penetration. Using a 28 m (91.86 ft) long array, the depth of penetration is still only 5.9 m (19.36 ft), which is not deeper than the foundation. Despite this, the strong charge build up to 5.25 m (17.22 ft) is still noted. The other areas of strong charges are likely due to the other H-piles next to where the array was set up.

FULL-SCALE BRIDGE TEST

Finally, once all useful foundations at the NGES were tested several times and the data were processed, the research team tested three bridges within the Brazos District with known foundations. All of these bridges have straight shaft concrete piles, one with 3.66 m (12 ft) piles over no water, one with 6.10 m (20 ft) piles with no water, and one with 3.66 m (12 ft) piles over a very shallow creek. The first two were tested to determine the maximum depth of penetration to which accurate data can be gathered, so a foundation depth could be estimated. The bridge with a shallow creek was tested because it is a shallow foundation that would enable good results and introduced a new variable, water.

Clear Creek Bridge

Bridge 17-145-1147-01-017 is located in Leon County, Texas on FM 977, 1.15 miles southeast of FM 3. It is a minor collector road that was built in 1988 and is 55.5 m (182.1 ft) long and 10.5 m (34.5 ft) wide from curb to curb. It crosses the Clear Creek; however, the creek is so low that only one pile group goes through it. Two dry pile groups, including the one tested, can be seen in Figure 12-27.

Figure 12-27. Bridge 17-145-1147-01-017.

The array was set up two different ways on separate testing days. First, the electrode spacing was the standard 1 m (3.28 ft) in order to gather data to 5.9 m (19.36 ft), deeper than the 3.66 m (12 ft) piles. Results are shown in Figure 12-28.

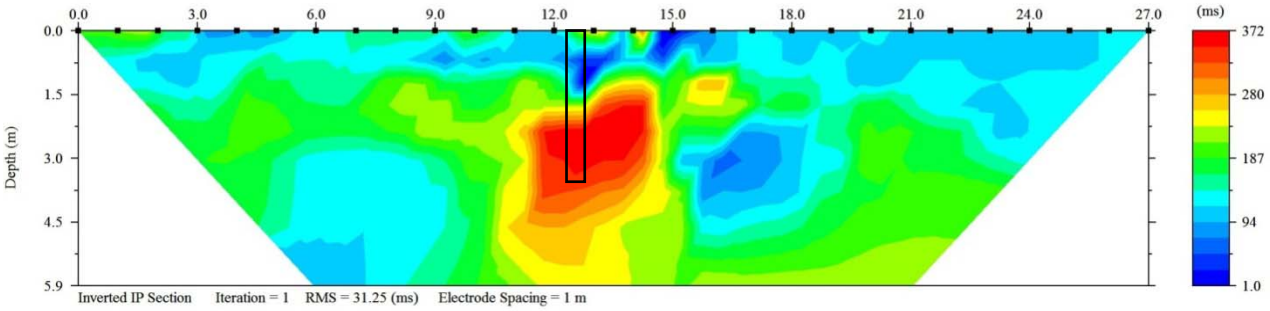

Figure 12-28. Bridge 17-145-1147-01-017 with 1 m (3.28 ft) Spacing.

The results gathered data to the full depth of the pile; however, they did not show a high chargeability at the top of the pile. This may be due to the fact that the current is not transmitted in the 2D plane; instead, it spreads outward in a circular 3D plane that may not capture the upper portion of the foundation. Despite this, a strong chargeability is shown at the bottom half of the foundation with a chargeability much higher than that of natural objects within the ground. The chargeability of the foundation, however, appears to cover a much larger area than the actual foundation. This anomaly occurs when the foundation is not as wide as the electrode array. For this reason, the bridge over Clear Creek was retested with an electrode spacing of 0.57 m (1.87 ft), the width of the widest part of the foundation. Results are shown in Figure 12-29.

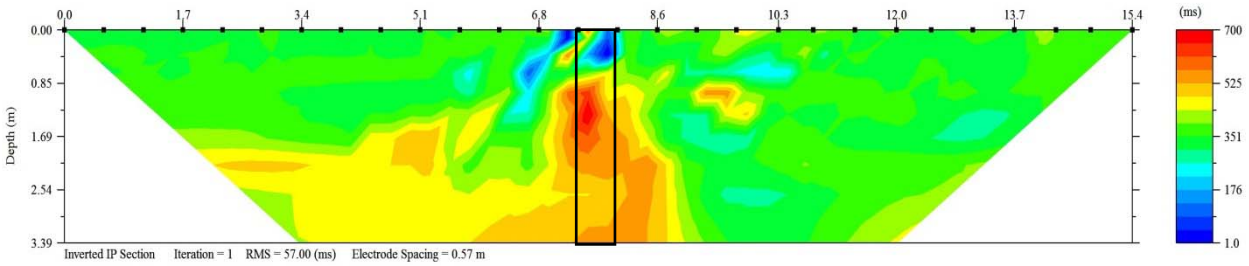

Figure 12-29. Bridge 17-145-1147-01-017 with .57 m (1.87 ft) Spacing.

Despite the smaller electrode spacing, which confined the IP response to the width of the foundation, the results no longer penetrated to the full depth of the foundation, so there is no strong stop in the response as in Figure 12-27. These different testing procedures show the importance of gathering data beyond the depth of the foundation.

Davidson Creek Bridge

Bridge 17-026-0116-03-037 is located in Burleson County, Texas on SH 21 0.2 miles northeast of SH 36 outside of Caldwell, Texas. It is a principal arterial road that was built in 1968 and reconstructed in 1988. It is 97.5 m (319.9 ft) long and 19.9 m (65.3 ft) wide from curb to curb. Davidson Creek was entirely dry at the time of testing as shown in Figure 12-30.

Figure 12-30. Bridge 17-026-0116-03-037.

A 10.8 m (35.43 ft) long electrode array was used, using 28 NP and 28 stainless steel electrodes spaced 0.4 m (1.31 ft) or the pile diameter. The Davidson Creek was dry at the time of testing.

However, the pile tested was chosen because the array could be set up on a nearly level ground surface, so that surveying was not necessary. Figure 12-31 shows the long array, along with the level ground surface.

Figure 12-31. Field Setup for Bridge 17-026-0116-03-037.

The small electrode spacing of 0.4 m (1.31 ft) led to a shallower depth of penetration of the data, 2.07 m (6.79 ft). Unfortunately, the pile was again deeper than the depth of penetration, 5.47 m (18 ft), which led to poor resolution in the inversion (see Figure 12-32).

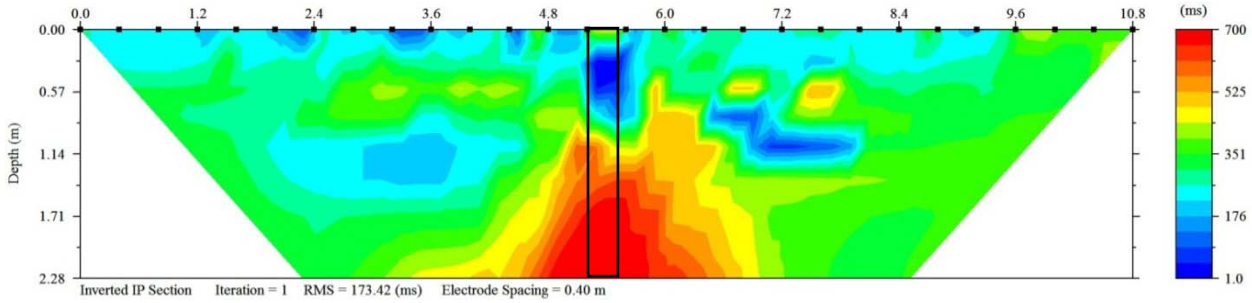

Figure 12-32. Inversion of Bridge 17-026-0116-037.

Again, the highly chargeable area at the bottom of the image is due to the foundation going much deeper than the data were collected. Also, this field test yielded lower quality results because the soil was found to be highly conductive, which was a new field anomaly. Numerous data sets were collected at this bridge, each showing the soil to be highly conductive. This affected the

output; however, by increasing the estimated noise of the IP data collected, the results were improved.

Gum Creek Bridge

Bridge 17-094-0315-02-019 is located in Grimes County, Texas, on SH 90, 3.75 miles north of SH 30 outside of Roans Prairie, Texas. It is a minor arterial road that was built in 1927 and reconstructed in 1960 and is 36.6 m (121.1 ft) long and 13 m (42.7 ft) wide from curb to curb. Gum Creek was flowing over two pile groups at the time of testing; stagnant water was in a small channel sitting in the traffic direction the full length of the bridge. Despite the stagnant water channel, the array was set up in the traffic direction to enable the test to be run through the water and keep the cables dry (see Figure 12-33.

Figure 12-33. Field Setup for Bridge 17-094-0315-02-019.

Electrodes were spaced 1 m (3.28 ft), again using 28 NP and 28 stainless steel electrodes. Two piles were tested, directly in the array path; however, two more were side scanned because of their nearness to the array. Also, the first electrode was placed within 1 m (3.28 ft) of the bridge abutment. Figure 12-34 shows the two piles that the array bisects.

Figure 12-34. Two Piles Tested through Water.

Note that the electrodes are not flush on the sides of the foundations, but are instead spaced 1 m (3.28 ft) apart. While this lowers the resolution of the results, more accurate results on the depth of the foundation are achieved when the array penetrates deeper than the foundation depth. The piles were located between the eighth and ninth electrodes and the 13th and 14th.

Several field tests were run on this bridge, as it was the first one tested through water. Most of the results were extremely noisy, with a high jump in the data over random windows in the IP data collection. Also, the water proved to make the subsurface highly chargeable, much higher than soil that was not fully saturated during the other tests. This test, Figure 12-35, shows some highly charged areas that are within the bounds of the chargeability when data are collected deeper than the foundation. The high area around the 20th electrode is due to another pile that was side scanned by the array, and the other high area near the 25th and 26th electrode is due to another pile. Figure 12-35 also shows the piles that were side scanned. Despite these promising results, the inversion took many iterations of different inversions to come to this conclusion. If the foundations were indeed unknown, a minimum depth of these foundations would have been difficult to determine with an acceptable degree of certainty.

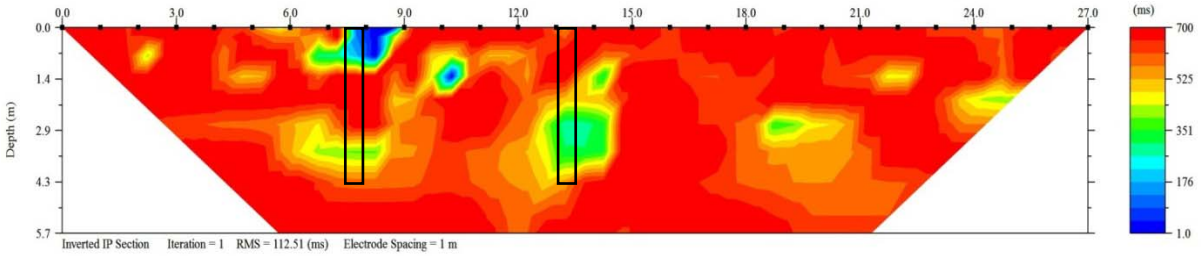

Figure 12-35. Inversion for Bridge 17-094-0315-02-019 through Water.

PART IV.
CONCLUSIONS

EVIDENCE-BASED APPROACH CONCLUSIONS

An evidence-based approach is proposed in this study, providing a comprehensive tool to determine the unknown bridge foundations. The proposed guidelines are capable of generating both deterministic and probabilistic predictions of foundation types and dimensions. It can also generate probabilistic prediction of soil resistance parameters (Su and Pb) when the soil-boring data are not available.

ANNs proved to be successful in recognizing complex patterns between embedment depth and foundation type. ANNs were also able to predict the bearing capacity of bridge foundations with reasonable accuracy.

Regarding the uncertainty in the ANN predictions, the Bayesian paradigm and the MCMC sampling method were implemented to quantify the uncertainty in the unknown determination process. This was achieved by conditioning estimates of the characteristics of the unknown foundation on the superstructure characteristics and the estimate of the corresponding bearing capacity, resulting in joint probability distributions for unknown features of a bridge foundation, rather than only one prediction. These allowed to measure the influence of incorporating evidence into the determination of unknown foundations and to assess the correlation (linear and non-linear) between the foundation's parameters. Furthermore, it was verified that for all problem types, single modes concentrated the most likely scenarios of the uncertain foundation parameters.

The use of the marginal posterior CDFs for different foundation types, dimensions and soil resistance parameters can be used to make probabilistic inferences for these parameters. For instance, for a specific embedment depth value, it is possible to assess the probability of not exceeding a specific depth. (It may be likely that the actual embedment depth exceeded the researchers' estimation.)

Results from the probabilistic approach for one of the bridges in the Bryan District showed that the actual unknown values are close to the predicted mode value (value with maximum probability) of the corresponding posterior distributions. This cross-validates the effectiveness of the proposed methodology.

The proposed guideline can be used to determine the unknown bridge foundations in any district if the conditions allow for an evidence-based approach to be implemented, to quantify the influence of varying pieces of information about the foundation characteristics of a given bridge.

It must be emphasized, that since the present study was based on a working database populated in the TxDOT Bryan District, results can only be applicable to this specific demarcation. Nevertheless, the proposed methodology can be used to make predictions about any unknown bridge foundation at any other place, as long as evidence about known foundation characteristics can be used to train and condition the corresponding models.

VIBRATION-METHOD CONCLUSIONS

The vibration method was tested in a laboratory setting and under field conditions at two bridges. It was also numerically modeled while field tests were conducted. In the laboratory setting, two concrete slabs were buried at different depths in the Haynes Coastal Engineering Laboratory at Texas A&M University using an experimental modal analysis. These slabs were buried in the 2D tow-dredge tank in the Haynes Lab. Using an accelerometer placed in the center of each slab and a rubber mallet, the research group measured the acceleration versus time of the vibrations of these slabs. After applying a Fast Fourier Transform to these data, the amplitude of the response versus the frequency was obtained for each slab. The results were as expected, showing a difference in the two frequencies; the foundation that was buried deeper had a higher frequency, which was also expected.

After a successful simplified laboratory test, the researchers moved to the field to test bridges. Using three accelerometers placed directly on the pile, the researchers attempted to excite the pile again using the mallet, using a hammer fit with a built-in force transducer, and using heavy traffic. Unfortunately, when inspecting these results, no dominant frequency could be seen as in the laboratory setting. Next, the researchers attached the three accelerometers to the bridge bent instead of the pile, this time in three different directions. Using heavy traffic and recording the vibrations with an oscilloscope, they again recorded acceleration versus time and transferred the data into the frequency domain. Again, no dominant frequency could be seen and the data appeared to be nosier than when attaching the electrodes directly to the pile.

While field experiments were implemented, several numerical models were also developed to determine the feasibility of modeling the field work in order to decrease the time spent in the field. These simplified and complex bridge models were created for a simultaneous project on bridge scour (Briaud et al. 2011). Unfortunately, a dramatic change in the frequency of the models was also not found when the pile lengths were increased. Thus, despite the promising laboratory work, because a dominant frequency could not be identified in field work and because numerical modeling showed that the frequency did not change dramatically with a change in the pile depth of embedment, the researchers shifted their efforts to enhance the geophysical team with IP testing.

ELECTRICAL RESISTIVITY IMAGING CONCLUSIONS

The 2D-ERI method is a powerful non-invasive geophysical technique for bridge foundation investigations. The method can be deployed in moderate to heavily vegetated, water-covered environments using underwater electrodes, such as those specially designed for this project. The dipole-dipole electrode configuration is preferred since it has good capabilities to map slender vertical structures. A fully 3D-ERI survey is time-consuming, and the resulting images are not much better than their 2D counterparts. Hence, 3D-ERI is not considered to be cost-effective at bridge sites.

The ERI method is made easier at bridge sites since the lateral positions of foundations are known in advance. The depth of a foundation can be estimated by visual inspection of the resistivity image, although precise determination of the length of slender foundations is challenging. The sign of the resistivity anomaly of a reinforced concrete foundation is related to its physical condition. A foundation in poor condition is typically a zone of low resistivity if there are conductive rebar elements in contact with soil. Conversely, an intact foundation in excellent conduction is likely to be a zone of high resistivity.

The ERI method has been tested with different electrode spacings on different sizes and types of foundation. Due to the reduction in spatial resolution of the resistivity method with depth, imaging a small and slender foundation with a size smaller than 1 m (3.28 ft) to a depth of greater than 5 m (16.40 ft) is difficult. There is also a tradeoff between electrode spacing and depth of penetration. The penetration depth of the dipole-dipole configuration is ~20 percent of the profile length. The

smallest advisable electrode spacing is 1 m (3.28 ft), using 56 electrodes. For a large foundation of greater than 3 m (9.84 ft) diameter, an appropriate electrode spacing is 1.5 m (4.92 ft).

Electrical resistivity of earth materials is related to bulk physical properties such as porosity, water content, clay content, lithology, and fracture density. The electrical resistivity method requires a significant resistivity contrast to image subsurface structures. For example, if the earth materials surrounding the foundation are intact rocks, the high background resistivity can approach that of an intact concrete foundation. If the surrounding earth materials are clay or shale, the low background resistivity can approach that of a reinforced concrete foundation in poor condition. In either of these cases, it is difficult to obtain a distinct foundation image.

In water-covered areas, direct contact of electrode stakes to the riverbed is recommended to achieve greater sensitivity to foundations than could be obtained with floating electrodes. Depth of water should be not more than two to three times the electrode spacing. Bridge sites should be accessed during non-flood season. Bridge foundation materials may be steel, wood, concrete, or masonry. In this research, the ERI method has been carried out on concrete foundations only. It is often sufficient to image only the upper portion of the foundation to assess bridge safety from scour hazard. The researchers find, in general, that it is possible to image and identify foundations possessing large resistivity contrasts to their scour-critical depths.

IP CONCLUSIONS

IP is a new nondestructive geophysical technique for unknown bridge foundations. The arrays used for IP are similar to those used for 2D-ERI, so IP can be easily assimilated into a testing plan where resistivity testing is used and vice versa. Also, as with ERI, the dipole-dipole electrode configuration is preferred since it yielded the best results for reinforced foundations. When comparing the standard apparent chargeability measurement to a modified normalized chargeability measurement, normalized chargeability greatly reduces noise, making the inversion more clear. Field measurements can be converted to normalized chargeability by preprocessing the data. This preprocessing involves dividing the IP windows by the resistivity value for that point. The data can then be uploaded into *EarthImager 2D*.

It was determined through both forward modeling and field testing that the electrode spacing is highly influential on the quality of the inversion output. While similar to ERI, a wider electrode spacing will create a longer array that in turn will increase the depth of penetration of the dipole-dipole configuration. If the spacing is wider than the foundation width, there is a loss of resolution in the inversion. This loss or resolution leads to the foundation appearing to be wider than it in fact is. However, a more definitive foundation depth can be seen if this larger array has a depth of penetration that exceeds than the foundation depth.

The depth of penetration is also related to the amount of space available for testing and the number of electrodes used. While data were only collected to 3.66 m (12 ft), if more non-polarizing electrodes and cables are obtained, a larger array can be used if space is available, which will gather data from greater depths. Despite this, a trend can be seen in Table 13-1. Reinforced concrete appears to have a normalized chargeability between 350 and 400 mV/V on average when data are collected deeper than the foundation depth. Each of these images presented shows a clear foundation depth, overestimating the actual foundation by no more than 0.64 m (2.10 ft). For the foundations where data were not collected deeper than the actual foundation, the chargeability is much higher, 671−700 mV/V. This high chargeability appears clustered at the bottom of the inversion directly below the location of the foundation, which can be seen from the surface. Using this information, a minimum depth of the foundation can be given; this depth can be used to update the bridge database for assessing scour-critical bridges.

Finally, while it is possible to test bridge foundations through water using IP, the inversion process is much more complex. While the results shown for the Gum Creek Bridge provided accurate results, this was achieved after many iterations. Without previous knowledge of the bridge foundation depth, this testing procedure would be difficult to use with an appropriate degree of certainty.

Table 13-1. Summary of IP Images Presented.

Foundation Depth		Chargeability	Material	Location	Comment
m	ft	mV/V	-	-	-
0.8	2.62	152	Reinforced Concrete	NGES	-
Unknown Pile		1	Concrete	NGES	Believed to be unreinforced
10.8	35.43	700	Reinforced Concrete	NGES	Data not collected deep enough
1.5	4.92	427	Steel	Riverside Campus	Gas Pipe
1	3.28	371	Reinforced Concrete	NGES	-
Unknown Pile		671	Steel	NGES	Data not collected deep enough
3.66	12	372	Reinforced Concrete	Leon County	-
3.66	12	700	Reinforced Concrete	Leon County	Data not collected deep enough
6.1	20	700	Reinforced Concrete	Burleson County	Data not collected deep enough
3.66	12	351	Reinforced Concrete	Grimes County	Water

The researchers feel that IP can be used for determining the depth of unknown foundations made of both steel and reinforced concrete provided that access is available below the super structure to the bridge foundations. If there are enough electrodes or enough space for an array that will provide results with a depth of penetration deeper than the unknown foundation, a foundation depth can be given within less than 1 m (3.28 ft). If the depth of penetration is not deeper than the foundation depth, a minimum depth of the foundation can be estimated based on the depth of penetration.

REFERENCES

AASHTO. 2002. AASHTO Standard Specifications for Highway Bridges. American Association of State Highway and Transportation Officials.

AASHTO. 2002. LRFD Highway Bridge Design Specifications. American Association of State Highway and Transportation Officials,.

AGI (Advanced Geosciences, I. 2006. *Instruction Manual for the SuperSting^{tm} with Swift^{tm} Automatic Resistivity and Ip System*.

Altair. 2003. *Altair Hypermesh 6.0*.

Apparao, A., Srinivas, G.S., Sarma, V.S., Thomas, M.S., and Prasad, P.R. 2000. Depth and Detection of Highly Conducting Volume Polarizable Targets Using Induced Polarization. *Geophysical Prospecting* **48**, 979-813.

Archie, G.E. 1942. The Electrical Resistivity Log as an Aid in Determining Some Reservoir Characteristics. *Trans. Am. Inst. Mining. Metall. Eng.* **146**, 54-61.

Asquith, G.B. 1995. Determining Carbonate Pore Types from Petrophysical Logs, in P.H. Pause and M.P. Candelaria (Eds.). *Carbonate Facies and Sequence Stratigraphy: Practical Applications of Carbonate Models*, SEPM Permian Basin Section, 69-80.

Ballouz, M., Nasr, G., and Briaud, J.L. 1991. Dynamic and Static Testing of Nine Drilled Shalfts at Texas A&M University Geotechnical Research Sites. Texas A&M University.

Bard, A.J., and Faulkner, L.R. 1980. *Electrochemical Methods, Fundamentals and Applications*. John Wiley and Sons.

Bateni, S.M., Borghei, S.M., and Jeng, D.S. 2007. Neural Network and Neuro-Fuzzy Assessments for Scour Depth around Bridge Piers. *Engineering Applications of Artificial Intelligence* **20**, 401-14.

Bavusi, M., Rizzo, E., and Lapenna, V. 2006. Electromagnetic Methods to Characterize the Savoia Di Lucania Waste Dump (Southern Italy). *Environmental Geology*, 301-08.

Bowles, J.E. 1968. *Foundation Analysis and Design*. McGraw-Hill.

Briaud, J.-L., Hurlebaus, S., Chang, K.-A., Yao, C., Sharma, H., Yu, O.-Y., Darby, C., Hunt, B.E., and Price, G.R. 2011. Realtime Monitoring of Scour Events Using Remote Monitoring Technology. Texas A&M University.

Browne, D. 1982. Design Prediction of the Life for Reinforced Concrete in Marine and Other Chloride Environments. *Durability of Building Materials* **1**, 113-25.

Castilho, G., and Maia, D. A Successful Mixed Land-Underwater 3D Resistivity Survey in an Extremely Challenging Environment in Amazônia. *Proceedings of the 21st SAGEEP Meeting*, 1150-58.

Chung, H.J., Kim, J.H., Park, K.P., Kwon, H.S., Choi, H.S., Kim, K.S., and Kim, J.S. 2001. Application of Geophysical Results to Designing Bridge over a Large Fault. *Fourth Asian Young Geotechnical Engineers Conference*.

Conrad, C. 2010. Electrical Resistivity Side Scanning for Bridge Foundation Investigation. in GTS Technologies Inc. (ed.).

Dahlin, T. 2001. The Development of Dc Resistivity Imaging Techniques. *Computers & Geoscience* **27**, 1019 - 29.

Dahlin, T., Leroux, V., and Nissen, J. 2002. Measuring Techniques in Induced Polarization Imaging. *Applied Geophysics*, 279-98.

Daily, W., and Owen, E. 1991. Cross-Borehole Resistivity Tomography. *Geophysics* **56**, 1228-35.

Demuth, H., Beale, M., and Hagan, M. 2009. Matlab Neural Network Toolbox User's Guide. The MathWorks.

Dunn, P. 2010. *Comparison of Cone Model and Measured Dynamic Impedance Functions of Shallow Foundations*. Dissertation, University of Florida.

Gharibi, M., and Bentley, L.R. 2000. Resolution of 3-D Electrical Resistivity Images from Inversions of 2-D Orthogonal Lines. *Journal of Environmental Engineering Geophysics* **10**, 339-49.

Gibbens, R. 1995. *Load Tests on Five Large Spread Footings on Sand and Evaluation of Prediction Methods*. Texas A&M.

Gonzalez, J.A., Lopez, W., and Rodriguez, P. 1993. Effect of Moisture Availability on Corrosion Kinetics of Steel Embedded in Concrete. *Corrosion* **50**, 1004-10.

Haykin, S. 1999. *Neural Networks; a Comprehensive Foundation*. Prentice hall International, Inc.

Hiltunen, D., and Roth, M. 2003. Investigation of Bridge Foundation Sites in Karst Terrane Via Multi-electrode Electrical Resistivity. *The 3rd International Conference on Applied Geophysics - Geophysics 2003*.

Hubbard, S., Zang, J., Monteiro, P., Peterson, J., and Rubin, Y. 2003. Experimental Detection of Reinforcing Bar Corrosion Using Nondestructive Geophysical Techniques. *ACI Materials Journal*, 501-10.

Humkeler, F. 1996. The Resistivity of Pore Water Solution-a Decisive Parameter of Rebar Corrosion and Repair Methods. *Construction and Building Materials* **10**, 381-89.

Kaya, A. 2010. Artificial Neural Network Study of Observed Pattern of Scour Depth around Bridge Piers. *Computers and Geotechnics* **37**, 413-18.

Keller, G.V., and Frischknecht, F.C. 1966. *Electrical Methods in Geophysical Prospecting*. Pergamon Press.

Kim, J.H., Yi, M.J., Song, Y., Cho, S.-J., Chung, S.-H., and Kim, K.S. 2002. Dc Resistivity Survey to Image Faults beneath a Riverbed. *Symposium on the Application of Geophysics to Engineering and Environmental Problems (SAGEEP), 13IDA10*.

Kwon, H.S., Kim, J.H., Ahn, H.Y., Yoon, J.S., Kim, K.S., Jung, C.K., Lee, S.B., and Uchida, T. 2005. Delineation of a Fault Zone beneath a Riverbed by an Electrical Resistivity Survey Using a Floating Streamer Cable. *Geophysical Exploration* **58**, 50-58.

LaBrecque, D., and Daily, W. 2008. Assessment of Measurement Errors for Galvanic-Resistivity Electrodes of Different Composition. *Geophysics* **73**, F55-F64.

Lee, T.L., Jeng, D.S., Zhang, G.H., and Hong, J.H. 2007. Neural Network Modeling for Estimation of Scour Depth around Bridge Piers. *Journal of Hydrodynamics, Ser. B* **19**, 378-86.

Leroux, V., Torleif, D., and Svensson, M. 2007. Dense Resistivity and Induced Polarization Profilling for a Landfill Restoration Project at Harlov, Souther Sweden. *Waste Management and Research*, 49-60.

Loke, M.H. 2000. Electrical Imaging Surveys for Environmental and Engineering Studies: A Practical Guide to 2-D and 3-D Surveys.

Loke, M.H. 2010. Tutorial: 2D and 3D Electric Imaging Surveys. Geoelectric Company.

Loke, M.H., and J.W. Lane, J. 2004. Inversion of Data from Electrical Resistivity Imaging Surveys in Water Covered Areas. *Exploration Geophysics* **35**, 266-71.

LSTC. 2003. *Ls-Dyna Keyword User's Manual*. Livermore Software Technology Corporation.

Maser, K.R., Sanqeui, M., Lichtenstein, A., and Chase, S.B. 1998. Determination of Bridge Foundation Type from Structural Response Measurements. *Nondestructive Evaluation Techniques for Aging Infrastructure and Manufacturing*, SPIE, 55-67.

McCulloch, W., and Pitts, W. 1943. A Logical Calculus of the Ideas Immanent in Nervous Activity. *Bulletin of Mathematical Biology* **5**, 115-33.

McLemore, S., Zendegui, S., Whiteside, J., Sheppard, M., Gosselin, M., Demir, H., Passe, P., and Hayden, M. 2010. Unknown Foundation Bridges Pilot Study. Federal Highway Administration & Florida Department of Transportation.

Mercado, E.J., and O'Neil, M.W. 2003. Methods to Measure Scour Depth and the Depth of Unknown Foundations. *3rd International Conferences on Applied Geophysics*, Geophysics.

Meyer, C., Burkard, U., and Barlieb, C. 2007. Archaeological Questions and Geophysical Solutions: Ground-Penetrating Radar and Induced Polarization Investigations in Munigua, Spain. *Archaeological Prospection* **14**, 202-11.

Olson, L. 2005. Dynamic Bridge Substructure Evaluation and Monitoring. in FHWA (ed.).

Olson, L., Jalinoos, F., and Aouad, M.F. 1998. Determination of Unknown Subsurface Bridge Foundations: NCHRP 21-5 Interim Report Summary. in FHWA (ed.).

Pellerin, L. 2002. Applications of Electrical and Electromagnetic Methods for Environmental and Geotechnical Investigations. *Surveys in Geophysics*.

Petiau, G. 2000. Second Generation of Lead-Lead Chloride Electrodes for Geophysical Applications. *Pure and Applied Geophysics* **157**, 357-82.

Poggio, T., and Girosi, F. 1990. Regularization Algorithms for Learning That Are Equivalent to Multilayer Networks. *Science* **247**, 978-82.

Polder, R.B. 2001. A Rilem Tc-154 Technical Recommendation: Test Methods for on Site Measurement of Resistivity of Concrete. *Construction and Building Materials* **15**, 125-31.

Rix, G.J. 1995. Interpretation of Nondestructive Tests on Unknown Bridge Foundations Using Artificial Neural Networks. *Nondestructive Evaluation of Aging Structures and Dams* **2457**, 102-12.

Robert, C.P. 2007. *The Bayesian Choice: From Decision-Theoretic Foundations to Computational Implementation*. Springer.

Robinson, B., and Webster, S. 2008. Successful Testing Methods for Unknown Bridge Foundations. *Fifth Highway Geophysics - NDE Conference*, 101-10.

Samouëlian, A., Cousin, I., Tabbagh, A., Bruand, A., and Richard, G. 2005. Electrical Resistivity Survey in Soil Science: A Review. *Soil and Tillage Research* **83**, 173-93.

Santamarina, J.C., Rinaldi, V., Fratta, D., Klein, K., Wang, Y.H., Cho, G.C., and Cascante, G. 2005. *A Survey of Elastic and Electromagnetic Properties of near-Surface Soils*. SEG Press.

Sayed, S.M., Sunna, H., and Moore, P.R. 2011. Re-Classifying Bridges with Unknown Foundations. *5th international conference on scour and erosion*.

Shahin, M., & Jaksa, M. 2008. State of the Art of Artificial Neural Networks in Geotechnical Engineering. *Electronic Journal of Geotechnical Engineering* **8**, 1-26.

Slater, L., and Lesmes, D. 2002. Ip Interpretation and Environmental Investigations. *Geophysics*, 77-88.

Sogade, J., Scira-Scappuzzo, F., Vichabian, Y., Shi, W., Rodi, W., Lesmes, D., and Morgan, F.D. 2006. Induced-Polarization Detection and Mapping of Contaminant Plumes. *Geophysics* **71**, B75-B84.

Specht, D.F. 1991. A General Regression Neural Network. *IEEE Transactions on Neural Networks* **2**, 568-76.

Stein, S., and Sedmera, K. 2006. Risk-Based Management Guidelines for Scour at Bridges with Unknown Foundations. National Cooperative Highway Research Program (NCHRP), Web-only Document-107, Project 24-25.

Su, J.K., Yang, C.C., Wu, W.B., and Huang, R. 2002. Effect of Moisture Content on Concrete Resistivity Measurement. *Journal of the Chinese Institute of Engineers* **25**, 117-22.

Summers, B.R. 2006. *Petrophysical Investigation of Porosity Distribution in the Geneva Dolomite Member of the Grand Tower Formation in Marion County, Illinois*. Dissertation, Northern Illinois University.

Suzuki, O., Shimamura, M., Abe, M., and Matsunuma, M. 2007. A Healthy Monitoring System for Railway Bridge Piers. *Third International Conference on Structural Health Monitoring of Intelligent Infrastructure*, ISHMII, 13-16.

Tipler, P.A. 1982. *Physics*. Worth Publishers, Inc.

Touma, F.T., and Reese, L.C. 1969. The Behavior of Axially Loaded Drilled Shafts in Sand. Center of Highway Research, The University of Texas at Austin.

Trenn, S. 2008. Multilayer Perceptrons: Approximation Order and Necessary Number of Hidden Units. *Neural Networks, IEEE Transactions on* **19**, 836-44.

Tuutti, K. 1982. Corrosion of Steel in Concrete. In: Polder R.B., 2001. Test Methods for on Site Measurement of Resistivity of Concrete-a Rilem Tc-154 Technical Recommendation. *Construction and Building Materials* **15**, 125-31.

TxDOT. 2006. *Geotechnical Manual*. Texas Department of Transportation (TxDOT).

TxDOT. 2011. Online Standard Sheets.

Worthington, P.F. 1993. The Uses and Abuses of the Archie Equations, I: The Formation Factor - Porosity Relationship. *Journal of Applied Geophysics* **30**, 215-28.

Yuen, K.V. 2010. *Bayesian Methods for Structural Dynamics and Civil Engineering*. John Wiley & Sons.

Zonge, K., Wynn, J., and Urquhart, S. 2005. *Resistivity, Induced Polarization and Complex Resistivity*. SEG Press.

Zounemat-Kermani, M., Beheshti, A.A., Ataie-Ashtiani, B., and Sabbagh-Yazdi, S.R. 2009. Estimation of Current-Induced Scour Depth around Pile Groups Using Neural Network and Adaptive Neuro-Fuzzy Inference System. *Applied Soft Computing* **9**, 746-55.

APPENDIX

FIGURES

This section includes figures that have not been presented in the main text.

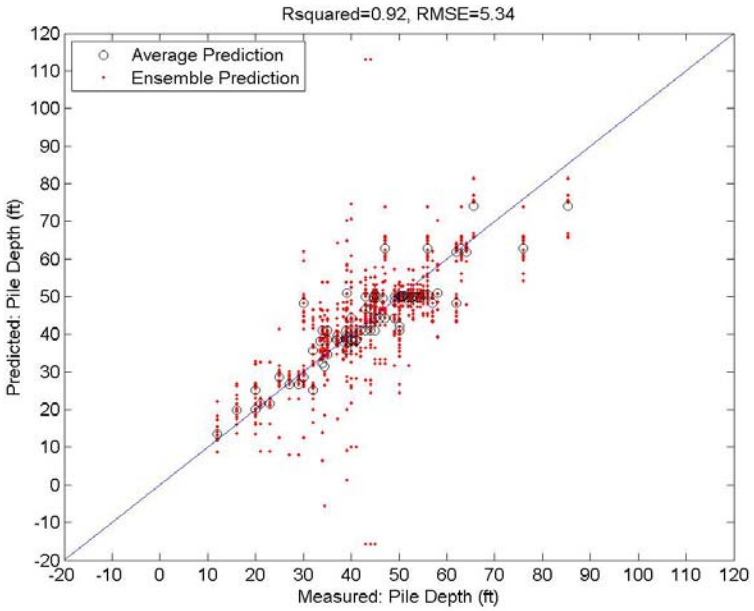

Figure A-1. Ensemble Predictions of MLP-PL10 for Drilled Shafts.

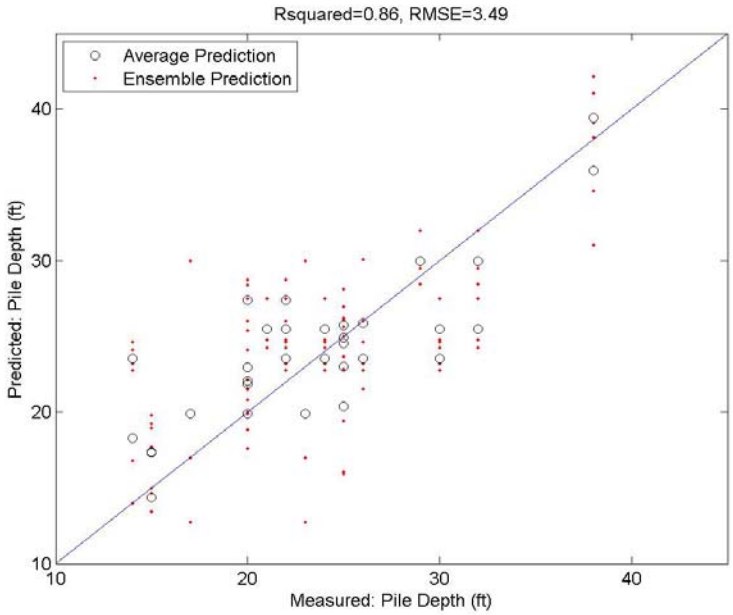

Figure A-2. Ensemble Predictions of MLP-PL10 for Steel Piles.

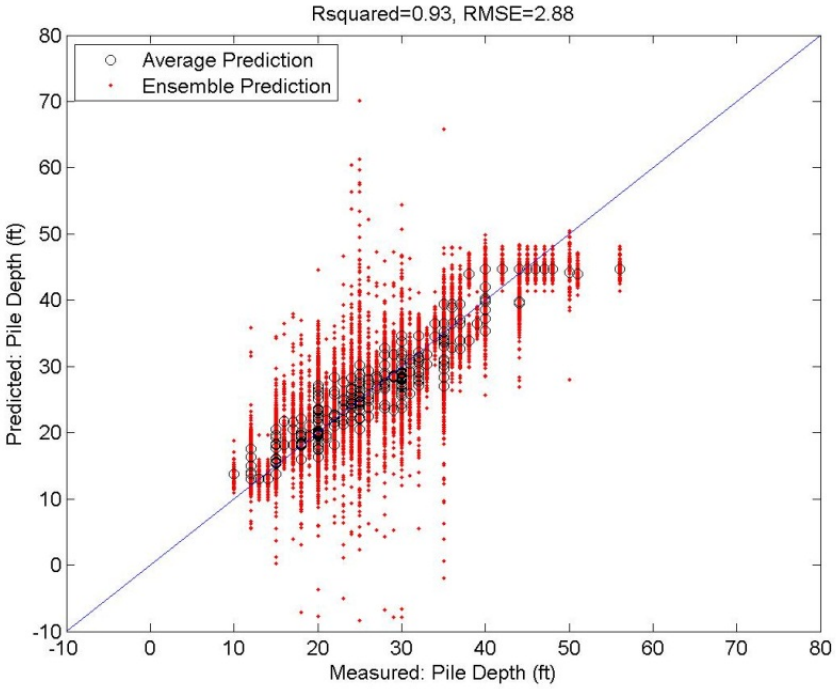

Figure A-3. Ensemble Predictions of MLP-PL11 for Concrete Piles.

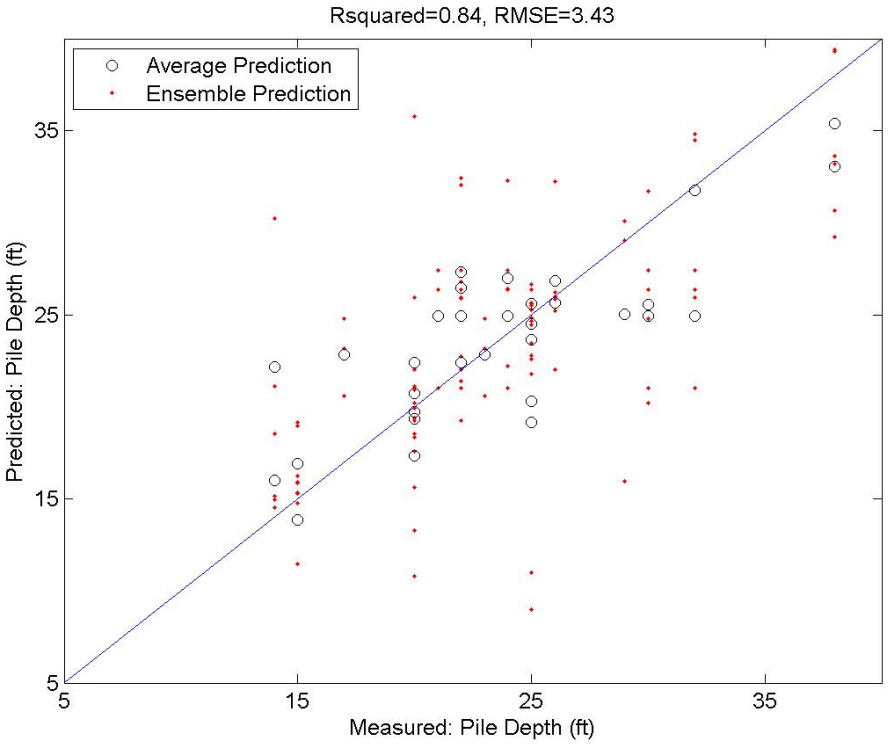

Figure A-4. Ensemble Predictions of MLP-PL11 for Steel Piles.

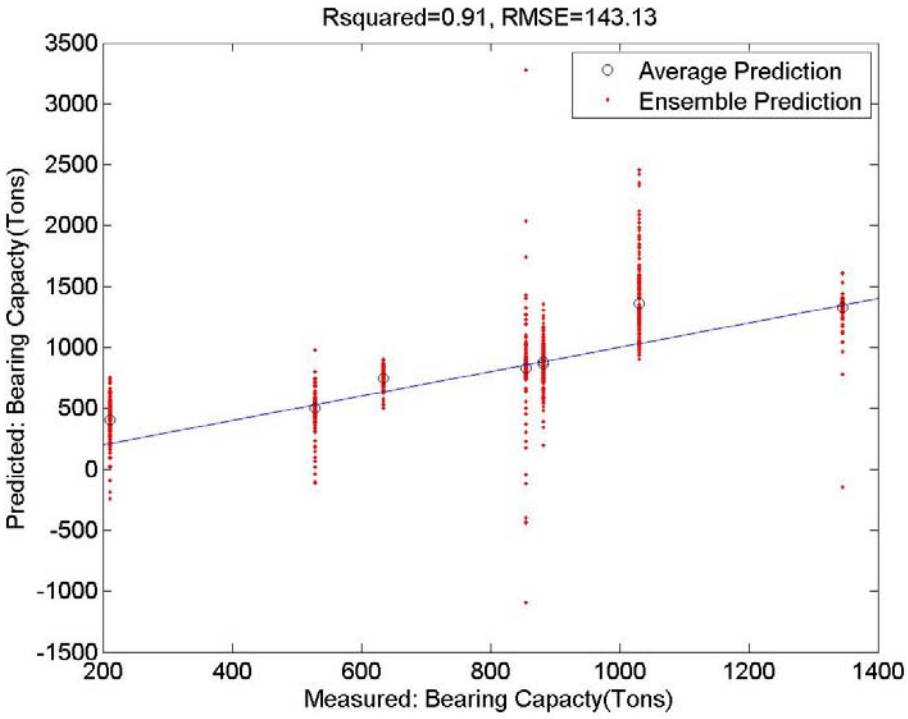

Figure A-5. MLP-BC10 Predictions for Drilled Shafts for Randomly Selected Bridge Piers.

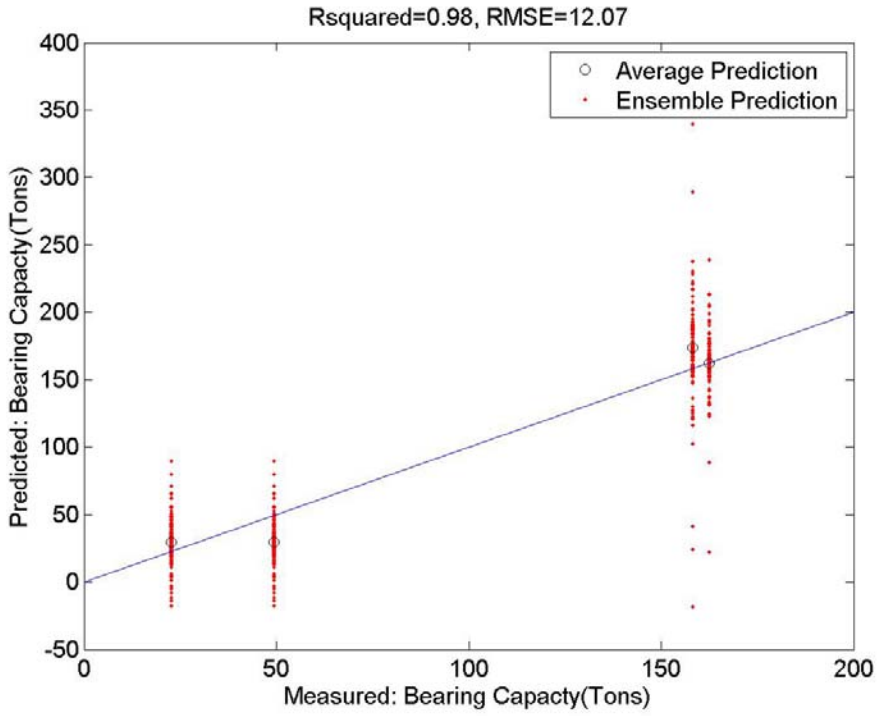

Figure A-6. MLP-BC10 Predictions for Steel Piles for Randomly Selected Bridge Piers.

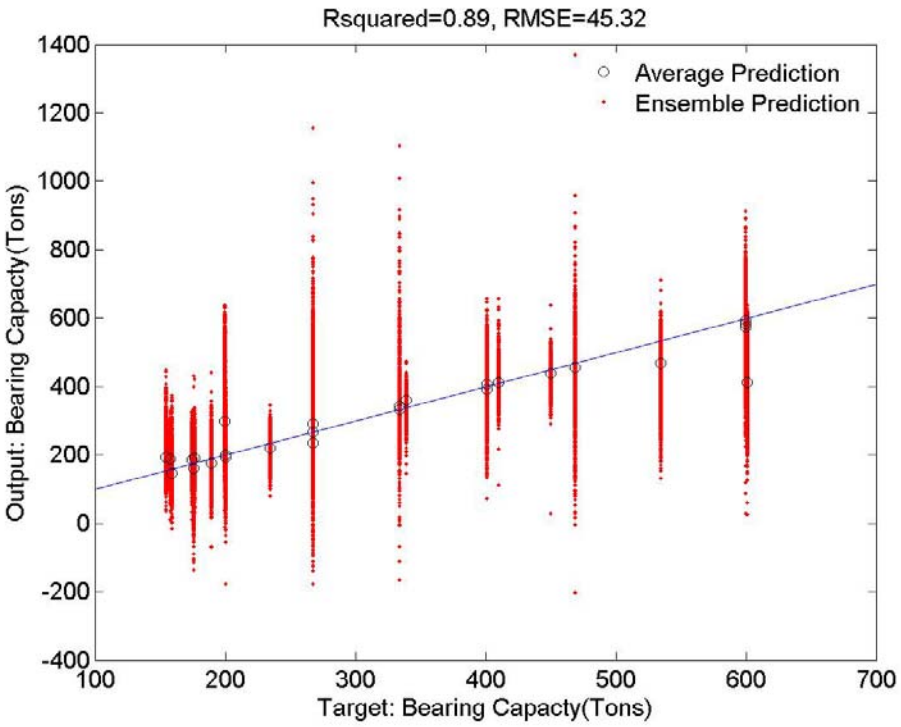

Figure A-7. MLP-BC11 Predictions for Concrete Piles for Randomly Selected Bridge Piers.

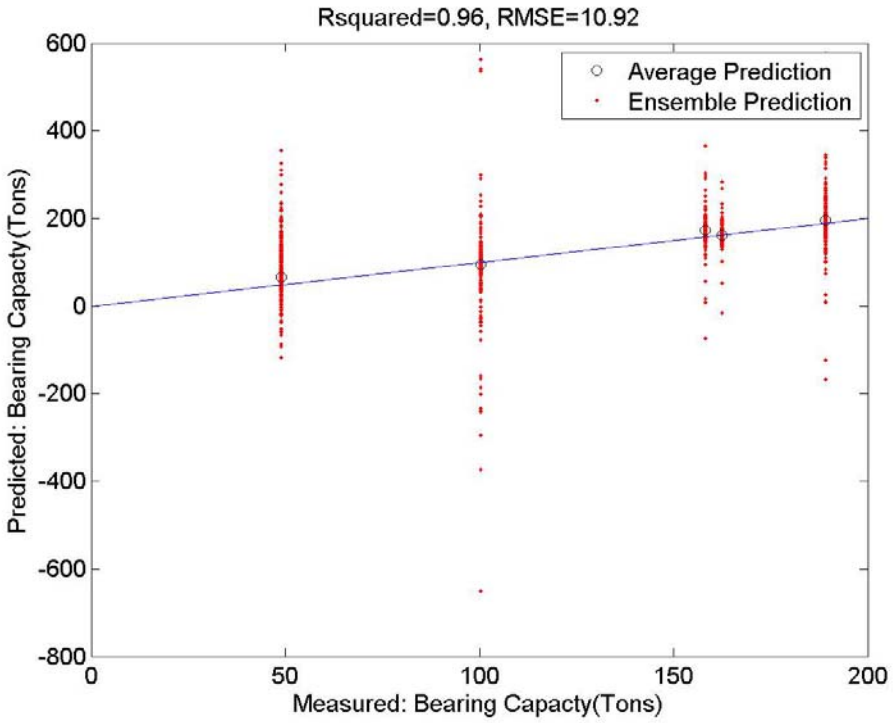

Figure A-8. MLP-BC11 Predictions for Steel Piles for Randomly Selected Bridge Piers.

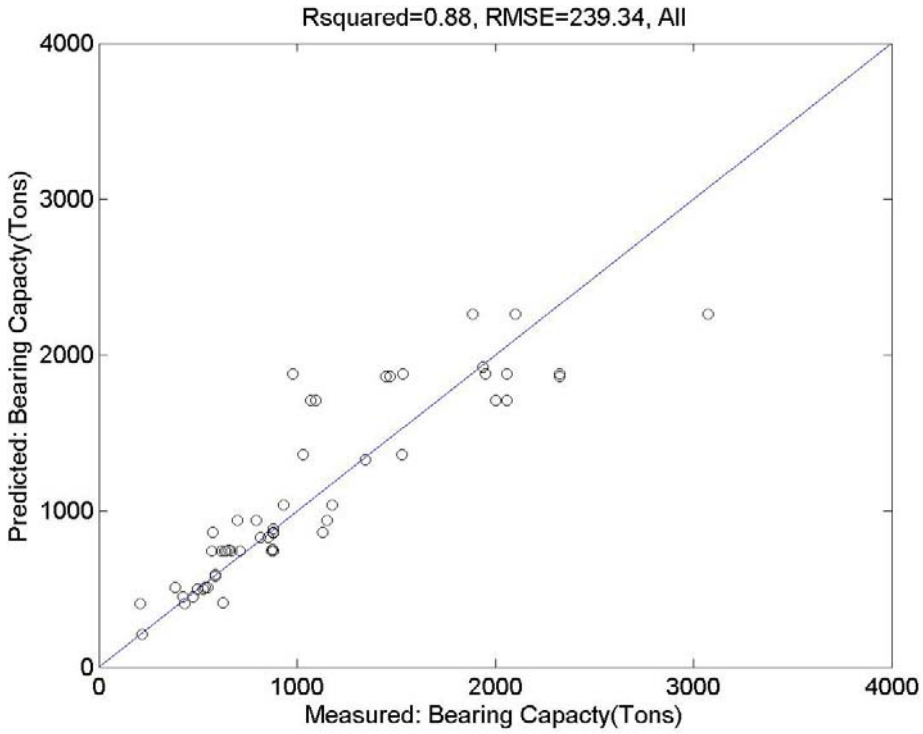

Figure A-9. MLP-BC10 Predictions for Drilled Shafts, for All Data Points.

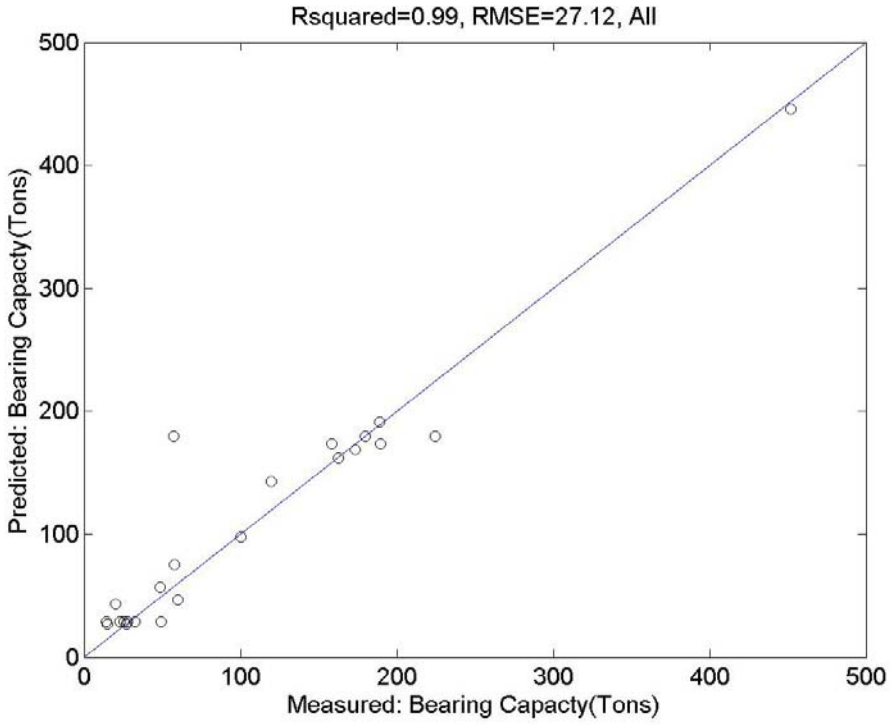

Figure A-10. MLP-BC10 Predictions for Steel Piles, for All Data Points.

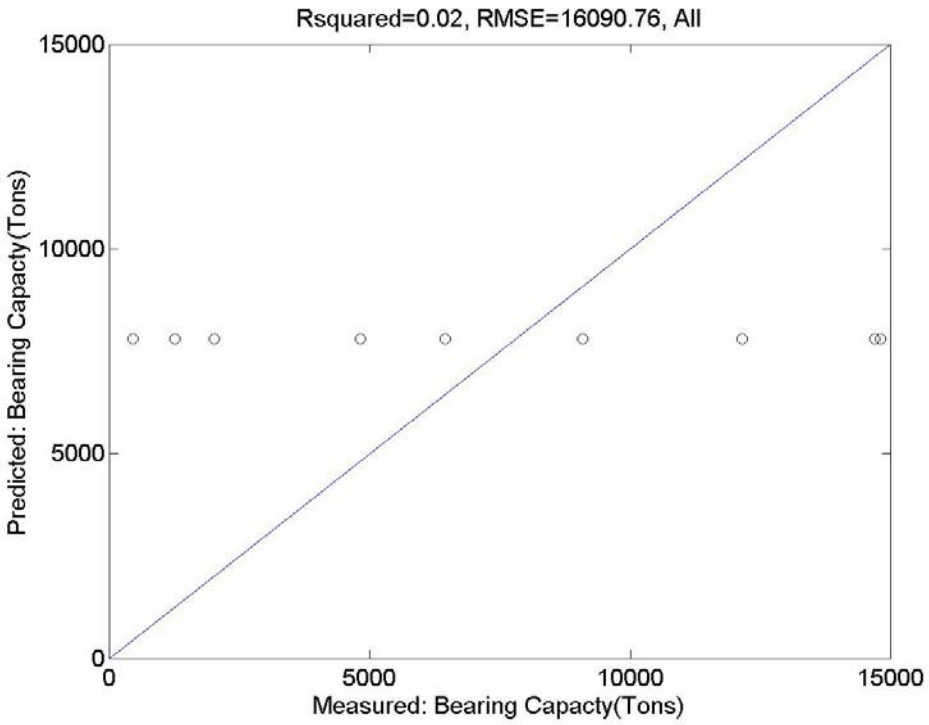

Figure A-11. MLP-BC10 Predictions for Spread Footings, for All Data Points.

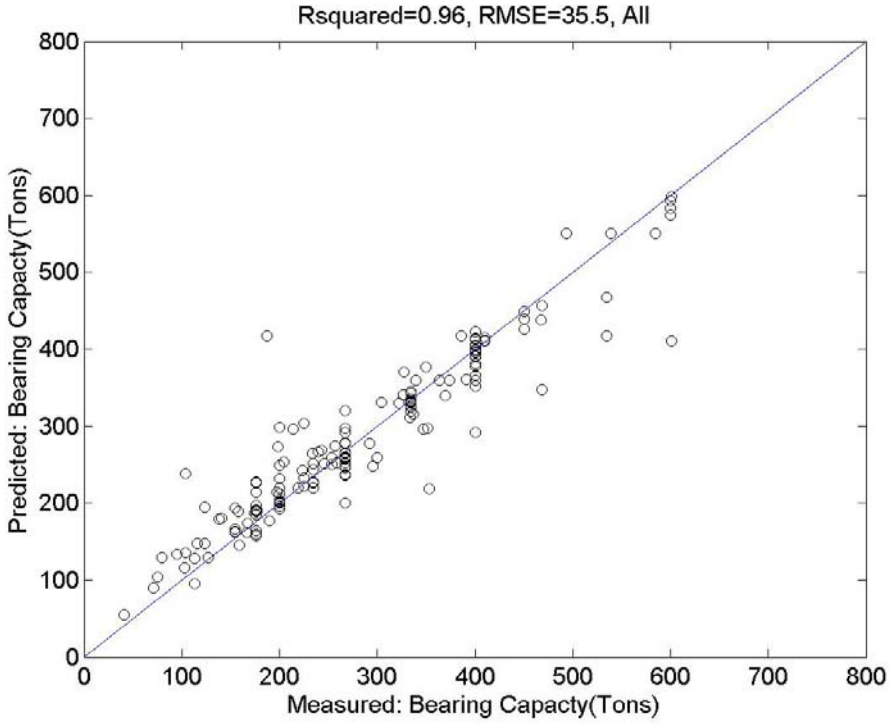

Figure A-12. MLP-BC11 Predictions for Concrete Piles, for All Data Points.

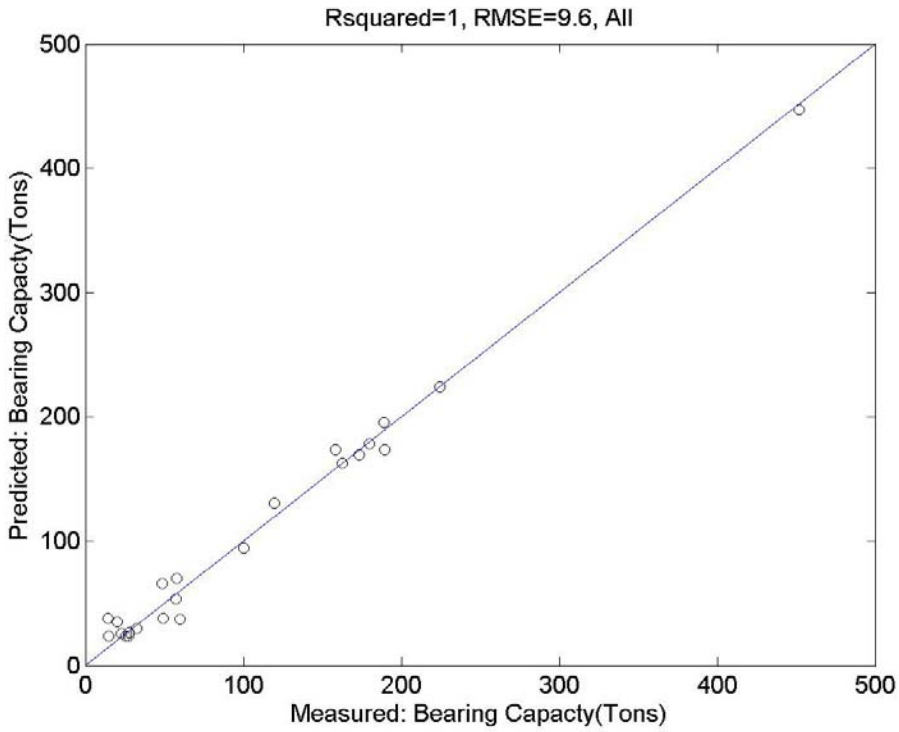

Figure A-13. MLP-BC11 Predictions for Steel Piles, for All Data Points.

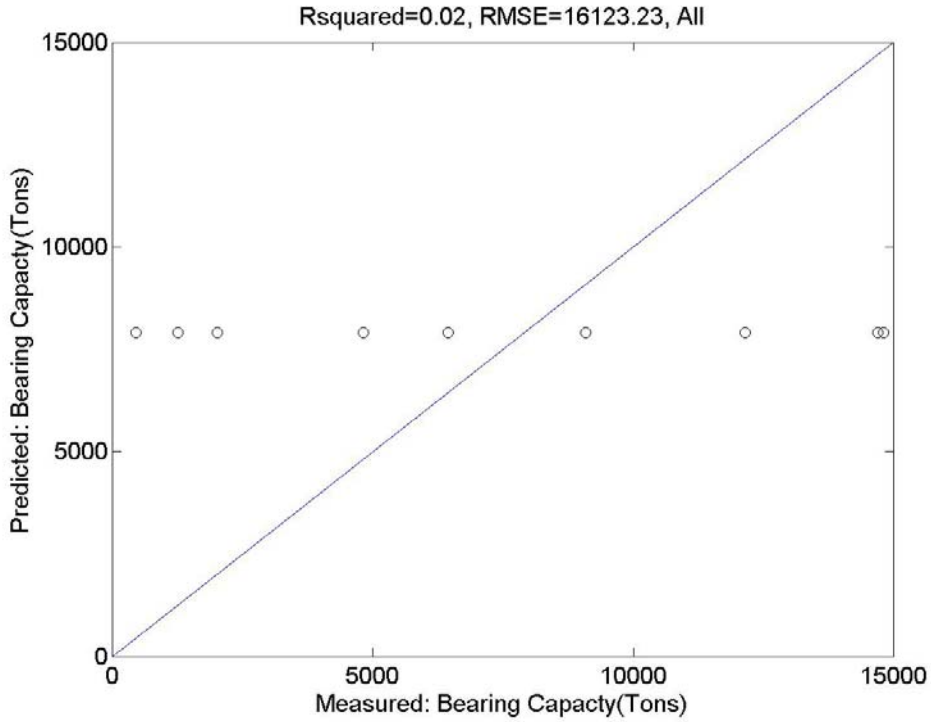

Figure A-14. MLP-BC11 Predictions for Spread Footings, for All Data Points.

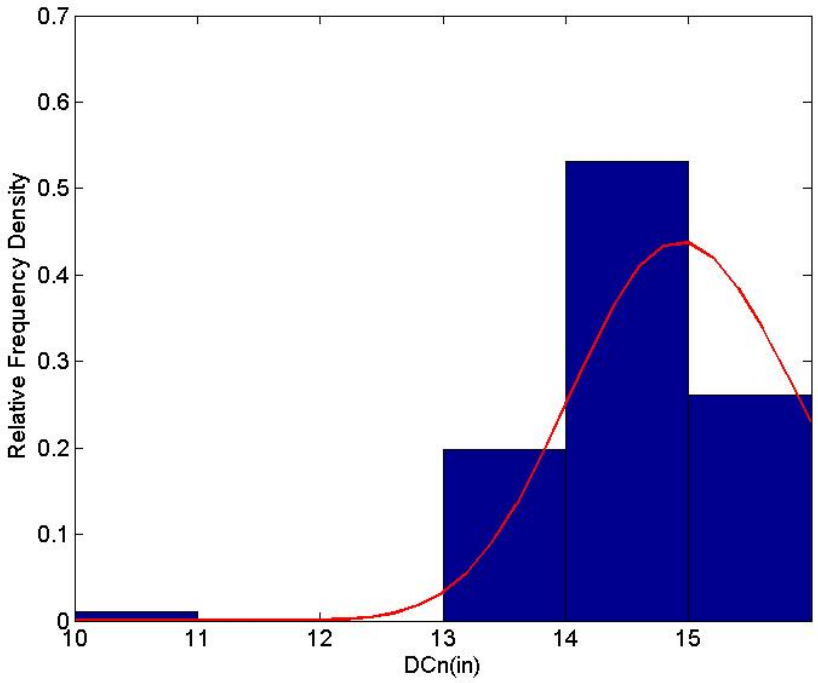

Figure A-15. Prior Distribution and Histogram for Size of Square Concrete Piling (DCn).

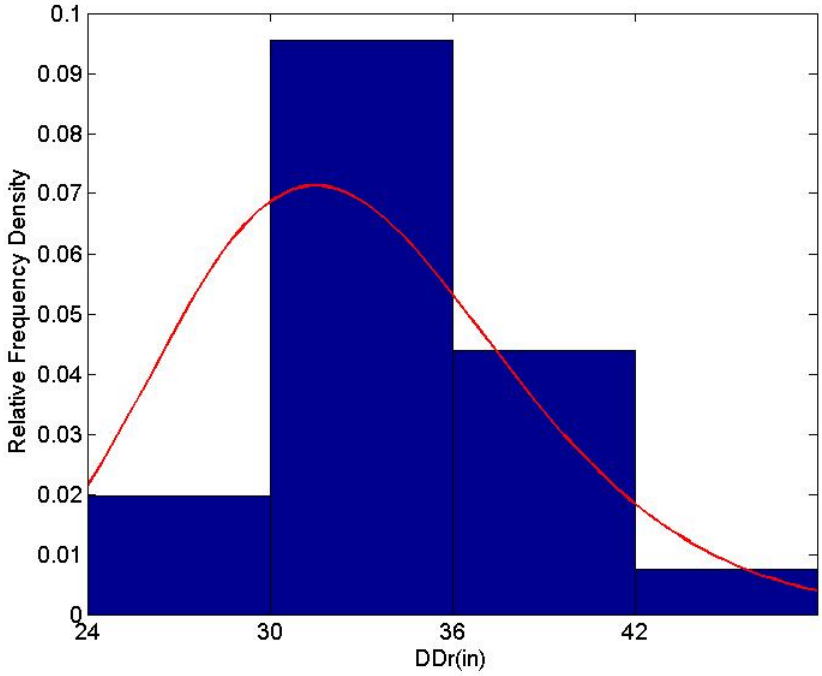

Figure A-16. Prior Distribution and Histogram for Diameter of Drilled Shafts (DDr).

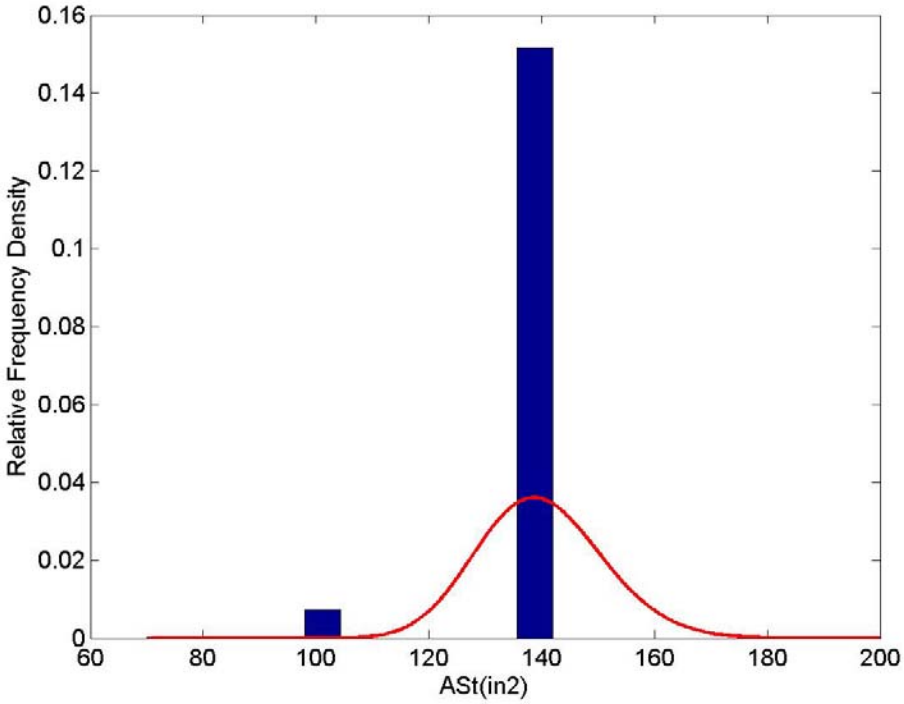

Figure A-17. Prior Distribution and Histogram for Full Cross-Section Area of Steel Pilings (ASt).

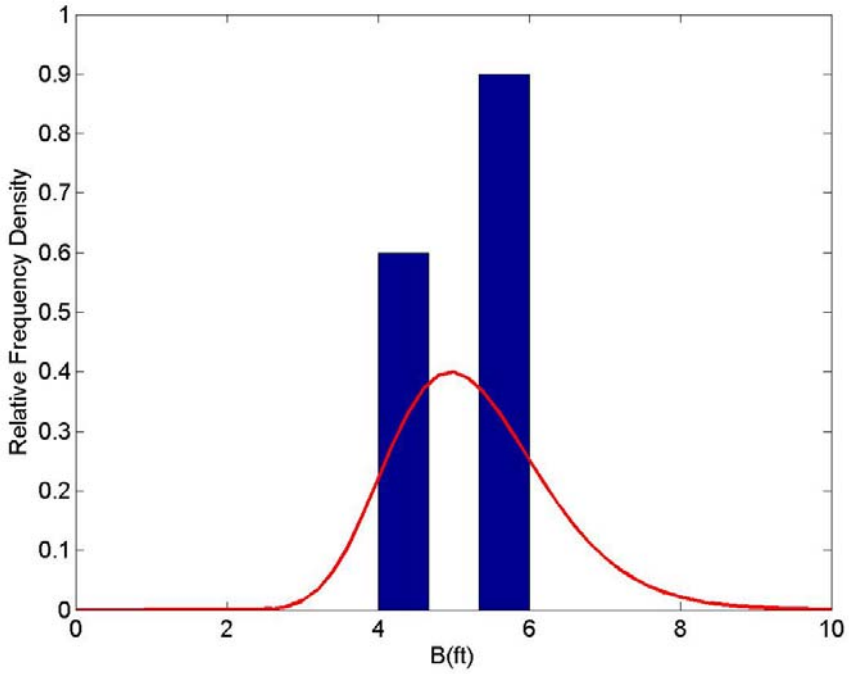

Figure A-18. Prior Distribution and Histogram for Width of Spread Footings (B).

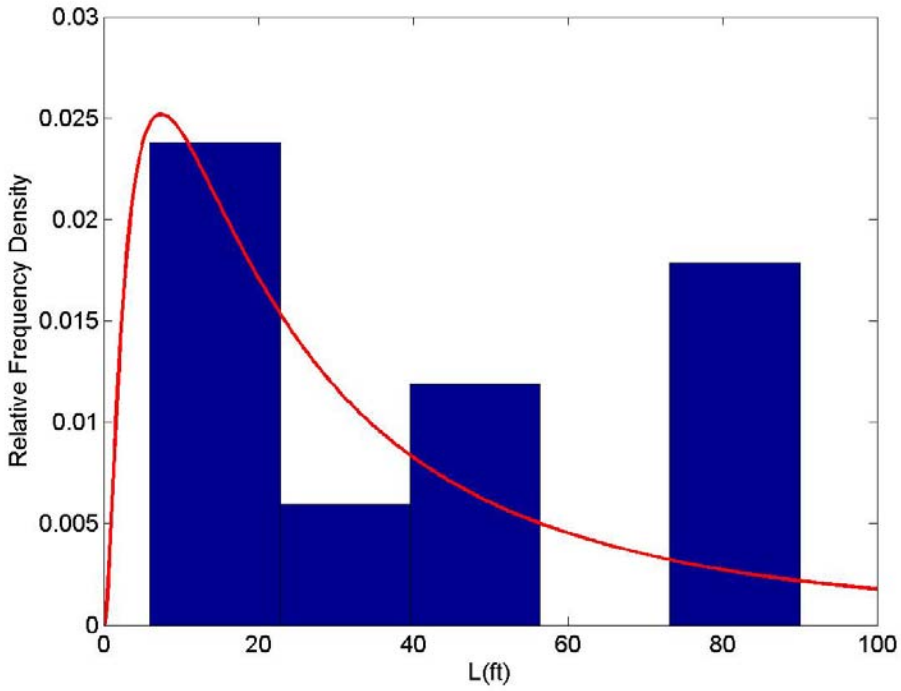

Figure A-19. Prior Distribution and Histogram for Length of Spread Footings (L).

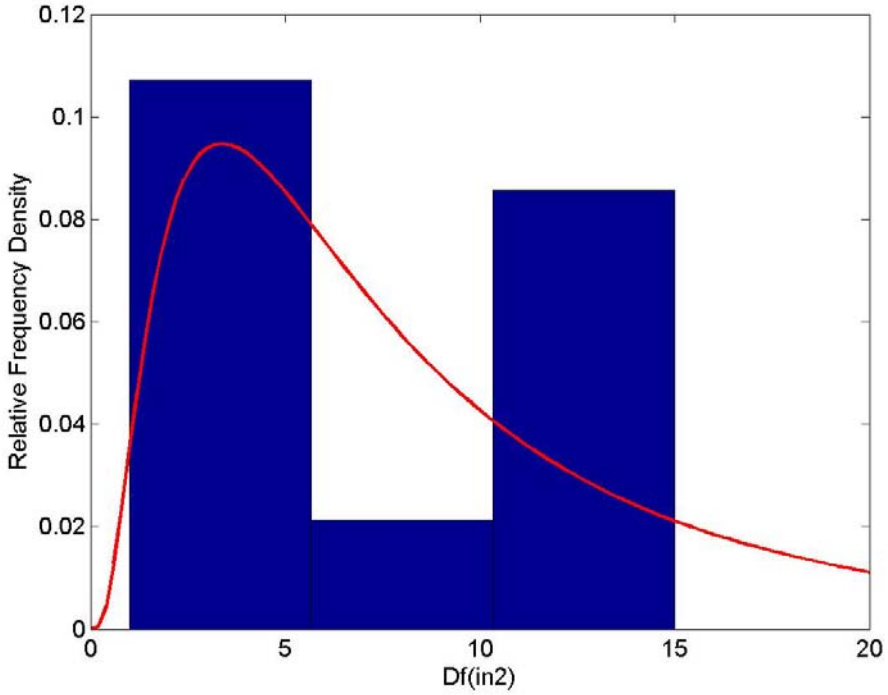

Figure A-20. Prior Distribution and Histogram for Embedment Depth of Spread Footings (Df).

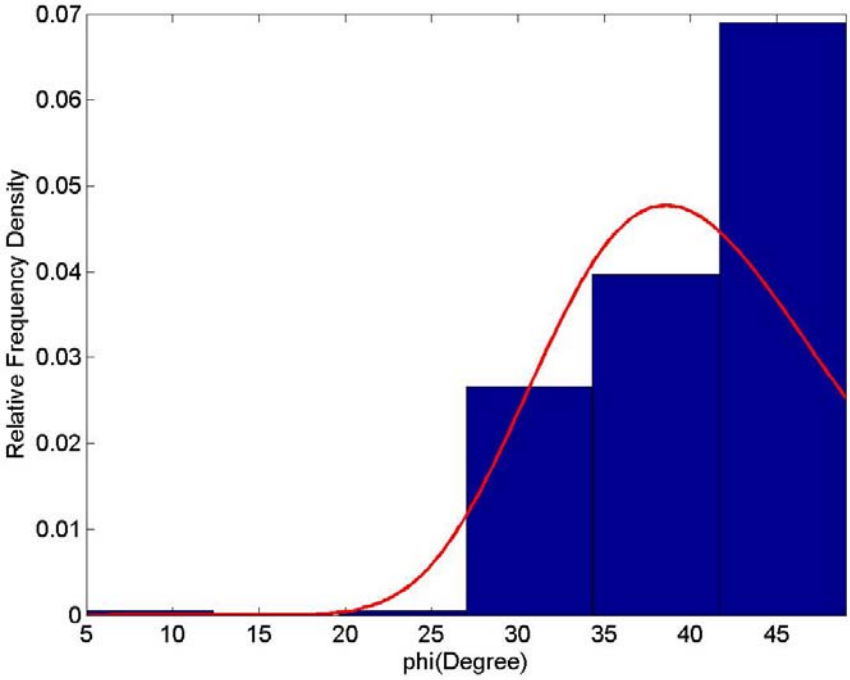

Figure A-21. Prior Distribution and Histogram for φ.

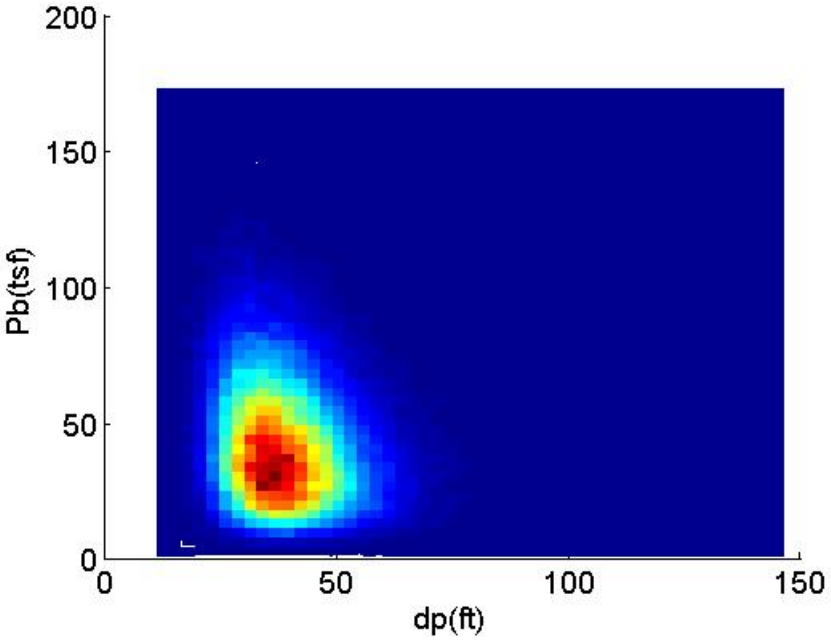

Figure A-22. Joint Relative Frequency Density of the Posterior for Pb and dp.

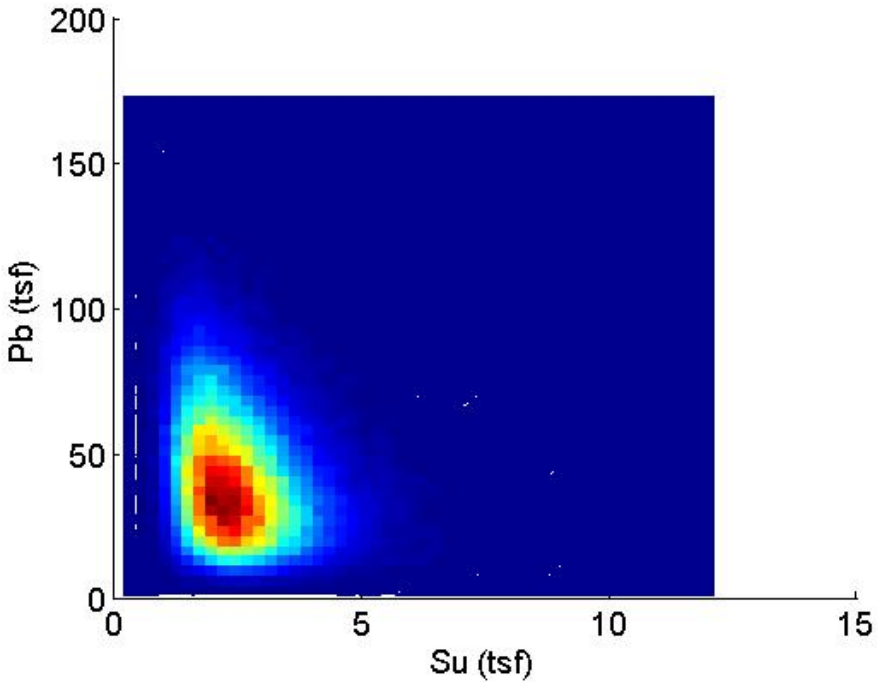

Figure A-23. Joint Relative Frequency Density of the Posterior for Pb and Su.

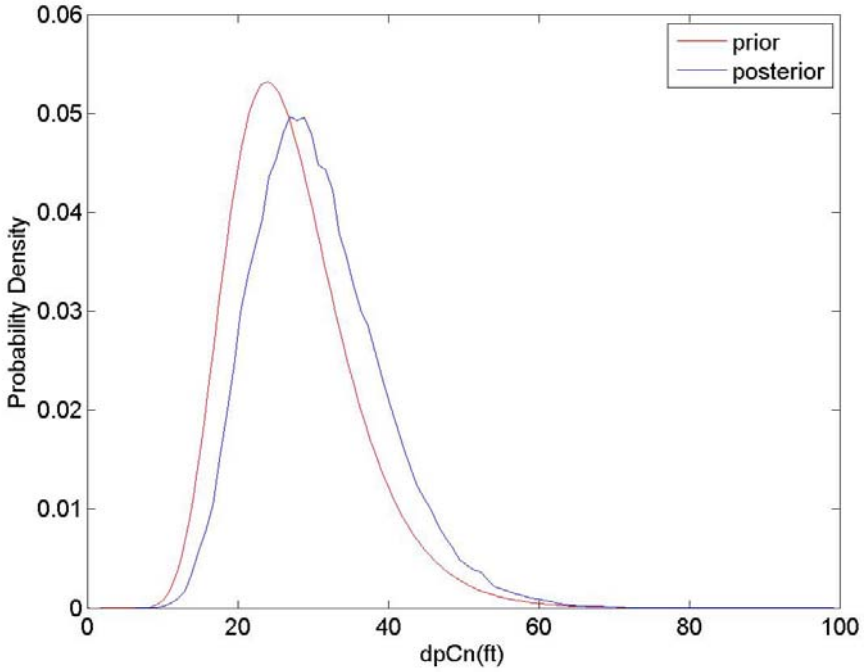

Figure A-24. Prior and Marginal Probability Distribution of Posterior for dpCn for Problem 01.

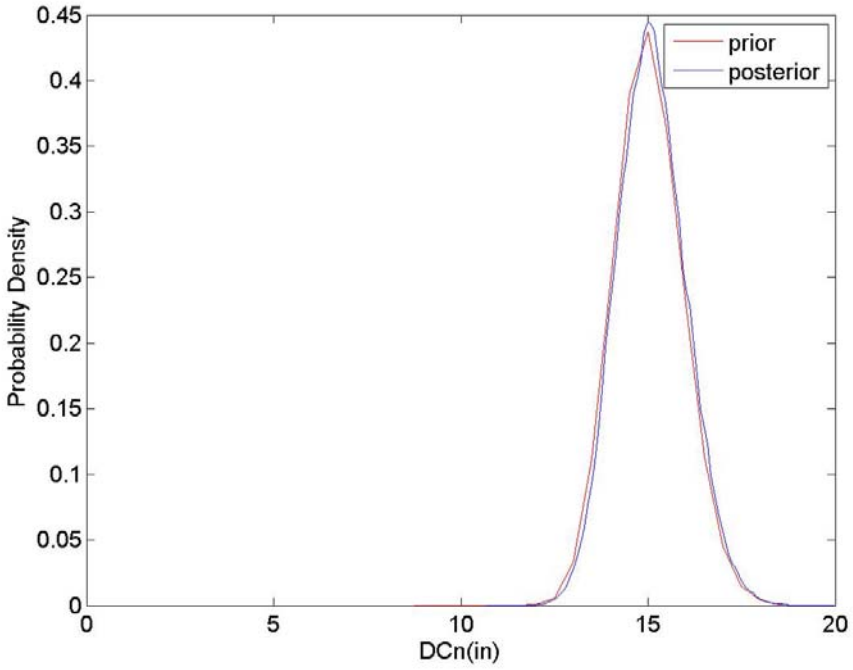

Figure A-25. Prior and Marginal Probability Distribution of Posterior for DCn for Problem 01.

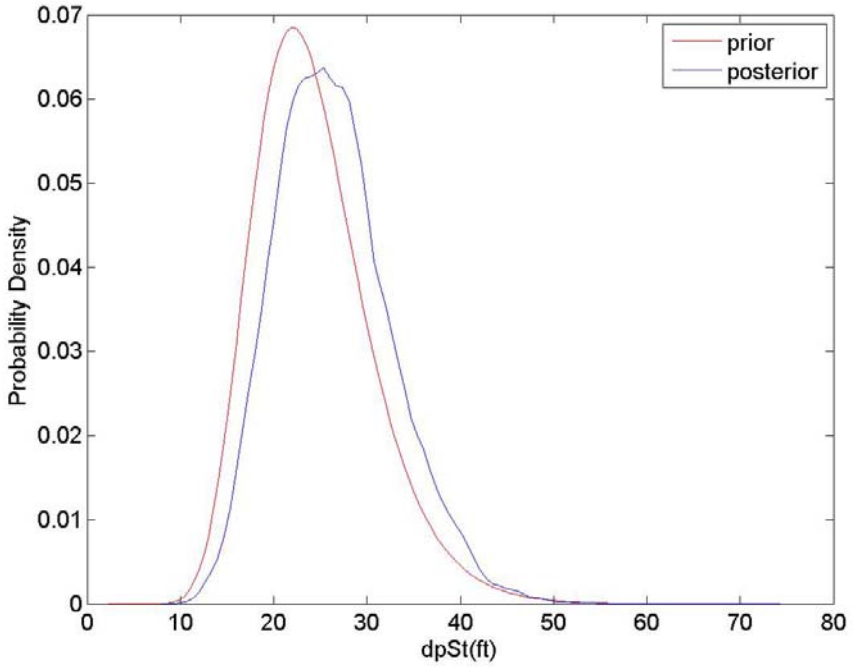

Figure A-26. Prior and Marginal Probability Distribution of Posterior for dpSt for Problem 01.

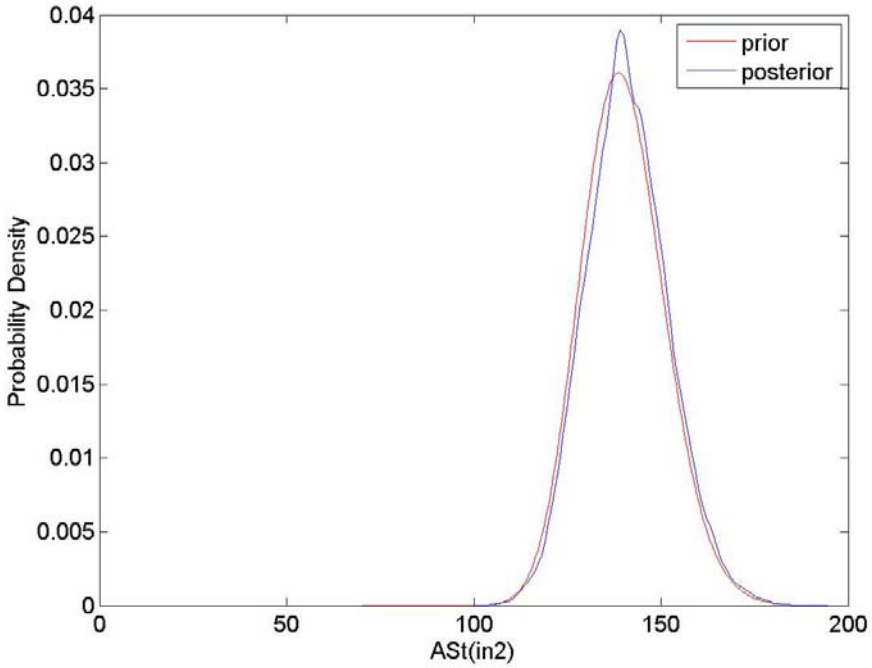

Figure A-27. Prior and Marginal Probability Distribution of Posterior for ASt for Problem 01.

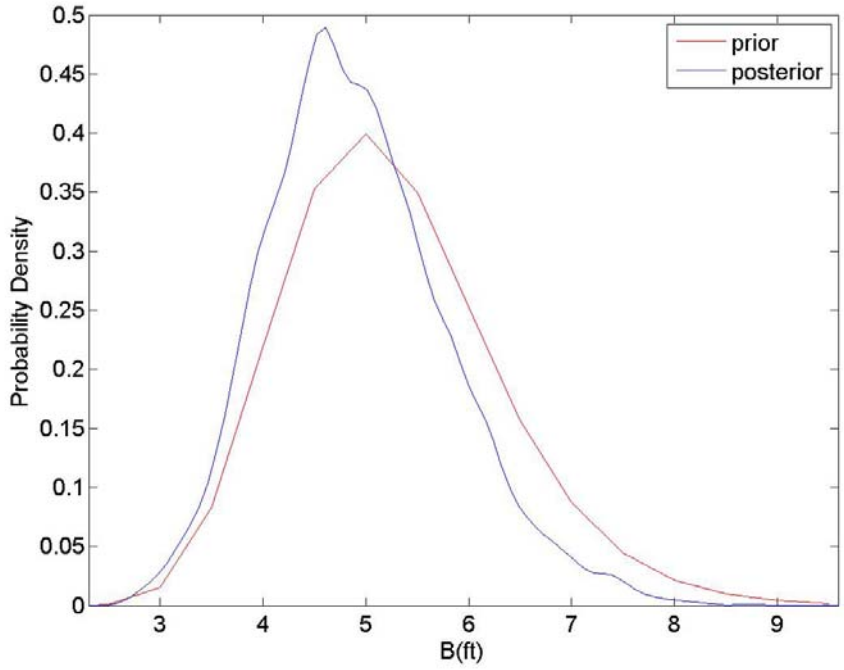

Figure A-28. Prior and Marginal Probability Distribution of Posterior for B for Problem 01.

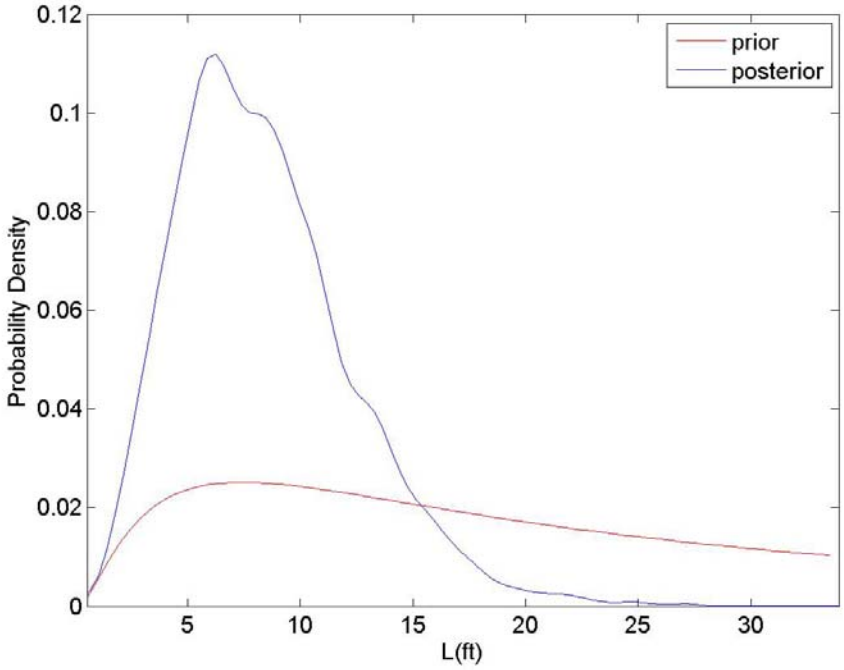

Figure A-29. Prior and Marginal Probability Distribution of Posterior for L for Problem 01.

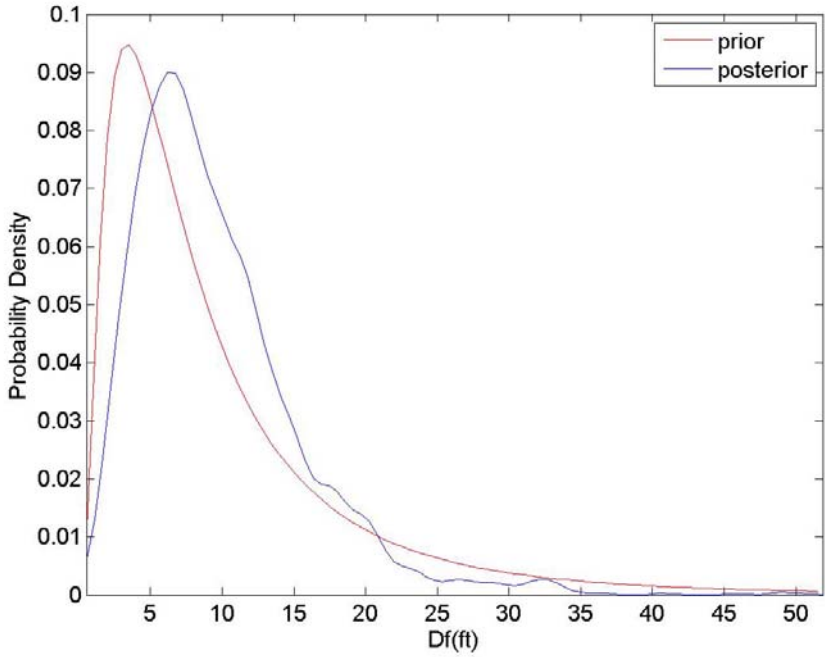

Figure A-30. Prior and Marginal Probability Distribution of Posterior for Df for Problem 01.

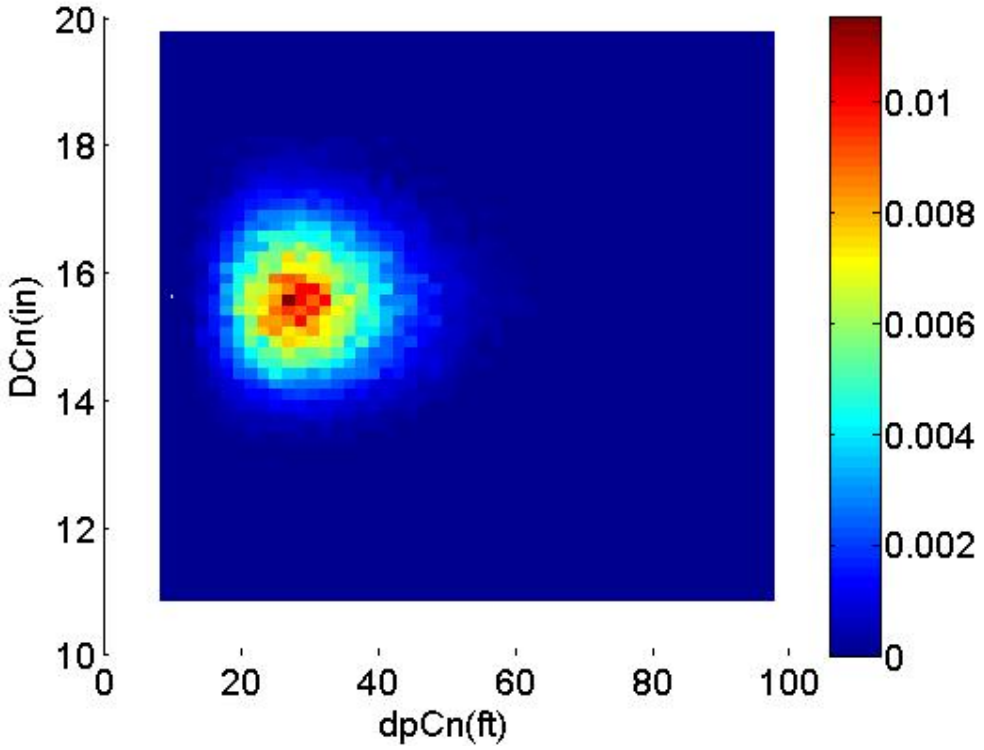

Figure A-31. Joint Relative Frequency Density of the Posterior for dpCn and DCn.

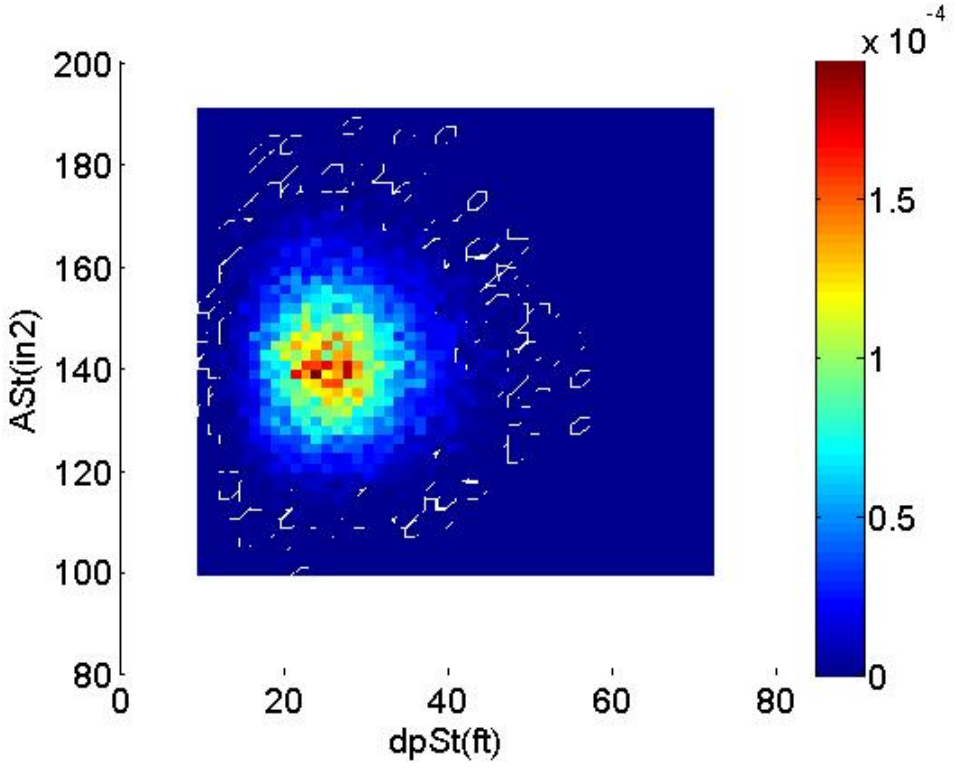

Figure A-32. Joint Relative Frequency Density of the Posterior for dpSt and ASt.

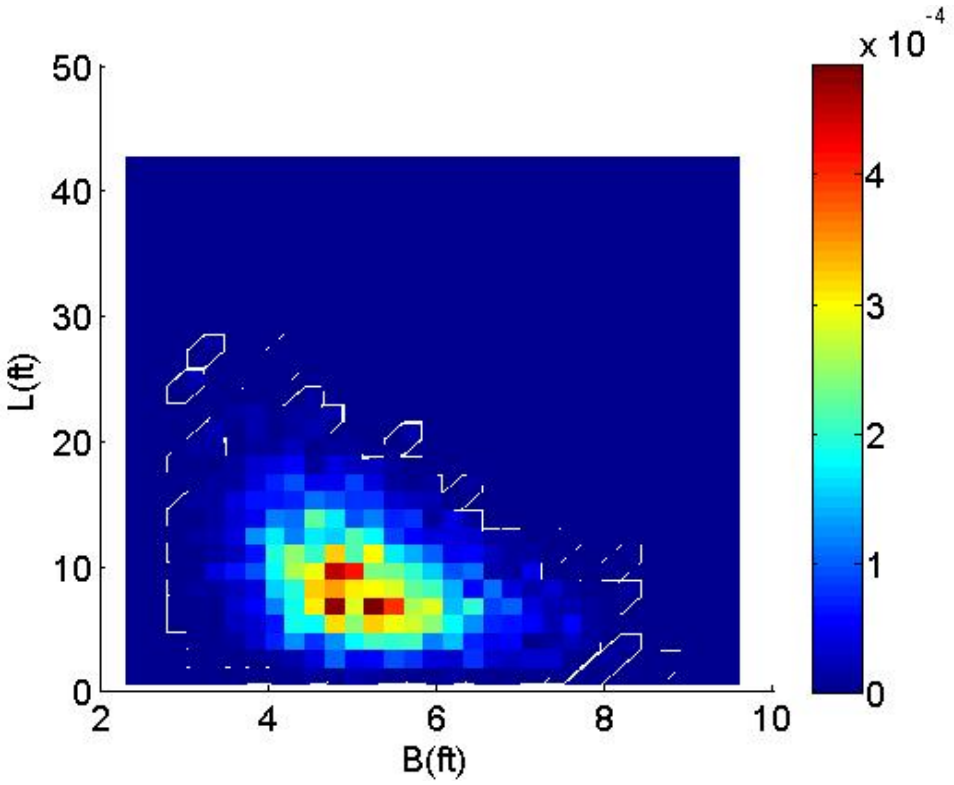

Figure A-33. Joint Relative Frequency Density of the Posterior for B and L.

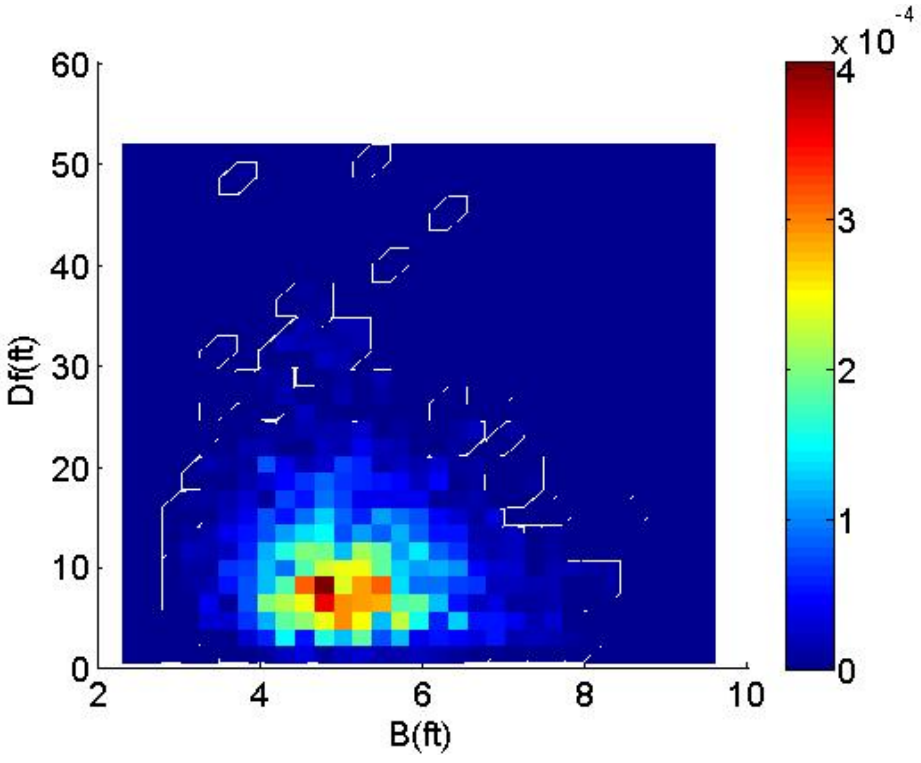

Figure A-34. Joint Relative Frequency Density of the Posterior for Df and B.

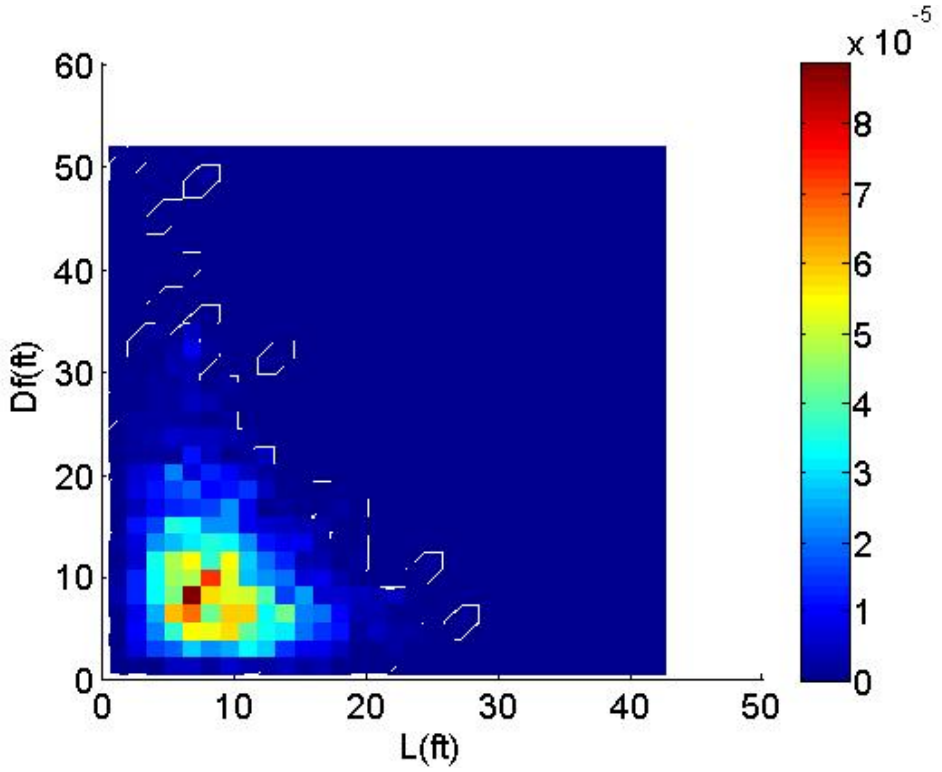

Figure A-35. Joint Relative Frequency Density of the Posterior for Df and L.

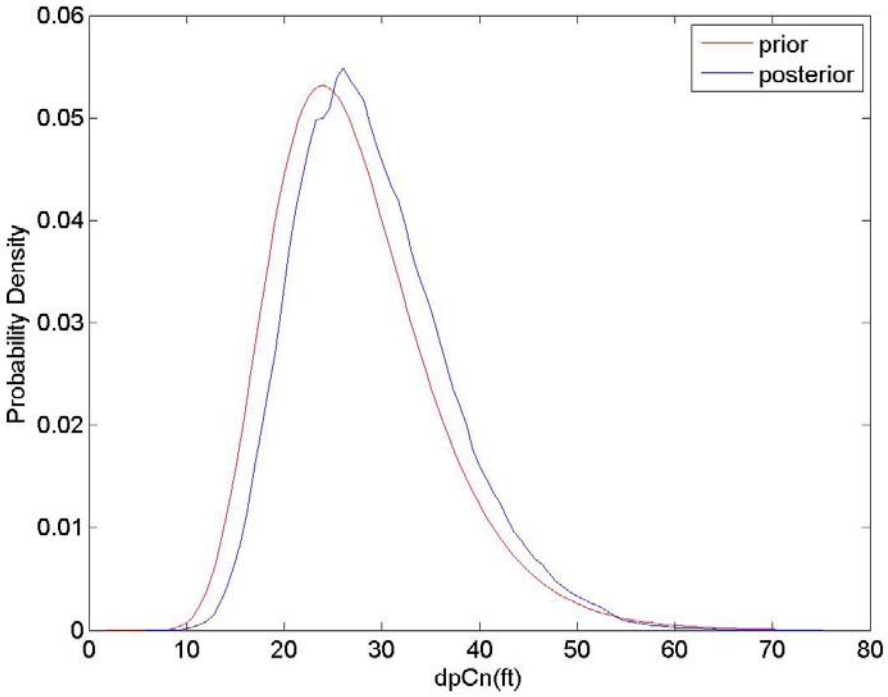

Figure A-36. Prior and Marginal Probability Distribution of Posterior for dpCn for Problem 00.

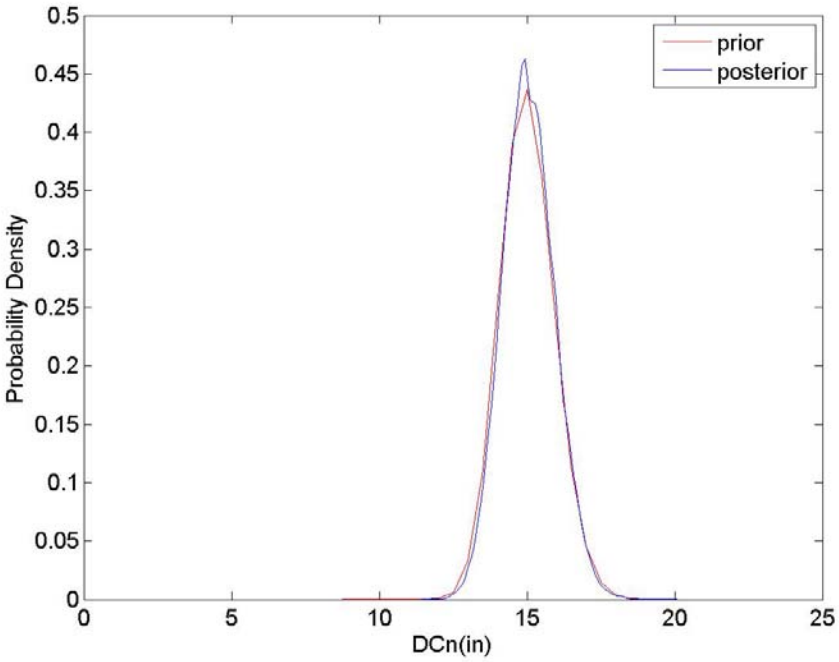

Figure A-37. Prior and Marginal Probability Distribution of Posterior for DCn for Problem 00.

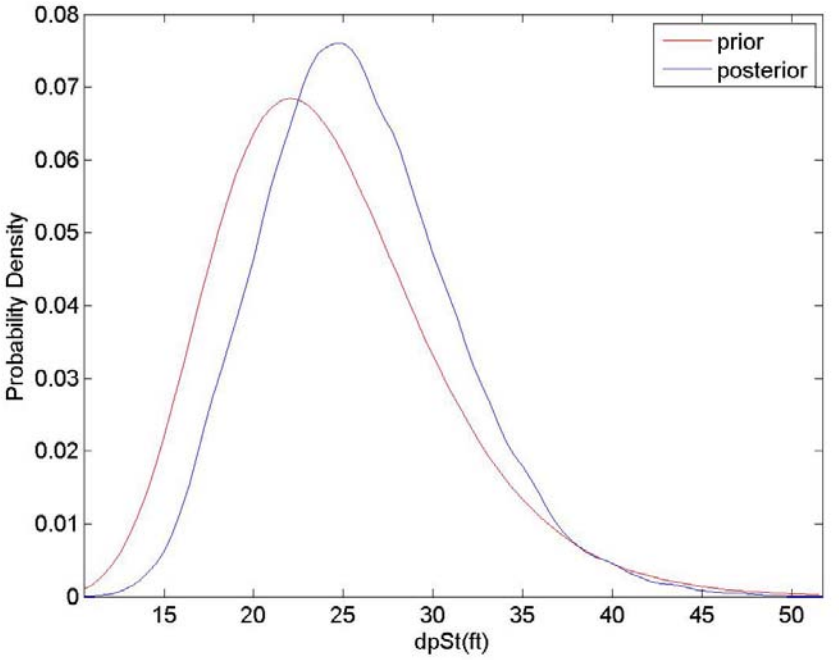

Figure A-38. Prior and Marginal Probability Distribution of Posterior for dpSt for Problem 00.

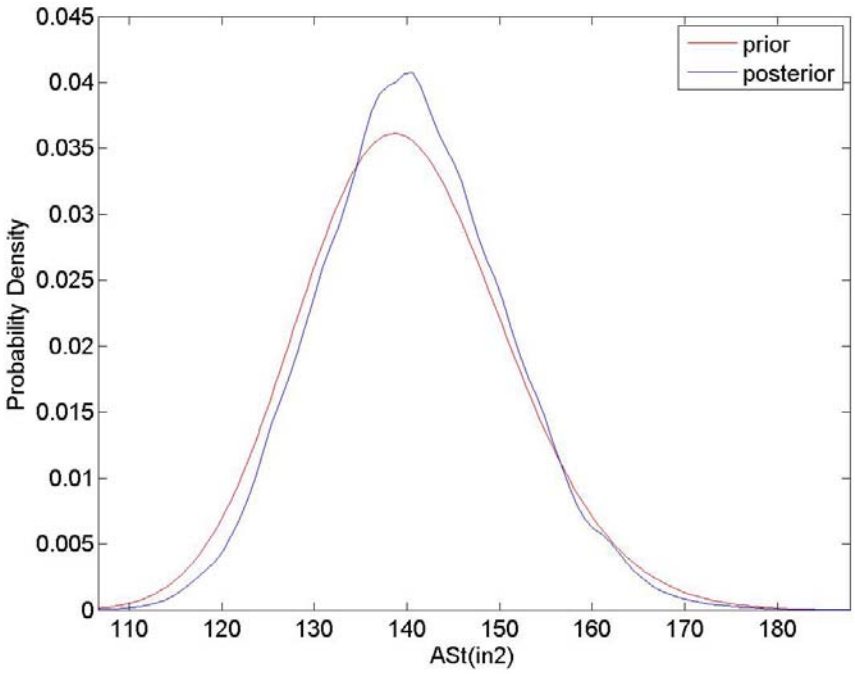

Figure A-39. Prior and Marginal Probability Distribution of Posterior for ASt for Problem 00.

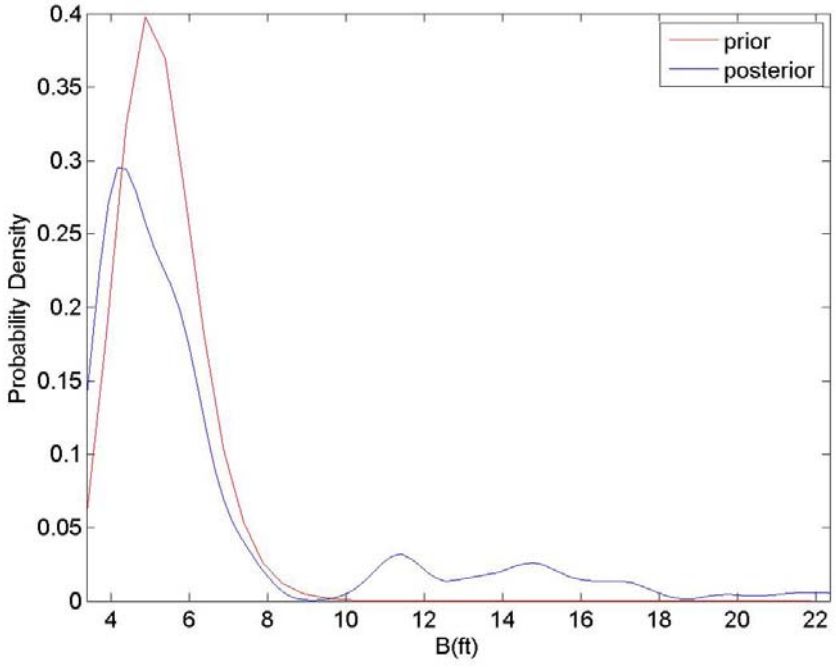

Figure A-40. Prior and Marginal Probability Distribution of Posterior for B for Problem 00.

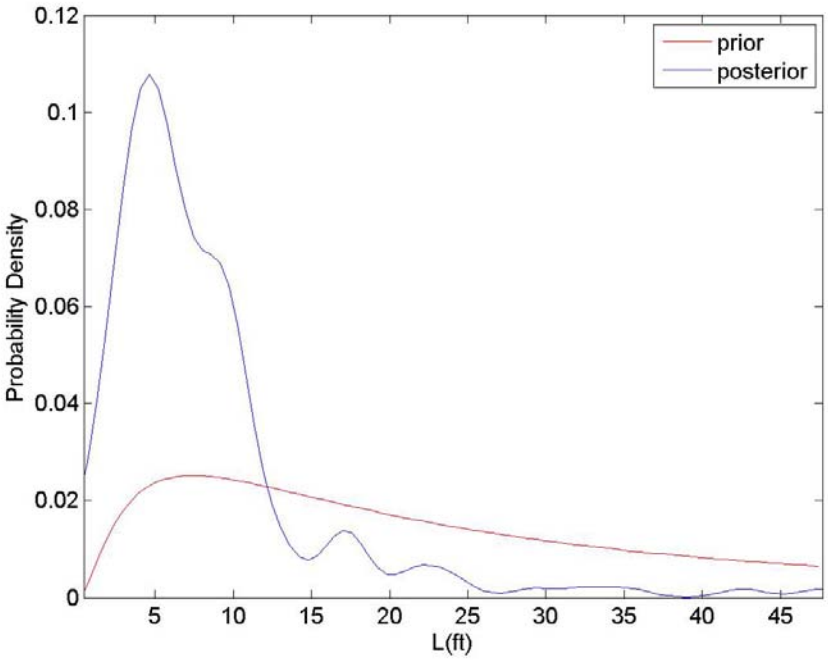

Figure A-41. Prior and Marginal Probability Distribution of Posterior for L for Problem 00.

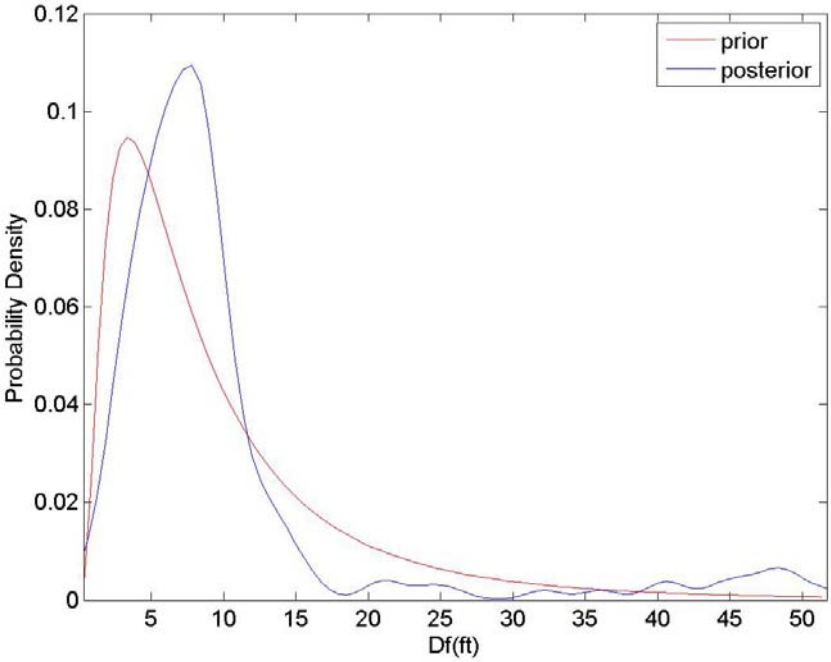

Figure A-42. Prior and Marginal Probability Distribution of Posterior for Df for Problem 00.

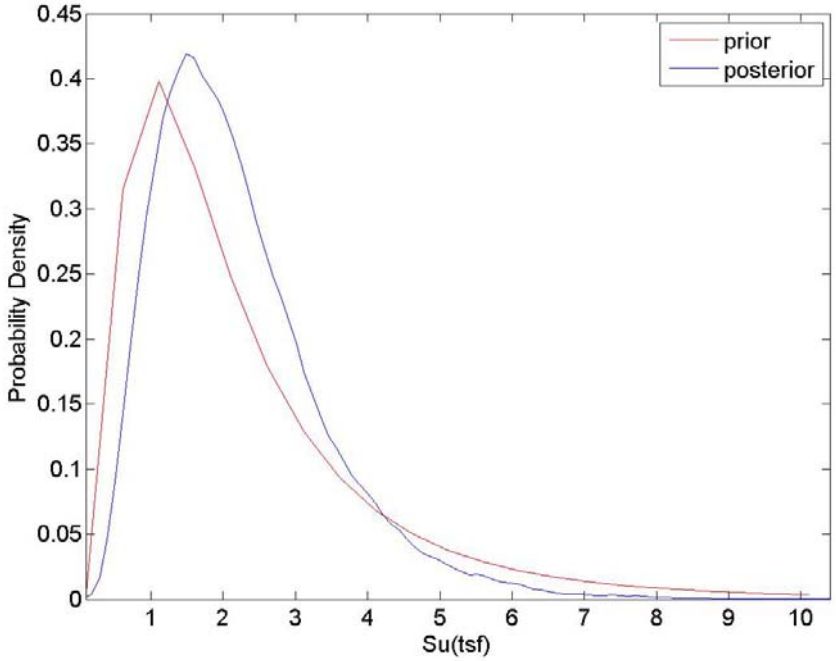

Figure A-43. Prior and Marginal Probability Distribution of Posterior for Su for Problem 00.

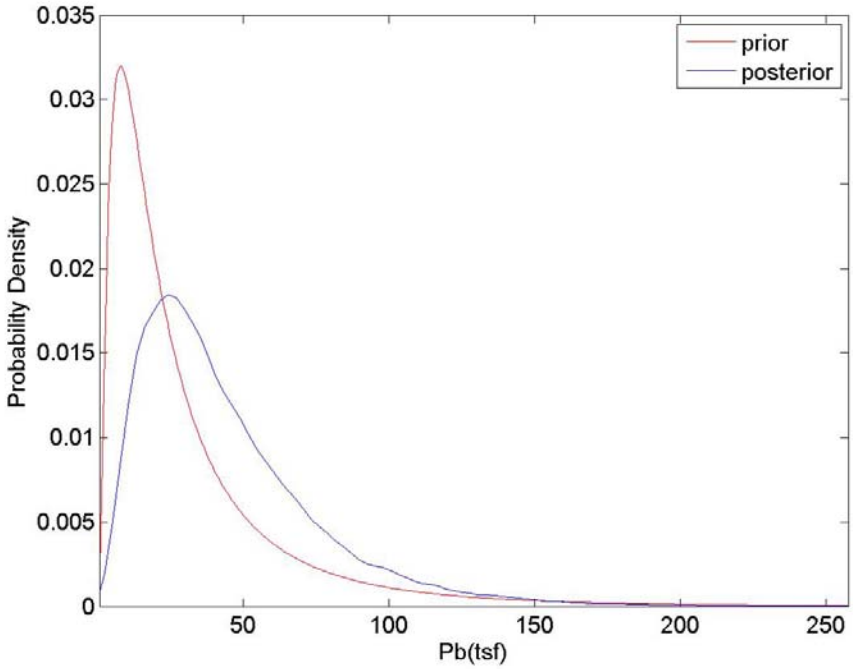

Figure A-44. Prior and Marginal Probability Distribution of Posterior for Pb for Problem 00.

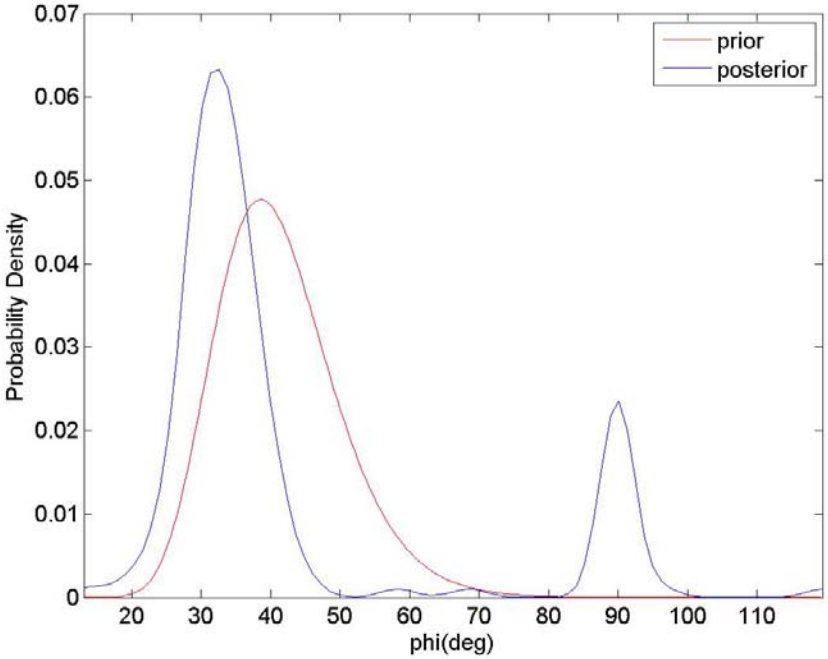

Figure A-45. Prior and Marginal Probability Distribution of Posterior for phi for Problem 00.

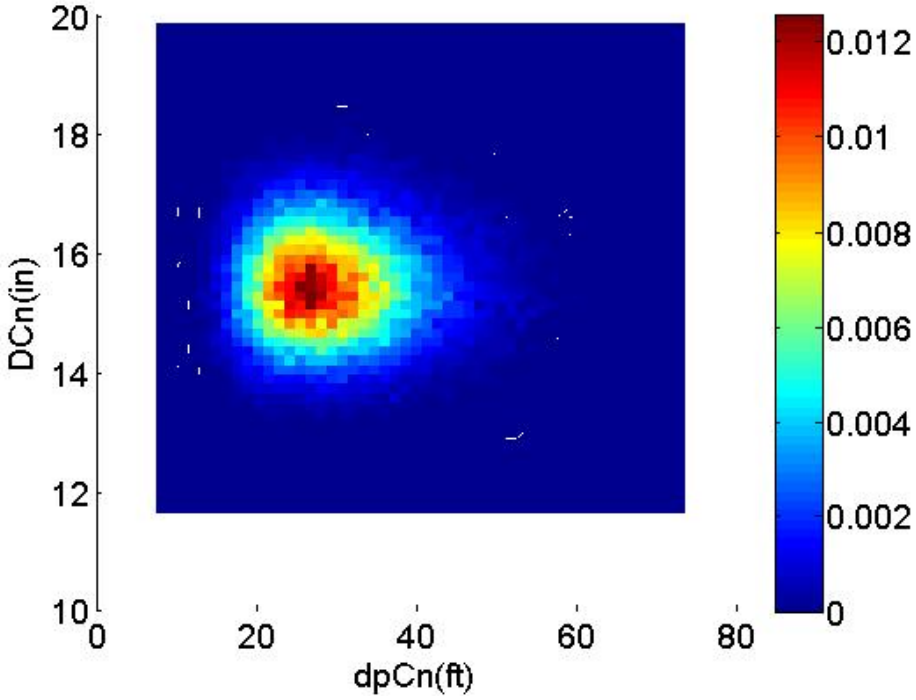

Figure A-46. Joint Relative Frequency Density of the Posterior for DCn and dpCn for Problem 00.

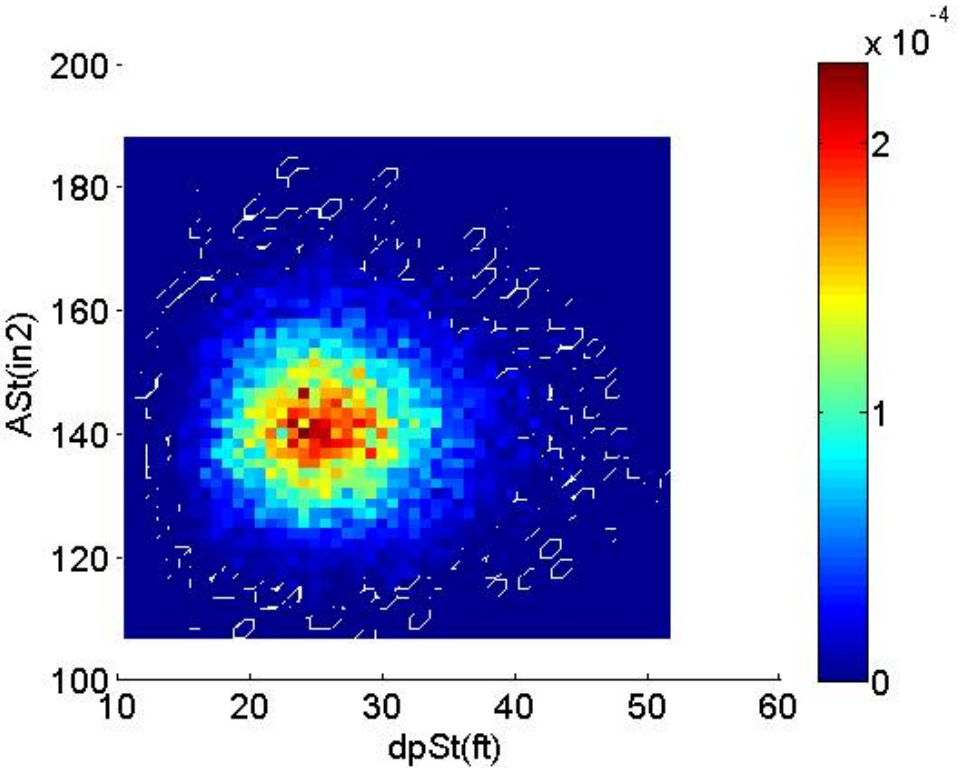

Figure A-47. Joint Relative Frequency Density of the Posterior for ASt and dpSt for Problem 00.

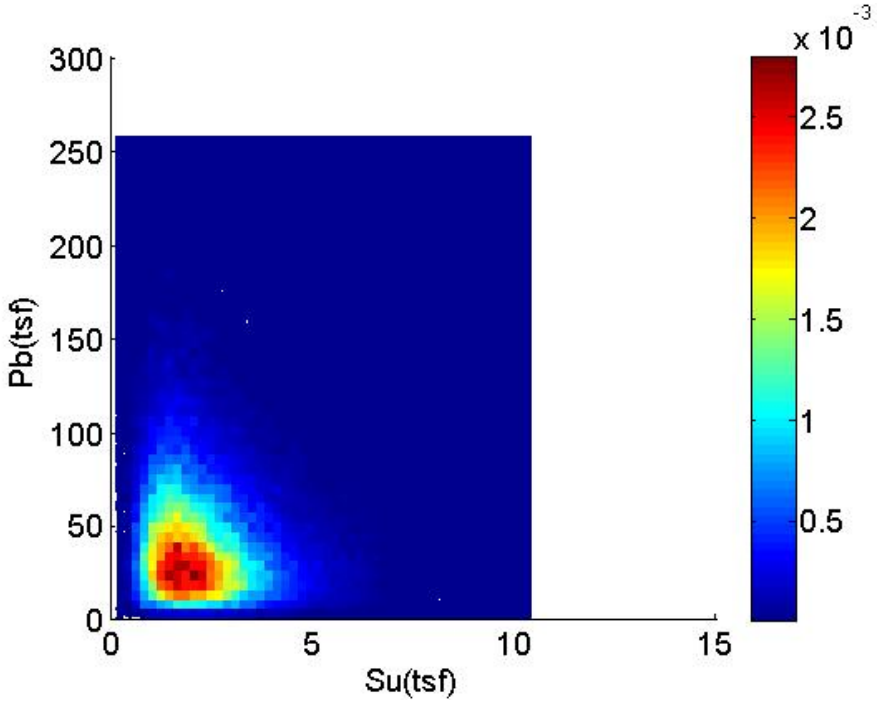

Figure A-48. Joint Relative Frequency Density of the Posterior for Su and Pb for Problem 00.

DEVELOPED CODES

This section includes codes developed in this study.

MATLAB code developed for estimating total load of a bridge bent:

```
clc;
clear;
% Get the bridge info table
x=load('bridge_info.txt')
% Define the superstructure type and find corresponding load
parameters
loadfunc=load('1125-DrSh.txt')
m=size(x,1)
for i=1:m
% Find the corresponding typical RW for the bridge
% important: Remember to change the bins depending on the loadfunc
table typical RW & Skews
RwBins=[24 28 30 38 44];
MaxRwBin=max(RwBins);
RWDis=[abs(x(i,1)-RwBins(1,1)),abs(x(i,1)-RwBins(1,2)),abs(x(i,1)-
RwBins(1,3)),abs(x(i,1)-RwBins(1,4)),abs(x(i,1)-RwBins(1,5))];
[RwDis,IRw]=min(RWDis);
Rw(i)=RwBins(IRw);
 % find the corresponding typical skew for the bridge
SkBins=[0 15 30 45];
SkDis=[abs(x(i,2)-SkBins(1,1)),abs(x(i,2)-SkBins(1,2)),abs(x(i,2)-
SkBins(1,3)),abs(x(i,2)-SkBins(1,4))];
[SkDisn,ISk]=min(SkDis);
Sk(i)=SkBins(ISk);
% start calculating load for each bent using load parameters
j=0
while j<size(loadfunc,1)
    j=j+1;
    if x(i,1)<=MaxRwBin
    if loadfunc(j,1)==Rw(i) & loadfunc(j,2)==Sk(i)
        TotLoad(i,1)=loadfunc(j,3)*x(i,3)+loadfunc(j,4);
        break
    end
    elseif x(i,1)> MaxRwBin
        if loadfunc(j,1)==Rw(i) & loadfunc(j,2)==Sk(i)
        TotLoad(i,1)=x(i,1)/MaxRwBin
*(loadfunc(j,3)*x(i,3)+loadfunc(j,4));
        break
        end
    end
end
end
```

VALIDATION OF LOAD ESTIMATION PROCEDURE-BRIDGE ID: 17-82-2144-01-002

L_1=75 ft, L_2=45 ft, RW=32 ft

Est. total load per shaft using the proposed method=114 tons

The estimated quantities table for this bridge is extracted from the bridge as-built plans:

SUMMARY OF ESTIMATED QUANTITIES

BID ITEM DESCRIPTION / BRIDGE ELEMENT	DRILLED SHAFT (18 IN)	DRILLED SHAFT (30 IN)	CL C CONC (ABUT)	CL C CONC (BENT)	CL S CONC (APPR SLAB)	REINF CONC SLAB	PRESTR CONC BEAM (TY C)	CONC SURF TREAT (CLASS I)	ARMOR JOINT (WITH SEAL)	RIPRAP (STONE COMMON) (DRY) (12 IN)	RAIL (TY T203)
	LF	LF	CY	CY	CY	SF	LF	SY	LF	CY	LF
2 - ABUTMENTS	146	292	64.0		80.6				79.2		88
2 - INTERIOR BENTS		168		38.1							
1 - 165.00' PRESTR CONC BEAM UNIT						5280	655.45	575			330
TOTAL	146	460	64.0 (1)	38.1 (1)	80.6	5280	655.45	575	79.2	282	418

Dead Load: Weight of superstructure items:
Interior bent cap = 1/2 * (38.1 * 4.05) = 77.16 kips
Drilled Shafts = 1/2 (168 × 0.15 × л × (30/12) ^ 2/4) = 61.85 kips
Concrete slab = 8/12 × 32 × (75 + 45)/2 × 0.15 = 192 kips
Railing = (75 + 45) ×0.38=45.6 kips
Beams = 4 × (75 + 45)/2x0.516=123.8 kips
Sum = 50045 kips = 250.23 tons

Live Load-HL93
2 × (0.32 (75 + 4) − (448/75 + 112/45)+72) = 203.88 kips = 101.94 tons

Total Load
250.23 + 101.94 = 352.22 tons/bent = 352.22/3 = 117.41 tons/shaft

Error of Estimation
(117.41 − 114)/114 = 2.99%